



HAL
open science

Hydrodynamics of oil in contact with an aqueous foam : wetting, imbibition dynamics and flow in rough confined media

Rémy Mensire

► **To cite this version:**

Rémy Mensire. Hydrodynamics of oil in contact with an aqueous foam : wetting, imbibition dynamics and flow in rough confined media. Reactive fluid environment. Université Paris-Est, 2016. English. NNT : 2016PESC1137 . tel-01459477

HAL Id: tel-01459477

<https://pastel.hal.science/tel-01459477>

Submitted on 7 Feb 2017

HAL is a multi-disciplinary open access archive for the deposit and dissemination of scientific research documents, whether they are published or not. The documents may come from teaching and research institutions in France or abroad, or from public or private research centers.

L'archive ouverte pluridisciplinaire **HAL**, est destinée au dépôt et à la diffusion de documents scientifiques de niveau recherche, publiés ou non, émanant des établissements d'enseignement et de recherche français ou étrangers, des laboratoires publics ou privés.



UNIVERSITÉ
— PARIS-EST

Navier

Graduate School

Science, Engineering and Environment

Laboratoire Navier - UMR 8205 CNRS - ENPC - IFSTTAR

Dissertation

Presented in candidacy for the degree of DOCTOR OF PHILOSOPHY
of PARIS-EST UNIVERSITY

by

Rémy MENSIRE

**Interfacial hydrodynamics between oil and aqueous
foams: wetting, imbibition dynamics and flow into rough
confined media**

Specialty: Mechanical Engineering - Physics of fluids

Defended on September 28th 2016 in front of the following jury:

Referee	Emmanuelle RIO	(Paris-Sud University - LPS)
Referee	Yannick PEYSSON	(Institut Français du Pétrole - Energies Nouvelles)
Examiner	Cyprien GAY	(Paris-Diderot University - MSC)
Jury chair	Hugues BODIGUEL	(University of Grenoble - LRP)
Supervisor	Elise LORENCEAU	(Paris-Est University - Laboratoire Navier)
Co-advisor	Howard A. STONE	(Princeton University)



Thesis supported by the Corps des Ponts, des Eaux et des Forêts and the Agence Nationale de la Recherche (ANR-11-JS09-012-WOLF) and completed at:

Laboratoire Navier - UMR 8205 CNRS - ENPC - IFSTTAR

2, allée Képler

77420 Champs-Sur-Marne

France



In collaboration with the **Complex Fluids Group**

at Princeton University

Department of Mechanical and Aerospace Engineering

Engineering Quadrangle, Olden Street

08544 Princeton, New Jersey

United States of America

Résumé

L'extraction de matières premières du sol à des fins énergétiques (récupération assistée d'huile) et environnementales (dépollution des sols) fait l'objet de recherches intensives en lien avec des thématiques telles que la séquestration du carbone ou la fracturation hydraulique. L'objectif est de trouver des méthodes moins destructives, moins gourmandes en matériel et en énergie, mais aussi plus efficaces et moins coûteuses.

Nous proposons d'étudier une méthode alternative aux moyens conventionnels avec l'utilisation de mousses aqueuses comme agent extracteur d'huile. Les mousses aqueuses sont souvent utilisées en présence d'huile : dans des applications quotidiennes comme la cosmétique et la détergence, mais aussi dans des domaines moins connus comme la décontamination des centrales nucléaires ou l'industrie pétrolière. Ainsi, des tensioactifs et du gaz sont couramment injectés dans le sol afin d'améliorer les procédés de récupération de pétrole.

Nous explicitons deux mécanismes d'extraction que nous quantifions en termes d'efficacité et de stabilité. Tout d'abord, la mousse peut aspirer de l'huile en son sein, comme le ferait une éponge. Ensuite, lorsque celle-ci est mise en écoulement, elle peut entraîner de l'huile confinée dans la rugosité d'une surface par cisaillement. Notre étude s'appuie en particulier sur une analyse théorique et expérimentale, à la fois multi-échelle, statique et dynamique pour laquelle nous avons systématiquement fait varier les paramètres géométriques (configuration de l'huile, taille des bulles et fraction volumique de liquide dans la mousse) et physico-chimiques (tensions interfaciales, rigidité des interfaces entre bulles et viscosité).

Mots-clés:

Tensioactifs, Mousses aqueuses, Huile, Etalement de gouttes, Imbibition, Instabilité hydrodynamique, Microfluidique, Surfaces texturées, Milieux poreux.

Abstract

The extraction of raw materials from the soil for energetical (enhanced oil recovery) and environmental purposes (soil remediation) is the subject of intense fundamental and applied research. This field is related to other important topics, such as carbon sequestration and hydraulic fracturing. The goal is to find fewer destructive, as well as energy and material-saving methods. These techniques should also be cost-effective and more efficient.

To find a substitution to conventional means, we study an alternative method that puts aqueous foams on the map as the extracting material. Aqueous foams are often used in numerous daily applications, such as cosmetics and detergency, but also in less known fields, such as the decommissioning of nuclear power plants and the oil industry. Thus, surfactants and gas are commonly injected into the soil to improve the recovery processes of oil.

We explain two extraction mechanisms that we quantify in terms of efficiency and stability. On one hand, the foam is able to absorb oil, similarly to a solid sponge. On the other hand, when a flow of foam is induced, the foam can entrain oil confined in the roughness of a surface by shearing the oil-water interface. Our work especially lies on a theoretical and experimental analysis, which is multiscale, static and dynamical. We systematically vary the geometrical parameters (oil configuration, bubble size and liquid fraction in the foam) and the physical and chemical parameters (interfacial tensions, interfacial rigidity and viscosity).

Keywords:

Surfactants, Aqueous foams, Oil, Drop spreading, Imbibition, Hydrodynamical instability, Microfluidics, Liquid-infused surfaces, Porous media.

Acknowledgements

This thesis represents the end of my student path but the beginning of a new chapter in my life. This work would not have been possible without the help and the support of many people to whom I am very grateful.

First, of course, I would like to thank **my parents**. You constantly support me to get the best of me. You encourage me for any plan and project I have in and out of my studies. You offer me the best possible conditions to fulfill my dreams and learn so many things in different fields: science, sport, music, travels, literature and so on. Now, I have so many options in my life and my job career and I give you credit for that. You know that I like going in every direction, I am very curious about everything and I am picky to make decisions. But the most important thing is that you teach me to fight for everything, to give the maximum I can to have no regrets, to do what I like and this is what I have tried to do. A big thank you, I love you.

Second, I obviously thank my supervisor **Prof. Elise Lorenceau** for supporting me and helping me during those hard three years. Well, actually five years, since I met Elise during my Master's internship... You are an incredible scientific mentor and researcher who gave me meaningful advice on my projects and encouraged me to keep going in the right direction: always stay positive, never give up. You let me carry out my own thinking process and experiments, which I really appreciate. And you let me meet your nice kids, so thanks to Louison, Lucile and Jules for your smiles, your enthusiasm and your questions (I'm sure you got some...), you have a great Mom.

Third, I address my deep acknowledgements to **Prof. Howard A. Stone**. You hosted me in your Complex Fluid group at Princeton University with open arms. I was so lucky to be able to work with you, I learnt so many things and you made my time in Princeton so enjoyable. I wish every student in fluid dynamics and soft matter could learn as many things as I learnt from you and your whole group.

I am also very grateful to the following people from the Navier Institute with whom I spent three amazing years at work but also off-work:

- **Alizée Lehoux**: you are a very special friend to me. We had a lot of fun and nice and burning discussions, as well as joking time. We shared unique moments whenever we spent time together: swimming, running, strolling, tasting original food products but not only... I am sure we will nurture this bond. Keep swimming, you are the only speaking dolphin I know!
- **François Gorlier**: my roommate. What can I say? The most enjoyable guy in the lab. You are

a superhero who speaks to himself but I like that. Do not forget the music quizzes...

- **Jennifer Fusier**: my dear lab delegate. You are the most persevering person. Keep going, you will succeed. Do not forget to work on your arm strength and become a board game master.

- **Blandine Feneuil**: the professional runner and seamstress. So quiet but full of energy. Keep running, running and running to catch me...

- **Benjamin Haffner, Benoit Laborie and Guillaume Chivot**: I had a lot of fun while joking with you, my former labmates. You are heavy drinkers but you always had a positive attitude!

I also want to give a special credit to **Mathilde Maillard, Marine Fourmentin, Lucie Ducloué, Emmanuel Keita, Antoine Morandea, Thibault Chevalier, Aymeric Mouquet, Xiao Zhang, Dr. Romain Morini and Dr. Keyvan Piroird**.

Then, I have a special word for the following members of the Complex Fluids group and students at Princeton University:

- **Jesse T. Ault**: one of the most clever and reactive labmates I have ever met. The imbibition project would not have succeeded without your help. You were the only American left (maybe not now...), so keep carrying the Stars and the Stripes high in the lab! And stop eating food in tin cans!

- **Dr. Jason S. Wexler**: like Jesse, you laid the foundations for the microfluidic project. Bold and curious, you always had inventive ideas with this West Coast relaxed attitude!

- **Dr. Hyungsoo Kim and Dr. Sangwoo Shin**: the Korean daddies (whisky and microfluidic experts!). You also assisted me for my projects by your advice and your intuition.

- **Ching-Yao Lai**: you have become one of my nice friends. You are always the first one to help people be integrated into the group and Princeton's life. Keep doing it, it is invaluable.

- **Jie Feng**: the paper machine. I will always remember our wonderful karaoke time in New York and your help on the spreading project!

- **Kevin Kim**: my deskmate. You have also become a close friend. Do not work too hard and do not sleep in the lab!

- **Suin Shim**: you are the best piano player I have ever met and heard. Always quiet but ready for a drink, I love this attitude.

- **Dr. Janine Nunes**: well, you allow this group to run so smoothly. What will happen when you leave...

- **Mrs. Jill F. Ray**: like Janine at another level, you enable the Department of Mechanical and Aerospace Engineering to run perfectly. And you also make visiting scholars and students feel comfortable.

- **Ting-Hsuan Chen**: my best friend in Princeton. I am so glad to have met you. Not only are you a remarkable young researcher, but you are also one of the most open-minded people I have ever met. Thanks to your dynamism and your support, you make me discover off-campus life

and many cultural stuffs in Princeton, New Jersey and many other places!

I can also mention the following people that made my stay in Princeton enriching and unforgettable: **Matt Fu, Christine Viveiros, Cat Shen, Clay Byers, Mike Hepler, Yibin Zhang, Liz Davison, Julien de Lanversin, Sophia Li, Mircea Davidescu, Ai-Lei Sun and Dr. Romain Fardel.**

Professionally speaking, I would like to thank the professors I have met along the way and who brought relevant advice and help for my different projects: **Profs Olivier Pitois, Isabelle Cantat, Etienne Reyssat, José Bico, François Gallaire and David Quéré.** And also all the people in support of my research: **Augustin Guibaud, David Hautemayou, Cédric Mézière, Prof. Stéphane Rodts, Dr. Denis Courtier-Murias, Carmen Sanchez and Nathalie Cherer.**

Finally, I thank **Profs Emmanuelle Rio, Yannick Peysson, Hugues Bodiguel and Cyprien Gay** for the time they dedicated to review my thesis and to be part of my jury.

Thanks to all of you!!!



Figure 1: Thank you!

Contents

Main parameters	1
Introduction	3
1 Aqueous foams and their applications in environment and energy	9
1.1 The physics of interfaces and surfactants	13
1.1.1 Interfacial energy, tension and force	13
1.1.2 Interface, drop and bubble	15
1.1.3 Surfactants: who are you?	18
1.1.4 Effect of surfactants on the interfacial mechanics	22
1.1.5 Soap film: a fragile structure	25
1.2 Aqueous foams: definition, structure, characteristics and main properties	27
1.2.1 Foam structure	28
1.2.2 Main properties of foams	31
1.2.3 How foams flow...	32
1.3 Applications in environment and energy	37
1.3.1 Foams in everyday life	38
1.3.2 Towards a cleaner environment: soil remediation	39
1.3.3 Towards more energy supply: enhanced oil recovery	43
1.4 Conclusions	44
2 Oil-foam interactions and stability	47
2.1 Stability of a soap film towards oil	50

2.1.1	Liquid antifoams	50
2.1.2	Mechanisms of film rupture	51
2.2	Stability of oil-filled Plateau borders	55
2.2.1	In-situ interactions between oil and Plateau borders	55
2.2.2	Pseudoemulsion film and foam stability	58
2.3	Experimental study of the stability of oil-laden foams	60
2.3.1	Testing procedure	60
2.3.2	Morphology of gravitational imbibition into foams	63
2.4	Conclusions	67
3	Plateau borders and oil: equilibrium shape and coalescence	69
3.1	Picture of oil invasion in Plateau borders by numerics	72
3.1.1	Oil slug in a Plateau border	72
3.1.2	Interfacial energy comparison with <i>Surface Evolver</i>	75
3.2	Breaking dynamics in the oil-filled Plateau borders	77
3.2.1	The Rayleigh-Plateau instability	78
3.2.2	Breaking of an emulsified viscous cylinder	81
3.3	Conclusions	88
4	Soap films and oil: dynamics of rising oil droplets spreading at the air-water interface	91
4.1	Spreading of oil on solid surfaces	94
4.1.1	Wetting theory on solid surfaces	94
4.1.2	Dynamics of liquid spreading on air-solid interfaces	98
4.2	Spreading of oil on air-water interfaces from the air phase	100
4.2.1	Liquid-liquid wetting	101
4.2.2	Regimes of oil spreading on air-water interfaces	102
4.3	Spreading of oil rising from the aqueous phase at air-water interfaces	106
4.3.1	Experimental results	106
4.3.2	Short-time dynamics	108
4.3.3	Long-time dynamics	111

4.4	Conclusions	116
5	Oil imbibition into aqueous foams	117
5.1	Imbibition through liquid foams	121
5.1.1	1D Imbibition through solid porous media	121
5.1.2	Liquid flow in dry aqueous foams	126
5.2	Point-source imbibition from an oil-filled pore	132
5.2.1	3D imbibition from a point-source for miscible liquids	132
5.2.2	3D imbibition from a point-source for immiscible liquids	135
5.2.3	Experimental imbibition front	137
5.2.4	Comparison with experimental results	140
5.3	Capillary rise into aqueous foams for miscible and immiscible liquids	143
5.3.1	Oil absorption: characteristics and picture	144
5.3.2	Theoretical analysis	145
5.4	Oil recovery by a moving foam	154
5.4.1	Experimental configuration	154
5.4.2	Modelization of the imbibed moving foam	156
5.5	Conclusions	161
6	Foam - oil interactions in micropatterned structures	163
6.1	Textured and liquid-infused surfaces	167
6.1.1	Wetting of rough surfaces	167
6.1.2	Failure of textured surfaces	172
6.2	Surfactant-driven oil extraction from micropatterned channels	178
6.2.1	Materials	179
6.2.2	Experimental observations and results	182
6.2.3	Effect of surfactants on the extraction dynamics	183
6.2.4	Extraction instability	189
6.3	Foam-driven oil extraction from micropatterned channels	190
6.3.1	Controlled foam generation	191

6.3.2	Experimental results and discussion	193
6.4	Conclusions	198
Conclusions and future work		201
A	Examples of flow dynamics by resolution of Stokes' equation	207
A.1	Spreading dynamics of a liquid droplet on a solid surface	208
A.1.1	Lubrication approximation	208
A.1.2	Thin film equation	209
A.1.3	Spreading laws	209
A.2	Poiseuille flow	210
A.2.1	In a cylindrical tube	211
A.2.2	Between two plates	211
B	Rayleigh-Plateau instability of a viscous fluid in another viscous fluid	213
B.1	Inertia-dominated regime	214
B.2	Viscous-dominated regime	215
C	Microfluidic fabrication: the "sticker technique"	219
C.1	Fabrication of the channel	220
C.1.1	Fabrication of the sticker	220
C.1.2	Fabrication of the pattern	220
C.2	Sketch of the microfabrication	220
D	Properties of textured surfaces	223
D.1	Properties of superhydrophobic surfaces	224
D.1.1	Self-cleaning	224
D.1.2	Controlling the hydrophobicity	224
D.1.3	Tuning the oleophobicity	225
D.2	Properties of liquid-infused surfaces	227
D.2.1	Rolling and pinning effects on liquid-infused surfaces	227
D.2.2	Conditions for slippery surfaces	228

Bibliography

231

List of Figures

1	Thank you!	viii
2	a. <i>Child with a soap bubble</i> by Rembrandt (1606-1669). b. <i>Soap bubbles</i> by Edouard Manet (1832-1883).	4
3	For the better: a. Cappucino. b. Beer foam. For the worse: c. foam-induced river pollution.	5
4	Liquid-infused surface in a micrometer channel. Surfactants and foams are injected to drag oil out of the patterned surface.	7
1	Aqueous foams and their applications in environment and energy	9
1.1	Formation of a liquid film inside a frame.	14
1.2	a. A gerris “walking on water”. b. A needle floating at the surface of a water bath.	15
1.3	Surface minimization of the interfacial area of a given volume of gas comprised inside a cubical bubble. It evolves towards a sphere, which is the shape corresponding to the minimization of the interfacial energy, as shown by the different values of the dimensionless interfacial area Σ_d . Numerical simulations by the software <i>Surface Evolver</i> [20, 21]. The dimensionless interfacial area Σ_d is indicated in every image and decreases from the cube of unit length 1 to the sphere.	16
1.4	Variations of the drop radius R_d for the calculations of the Laplace pressure.	16
1.5	Pendant drop method with the fitting of the drop shape.	18
1.6	Chemical composition and structure of common surfactants. The red area is the polar hydrophilic head and the grey area is the hydrophobic tail.	19
1.7	Typical evolution of the air-water interfacial tension γ_{aw} with the bulk surfactant concentration c for SDS and CAPB-SLES-Mac solutions.	20
1.8	Soap film with surfactants at the air-water interfaces.	21
1.9	Liquid film pulled from a surfactant solution.	22
1.10	a. Interface under compression - dilatation. b. Interface under shear.	22

1.11	Deformation of a soap film under dilatation: "healing" process by air-water interfacial tension gradient from γ_{aw}^- to γ_{aw}^+	24
1.12	a. Measurements of the air-water dilatational modulus $ E^* $ for two types of surfactants: CAPB-SLES-Mac and SDS. b. Measurements of the oil-water dilatational modulus $ E^* $ for two types of surfactants: CAPB-SLES-Mac and SDS. c. Typical variations of air-water interfacial tension γ_{aw} d. Typical variations of interfacial area with respect to time t . Curves are given for CAPB-SLES-Mac with the following parameters: $\gamma_{aw} = 23.7$ mN/m ($c = 10$ g/L) at equilibrium, initial drop volume $V_d = 2$ μ L, oscillation amplitude $\delta V_d = 0.2$ μ L and frequency $f = 0.2$ Hz.	25
1.13	a. Shrinking of a film by the motion of regions of smaller thickness. b. Marginal regeneration in a film. The black films (regions of smaller thickness) generate a recirculation of water inside the film. Below: Top view of a film close to the frame.	26
1.14	Opening dynamics of a film.	27
1.15	Foam topology: dry foam (a), wet foam (b) and suspension of bubbles (c).	28
1.16	Plateau borders (red), films (green), vertices (blue) and the Plateau laws.	29
1.17	Plateau border and its curvature radii R_1 and R_2 for a dry foam.	30
1.18	Kelvin cell and its typical geometrical features.	30
1.19	Rheological laws of complex and simple fluids.	33
1.20	a. Variation of the shear stress τ_{xy} with respect to the deformation ϵ for a foam of witconate-PEO in a plate-plate geometry [101]: $\phi_l = 0.03$, $\dot{\epsilon} = 0.042$ s ⁻¹ . b. Flow curve $\tau(\dot{\epsilon})$ for a foam of commercial surfactant in a Couette geometry [87]. The liquid fractions are given in the legend. The yield stress tends to disappear for high liquid fractions above 0.5 for which the foam looks more like a suspension of bubbles. The dotted lines are the Herschel-Buckley fit with the power law coefficient n varying from 1 for $\phi_l = 0.4$ to 0.66 and 0.5 for $\phi_l \approx 0.2$	34
1.21	Apparent viscosity η_{app} as a function of the applied shear stress τ_{xy} in a creep experiment for a CAPB-SLES-Mac foam with a 60 μ m bubble radius (see Chapter 6). The equilibrium yield stress τ_Y is indicated by the red arrow.	35
1.22	T1 event in 2D with ϵ the strain and ϵ_Y the yield strain. a. Initial state. b. Shear state where u is the displacement at the top of a bubble. c. Unstable state. d. Final state.	36
1.23	Dimensionless flow curves for different wet foams ($\phi_l = 0.1$) generated from surfactant solutions of SLES-CAPB (Mac is myristic acid and Lac is lauric acid) with mobile (without fatty acids) and rigid interfaces (with fatty acids Mac and Lac) [81].	37
1.24	Examples of industrial applications.	39
1.25	Map of the degraded sites worldwide (Source: UNEP).	40

1.26	Physical method for soil remediation: soil ventilation.	41
1.27	Physical methods for soil remediation: a. Pollution confinement. b. Pollution solidification.	41
1.28	Remediation by chemical reactions.	42
2	Oil-foam interactions and stability	47
2.1	a. Emergence of oil at the air-water interface. b. Spreading of oil at the air-water interface.	51
2.2	Spreading fluid entrainment mechanism. The red arrows indicate the oil spreading while the green arrows designate the outward flow of water inside the film.	52
2.3	Geometry of the oil drop during bridge formation.	53
2.4	a. Unstable bridge: $\alpha_{ow} < 90^\circ$. b. Stable bridge: $\alpha_{ow} > 90^\circ$	55
2.5	a. Bridging-dewetting mechanism. b. Bridging-stretching mechanism (black and white snapshots showing experimental observations [56]). c. Stable bridging.	56
2.6	Stages of film thinning with oil droplets expelled to the Plateau border.	57
2.7	Spreading-wave generation.	58
2.8	Pseudoemulsion film at the frontier between the oil phase and the air phase	59
2.9	Disjoining pressure Π (Pa) as a function of film thickness e (nm) for SDS (concentration = 0.1 M) and dodecane [15].	59
2.10	a. "Foamulsion" with rapeseed oil droplets - oil fraction: 70 % [161]. b. "Foamulsion" with octane droplets [103].	60
2.11	a. Experimental set-up for the stability experiments. b. Typical response of the foam to oil invasion for three different oil-foaming solution combinations: sunflower oil - CAPB+SLES+Mac, silicon oil - CAPB+SLES+Mac and sunflower oil - saponin (from top to bottom). Oil appears white due to a fluorescent agent (Yellow Black from Rohm and Haas).	62
2.12	a. (S , E) diagram for the tested oils. b. (B , E) diagram for the tested oils. Two points correspond to miscible liquids: CAPB+SLES+Mac+Glycerol with $\eta_w = 10$ mPa.s and $\eta_w = 100$ mPa.s. The symbol * designates the surfactant CAPB-SLES-Mac.	63
2.13	Experimental set-up for the forced drainage experiment.	64
2.14	a. Invasive regime for $Q = 5$ mL/h (olive oil). b. "Fracture" regime for $Q = 20$ mL/h (sunflower oil).	65
2.15	Draining front h as a function of time t for the forced drainage of olive oil (OO) and sunflower oil (SO). The injection flow rate Q (mL/h) and the initial liquid fraction ϕ_i are indicated in the legend.	65

2.16	Flow morphology of a simple fluid flow (air) in a frictional fluid or granular mixture in a $(\log \phi^{-1}, \log Q)$ diagram where ϕ is the solid fraction and Q the injection flow rate. The figure is extracted from [162].	66
2.17	Experimental observations of air injection into a confined granular suspension. a. Percolation regime at low flow rate. b. "Fracture" regime at high flow rate. The pictures are extracted from [186].	67
3 Plateau borders and oil: equilibrium shape and coalescence		69
3.1	Configurations of the oil droplet in the Plateau border for different droplet sizes r^* , where $r_c^* = 2/\sqrt{3} - 1$ is the critical dimensionless radius for which the oil droplet first touches the walls of the Plateau border. In the far right image, the dotted lines indicate that oil can also swell the Plateau border and invert the curvature.	73
3.2	Oil droplets in Plateau borders [132]. a. Side-view. b. Cross-section. From top to bottom: $K = 1, 0.5, 0.2$ and 0.1 ; the oil-water interfacial tension γ_{ow} decreases. From left to right: $r^* = 0.2, 0.4, 0.7$ and 1 ; the volume of oil increases.	74
3.3	Dimensionless pressure difference between the pseudoemulsion film and the Plateau border Δp_f^* with respect to the dimensionless size of the oil droplet r^* [132].	75
3.4	Simulations by <i>Surface Evolver</i> . a. Inner configuration. b. Outer configuration.	76
3.5	Energy calculations using simulations by <i>Surface Evolver</i> : total interfacial energy E_I as a function of the volume ratio V_o/V_w . a. Sunflower oil (Sun) and olive oil (Olive)-CAPB+SLES+Mac. b. Silicon oil with $\eta_o = 100$ mPa.s (Si 100) and silicon oil with $\eta_o = 10$ mPa.s (Si 10)-CAPB+SLES+Mac. c. Silicon oil with $\eta_o = 10$ mPa.s (Si 10) and sunflower oil (Sun)-CAPB+SLES+Mac. d. Silicon oil with $\eta_o = 10$ mPa.s (Si 10) and hexadecane (Hex)-CAPB+SLES.	76
3.6	Mechanism of the Rayleigh-Plateau instability. From top to bottom: cylindrical thread, wave perturbation, breaking into small droplets.	79
3.7	Growth rate $\sigma_{RP}t_c$ as a function of kr_c in the inertial regime. The maximum growth rate is obtained for $k_{max}r_c \approx 0.7$	80
3.8	Dimensionless growth rate $\sigma_{RP}t_c$ as a function of kr_c in the viscous regime. The blue round dots designate the case $\eta_c > \eta_f$, while the orange triangular dots designate the case $\eta_c < \eta_f$. In both cases, the maximum growth rate is obtained for $k_{max}r_c = 0$	82
3.9	Experimental set-up presenting the slender Plateau border filled with oil at the junction between three soap films.	83
3.10	Snapshots of the breaking dynamics. Oil: olive oil; drop volume: $\Omega = 1.5 \mu\text{L}$	84

3.11	Side-view of the breaking process. a. Initial oil-filled Plateau border [137]. b. Breaking of the lower rear film. The Plateau border is ejected to the opposite direction. c. Oil-filled film before the Rayleigh-Plateau instability.	84
3.12	Wavelength λ_{max} as a function of the slug radius R_{oil} . The coloured dotted lines are the theoretical predictions [183]. The black dotted line is the prediction for the inertia-dominated regime [149] and the orange dotted line, the prediction for the viscous-dominated regime when the viscosity of the outer fluid is neglected.	85
3.13	Theoretical ratio wavelength of maximum growth - cylinder radius λ_{max}/R_{oil} as a function of the viscosity ratio η_o/η_w [183]. The solutions for our oil-foaming solution systems are indicated with the same color code as in Fig. 3.12.	85
3.14	Theoretical radius of the oil droplet R_d as a function of $(\lambda_{max}R_{oil}^2)^{1/3}$ for paraffin oil, olive oil and hexadecane. The oil radius R_{oil} is deduced from the volume Ω of the oil slug. The black dashed line represents the theoretical prediction from Eq. 3.7. Inset: Theoretical radius R_d as a function of $(\lambda_{max}R_{oil})^{1/2}$ by assuming a pancake-like shape. The black dashed line is the theoretical prediction as detailed in the text. We observe that the agreement is not quantitative.	86
4 Soap films and oil: dynamics of rising oil droplets spreading at the air-water interface		91
4.1	Liquid droplet on a solid surface in partial wetting.	95
4.2	Energy of the film E_S as a function of the thickness e for pseudo-partial wetting.	97
4.3	Spreading droplet and its precursor film.	99
4.4	Spreading regimes for a liquid droplet on a solid hydrophilic surface for PDMS with $\eta_l = 1$ Pa.s. From top to bottom, $\Omega_d = 37.9, 5.8, 4.03, 1.35, 0.35$ μL . The data are extracted from [31].	101
4.5	Topology of an oil lens spreading on a water surface in the limit where the gravity effects are negligible, i.e. the shape of the drops is only dictated by interfacial tension.	102
4.6	Oil-water interfacial tension γ_{ow} as a function of time t for the silicon oil ($\eta_o = 100$ mPa.s) - SDS system. The legend indicates the bulk concentration of surfactants.	102
4.7	Oil lens spreading at the air-water interface.	103
4.8	Spreading radius r as a function of time t for oil spreading on water-surfactants solutions [13]. Oil: PDMS (Polydimethylsiloxane $\eta_o = 100$ mPa.s). Aqueous bath: C ₁₆ TAB, Water, AOT (Dioctyl sulfosuccinate sodium) and C ₁₀ E ₅ . The black lines are the fit from Eq. 4.19.	104
4.9	Viscous oil lens spreading at the surface of a water bath.	105
4.10	Experimental set-up. The oil droplet rises from the immersed needle and spreads at the bath surface.	107

4.11	Configurations of an oil droplet at the air-water interface according to the values of the entry E and spreading S coefficient.	108
4.12	Snapshots of the spreading dynamics. a. No-surfactant case (aqueous solution = water and oil = silicon oil, $\eta_o = 5$ mPa.s); $R_d = 3.72$ mm and $Oh = 73.3$. b. Surfactant case in the short-time regime from $t = 0$ s to 0.4 s (aqueous solution = SDS solution, $C_{SDS} = 2$ g/L and oil = silicon oil, $\eta_o = 20$ mPa.s); $R_d = 2.84$ mm and $Oh = 7.7$. c. Surfactant case in the long-time regime from $t = 0.66$ s to 60 s (aqueous solution = SDS solution - $C_{SDS} = 2$ g/L and oil = silicon oil, $\eta_o = 20$ mPa.s); $R_d = 3.76$ mm and $Oh = 8.9$. The thick black line is the injection needle.	109
4.13	Dimensionless spreading radius R as a function of the dimensionless time T_{Oh} . The open dots correspond to a bath solution without surfactants and the close dots with surfactants. The type of oil - η_o (mPa.s) - C_{SDS} (per liter), Bo and Oh are indicated in this order in the legend. A corresponds to an attached droplet. The dashed line is Eq. 4.27. The black arrow in the snapshot indicates the direction of the oil movement.	110
4.14	Dimensionless spreading radius R as a function of the dimensionless time T_{Oh} for the spreading of paraffin oil on water. Dimensionless numbers: $Oh = 13$, $Bo = 2.7$ and $Oh_{eff} = 3.6$. The transition time and radius are $T_{Oh-ST-LT} \approx Oh_{eff}^2/f(Oh)^3 \approx 3.8$ and $R_{ST-LT} \approx Oh_{eff}/f(Oh)^{3/2} \approx 2$	111
4.15	Dimensionless spreading radius R as a function of the dimensionless time T^* . The type of oil - η_o (mPa.s - C_{SDS} (per liter), Bo , Oh and R_g are indicated in this order in the legend. L in Si100 2g L is for a droplet attached to the needle for 1 h in the aqueous bath before spreading (in case surfactant dynamics matters). The dashed line is a guide line for the power law $T^{*1/8}$	113
4.16	Phase diagram (Bo , R) for a given Oh in the surfactant case. The transitions for different values of Oh between the short-time and the long-time regimes are plotted in the red dashed line (for $Oh \gg 1$) and in the orange dashed line (for $Oh \ll 1$). We have $f(Oh) = Oh^2 / (-1 + \sqrt{1 + 4Oh^2})$. The curve $R = 1/Bo^{1/2}$ defines the transition between capillary and gravity-dominated regime (capillary length). The curves $R = f(Oh)^{1/6}Bo^{1/6}$ and $R = f(Oh)^{1/8}$ correspond to the transitions between the short-time and the long-time dynamics.	114
4.17	a. Schematic representation of the shear stress contributions at the air-oil interface $\tau_{air/oil}$ and at the oil-water interface $\tau_{oil/water}$ when the oil droplet initially spreads. b. Side-view of a typical short-time spreading dynamics (paraffin oil with surfactants) highlighting an oscillatory and a spring-like behaviour.	115
5	Oil imbibition into aqueous foams	117
5.1	Liquid rising in a capillary tube.	122

5.2	a. Imbibition in an open corner. b. Imbibition in an open wedge.	124
5.3	a. Diffusive Lucas-Washburn's regime. b. Wedge regime. c. Regime in a diverging channel.	125
5.4	a. Osmotic cell: the pressure p in the foam is controlled by the distance h_{foam} between the membrane and the location of the meniscus in the U-tube. b. Dimensionless osmotic pressure measured from an osmotic cell as a function of the liquid fraction ϕ_l for a monodisperse, polydisperse emulsion (oil droplets in water) and an ordered monodisperse foam ($\phi_l^* = 0.26$) [88].	127
5.5	Porous model: network of cylindrical pores randomly oriented by the angle β	128
5.6	Coefficient K_c as a function of the Boussinesq number Bq for different velocity profiles [42].	131
5.7	a. Typical numerical solution of Eq. 5.34 for the dimensionless Plateau border area α for $Bo = 0$ and $\tau = 1000$. b-d. Numerical solutions of the imbibition front for different times $\tau = 10, 50, 100$ and 500 with Bond numbers $Bo = 0, 1.6$ and 5.	134
5.8	a. Cross-section of a Plateau border for a dry aqueous foam. b. Cross-section of a Plateau border filled with oil for a dry aqueous foam. S_{PB} and S_f , respectively, denote the areas of the side surfaces of the Plateau borders and the surface of the films that are connected to the Plateau borders. S_o represents the area of the oil-water interfaces.	135
5.9	Experimental set-up. A 30 cm-long PTFE tube (2 mm-diameter) is filled with the imbibing liquid (mixtures of foaming solution-glycerol or oil) and terminated by a 1 cm-long capillary tube (1 mm diameter) that enables the connection with the foam. A motion controller allows maintenance of the pressure of the liquid phase input at atmospheric pressure p_{atm}	139
5.10	Snapshots of the imbibition front for a 30-second timescale. The imbibing liquid (glycerol-foaming solution) is fluorescent and the front is defined as the boundary between the brighter and darker fluorescent areas. The liquid-filled tube is displaced upwards by a millimeter in the first snapshot to ensure contact between the source and the foam.	140
5.11	Evolution of the vertical front position z_f with respect to time t for two data sets. The round dots correspond to a glycerol-foaming solution and the square dots to olive oil. The bubble radius R_b , the initial liquid fraction ϕ_i , and the viscosity $\eta_{o/w}$ of the imbibing oil or aqueous solution are indicated, respectively, in the legend.	141
5.12	Vertical front position z_f with respect to time in dimensionless coordinates for immiscible oils (open dots) and miscible aqueous liquids (closed dots). The experimental curves are obtained for two $R_b = 1$ and 2 mm, different $\phi_i, \eta_{o/w}$ and Bo . The numerical solutions of Eq. 5.34 for Bond numbers $Bo = 0, 1.6$ and 5, deduced from Eq. 5.34, are plotted by the dashed lines. The self-similar power law evolution in $\tau^{1/2}$ in the no-gravity case (Eq. 5.44) is shown.	141

- 5.13 a. Experimental set-up. b. Geometrical elements of foams: vertices, Plateau borders and foam films. c. Slender Plateau border with a radius of curvature r_{PB} . d. Capillary rise of oil in a dry aqueous foam. The olive oil drop appears white thanks to a fluorescent dye and invades the network of Plateau borders. The time interval between each frame is 67 s. The scale bar is 3 mm. 145
- 5.14 Height of the rising front for olive oil as a function of time for different initial liquid fractions and one mean bubble radius $R_b = 1.8$ mm. Inset: log-log scale of the data corresponding to $\phi_i = 0.7 \times 10^{-4}$. The plain line corresponds to the $t^{1/2}$ dynamics detailed in [29], while the dashed line illustrates the $t^{1/4}$ dynamics. 146
- 5.15 Drainage solution. 148
- 5.16 Dimensionless imbibition height Z_f as a function of the dimensionless time τ deduced from numerical resolution of Eq. 5.49 with the comparison to the self-similar solution given by Eq. 5.52 for different Bond numbers $Bo = 0.4, 1.6$ and 4 . Experimental data for $Bo = 2.1$ and two different initial liquid fractions ϕ_i are also plotted and do not converge towards a unique solution. 149
- 5.17 Typical profile of the fluorescence intensity I of a single node during olive oil imbibition as a function of the vertical coordinate z for different times t . A peak corresponds to an oil-filled node or an oil-filled Plateau border, a hole to air in the bubbles. 150
- 5.18 Typical evolution of the fluorescence intensity I of a single node during sunflower oil imbibition as a function of the node's vertical coordinate z . Initially, the node is located at $x = 1$ mm and $z = 7.9$ mm . The intensity of fluorescence is in arbitrary units and the different curves correspond to fluorescence intensity measurements taken at different times. The black arrow indicates the evolution of time. Inset: Width of the peak of intensity σ_I (defined at half of the maximum intensity) as a function of time t . The red arrow highlights the time at which the oil front has reached the node. 151
- 5.19 Oil imbibing a Plateau border. 152
- 5.20 Normalized imbibition front α^*h as a function of normalized time t^* in log-log plot. In the legend, AS1, AS10 and AS100 respectively stand for Aqueous Solution with $\eta_l = 1.4, 10$ and 100 mPa.s, while OO and SO stands for Olive Oil and Sunflower Oil. The black line corresponds to $(1 + \alpha^*h)^4 + \frac{4}{1 + \alpha^*h} - 5 = b \frac{2\delta_a}{15\sqrt{3}} t^*$ with $b \sim 0.3$, while the two dashed lines represent the power laws: $t^{1/2}$ at early times and $t^{1/4}$ at late times. 153
- 5.21 Experimental set-up for the oil recovery by a moving foam. The foam is first generated through a column. The upper part of the column is removable and flipped at 90° onto a syringe pump with a piston at one end. Then, the oil reservoir is connected to the reversed column at the atmospheric pressure p_{atm} before starting the injection of foam on top of the extraction point. 155

5.22	Imbibition profiles for immiscible liquids (olive oil) for successive times t . a. Initial liquid fraction $\phi_i = 3.4 \times 10^{-3}$, injection flow rate $Q = 100$ mL/h and bubble radius $R_b = 1$ mm. b. $\phi_i = 2.7 \times 10^{-3}$ and $Q = 200$ mL/h. c. $\phi_i = 2.4 \times 10^{-3}$ and $Q = 400$ mL/h. The red arrow indicates the extraction point and the green arrow the movement of the foam.	156
5.23	Imbibition profiles for miscible liquids (CAPB+SLES+Mac-glycerol) for successive times t . a. Initial liquid fraction $\phi_i = 2.6 \times 10^{-3}$, injection flow rate $Q = 200$ mL/h and bubble radius $R_b = 1$ mm. b. $\phi_i = 1.9 \times 10^{-3}$ and $Q = 200$ mL/h. c. $\phi_i = 1.7 \times 10^{-3}$ and $Q = 400$ mL/h. The red arrow indicates the extraction point and the green arrow the movement of the foam.	157
5.24	Mean extraction flow rate Q_o , for an injection time of 4 min and 30 s, as a function of the foam velocity U_f	158
5.25	Dimensionless extraction flow rate Q^* as a function of the dimensionless foam velocity U^* for the imbibition of olive oil with different initial liquid fractions ϕ_i in the foam. The orange line is the fit with Eq. 5.62 and $v_o(t) \sim t^{3/2}$. The blue and the purple dashed lines are, respectively, the fits with $v_o(t) \sim t^{1/3}$ and $\sim t^{1/2}$ deduced from the numerical simulation from §5.2.	159
5.26	Log-log plot of the dimensionless imbibed volume $V^* = \int_0^{R_f} \int_0^{Z_f} \alpha(R, Z, \tau) R dR dZ$ (where $R_f = r_f/R_b$ and $Z_f = z_f/R_b$ are the dimensionless coordinates of the front) for the static imbibition of §5.2 as a function of the dimensionless time τ for two different Bond numbers $Bo = 1.6$ and 5.	160
6 Foam - oil interactions in micropatterned structures		163
6.1	a. Wetting on a smooth surface with the Young contact angle θ_Y . b. Wetting on a rough surface with the apparent contact angle θ^* . c. Evolution of $\cos \theta^*$ with $\cos \theta_Y$ for a smooth and a rough surface of the same chemical nature [71]. The parameters ϕ_S and r_S are respectively the solid fraction and the roughness. The black plain line in the upper right part corresponds to Eq. 6.2.	168
6.2	Liquid droplet sitting on a solid-liquid composite surface.	169
6.3	Impregnation of a film in a textured surface. The solid fraction ϕ_S and the projected area A_P are indicated in a subfigure.	170
6.4	Liquid droplet sitting on a solid-air composite surface.	171
6.5	Transition from the regime of air cushion (1) to the Wenzel regime (2).	172
6.6	a. Touch down scenario [7]. b. Sliding scenario [7].	174

- 6.7 a. Shear-driven drainage of oil in a groove geometry [198]. b. Local configuration of the oil-water interface. The parameters L_o , $L(t)$, h , w , θ , r_{min} and u are, respectively, the length of the groove, the retention length, the height of the groove, the spacing in a groove, the receding contact angle, the minimal radius of curvature and the flow velocity. 175
- 6.8 Dimensionless retention length $\tilde{L} = L/L_\infty$ as a function of the dimensionless time $\tilde{t} = t/t_c$. The blue, the red and the gray curves correspond to experimental results of drainage of silicon oils by water, respectively for oil viscosity $\eta_o = 42.7$ mPa.s and injection flow rate $Q = 1$ mL/min, $\eta_o = 201$ mPa.s and $Q = 2$ mL/min and $\eta_o = 42.7$ mPa.s and $Q = 2$ mL/min. The dotted lines are the theoretical predictions [198]. Both figures are extracted from [198]. 178
- 6.9 Geometry of the microfluidic channel with the liquid-infused micropattern imprinted on the upper side of the channel. a. Analogy between a real microfracture and a liquid-infused substrate. b. Top-view of the channel, with the oil fluorescing green-yellow. c. Side-view of the channel consisting of one wall with an array of posts. 179
- 6.10 Equilibrium oil-water interfacial tension γ_{ow} (mN/m) as a function of the surfactant concentration c (g/L) for SDS-Olive oil (O) and CAPB-SLES-Mac-Olive oil (O) combinations. The blue and the red dashed lines are guide lines. 181
- 6.11 Top views of typical oil extractions (olive oil) by a surfactant solution (CAPB - SLES - Mac - 10 wt% glycerol). Fluorescent dyed oil appears green-yellow. The small green-yellow dots correspond to some oil droplets stuck on the epoxy surface when the channel was initially cleared of oil in the first place. The flow is from left to right. a. Extraction with a uniform front; $Q = 0.05$ mL/min and $\gamma_{ow} = 4.2$ mN/m, time interval: 5 h. b. Extraction with an unstable pattern; $Q = 5$ mL/min and $\gamma_{ow} = 4.2$ mN/m, time interval: 5 min. 183
- 6.12 Extraction efficiency α as a function of time t for different draining liquid - oil combinations with the following variable parameters: a. γ_{ow} (mN/m). b. Q (mL/min) (Inset: α as a function of Qt). c. η_o (mPa.s). d. H (μ m). S and O are, respectively, the surfactant type, the oil type. 184
- 6.13 Extraction efficiency α as a function of the injected volume Qt for SDS - olive oil combination, with the capillary number $Ca \approx 0.015$ and 0.005 defined in Eq. 6.19b. 184
- 6.14 Confocal snapshot of the oil-water interface in the texture cavity. The geometrical parameters are indicated on the picture: δ is the deflection. 186
- 6.15 a. Movement of the A - B interface parallel to the flow of mean velocity U with the viscosity ratio $\eta_B/\eta_A > 1$. b. Movement of the same A - B interface for our post pattern with the interface receding perpendicular to the main flow of mean velocity U 187

- 6.16 Measurements of the receding contact angle θ as a function of Ca for CAPB - olive oil (red dots) and CAPB - silicon oil 1 (blue dots) combinations. Oil appears red in the confocal microscope and the green line is the laser reflection between the glass and the aqueous phase. Lower right: Evolution of the numerical factor c_d with respect to θ 187
- 6.17 a. Experimental efficiency α_{exp} as a function of $g(t)$ for CAPB - olive oil, CAPB - silicon oil 1 and CAPB - silicon oil 2 combinations. b. $f(\alpha_{exp})$ as a function of $g(t)$ for different surfactant-oil combinations. The black dashed line is the theoretical prediction (Eq. (6.19a)) 188
- 6.18 Unstable two-layer Couette flow with layers of different viscosities η_w and η_o and different thickness h and $H - h$ 189
- 6.19 a. Typical unstable extraction pattern for posts and grooves with the same height and width. The surfactant solution - oil combination is SDS (2 g/L) - olive oil; $Q = 2$ mL/min and $t = 60$ min. Contrast is enhanced in the snapshots. b. Phase diagram where each point (γ_{ow}, Q) represents an experiment with the CAPB - olive oil, the CAPB - silicon oil 1 and the SDS - olive oil combinations. Unstable extraction is represented by red dots and stable extraction by green dots. The dashed black line defines the stable regime for pure aqueous solutions - olive oil (the silicon oil 1 case is further to the right of the diagram). 190
- 6.20 Description of the microfluidic fabrication by photolithography. Colors are here to distinguish each component. They do not correspond to a physical reality. 191
- 6.21 Flow-focusing device with the main geometrical features: $w_g = 200$ μm , $w_l = 300$ μm , $w_c = 60$ μm , $l_c = 100$ μm and $w_o = 500$ μm . The height H of the channel is 27 μm or 72 μm 192
- 6.22 Bubble volume V_b (nL) as a function of the ratio pressure-flow rate p/q (Psi/m³/s). Below: bubbles (radius $R_b \approx 30$ μm) accumulating in the outlet reservoir. 193
- 6.23 a. Top-view of olive oil extraction by an aqueous foam with $R_b = 100$ μm and $Q = 50$ $\mu\text{L}/\text{min}$. Fluorescent dyed oil appears green-yellow. The flow is from left to right. b. Foam flow in the channel with D , the film thickness between the substrate and the bubbles. 194
- 6.24 Efficiency α as a function of the injected volume Qt . a. Olive oil extraction by a foam with $R_b = 30$ μm . b. Silicon oil 1 extraction by a foam with $R_b = 30$ μm . c. Extraction for silicon oil 2 and $R_b = 30, 100$ and 200 μm , and $H = 179$ μm . d. Comparison between surfactant solutions and foams with a varying channel height (89 or 178 μm). In the legend, O , Q ($\mu\text{L}/\text{min}$), R_b (μm) and H (μm) are, respectively, the oil type, the injection flow rate, the mean bubble radius and the channel height. 195

6.25	a. Measurements of the receding contact angle θ as a function of $\tilde{C}a$. b. Experimental efficiency α_{exp} as a function of $G(t) = \frac{c_s h}{W H D L_o} \frac{\eta_w}{\eta_o} \frac{1}{c_d} Q t$ for some oils, Q ($\mu\text{L}/\text{min}$) and R_b (μm). c. $f(\alpha_{exp})$ as a function of $G(t)$ for the same parameters. $f(\alpha_{exp}) = G(t)$ is represented by the black dashed line.	196
6.26	a. Dimensionless film thickness $D^* = D/H$ as a function of the outer capillary number Ca^* for all data sets. Inset: Film thickness D as a function of Ca^* for the same data set. b. Dimensionless applied shear stress $\tau_{xy}^{foam*} = \tau_{xy}^{foam} H/\gamma_{aw}$ as a function of Ca^* for all data sets. The green dashed line represents the values predicted by Denkov et al. [57] with H as a rescaling length for a liquid fraction $\epsilon = 0.2$	198
6.27	Typical NMR spectrum for an oil-laden foam with the intensity I as a function of the relaxation time T_1 . The relaxation times are $T_1 \approx 0.5$ ms for water in foams and $T_1 \approx 100$ ms for oil. We use gadolinium as a contrasting agent (and EDTA as a chelating agent). Gadolinium is able to shorten the T_1 - typically for a pure water solution from 2 s to 10 ms according to the concentration of gadolinium.	205
A	Examples of flow dynamics by resolution of Stokes' equation	207
A.1	Spreading a liquid droplet on a solid surface.	208
A.2	Poiseuille flows in circular and rectangular pipes.	211
B	Rayleigh-Plateau instability of a viscous fluid in another viscous fluid	213
B.1	Geometry of the axisymmetric unstable jet.	214
C	Microfluidic fabrication: the "sticker technique"	219
C.1	a. Fabrication of the microfluidic channel. b. Fabrication of the textured pattern.	221
C.2	a. PDMS mold for the main channel. b. Negative of the textured pattern on a silicon wafer. c. Microfluidic channel ready for experiments.	221
D	Properties of textured surfaces	223
D.1	a. Gull feather repelling water (<i>Source: matthewwills.com</i>). b. Water droplets rolling down a lotus leaf (<i>Source: Hydrobead</i>). c. Water (in blue - $\gamma_{aw} = 72.1$ mN/m) and rapeseed oil (in red - $\gamma_{aw} = 35.5$ mN/m) on a shelduck feather dip-coated in a solution of 50/50 fluorodecyl POSS/Tecnoflon [173]. d. Water (blue) and octane (red) droplets on a textured surface (<i>Source: Scientific American</i>).	224

D.2	Anchored air-liquid contact line around a defect on a solid surface.	225
D.3	Different texture geometries enhancing hydrophobicity and oleophobicity (images from Scanning Electron Microscopy). a. Electrospun fibers of PMMA (poly(methyl)methacrylate)-fluorodecyl POSS [185]. b. Barbules of a duck feather dip-coated in fluorodecyl POSS/Tecnoflon [37]. Electrospun beads on strings of fluorodecyl POSS [185]. d. Mesh geometry dip-coated in fluorodecyl POSS/Tecnoflon [36].	226
D.4	a. Texture without any reentrant curvature: $\Psi > 90^\circ$ and $\theta_Y < \Psi$. b. Texture with a reentrant curvature: $\Psi < 90^\circ$ and $\theta_Y > \Psi$ [185].	226
D.5	Liquid drop sliding down an inclined surface.	227
D.6	Contact angle hysteresis $\Delta\theta$ ($^\circ$) as a function of the air-liquid interfacial tension γ_{al} (mN/m) [199]. The red squares, the orange rounds and the green triangles correspond to three different liquid-infused surfaces (fluorinated lubricant and teflon/epoxy material). The blue diamonds refer to measurements on omniphobic surfaces in [185].	228
D.7	a. Immiscible droplet floating on the lubricant layer covering the whole texture (complete wetting). b. Immiscible droplet floating on the liquid-infused surface. c. Sinking of the droplet towards the bottom of the cavities.	228

List of Tables

1 Aqueous foams and their applications in environment and energy	9
1.1 Typical air-liquid interfacial tensions γ_{al} for some common liquids.	14
2 Oil-foam interactions and stability	47
2.1 Oil and foaming solutions used for the characterization of the stability of oil-laden foams. The air-water γ_{aw} , air-oil γ_{ao} and γ_{ow} interfacial tensions (in mN/m) are given, as well as the entry E , spreading S and bridging B coefficient (in mN/m) defined in §2.1.1. We also indicate the oil viscosity η_o (mPa.s) and the oil density ρ_o	62
3 Plateau borders and oil: equilibrium shape and coalescence	69
3.1 Characteristics of the different oils used to fill the Plateau border. The interfacial tensions γ_{ao} (air-oil), γ_{ow} (air-water)(mN/m), the oil viscosity η_o (mPa.s), the oil density ρ_o and the coefficients E , S and B (mN/m) are given.	82
4 Soap films and oil: dynamics of rising oil droplets spreading at the air-water interface	91
4.1 Interfacial tensions γ_{aw} , γ_{ao} and γ_{ow} (mN/m) with calculated entry E and spreading coefficients S_o of the oils and aqueous solutions. The dynamic viscosity η_o (mPa.s) and the density ρ_o (for each oil), and the surfactant concentration C_{SDS} (for each aqueous solution) are given.	107
5 Oil imbibition into aqueous foams	117

5.1	Characteristics of the imbibing liquids and foaming solution. γ_{ow} (mN/m) is the oil-water interfacial tension, η (mPa.s) the dynamic viscosity, ρ (g/cm ³) the density, R_b (mm) the average bubble radius of the foam and B the Bond number defined in (5.34).	138
6	Foam - oil interactions in micropatterned structures	163
6.1	Characteristics of the aqueous solution - oil combinations. Here, η_w (mPa.s) and η_o (mPa.s) are, respectively, the shear viscosity of water and oil.	180
6.2	Interfacial tensions γ_{aw} , γ_{ao} and γ_{ow} (mN/m) with calculated entry E and spreading coefficients S of the oils and surfactant solutions. The dynamic viscosity η_o (mPa.s), the density ρ_o (for each oil), and the surfactant concentration C (for each surfactant solution) are given.	181
A	Examples of flow dynamics by resolution of Stokes' equation	207
B	Rayleigh-Plateau instability of a viscous fluid in another viscous fluid	213
C	Microfluidic fabrication: the "sticker technique"	219
D	Properties of textured surfaces	223

Main parameters

Measured parameters

Variables	Parameters	Variables	Parameters
γ_{al}	Air-liquid interfacial tension	γ_{sl}	Solid-liquid interfacial tension
γ_{sa}	Solid-air interfacial tension	γ_{aw}	Air-water interfacial tension
γ_{ow}	Oil-water interfacial tension	γ_{ao}	Air-oil interfacial tension
γ	Interfacial tension	ρ	Density
ρ_l	Liquid density	ρ_o	Oil density
ρ_w	Water density	η_l	Liquid shear viscosity
η	Shear viscosity	θ_Y	Young contact angle
η_o	Oil shear viscosity	η_w	Water shear viscosity
p_{atm}	Atmospheric pressure	P_b	Bubble pressure
ϕ_l	Liquid fraction	ϕ_o	Oil fraction
ϕ_w	Water fraction	ϕ_i	Initial liquid fraction
R_b	Bubble radius	R_d	Drop radius
r_t	Tube radius	r_c	Cylinder radius
g	Gravity acceleration	t	Time
x	Horizontal coordinate	$y - z$	Vertical coordinate
τ_{xy}	Shear stress	ϵ	Strain
$\dot{\epsilon}$	Strain rate	Σ	Interfacial area
V	Volume of liquid		

Main variables

Variables	Parameters	Variables	Parameters
E	Entry coefficient	S	Spreading coefficient
B	Bridging coefficient	Π	Disjoining pressure
Π_o	Osmotic pressure	r_{PB}	Curvature radius of the Plateau border
p	Mechanical pressure	p_o	Pressure in the oil phase
p_w	Pressure in the water phase	ℓ_{PB}	Plateau border's length
V_o	Volume of oil	V_w	Volume of water
E_I	Interfacial energy		

Introduction

“The world’s a bubble: and the life of Man less than a span.” *The Life of Man*, Sir Francis Bacon (1561-1626).

Yesterday morning, I took a cup of cappucino with my breakfast. Then, I had a refreshing shower and spread a moisturizing cream onto my face. After work, I went back home by the park and saw an artist entertaining the passers-by while dipping a long rope into a bath of liquid. Later, I had a marvelous dinner with a cup of champagne. Why am I telling you what I did yesterday? Because in all these insignificant events of anyone’s life, I encountered this intriguing physical object filled with gas inside a thin liquid film that one calls bubble. Philosophers and painters already understood their importance and beauty by portraying bubbles no later than the 16th century.

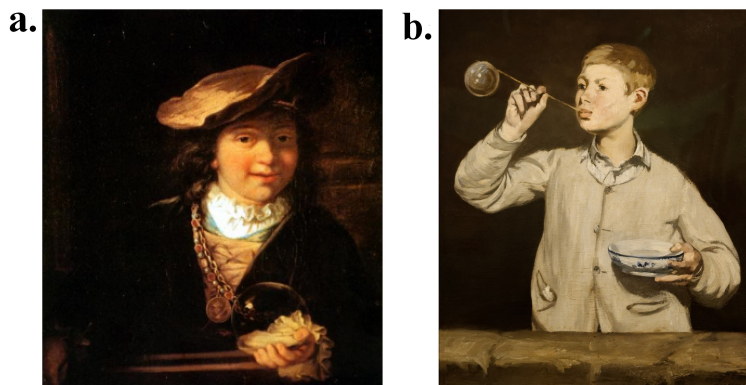


Figure 2: a. *Child with a soap bubble* by Rembrandt (1606-1669). b. *Soap bubbles* by Edouard Manet (1832-1883).

But bubbles rarely travel alone. Flocked into a group, they become liquid foams. Foams - especially aqueous foams if they are water-based - are everywhere. We need them to shave the face and the skin hair, we find them in all kinds of cosmetics and creams, we create foams for any cleaning activities from body care to detergency, we eat foams in many desserts from cakes to ice creams. They bring comfort, decorate, enhance taste and enable to sell products for a small cost. Everyday life is not the only place where foams are essential. In civil engineering, the quest for better building insulation focuses on foams as a way to include more air. Fire-fighters sprinkle foams to block the connection between oxygen and fire. Mining resorts to foams in separation processes because their interfaces can capture fine particles very easily and their density is lower than any other liquid. Eventually, oil companies and decontamination agencies include foams in their strategy to capture oil and contaminants by decreasing the interfacial tension and benefiting from their high expansion property. Due to their high composition in air, they also generate less waste, which might be interesting for environmental issues.



Figure 3: For the better: a. Cappuccino. b. Beer foam. For the worse: c. foam-induced river pollution.

The wide variety of applications is only made possible because foams exhibit original physical features and properties. In the world of hydrodynamics and soft matter, foams are part of the complex fluids' branch with polymers, colloidal suspensions, emulsions, gels and yield stress fluids (ketchup, toothpaste) as some of their counterparts. The composition, the structure, the motion and the flow (the so-called rheology) of those fluids have been and are still the subject of intense research. With the development of new chemical formulations for the surfactants, complex foams, composed of air, aqueous solution and a third phase, which can be a solid, an immiscible liquid or a gel are now commonly encountered in strategic fields, such as civil engineering or plastic manufacturing. Chapter 1 recalls the nature of foams from surfactants to the assembly of bubbles. It insists on important physical and mechanical properties with an emphasis on environmental and energetical applications where foams interact with immiscible phases.

Such multiphasic interactions are at stake for the extraction of a liquid phase from a confined medium, typically in soil remediation and enhanced oil recovery. Yet, in many industrial cases, oil is used as an anti-foaming agent to destroy foams or to avoid their generation. However, in some appropriate conditions, oil droplets can increase the stability of foams and invade them without any damage. The antifoaming feature and the foam collapse strongly depend on the ability of oil to emerge at the air/water interface [56, 72]. In Chapter 2, we answer the related questions: what parameters determine the stability of a foam containing emulsified oils? How do foams react to the invasion and the flow of oil through the liquid microchannels, called Plateau borders, characteristic of the foam structure?

Then, we travel from the global scale of oil-laden foams to the scale of a Plateau border - i.e. the liquid microchannel of the foam in which the flow of oil occurs). The stability of oil-imbibed foams requires to understand the local picture of oil inside the foam components. Hence, we tackle the following questions: what is the geometry of an oil slug propagating through a Plateau border? What happens if an oil-filled Plateau border breaks due to an external perturbation? Chapter 3 describes how the stability of oil-filled Plateau borders can be understood by looking at the local energetical configuration of the three-phase system air-oil-water. We also try to

understand how this system evolves when an adjacent film bursts, inducing the rupture of the Plateau border.

Plateau borders drive oil inside the foam but films can also contain dispersed oil droplets in many situations (antifoaming action, oil-stabilized foams). Oil droplets have the ability to emerge and spread at the air-water interface. The questions here are: what is the local dynamics of oil spreading at the interface from the emergence of the droplet to the formation of an oil film? How does it compare to the common theories on the wetting of solid and liquid surfaces? Chapter 4 focuses on the interactions between soap films and oil. We study the dynamics of oil droplets rising to the air-water interface and spreading at this interface.

After looking at the interactions between oil and foams at the local scale, we wonder how oil can be driven inside the foam. In Chapter 5, we consider what happens when a large volume of oil is put into contact with a foam. Indeed, providing that the right chemical composition for the foam and a compatible oil are found, a foam can act as a liquid sponge: oil penetrates the foam through the liquid capillary microtubes (called Plateau borders) of the foam network, located at the bubbles' junctions. Thus, foams can be seen as physical systems in which imbibition processes can occur. Depending on the configuration of the oil reservoir and the relative motion of the foam compared to the imbibed liquid, different dynamics can occur. Hence, we reply to the following issues: how does oil imbibition in foams occur? What impact does the confinement and the characteristic size of the oil reservoir have on the imbibition dynamics? How can oil be transported by a moving foam if one wants to recover it?

In the last part, we move from the millimeter or centimeter scale, at which the imbibition of oil-laden foams occurs, down to the micrometer scale corresponding to the size of the pores in rock layers and soils. In real life situations, oil can be trapped in the roughness of confined media, as well as in the pores. Oil companies usually inject surfactants to untrap the oil phase. Trapping oil in experimental models can be done by using liquid-infused surfaces. These surfaces can be compared to an oil-filled rough medium. As depicted in Fig. 4, they are micropatterned surfaces of controlled size, which are used to create omniphobic objects, to reduce biofouling and to enhance drag reduction. The failure of these surfaces and the loss of the aforementioned properties, owing to the disappearance of the lubricating layer, is analogous to the issue of oil extraction from the roughness of confined media. We shed a new light on different questions: can we evaluate the quantity of oil extracted from a micropatterned and confined channel when surfactant solutions are injected? What is the extraction efficiency if foams are injected (industries often co-inject a gas phase with surfactants)? Chapter 6 focuses on the oil extraction from micropatterned surfaces, as sketched in Fig. 4. This chapter underlines the importance of textured and liquid-infused surfaces and how they can be used to study recovery processes from oil-filled

rough confined media.

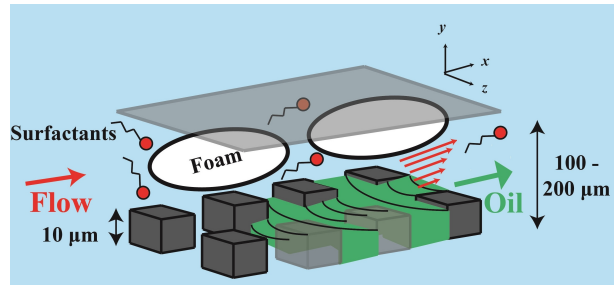


Figure 4: Liquid-infused surface in a micrometer channel. Surfactants and foams are injected to drag oil out of the patterned surface.

Chapter 1

Aqueous foams and their applications in environment and energy

Aqueous foams are multiscale objects whose structure involves different pieces: surfactants, films and bubbles. Their structure offers original properties for a multitude of daily and industrial applications, including environment and energy-related activities.

Contents

1.1 The physics of interfaces and surfactants	13
1.1.1 Interfacial energy, tension and force	13
1.1.1.1 Interfacial tension	13
1.1.1.2 Film and capillary force	14
1.1.2 Interface, drop and bubble	15
1.1.2.1 Drop and bubble formation	15
1.1.2.2 The Laplace law and pressure	15
1.1.2.3 Measuring the interfacial tension	17
1.1.3 Surfactants: who are you?	18
1.1.3.1 Structure and effect on interfacial tension	18
1.1.3.2 Stabilizing role	21
1.1.4 Effect of surfactants on the interfacial mechanics	22
1.1.4.1 Interfacial viscoelasticity	22
1.1.4.2 Resistance of a soap film	23
1.1.4.3 Rigid and mobile interfaces	24
1.1.5 Soap film: a fragile structure	25
1.1.5.1 How films shrink...	25
1.1.5.2 How films break...	27
1.2 Aqueous foams: definition, structure, characteristics and main properties	27
1.2.1 Foam structure	28
1.2.1.1 Influence of the liquid fraction ϕ_l on the structure and Plateau laws	28
1.2.1.2 Dry foams	29
1.2.2 Main properties of foams	31
1.2.2.1 Capillary suction and disjoining pressure	31
1.2.2.2 Osmosis in foams	31
1.2.3 How foams flow...	32
1.2.3.1 Foams are complex fluids	32
1.2.3.2 Relationship between the structure and the foam rheology	35

1.3 Applications in environment and energy	37
1.3.1 Foams in everyday life	38
1.3.1.1 Around us...	38
1.3.1.2 In industry	38
1.3.2 Towards a cleaner environment: soil remediation	39
1.3.2.1 Common remediation techniques: advantages and drawbacks	40
1.3.2.2 What foams can improve...	42
1.3.3 Towards more energy supply: enhanced oil recovery	43
1.3.3.1 Processes of enhanced oil recovery	43
1.3.3.2 Surfactants, foams and the quest of oil	44
1.4 Conclusions	44

Specific variables

Variables	Parameters	Variables	Parameters
E_C	Cohesion energy per molecule	e_S	Interfacial energy per molecule
a	Molecular size	\bar{T}	Temperature
L	Film length	m_{gerris}	Mass of the gerris
Δp_L	Laplace pressure	Σ_d	Dimensionless interfacial area
F	Tension force	δW	Work
R_1	First radius of curvature	R_2	Second radius of curvature
c	Bulk concentration of surfactants	Γ	Interfacial concentration of surfactants
G_S	Interfacial free enthalpy	n_S	Number of surfactant molecules at the surface
P	Thermodynamical pressure	Ω	Volume
\dot{S}	Entropy	k_B	Boltzmann constant
e	Film thickness	z_{max}	Maximal height
γ_{cmc}	Interfacial tension at the <i>cmc</i>	σ	Normal stress
σ_{xx}	Horizontal normal stress	σ_{yy}	Vertical normal stress
τ_{xy}	Shear stress	Σ_0	Initial interfacial tension
E_d	Interfacial dilatational elasticity	η_d	Interfacial dilatational viscosity
E_G	Gibbs-Marangoni elasticity	G_{shear}	Interfacial shear elasticity
η_{shear}	Interfacial shear viscosity	γ_0	Air-pure water interfacial tension
w	Oscillatory pulsation	f	Frequency
Q_f	Flow rate in the film	v	Flow velocity in the film
r_h	Hole radius	m_{rim}	Mass of the rim
v_{rim}	Velocity of the rim	ϵ_Y	Yield strain
λ	Structural constant	η_{app}	Apparent viscosity
τ_Y	Yield stress	k_p	Plastic viscosity
G'	Shear elastic modulus	G''	Loss shear modulus
G	Quasistatic shear modulus	ϵ	Strain
τ	Shear stress	τ_Y	Yield stress

1.1 The physics of interfaces and surfactants

In the following, foams mean aqueous foams (water-based) if not specified.

Let us start from the molecular scale. Foams exist because some particular molecules, called surfactants, appear as the key components for the whole structure. Broaching the subject of surfactants first requires to introduce our reader to the world of interfacial physics and capillarity.

1.1.1 Interfacial energy, tension and force

1.1.1.1 Interfacial tension

The existence of foams is related to the interfacial physics and its main characteristic parameter: the interfacial tension [79, 157].

A liquid is a condensed state whose molecules are attracted to each other. Molecules do not like lying at the surface of the liquid phase because they lose half of their interactions with their counterparts. Therefore, liquids adapt their shape to let the fewest possible surfaces appear.

We introduce the cohesion energy per molecule $-E_C$. The loss of half of the cohesion energy per molecule at the surface is written as the interfacial energy per molecule $e_S = E_C/2$. The interfacial energy can be written as $e_S = \gamma a^2$, where $\gamma = E_C/2a^2$ is the interfacial tension and a is the molecular size, with a^2 the area of one exposed molecule at the surface. The total interfacial energy E_I of a liquid system is found by adding up the contributions e_s of every single molecule at the surface. We can write $E_I = \gamma \Sigma$ where Σ is the total interfacial area.

We can now easily understand that creating interfaces costs the interfacial energy E_I . Indeed, an interface tends to reduce and to minimize its area, and to resist any deformation. Generating interfaces require an energy E_I per interfacial area Σ , whose value is the interfacial tension $\gamma = dE_I/d\Sigma$, expressed in N/m.

The higher the attractive interactions, the higher E_C , the higher γ . Table 1.1 reports some characteristic air-liquid interfacial tensions γ_{al} for common liquids. For oil, the liquid/vapour transition occurs at ambient temperature, which means that E_C is close to the Boltzmann thermal energy $k_B \tilde{T}$ where $k_B = 1.38 * 10^{-23} \text{ J.K}^{-1}$ is the Boltzmann constant and \tilde{T} the temperature. For water, hydrogen bonding is dominant, thus the air-water interfacial tension γ_{aw} is higher than the air-oil interfacial tension γ_{ao} . Mercury has the highest air-liquid interfacial tension, since metallic bonding is strongly cohesive ($E_C \approx 1 \text{ eV}$).

An interfacial tension arises as soon as one phase is in a condensed state. Therefore, an inter-

Liquids	Helium ($\tilde{T} = 4$ K)	Silicone oil	Ethanol	Glycerol	Water	Mercury
γ_{al} (mN/m)	0.1	20	23	63	72 - 73	485

Table 1.1: Typical air-liquid interfacial tensions γ_{al} for some common liquids.

facial tension also exists when two liquids are connected to each other. In that case, the value of the interfacial tension takes into account the attractive interactions of the molecules of the two condensed phases, but also the molecular interaction between the two condensed phases. A typical value of oil-water interfacial tension is around 20 mN/m. In this thesis, we deal with various interfacial tensions: air/water, air/oil, oil/water, solid/air, solid/liquid and air/liquid. To characterize the related interfacial tensions, we use the notation γ with different subscripts indicating the nature of the interface. For instance, γ_{ao} stands for the interfacial tension at the air-oil interface.

1.1.1.2 Film and capillary force

As sketched in Fig. 1.1, let us imagine that we draw a liquid film of length dx and width L . Its interfacial energy dE_I is $dE_I = 2\gamma_{aw}Ldx$, since we have two air-water interfaces. This energy corresponds to the work δW done to draw the film: $\delta W = Fdx$ where F is the applied force. Thus, $F = 2\gamma_{aw}L$ and γ_{aw} can be interpreted as the film tension.

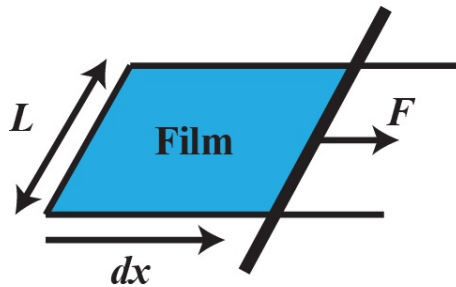


Figure 1.1: Formation of a liquid film inside a frame.

This capillary stiffness can be very high, which explains why some insects can walk on water or why a needle can float as well, as seen in Fig. 1.2. Indeed, the mass m_{gerris} of the gerris is small (≈ 2 g) and this insect has tiny hair which allows to pull a water film at its edge. The balance between the weight $m_{gerris}g$ (g is the constant of gravity acceleration and $g = 9.81 \text{ m.s}^{-2}$) and the capillary force $\gamma_{aw}L$ gives a length of hair of 0.2 m, which is a common feature of the gerris.

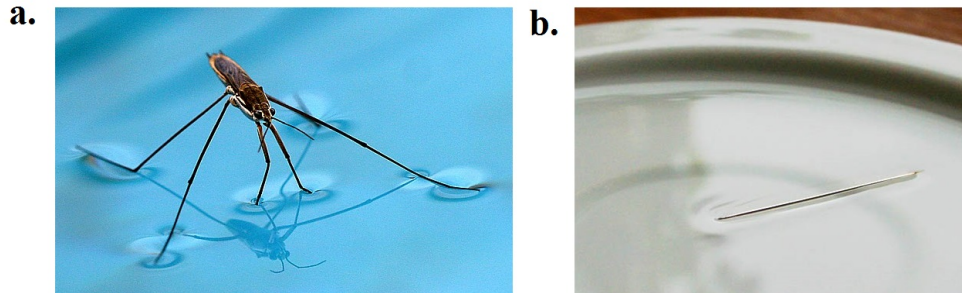


Figure 1.2: a. A gerris “walking on water”. b. A needle floating at the surface of a water bath.

1.1.2 Interface, drop and bubble

What shape can the interface take: plane, curved? This question is connected to the formation of drops and bubbles.

1.1.2.1 Drop and bubble formation

If we close the film containing a given quantity of gas or if we have a given volume of gas in a liquid bath, we create a bubble. If we invert the gas phase and the liquid phase, we obtain a drop. The drop and the bubble adopt a shape that minimize their interfacial energy E_I . Fig. 1.3 exhibits successive steps of calculations of the interfacial energy for a given volume of gas which is initially enclosed in a cubical bubble using the software *Surface Evolver* [20]. The shape corresponding to the minimum interfacial energy is the sphere when they are isolated and when external forces, such as wind and gravity, do not play any significant role.

1.1.2.2 The Laplace law and pressure

The spherical shape of the drop or the bubble implies a mechanical equilibrium inside the sphere, requiring that the inner pressure be higher than the outer pressure. Indeed, anyone has ever noticed that one needs to blow into a film to create a bubble, i.e. to induce an overpressure Δp_L . In 1750, Leidenfrost [116] showed this overpressure experimentally by pinching a straw into a bubble, which emptied the gas phase. In 1805, Laplace was the first to estimate Δp_L [114]. From Fig. 1.4, we calculate Δp_L for a drop of radius R_d in the air. When we increase R_d by a small displacement dR_d , the variation of interfacial energy dE_I is $dE_I = \gamma_{al}d(4\pi R_d^2) = 8\pi\gamma_{al}R_d dR_d$, where γ_{al} is the air-liquid interfacial tension. This increase of interfacial energy corresponds to the work δW of the pressure forces $\delta W = \Delta p_L d((4/3)\pi R_d^3) = \Delta p_L 4\pi R_d^2 dR_d$, which yields the

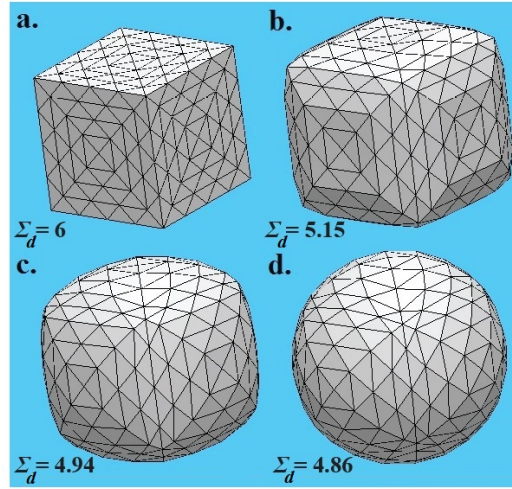


Figure 1.3: Surface minimization of the interfacial area of a given volume of gas comprised inside a cubical bubble. It evolves towards a sphere, which is the shape corresponding to the minimization of the interfacial energy, as shown by the different values of the dimensionless interfacial area Σ_d . Numerical simulations by the software *Surface Evolver* [20, 21]. The dimensionless interfacial area Σ_d is indicated in every image and decreases from the cube of unit length 1 to the sphere.

well-known Laplace law for a spherical drop in the air phase:

$$\Delta p_L = \frac{2\gamma_{al}}{R_d}. \quad (1.1)$$

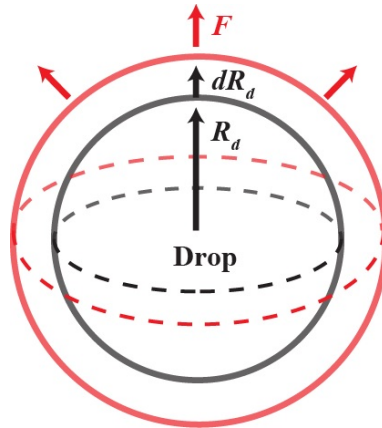


Figure 1.4: Variations of the drop radius R_d for the calculations of the Laplace pressure.

For bubbles whose film thickness is negligible, Eq. 1.1 becomes:

$$\Delta p_L = \frac{4\gamma_{al}}{R_b}, \quad (1.2)$$

since we have two air-liquid interfaces instead of a single one (R_b is the bubble radius). In both cases, the smaller the drop and the bubble, the higher the Laplace pressure. This difference of pressure explains the coarsening phenomena, i.e. the transfer of matter (air or liquid) from small to big neighbouring drops and bubbles through the continuous phase.

For any type of air-liquid and liquid-liquid interfaces, we can use Eq. 1.1 and 1.2 with the appropriate interfacial tension γ . And for any interfacial shape, we can use the generalized version of the Laplace law:

$$\Delta p_L = \gamma \left(\frac{1}{R_1} + \frac{1}{R_2} \right) \quad , \quad (1.3)$$

where R_1 and R_2 are the main radii of curvature of the interface. To evaluate the Laplace pressure in the following chapters, we basically estimate or calculate the radii of curvature and use Eq. 1.3.

1.1.2.3 Measuring the interfacial tension

Several methods exist to measure the interfacial tension γ [1]. These methods use force calculations and surface minimization described in §1.1.1.2 and §1.1.2.1:

- the Wilhelmy method where one measures the γ -dependent capillary force exerted on a blade that is pulled out from a liquid bath [200],
- the pendant drop method where the shape of the drop is fitted to the theoretical shape dictated by the balance between gravity and capillarity. It is the same procedure for sessile (drop deposited on a surface), rising (for instance when there is a difference of density between two liquids) and spinning (by elongation of a drop inside another liquid) drops [155],
- the capillary rise in a tube where the rising height is related to γ , by using the density, the radius of the tube and the gravity acceleration.

In this work, the technique that we use to measure all the interfacial tensions is the pendant drop method (see Fig. 1.5). The fitting of the drop shape is proceeded by two methods. In the first one, we directly use the result given by the dedicated measurement device *Teclis* which calculates γ through its own software. In the second one, we use our own code to extract γ from the drop image.

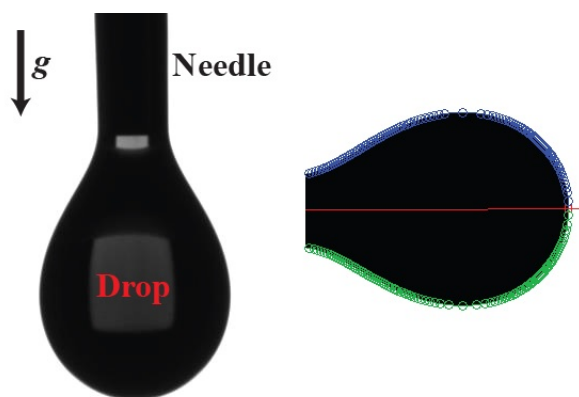


Figure 1.5: Pendant drop method with the fitting of the drop shape.

1.1.3 Surfactants: who are you?

Bubbles appear when air is incorporated in the liquid phase by shaking and mixing, but can also nucleate from a solid wall due to impurities. However, those bubbles can coalesce with each other in a fraction of seconds. Indeed, the attractive Van der Waals forces tend to decrease the film thickness until rupture. Thus, the question is: how do we increase their life expectancy? The answer : add surfactants!

1.1.3.1 Structure and effect on interfacial tension

Surfactants are original molecules with a polar head and a long carbon tail. Those two parts have different affinities for water. On one hand, the polar head is hydrophilic and likes being surrounded by water molecules. On the other hand, the carbon chain is hydrophobic and hates being in contact with the water phase. Surfactants are often said to be amphiphilic due to this dual character. Most polar heads are anionic (sulfate $-OSO_3^-$), cationic (ammonium $-N^+(CH_3)_3$) or non-ionic (ethylene polyoxyde). The hydrophobic tail is generally a long aliphatic chain (10 carbon atoms). Fig. 1.6 shows the structure of common surfactants including those used in this thesis.

Surfactants adsorb at the air-water interface until saturation with the polar head in the aqueous phase and the hydrophobic tail in the air. The rest of surfactants remains in solution. However, in solution, surfactant molecules can aggregate due to the preference of carbon chains to flock together and to expel the polar heads. These aggregates, called micelles, are in equilibrium with isolated molecules when the bulk concentration of surfactants c is above the critical micellar concentration (cmc) [94]. The cmc is an important parameter to characterize the nature of a

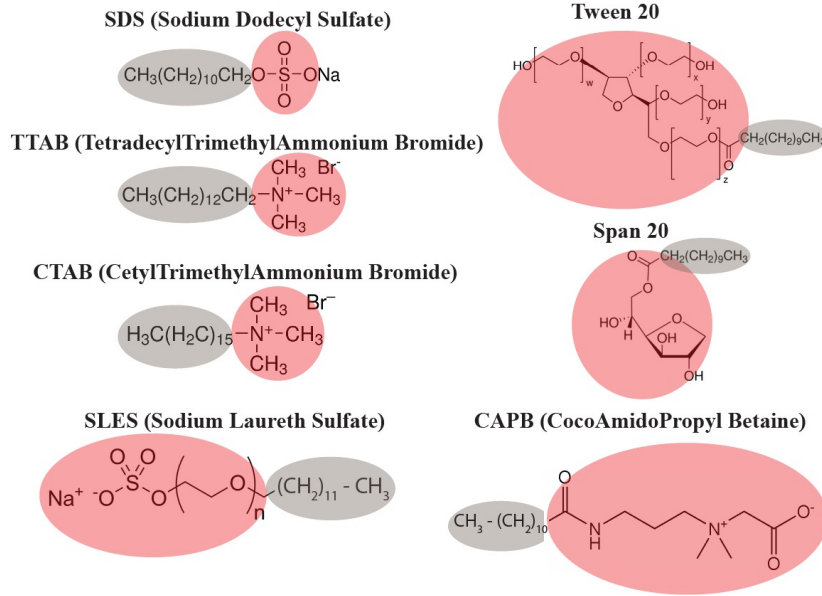


Figure 1.6: Chemical composition and structure of common surfactants. The red area is the polar hydrophilic head and the grey area is the hydrophobic tail.

surfactant and its effect on the interfacial tension.

Indeed, if one deposits a little droplet of surfactants on a water bath recovered by pepper, this latter will be expelled towards the outer ridge of the bath. In fact, pepper is put into motion by the surfactants that spread at the bath surface. This is only possible because surfactants decrease the interfacial tension. The air-liquid interfacial tension at the droplet location is lower than the air-liquid interfacial tension far from the droplet. Thus, the outer surface of the bath pulls on the inner surface and drags pepper with it. We can introduce the interfacial concentration of adsorbed surfactants Γ . The free enthalpy G_S is given by $G_S = n_S \mu + \gamma \Sigma$ where n_S and μ are, respectively, the number of molecules at the surface and the chemical potential of the dissolved surfactant (chemical potentials have to be equal between the surfactant at the interface and in the solution). We differentiate this relationship for dG_S , which gives:

$$dG_S = \mu dn_s + n_s d\mu + \gamma d\Sigma + \Sigma d\gamma. \quad (1.4)$$

Differentiating G_S with the first thermodynamical identity also gives $dG_S = \Omega dP - \tilde{S} d\tilde{T} + (\partial G_S / \partial n_S) dn_S + (\partial G_S / \partial \Sigma) d\Sigma = \Omega dP - \tilde{S} d\tilde{T} + \mu dn_S + \gamma d\Sigma$. The different physical parameters are the pressure P , the temperature \tilde{T} , the volume Ω , the entropy \tilde{S} , the number of molecules n_S , the chemical potential μ , the interfacial area Σ and the interfacial tension γ . Equating this expression with Eq. 1.4 yields $\Omega dP - \tilde{S} d\tilde{T} - n_s d\mu - \Sigma d\gamma = 0$. Constant pressure and temperature give:

$$d\gamma = -\Gamma d\mu \quad , \quad (1.5)$$

with $\Gamma = n_S/\Sigma$. When the bulk concentration c is small, we can consider the solution as ideal and write $\mu = \mu^0(\tilde{T}) + k_B\tilde{T} \ln c$, where $\mu^0(\tilde{T})$ is the reference potential. By differentiating μ , we get the well-known Gibbs' relationship [80]:

$$d\gamma = -k_B\tilde{T}\Gamma \frac{dc}{c}. \quad (1.6)$$

Thus, for adsorbed surfactants, if c increases, γ decreases. However, for $c > cmc$, μ remains constant with micelles in equilibrium with isolated molecules. Thus, γ stops decreasing and reaches a plateau value. Fig. 1.7 summarizes this dependence of γ on c . In this figure, we present the measurements of the air-water interfacial tension γ_{aw} for some of the surfactants used in our work (SDS for Sodium Dodecyl Sulfate and CAPB-SLES-Mac for CocoAmidoPropylBetaine-Sodium Laureth Sulfate-Myristic Acid).

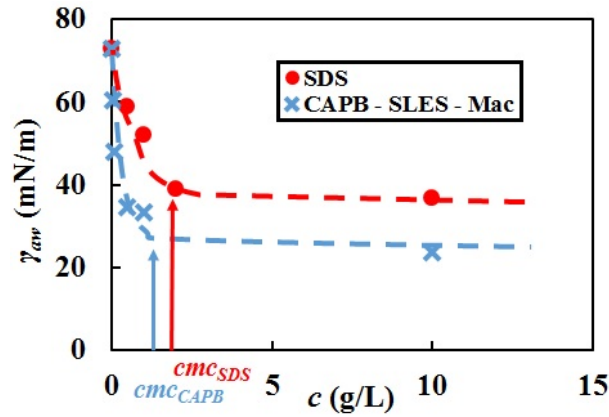


Figure 1.7: Typical evolution of the air-water interfacial tension γ_{aw} with the bulk surfactant concentration c for SDS and CAPB-SLES-Mac solutions.

However, when introducing surfactants into a solution, γ does not reach its equilibrium value instantaneously but slowly decreases with time. This time dependence is due to two factors: the surfactant molecule has to diffuse to the interface and has to adsorb at the interface. To do so, it has to overcome energy barrier (electrostatic or steric) and, at short times, the process can be kinematically limited. Thus, along with c , time has to be taken into account when measuring γ if the studied dynamics is examined at short times.

1.1.3.2 Stabilizing role

Fig. 1.8 depicts a soap film with the adsorption of surfactants at the air-water interfaces. When the polar head of the surfactant is charged, this geometry induces two charged monolayers that face each other with the polar heads oriented towards the aqueous phase. The Van der Waals attractions are compensated by the electrostatic repulsions induced by the charged heads. The balance between these forces defines an equilibrium thickness e . The repulsion between both interfaces is materialized by the disjoining pressure Π [4, 12].

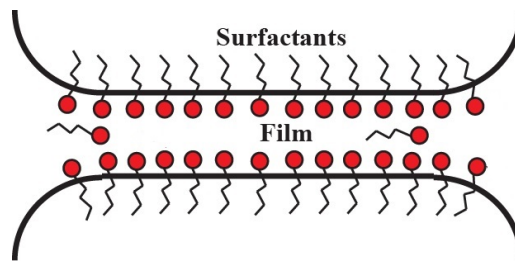


Figure 1.8: Soap film with surfactants at the air-water interfaces.

To illustrate this stabilizing role, Fig. 1.9 shows a film formed by pulling a frame out of a bath of surfactants [78]. Surfactants immediately adsorb at the air-water interfaces. Since the concentration of surfactants c is higher at the bottom than in the middle of the film, the interfacial tension γ_{aw} is lower at the bottom. Thus, an interfacial pressure gradient is created upwards. The upper part of the film “pulls” on the lower part. Therefore, balancing gravity and the interfacial capillary forces on an elementary volume of film (with two surfactant monolayers on each interface) yields:

$$\rho_w g e = 2 \frac{d\gamma_{aw}}{dz}, \quad (1.7)$$

where ρ_w is the solution density and z is the vertical position. Considering $c > cmc$ and integrating 1.7 between 0 ($\gamma_{aw} = \gamma_{cmc}$ which is the value of γ_{aw} at the cmc) and the maximum height z_{max} ($\gamma_{aw} = \gamma_0$ with γ_0 the air-pure water interfacial tension), we have an estimation of $z_{max} = 2(\gamma_0 - \gamma_{cmc})/\rho_w g e$. For $e = 1 \mu\text{m}$ and $\gamma_0 - \gamma_{cmc} \approx 50 \text{ mN/m}$, $z_{max} \approx 10 \text{ m!}$, as observed on giant soap films. The stability of a film is considerably enhanced by the presence of surfactants due to short-range interactions and interfacial tension gradients.

However, the role of surfactants in stabilizing soap films cannot be reduced to a simple decrease of interfacial tension: the interfacial tension of tap water is 50 mN/m . According to the theory presented above, we find $z_{max} \approx 4 \text{ m}$. Yet, it is impossible to withdraw a film out of tap water.

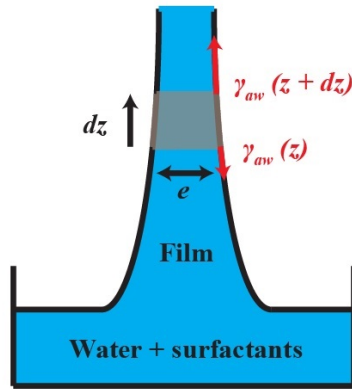


Figure 1.9: Liquid film pulled from a surfactant solution.

Surfactants modify the interfacial mechanics in a more complex way, as tentatively described below.

1.1.4 Effect of surfactants on the interfacial mechanics

Surfactants increase the stability of interfaces, especially the stability of soap films. However, all interfaces can still be deformed under normal and shear stresses. We characterize the ability of the interface to deform by viscoelastic parameters. The viscoelastic behaviour of an interface has a strong impact on the mechanical properties of macrostructures, such as foams [28].

1.1.4.1 Interfacial viscoelasticity

The interfacial area varies when a compression and a dilatation are applied to the interface [28]. The shape of the interface without any area variation can also change: in this case, a shear stress is applied. Fig. 1.10 sketches both situations.

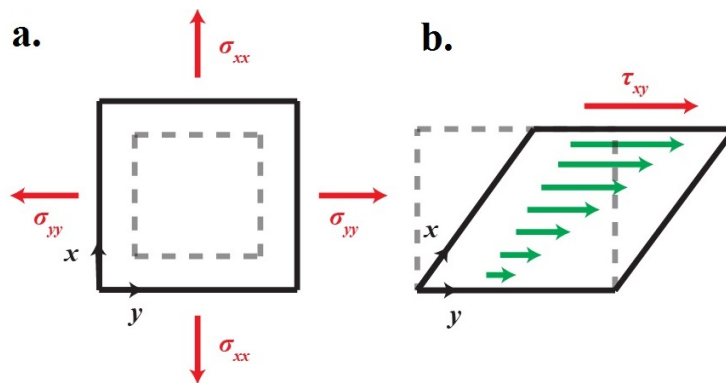


Figure 1.10: a. Interface under compression - dilatation. b. Interface under shear.

For an isotropic compression-dilatation sequence in small deformations, we can describe the normal stresses per unit length $\sigma = \sigma_{xx} = \sigma_{yy}$ and the shear stress per unit length τ_{xy} by:

$$\sigma = \gamma + E_d \frac{\delta\Sigma}{\Sigma} + \eta_d \frac{1}{\Sigma} \frac{d\Sigma}{dt} \quad , \quad \tau_{xy} = 0 \quad , \quad (1.8)$$

where η_d is the interfacial dilatational viscosity, E_d the interfacial dilatational elasticity and $\delta\Sigma$ the variation of interfacial area. In Eq. 1.8, the second term is the elastic contribution, while the third term represents the viscous contribution to the deformation. An elastic contribution appears because the variation $\delta\Sigma$ induces a variation of the interfacial surfactant concentration Γ , which also changes the value of γ and thus the interface “tension”. For insoluble surfactants, the variation of Γ is directly related to $\delta\Sigma$ and E_d is defined as the well-known Gibbs’- Marangoni elastic modulus $E_G = d\gamma/d \ln \Sigma$. For soluble surfactants, E_d depends on the frequency ω at which the interface is mechanically deformed in the case of periodic oscillations $\delta\Sigma_0 e^{i\omega t}$. We can define a complex interfacial dilatational modulus $E^*(\omega) = E_d(\omega) + i\omega\eta_d(\omega)$ and relate it to σ by:

$$\sigma = \gamma + Re(E^*(\omega)) \frac{\delta\Sigma_0}{\Sigma_0} e^{i\omega t}. \quad (1.9)$$

In the following sections, we refer to $|E^*(\omega)|$ as the parameter which allows us to characterize the mechanical response of an interface to normal stresses.

For shear deformation, it is also possible to define a shear stress σ_S with elastic and viscous contributions. Like the dilatational modulus, we can define a complex interfacial shear modulus $G^*(\omega) = G_{shear}(\omega) + i\omega\eta_{shear}$, where G_{shear} and η_{shear} are, respectively, the interfacial shear elasticity and the interfacial shear viscosity. More accurately, η_{shear} can depend on the interfacial shear rate when polymers are added to the interface for instance. In that case, η_{shear} also depends on the frequency ω .

The friction between molecules and the surfactant exchange between the interface and the bulk during deformation are influenced by the excitation of the interface, which explains the variations of the different elastic and viscous moduli with ω .

1.1.4.2 Resistance of a soap film

Looking at the interfacial viscoelasticity is essential because it plays an important role in the resistance of a soap film to the deformation, and thus to the stability of bigger structures with multiple interfaces like foams.

We can imagine a fluctuation of interfacial area because a film is stretched, as sketched in Fig. 1.11 [190]. The interfacial concentration of surfactants is higher at the edges than in the middle of the

film. This unfavourable situation creates an interfacial tension gradient which is proportional to the dilatational modulus $|E^*|$. The gradient drives surfactants back to the location where the concentration is the lowest. Moreover, this gradient also induces a liquid backflow to the same location by a Marangoni effect (i.e. a liquid flow induced by interfacial tension gradients). Eventually, the film does not break and is able to resist efficiently to the deformation.

The resistance of a film is mainly characterized by its dilatational and shear modulus $|E^*|$ and $|G^*|$ defined previously. By analogy to materials science, they recall the stiffness of a material. “Fracture” in the interfacial layer occurs if $|E^*|$ is too high, “plasticity” appears if $|E^*|$ is too small. The value of these parameters can influence the flow dynamics inside the film for example [28].

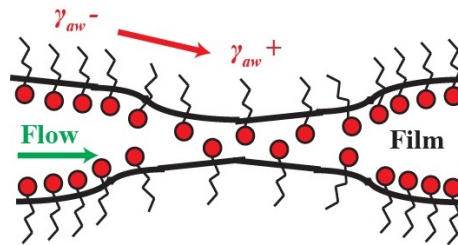


Figure 1.11: Deformation of a soap film under dilatation: “healing” process by air-water interfacial tension gradient from γ_{aw}^- to γ_{aw}^+ .

1.1.4.3 Rigid and mobile interfaces

The interfacial rigidity depends on the values of the dilatational modulus $|E^*|$ and the shear viscosity η_{shear} . When interfaces are non-rigid, they are called “mobile”. In this case, $|E^*|$ is basically of the order of a few mN/m and η_{shear} varies from 10^{-8} to 10^{-7} kg.s $^{-1}$ [28]. If interfaces are rigid, they are deemed as “immobile”. Then, $|E^*|$ increases around a few hundreds of mN/m and η_{shear} gets to 10^{-5} kg.s $^{-1}$. Fig. 1.12 shows measurements of $|E^*|$ for a mobile interface (SDS: Sodium dodecylsulfate) and an immobile interface (CAPB - Cocoamidopropylbetain - SLES: Sodium laurylethylsulfate - Mac: Myristic acid) with air and olive oil. To measure $|E^*|$, we apply 10 cycles of periodic oscillations to a pendant drop of volume $V_d = 1 - 2$ μ L at a frequency $f = 0.2$ Hz with a variable amplitude from 0.2 μ L (for small γ) to 2 μ L (for high γ). We can notice a strong difference from 10 - 20 mN/m to 300 mN/m for air-water interfaces in the case of rigid interfaces as γ decreases. The difference is less significant for oil-water interfaces [19] but still stiffer for CAPB solutions. Demonstrating the immobile character of the CAPB interfaces justifies the model used in Chapter 5.

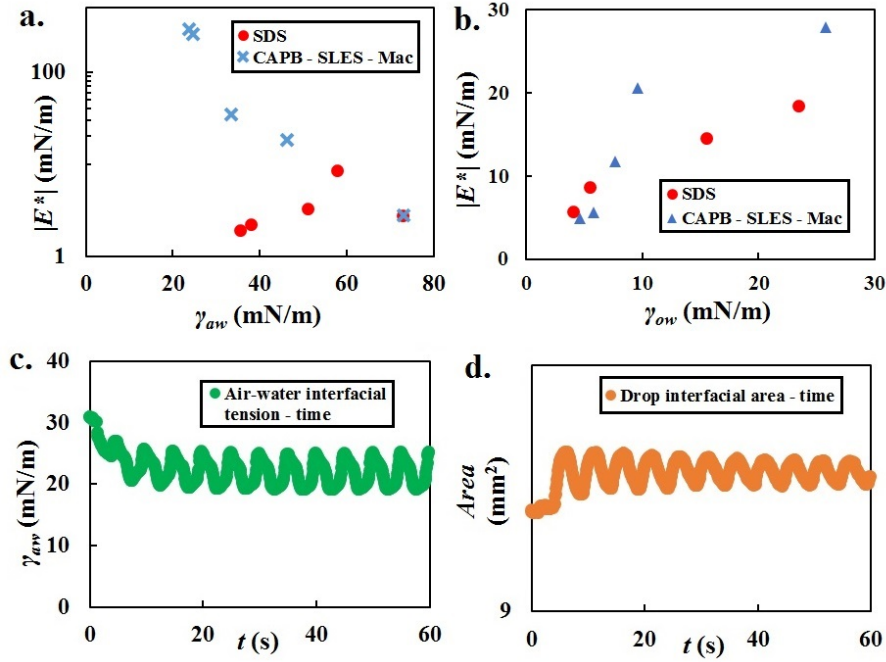


Figure 1.12: a. Measurements of the air-water dilatational modulus $|E^*|$ for two types of surfactants: CAPB-SLES-Mac and SDS. b. Measurements of the oil-water dilatational modulus $|E^*|$ for two types of surfactants: CAPB-SLES-Mac and SDS. c. Typical variations of air-water interfacial tension γ_{aw} . d. Typical variations of interfacial area with respect to time t . Curves are given for CAPB-SLES-Mac with the following parameters: $\gamma_{aw} = 23.7$ mN/m ($c = 10$ g/L) at equilibrium, initial drop volume $V_d = 2$ μ L, oscillation amplitude $\delta V_d = 0.2$ μ L and frequency $f = 0.2$ Hz.

We will see that interfacial mechanics has a strong influence on foam mechanics at a global scale, as observed in foam rheology or drainage.

1.1.5 Soap film: a fragile structure

Without any perturbation from other immiscible liquid and solid phases, a naked soap film is an evolving object that shrinks and that can break. Such phenomena involve different buoyancy and capillarity-driven mechanisms [154].

1.1.5.1 How films shrink...

As sketched in Fig. 1.1 and shown in Eq. 1.7, a vertical film can survive because surfactants bring rigidity to the film and drive a flow of water upwards. However, water can still drain downwards because of gravity, which could decrease the film thickness despite the surfactant-driven resistance. The flow rate downwards is relatively small. The flow of liquid is a Poiseuille flow. Balancing viscous forces and pressure gradient gives in scaling law $\eta_w v / e^2 \sim \Delta p / L$, where

η_w , v , e , Δp and L are respectively the water dynamic viscosity, the average flow velocity, the film thickness, the pressure difference between the top and the bottom of the film and the length of the film. Thus, $v \propto e^2$ and the flow rate is $Q_f \approx veW$ (where W is the film width), which gives $Q_f \propto We^3$, so the drainage process is very slow.

Due to water drainage, the film thickness can be smaller at one location and larger at another location. In the region of smaller thickness, the volume of water is smaller than the volume in the regions of larger thickness. Thus, because of buoyancy, the region of smaller thickness rises to the top of the film, as depicted in Fig. 1.13a. Such a movement, analogous to convection of fluid, can destabilize the film faster than classical drainage and entrain its rupture.

These convective fluid motions are emphasized by the presence of the edges of a film. As shown in Fig. 1.13b, the pressure p in the film around the frame is lower than the pressure close to the center of the film (atmospheric pressure p_{atm}). Hence, a flow is induced from the center to the edges. Regions of smaller thickness called black films appear and rise to the top of the frame due to buoyancy. This creates a turbulent flow from the edges to the middle of the film. This phenomenon, called marginal regeneration, also exists when the film is connected to a Plateau border, the curvature of the Plateau border inducing fluid motion. Marginal regeneration disturbs the film stability and can lead to rupture.

These mechanisms can be coupled with thermal fluctuations engendering a decrease of the film thickness, and also a diminution of the disjoining pressure Π . This speeds up the shrinking of the film and its rupture if the interfacial viscoelasticity defined in §1.1.4 is not sufficient enough.

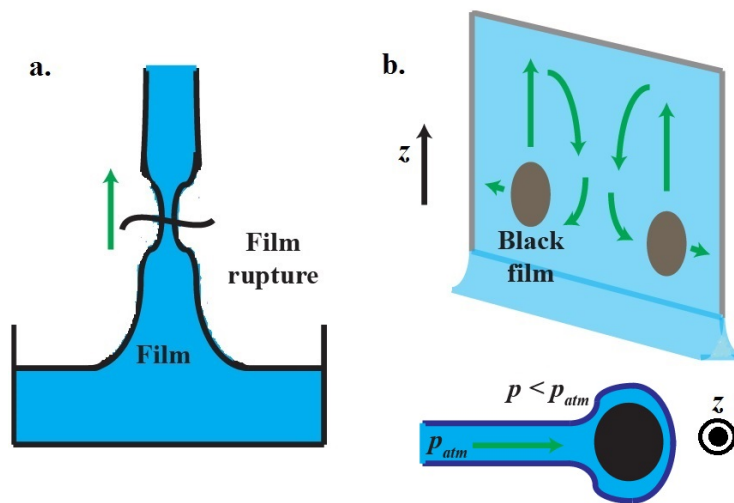


Figure 1.13: a. Shrinking of a film by the motion of regions of smaller thickness. b. Marginal regeneration in a film. The black films (regions of smaller thickness) generate a recirculation of water inside the film. Below: Top view of a film close to the frame.

1.1.5.2 How films break...

When a film breaks, the rupture dynamics can be well-described by the Taylor-Culick’s law [28, 49, 93, 154, 174, 181]. Fig. 1.14 presents the theoretical analysis of the film opening. In 1D dimension or in cylindrical coordinates, we can write the mass m_{rim} of the water rim around the edge of the hole as $m_{rim} = \rho_w e r_h$ where ρ_w and r_h are, respectively, the water density and the hole radius. The velocity v_{rim} of the hole edge is dr_h/dt . Then, the capillary force per unit length acting on the rim is $2\gamma_{aw}$. The balance between the quantity of motion $d(m_{rim}v_{rim})/dt$, with v_{rim} constant, and the capillary force yields the following equation for the hole velocity:

$$v_{rim} = \left(\frac{2\gamma_{aw}}{\rho_w e} \right)^{1/2}. \tag{1.10}$$

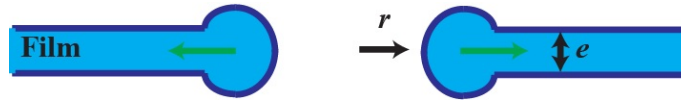


Figure 1.14: Opening dynamics of a film.

One can also state that the interfacial energy of the bubble per unit length $2r_h\gamma_{aw}$ is converted into the kinetic energy $(1/2)m_{rim}v_{rim}^2 = (1/2)\rho_w e r_h v_{rim}^2$, which gives $v_{rim} = (4\gamma_{aw}/\rho_w e)^{1/2}$. Eq. 1.10 actually violates energy conservation. However, it does not if one considers that dissipation also arises through the propagation of shock waves in the film. Recent works [135] have shown that the rigidity of the air-water interfaces modifies the Culick’s law and generates cracks in the breaking of a soap film.

1.2 Aqueous foams: definition, structure, characteristics and main properties

In §1.1, we travelled from the nanoscale of surfactants to the millimetric scale of isolated films and bubbles. We focus now on the scale of several bubbles which pack and interact with each other to generate aqueous foams [28, 158, 193].

1.2.1 Foam structure

An aqueous foam is a dispersion of gas bubbles in a water-based phase (generally an aqueous solution of surfactants). The structure of a foam highly depends on the liquid fraction ϕ_l , which is the ratio between the volume of liquid and the total volume of the foam.

1.2.1.1 Influence of the liquid fraction ϕ_l on the structure and Plateau laws

According to the liquid fraction, a foam adopts different structures:

- If $\phi_l > \phi_l^* = 0.26$ or 0.36 , the bubbles are spherical with no contact. The foam appears as a suspension of bubbles.
- If $\phi_l^* > \phi_l > \phi_l^{**}$, the bubbles touch each other and get packed together by deforming their interfaces. The foam is wet.
- If $\phi_l < \phi_l^{**}$, the bubbles are closely packed together and their geometry is polyhedral. The liquid phase is negligible and the foam is dry.

The transition value ϕ_l^* depends on the bubble assembly. This value is 0.26 for an ordered closed packing of bubbles and 0.36 for a random closed packing. The value of $\phi_l^{**} = 0.05$ for dry foams is an arbitrary value, it generally varies from 0.01 to 0.05 . Fig. 1.15 presents these three configurations.

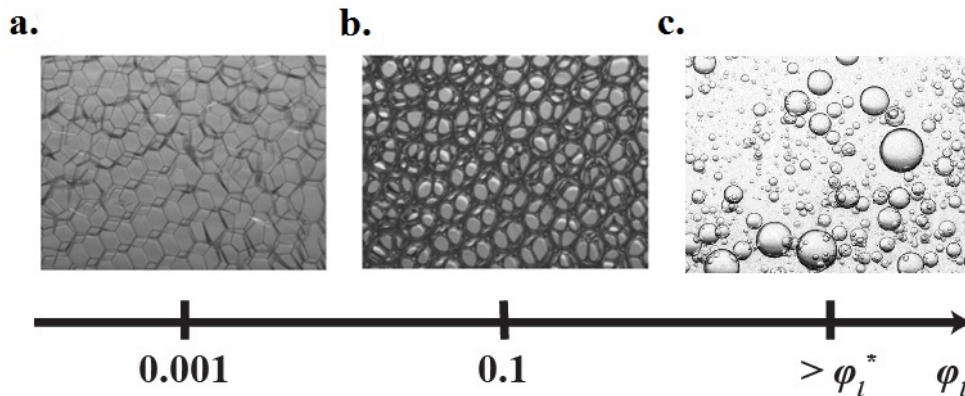


Figure 1.15: Foam topology: dry foam (a), wet foam (b) and suspension of bubbles (c).

For wet and dry foams, we can define specific structural features depicted in Fig. 1.16. When bubbles start being squeezed, thin films (≈ 100 nm to 1 μm width) between bubbles are therein created and meet each other by groups of three. The liquid microchannel (≈ 10 to 100 μm width and 100 μm to 1 mm length) that appears at their junction is called Plateau border (named after the physicist Joseph Plateau (1801-1883)). Four Plateau borders meet at the intersections called

vertices or nodes.

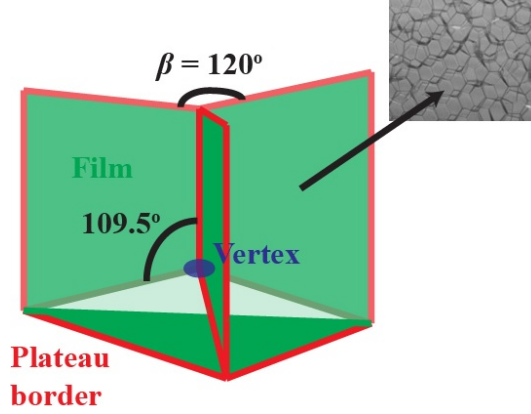


Figure 1.16: Plateau borders (red), films (green), vertices (blue) and the Plateau laws.

1.2.1.2 Dry foams

When the foam is sufficiently dry ($\phi_l < 0.01$), we can apply the Plateau laws [98, 140] to predict the structure of the foam. We assume that other conditions, such as mechanical equilibrium and incompressibility, are also fulfilled. As sketched in Fig. 1.16, the Plateau laws are given as follows:

- Films have a constant mean radius of curvature defined in Eq. 1.3.
- The angle β between two films is 120° . The interfacial forces induced by the three films and acting on a Plateau border transversely can only be balanced if $\beta = 120^\circ$.
- The Plateau borders meet together with an angle of 109.5° to form a tetraedron.

In this configuration, the Laplace law (Eq. 1.3) determines the curvature of the air-water interfaces and thus the pressure p in the liquid phase, i.e. in the Plateau borders and vertices. Fig. 1.17 shows the curvature radii of a Plateau where r_{PB} designates the typical width of a Plateau border. The negative curvature radius along the Plateau border cross-section is $R_1 \sim r_{PB}$ while the curvature radius in the Plateau border plane is $R_2 \sim R_b$ where R_b is the bubble radius. Since $r_{PB} \ll R_b$, Eq. 1.3 yields:

$$\Delta p = P_b - p \approx p_{atm} - p = \frac{\gamma_{aw}}{r_{PB}} \quad , \quad (1.11)$$

where the gas pressure in the bubbles is $P_b \approx p_{atm}$, which is the atmospheric pressure if we neglect the gas overpressure in the bubbles. For $r_{PB} \approx 10 \mu\text{m}$ and $\gamma_{aw} \approx 30 \text{ mN/m}$, $P_b - p \approx 3000 \text{ Pa}$. The liquid phase is thus in strong underpressure compared to the gas phase.

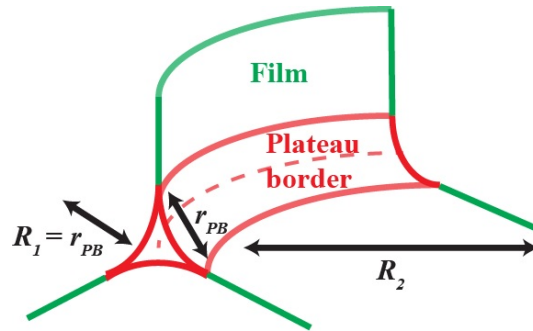


Figure 1.17: Plateau border and its curvature radii R_1 and R_2 for a dry foam.

We can estimate the value of r_{PB} and thus the capillary pressure, with respect to R_b and ϕ_l by considering a Kelvin structure [182] for the shape of a packed bubble in a dry foam, as sketched in Fig. 1.18. The Kelvin cell is a tetrakaidecahedron with 8 identical hexagonal faces and 6 identical square faces whose side is a Plateau border. Weaire and Phelan have brought corrections to this structure by considering pentagonal faces [194]. Meanwhile, for $\phi_l < 0.01$, we have, by geometrical calculations [28]:

$$r_{PB} = 1.74R_b\phi_l^{1/2}. \tag{1.12}$$

Thus, the lower the liquid fraction, the higher the capillary pressure, the lower the pressure in the liquid phase compared to the gas phase in the bubbles. This estimation is especially used in Chapter 5 for the study of the imbibition into aqueous foams.

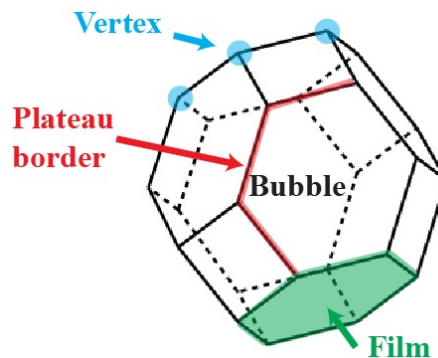


Figure 1.18: Kelvin cell and its typical geometrical features.

1.2.2 Main properties of foams

Owing to their peculiar structure presented in §1.2.1.2, foams are endowed with properties of considerable interest, especially in terms of pressure-driven flow inside the foam.

1.2.2.1 Capillary suction and disjoining pressure

Since the interfaces are parallel to each other in the films, their curvatures are very high and the subsequent pressure in the films is $p_f \approx P_b$ initially when the foam takes shape. Since $p \ll P_b$, the pressure in the Plateau border is lower than the pressure in the films, which triggers the motion of the liquid phase from the films to the Plateau borders. While a film is emptied from its liquid phase, the pressures get equilibrated and p_f decreases to reach p . For the film to be mechanically stable, a disjoining pressure $\Pi(e)$ (which depends on the film thickness e) must be exerted on the interface and its expression is given by:

$$\Pi(e) = P_b - p \approx \frac{\gamma_{aw}}{r_{PB}}. \quad (1.13)$$

From ϕ_l , R_b and Eq. 1.12, we deduce Π . Then by reporting this value on the theoretical calibration curves $\Pi(e)$ for each type of surfactants [11, 13–15], we can obtain the film thickness e and entirely determine the structural parameters of the foam at equilibrium.

1.2.2.2 Osmosis in foams

Since the pressure in the Plateau borders $p < p_{atm}$, if the foam is in contact with a reservoir at the atmospheric pressure p_{atm} , liquid rises from the reservoir to the foam through the Plateau border. Physically speaking, a foam wants to reduce its interfacial energy. If a foam is wet, it has fewer interfaces than a dry foam, which explains the imbibition of liquid. This imbibition phenomenon can be quantified by the osmotic pressure Π_o , which is the applied pressure to prevent liquid from entering the foam [143].

For a dry foam, Eq. 1.11 and Eq. 1.12, we deduce that:

$$\Pi_o = p_{atm} - p \approx \frac{\gamma_{aw}}{1.74R_b\phi_l^{1/2}}. \quad (1.14)$$

If the bubbles and the liquid fraction are small, we have more interfaces, thus the osmotic pressure is higher and imbibition more important with the aim to reduce the interfacial energy. As underlined before, the osmotic pressure depends on the variation of interfacial areas with the liq-

uid fraction. Simulations with the software *Surface Evolver* [21] allow to estimate this variation and are in good agreement with the empirical law for Π_o for $\phi_l < \phi_l^* = 0.26$ (thus generalize Eq. 1.14 for wet foams) calculated by Princen et al. [125, 143]:

$$\Pi_o = 7.3 \frac{\gamma_{aw}}{R_b \phi_l^{1/2}} (\phi_l - \phi_l^*)^2. \quad (1.15)$$

For dry foams, $\phi_l \ll \phi_l^*$, thus Eq. 1.15 is approximated by $\Pi_o = 7.3 \gamma_{aw} \phi_l^{*2} / R_b \phi_l^{1/2}$. For $\phi_l^* = 0.26$, $\Pi_o \approx 0.49 \gamma_{aw} / R_b \phi_l^{1/2}$ which is close to Eq. 1.14 given that $1/1.74 \approx 0.57$. So the consistency and the continuity between both models for dry and wet foams are ensured.

This osmosis and imbibition process in foams is at the origin of the work presented in Chapter 5.

1.2.3 How foams flow...

Along with the interactions between foams and external fluids, our work also focuses on the hydrodynamics of flowing foams in Chapter 6 especially. Therefore, introducing how a foam deforms and flows (i.e. its rheology) is of considerable interest. The interplay between the structural behaviour and the nature of the flow is particularly relevant.

1.2.3.1 Foams are complex fluids

The classification of "matter" is divided into several categories. On one hand, there is the simple fluids' world, such as water, oil or honey. These fluids are also called newtonian fluids. On the other hand, we have the elastic solids (or Hookean solids), such as metals and ceramics. In-between these two categories, one finds the complex fluids [45], such as toothpaste, ketchup, mayonnaise, cement, corn starch and liquid foams (as presented in the following). These fluids are known as non-newtonian fluids. The difference between the newtonian and the non-newtonian fluids lies on the response of the fluid to a deformation (which is assumed to be generally small to remain in the field of the theory of linear mechanics). The response of the fluid can be of different solid-liquid natures:

- elastic: the deformation is reversible. The fluid stores energy and can release it when coming back to its initial state.
- plastic: the deformation becomes irreversible above a certain threshold and the fluid keeps its final state without having the possibility to come back to its initial state.
- viscous: the fluid flows by losing energy (viscous dissipation).

Complex fluids combine all these features, while simple fluids are purely viscous and Hookean solids purely elastic.

The behaviour of a flowing complex fluid can be described and quantified by imposing a shear stress τ_{xy} or a small strain ϵ or a strain rate $\dot{\epsilon}$ on an elementary volume of fluid. For instance, for foams, this volume consists in several layers of bubbles. By applying a stress ramp at steady-state in a rheometer (respectively a strain ramp) and measuring the strain rate $\dot{\epsilon}$ (respectively the shear stress τ_{xy}), we can define τ_{xy} as:

$$\tau_{xy} = \chi(\epsilon, \dot{\epsilon}, t, \lambda) \quad , \quad (1.16)$$

where χ can be a function of $\dot{\epsilon}$, the strain ϵ , the time t and a structural constant λ taking the change of inner structure into account. For a purely viscous newtonian fluid, the shear stress only depends on the shear rate through the relationship $\tau_{xy} = \eta\dot{\epsilon}$ where η (Pa.s) is the shear viscosity, which is among the usual values (with the air-liquid interfacial tension for instance and the density) given to characterize a fluid. For a purely elastic material, the shear stress only depends on the strain through the relationship $\tau = G\epsilon$ where G is the shear modulus of the material. The most common rheological laws are summarized in Fig. 1.19.

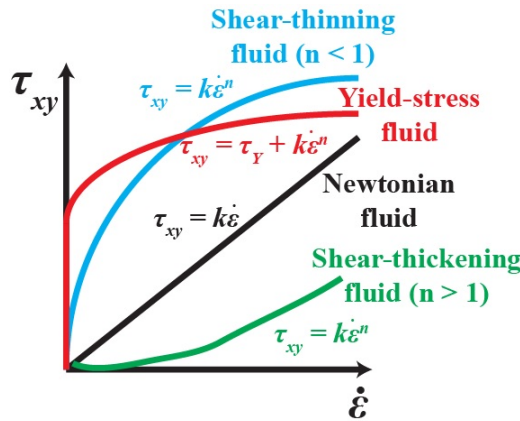


Figure 1.19: Rheological laws of complex and simple fluids.

For all complex fluids, the apparent shear viscosity $\eta_{app} = \tau_{xy}/\dot{\epsilon}$ depends on $\dot{\epsilon}$, while $\eta_{app} = \eta$ and is constant for newtonian fluids. The viscoelastic behaviour of a complex fluid can also be detected by applying a small oscillatory deformation and measuring the shear elastic modulus G' and the loss shear modulus G'' , and thus the complex shear modulus $G^* = G' + iG''$. This test is equivalent to the test used to characterize the rheological behaviour of a 2D film by measuring its interfacial shear modulus $|E^*|$ (see Eq. 1.9).

Among the family of complex fluids, a 3D foam can be assimilated and well-described as a yield stress fluid [45]. A yield stress fluid is a fluid that does not flow as long as the applied shear

stress τ_{xy} is below a threshold value τ_Y called yield stress. When $\tau_{xy} < \tau_Y$, the fluid remains in an elastic reversible state (or viscoelastic when viscous effects are taken into account at small stress amplitudes) and does not flow. However, when $\tau_{xy} > \tau_Y$, the foam deforms irreversibly and flows. The rheological behaviour can be written as the Herschel-Buckley law:

$$\begin{aligned} \dot{\epsilon} &= 0 & \text{if} & \tau_{xy} < \tau_Y, \\ \tau_{xy} &= \tau_Y + k_p \dot{\epsilon}^n & \text{if} & \tau_{xy} > \tau_Y, \end{aligned} \quad (1.17)$$

with k_p the constant plastic viscosity and n a power coefficient. Foams are shear-thinning yield-stress fluids since $n < 1$. The typical variations of the shear stress with respect to deformation and shear rate (rheogram - flow curve) are given in Fig. 1.20.

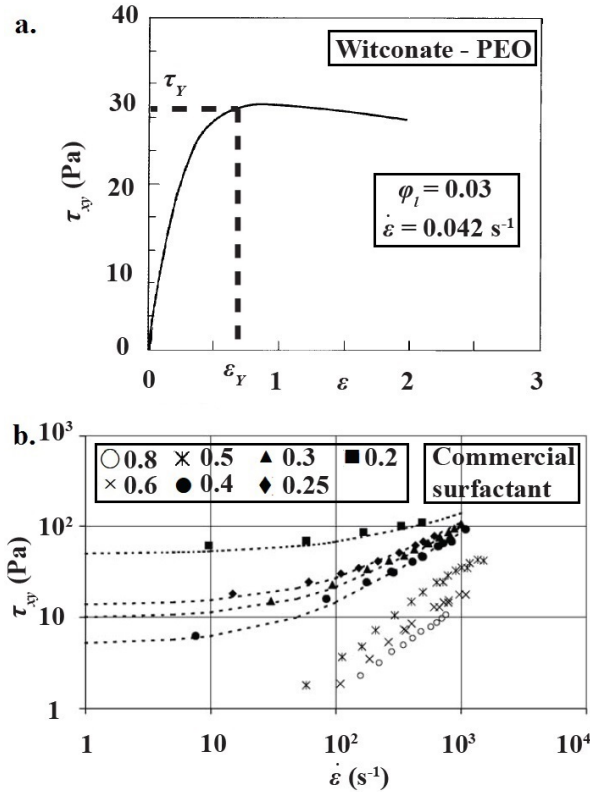


Figure 1.20: a. Variation of the shear stress τ_{xy} with respect to the deformation ϵ for a foam of witconate-PEO in a plate-plate geometry [101]: $\phi_l = 0.03$, $\dot{\epsilon} = 0.042 \text{ s}^{-1}$. b. Flow curve $\tau(\dot{\epsilon})$ for a foam of commercial surfactant in a Couette geometry [87]. The liquid fractions are given in the legend. The yield stress tends to disappear for high liquid fractions above 0.5 for which the foam looks more like a suspension of bubbles. The dotted lines are the Herschel-Buckley fit with the power law coefficient n varying from 1 for $\phi_l = 0.4$ to 0.66 and 0.5 for $\phi_l \approx 0.2$.

For the foam we use in Chapter 6, we determine the yield stress by a creep experiment. In a cone-plate geometry (rheometer Anton-Paar), we apply a constant shear stress for 120 s to a

foam sample (2 mm thick initially) whose bubble radius is 60 μm . We measure the deformation ϵ (or strain) as a function of time, from which we deduce the shear rate $\dot{\epsilon}$ at any moment. The shear rate decreases with time, so the apparent viscosity $\eta_{app} = \tau_{xy}/\dot{\epsilon}$ increases. Once the shear stress is removed after 120 s, the deformation and the apparent viscosity (infinite shear rate) drop abruptly to a value close to 0. We run a series of creep experiments for different successive shear stresses and record the value of the apparent viscosity at the moment where the shear stress is removed (yield point). Fig. 1.21 plots the apparent viscosity as a function of the applied shear stress.

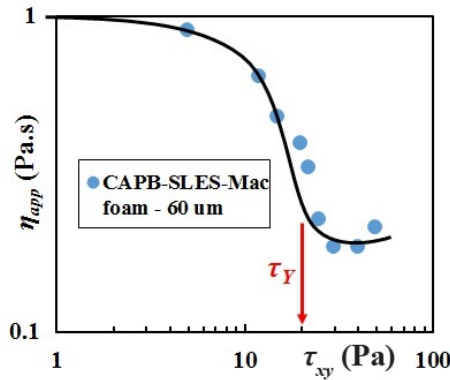


Figure 1.21: Apparent viscosity η_{app} as a function of the applied shear stress τ_{xy} in a creep experiment for a CAPB-SLES-Mac foam with a 60 μm bubble radius (see Chapter 6). The equilibrium yield stress τ_Y is indicated by the red arrow.

The drop in the value of the apparent viscosity, characteristic of a viscous flow behaviour, corresponds to the equilibrium yield-stress point. We find a value of $\tau_Y \approx 20$ Pa, which is of the same order of magnitude as the one measured in Fig. 1.20.

1.2.3.2 Relationship between the structure and the foam rheology

Now, how do τ_Y , k_p and n vary from one foam to another? [41, 60] It all depends on the initial structure of the foam and on the nature of the surfactants.

When a shear deformation is applied to a foam in a quasistatic configuration, the moment when the foam starts flowing (i.e. at the yield stress τ_Y) corresponds to the local situation where four Plateau borders meet with each other at one vertex. According to the Plateau laws (§1.2.1.2), this is highly unstable. Thus, both adjacent bubbles separate from each other by the creation of a new Plateau border: this rearrangement is called *T1* event [150, 151, 195] and shown in Fig. 1.22.

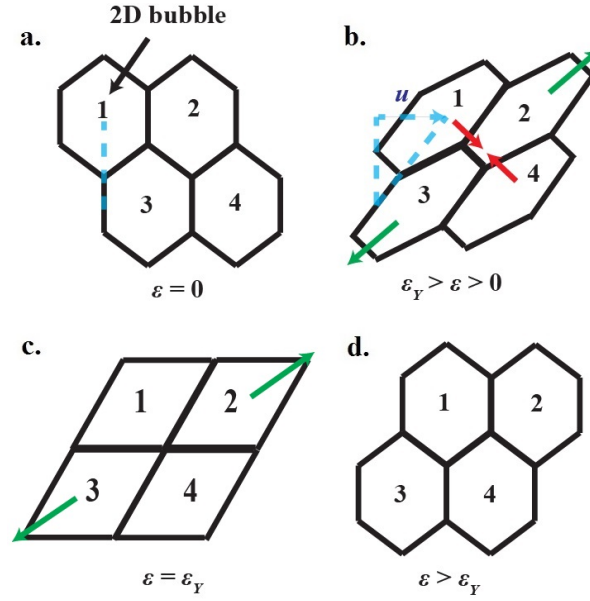


Figure 1.22: T1 event in 2D with ϵ the strain and ϵ_Y the yield strain. a. Initial state. b. Shear state where u is the displacement at the top of a bubble. c. Unstable state. d. Final state.

As sketched in Fig. 1.22b, one can show that, when subjected to a deformation ϵ , the perimeter length of a bubble in the direction of the shear plane is on the order of $R_b(1+\epsilon^2)^{1/2}$. The associated energy is $E_S \approx \gamma_{aw}R_b(1+\epsilon^2)^{1/2}$. The related elastic force is $F_{elastic} = dE_S/du \approx \gamma_{aw}\epsilon/(1+\epsilon^2)^{1/2}$, where $u = R_b\epsilon$ is the displacement at the top of a bubble. The shear stress τ is the shear force per horizontal length, i.e $\tau \approx F_{elastic}/R_b$. Hence, $\tau \approx \gamma_{aw}\epsilon/R_b(1+\epsilon^2)^{1/2}$. For small deformations $\epsilon \ll 1$, we have $\tau \approx \gamma_{aw}\epsilon/R_b$ at first order. Since the quasistatic shear modulus G is defined by $\tau \approx G\epsilon$. We have:

$$G \approx \frac{\gamma_{aw}}{R_b}. \quad (1.18)$$

At the yield point where four Plateau borders meet with each other (1.22c), the deformation reaches a value of order 1, since a bubble is deformed on a length close to the bubble radius, thus $\epsilon_Y \approx 1$. Thus, we have $\tau_Y \approx G\epsilon_Y \approx G$ and finally:

$$\tau_Y \approx \frac{\gamma_{aw}}{R_b}. \quad (1.19)$$

For $\gamma_{aw} = 30$ mN/m and $R_b = 1$ mm, $\tau_Y = 30$ Pa. This value is small compared to usual plasticity yield values for common solids, such as metals, which varies from 10^9 to 10^{11} Pa. Therefore, the word “soft matter” is well-adapted to describe the mechanical behaviour of foams.

This estimation of the yield stress is a good approximate for dry foams in which the liquid phase

has little influence on the global behaviour of the foam. Yet, when foams are wetter, the liquid fraction ϕ_l has a great importance and $\tau_Y \sim (\gamma_{aw}/R_b)(\phi_l^* - \phi_l)^2$ [142] where ϕ_l^* is the ordered (0.26) or disordered (0.36) maximum packing fraction.

The power coefficient n strongly depends on the nature of the air-water interfaces [57], thus on the nature of the surfactants, as stated in §1.1.4. For mobile interfaces (small dilatational modulus $|E^*|$), such as SDS, the interfaces are compressible and can deform and roll around the bubbles. This means that dissipation mainly occurs in the Plateau borders and $n \approx 0.5$. However for rigid interfaces (high dilatational modulus $|E^*|$), such as the CAPB solution mainly used in Chapter 2, 3, 5 and 6, the interfaces are incompressible, move with the bubbles and slide upon each other. This means that dissipation mostly occurs in the films. In that case, $n \approx 0.2$. Typical measurements from [81] show these two power laws in Fig. 1.23. Eventually, the plastic viscosity k_p is highly dependent on the air-water interfacial tension, but also on the bubble radius and the liquid fraction. More generally, the interfacial rigidity has a strong influence on the foam rheological parameters.

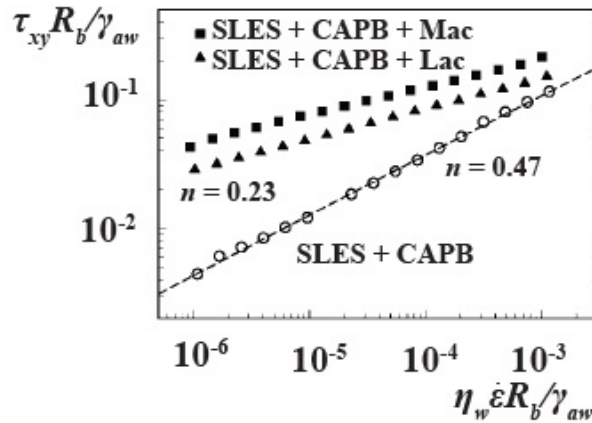


Figure 1.23: Dimensionless flow curves for different wet foams ($\phi_l = 0.1$) generated from surfactant solutions of SLES-CAPB (Mac is myristic acid and Lac is lauric acid) with mobile (without fatty acids) and rigid interfaces (with fatty acids Mac and Lac) [81].

The question of viscous dissipation and the local role of the interfaces is tackled into detail in Chapter 6.

1.3 Applications in environment and energy

As underlined in §1.1 and §1.2, foams have a complex structure with many physical, chemical and mechanical properties that can be quantified experimentally and described theoretically.

These properties allow to use foams in numerous applications with a special emphasis on soil remediation and enhanced oil recovery, which are the potential targets of our study.

1.3.1 Foams in everyday life

Foams are everywhere around us. They naturally appear when air or any gas is mixed with liquid. If surfactants are added, they can hold longer and form a dense structure of bubbles involved with entertaining, practical and industrial applications.

1.3.1.1 Around us...

Every foam constituent presented in §1.2.1.2 is related to a specific property. The gas phase represents 99 % of the foam volume. Thus, such a quantity provides a huge insulating reservoir, as air is known to be a very good insulator. Firefighters use the same idea to sprinkle a carpet of thick foam preventing fire from being nurtured by oxygen. They also use the lower density of foams compared to water and hydrocarbons to cover up fire.

For detergency issues, surfactants have a strong effect on the cleaning process but foams do not. They are a marketing symbol which enables to sell more body care products. Foams appear if contaminants and dirt vanish, typically for dishwashing issues. Thus, they are a good indicator of the cleaning efficiency. On the opposite, if foams appear in nature (sea, river), it means that waters are contaminated by waste containing surfactants.

We probably eat foams at least once per day. Creams, beers, champagne, gazeified drinks are or have foams in their contents. The foamy nature acts as a flavor enhancer owing to the number of interfaces. They ensure a stronger and "refreshing" contact between our taste sensors and the product we eat and drink. We can even find more foam-based products if we consider that cakes and bread were a foamy paste before baking.

The yield stress character of a foam is particularly at stake for shaving activities. Foams offer more comfort and coverage due to their solid-liquid nature. A single motion of razor blade allows to get rid of the shaving foam efficiently.

1.3.1.2 In industry

Apart from daily activities, foams have considerable interest in industrial applications [174]. Since air is its main constituent, foams are cheap products and companies make a large economic margin by selling air. They also generate less waste. When a facility or a soil is decontaminated

with a foam, it is cost-saving and environment-friendly, since less energy is used to separate the noxious agents from the foam.

Foams can also be spread very easily and very quickly. This is relevant for fire fighting but also insulating any chemical accidents and dampening explosions. The liquid phase can transport and capture different matters: solid (in case of a separation process like froth flotation), molecular (for medicinal purpose) and liquid (as we see in this study).

The structure of the foam, half-solid, half-liquid, and its flow properties are beneficial to push extractible liquids, such as in enhanced oil recovery. The dual structure enables to use foams as a precursor for the generation of solid foams. Aluminum foams (for car bumpers), polyurethane foams (for seats and mattresses), cement foams (for building insulation) are all intense subjects of fundamental and applied research.

Some of these aforementioned examples are illustrated in Fig. 1.24.

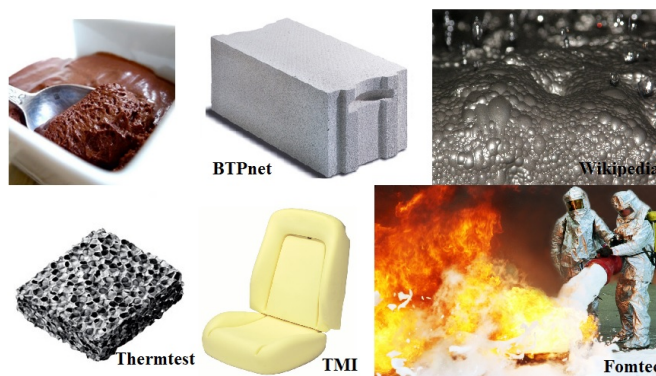


Figure 1.24: Examples of industrial applications.

In the following sections, we focus on two applications related to the extent of this work: soil remediation and enhanced oil recovery.

1.3.2 Towards a cleaner environment: soil remediation

The pollution of soils is a burning issue of public health and environmental awareness. Recently, an “Atlas de la France toxique” has been published. This book shows how contaminated soils (and waters) are located in France. A map of the polluted and degraded sites worldwide, published by the UNEP (United Nations Environment Program), is shown in Fig. 1.25. Worldwide, the situation is even worse due to population growth, industrial development and intensified agriculture.

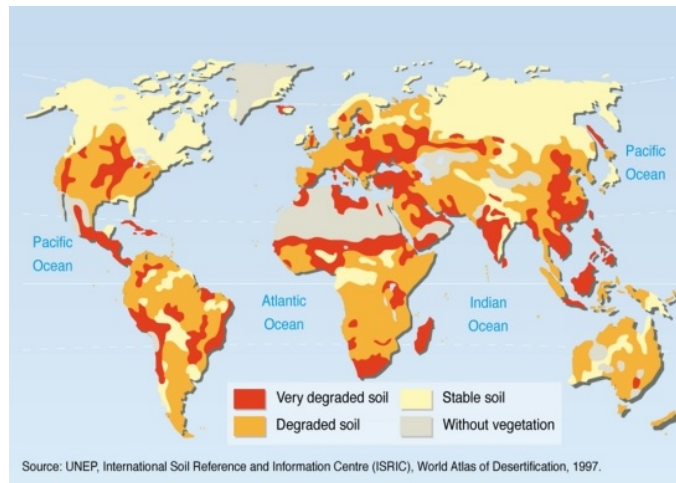


Figure 1.25: Map of the degraded sites worldwide (Source: UNEP).

However, heavy technical solutions exist to tackle this problem. But research on new ones, including foam engineering, is on track.

1.3.2.1 Common remediation techniques: advantages and drawbacks

We insist on some of the main remediation techniques. Our description is not comprehensive. Thus, more details can be found in [43]. Three different categories of processes can be highlighted and avoid the excavation of polluted land, which is cost-effective, heavy in means and tools, and destructive.

First, we have the physical methods. One can directly extract the pollutants from the soil without losing the treated area. As sketched in Fig. 1.26, many deep wells are dug into the porous soil. From one or several wells, air is injected and the soil is ventilated. This technique is particularly efficient for volatile pollutants. It is also possible to entrain the pollution by air injection into the ground waters and to pump these waters through extraction wells. The non-destruction of the soil is a strong advantage. However, the heterogeneity and the variable permeability of the soil are the main drawback, as well as the entrainment of organic matter during extraction.

Another physical method is to trap the pollution inside the soil. One can confine the polluted area with a surface coverage or directly solidify the pollution by the injection of concrete. This process is represented in Fig. 1.27. This technique is relevant for a high volume of pollutants. Meanwhile, one does not get rid of the pollution and the confinement requires a long-term control and monitoring.

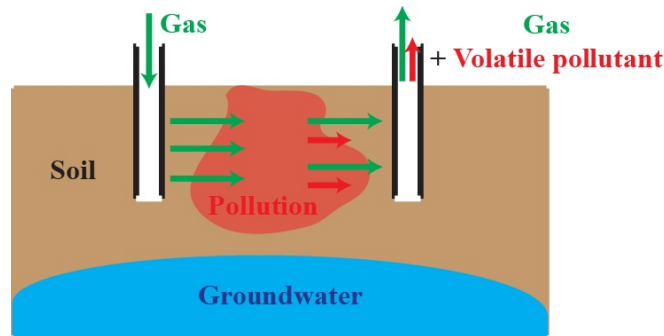


Figure 1.26: Physical method for soil remediation: soil ventilation.

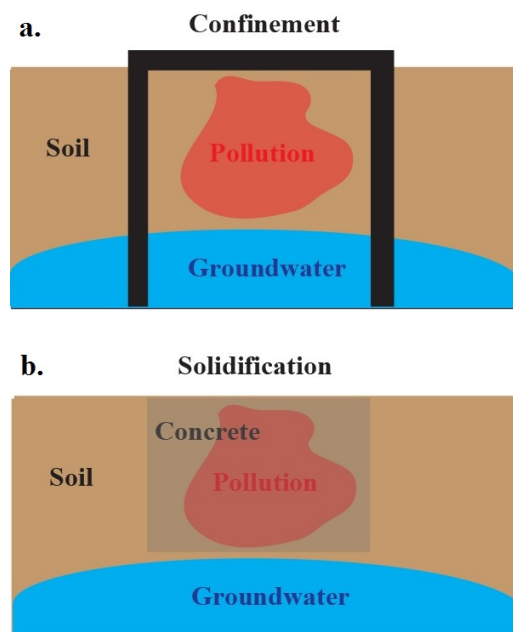


Figure 1.27: Physical methods for soil remediation: a. Pollution confinement. b. Pollution solidification.

Second, we have chemical methods. The principle is to “clean” the soil with chemical agents, as shown in Fig. 1.28. Pollutants react with chemicals by oxidation and reduction. The reaction products are drained to the ground waters. These latter are then pumped by extraction wells. This technique is efficient for soluble and concentrated pollutants, as well as permeable terrains. Yet, it does not hinder the transfer of pollutants from one place to another by adsorption or trapping in the pores. Soil heterogeneity and the high volume of waters to be treated are also real obstacles.

Third, we have biological methods. They resort to plants to remediate soils, also known as phytoremediation. This method is completely environment-friendly and renewable. It is efficient for small areas of pollution close to the surface, as far as the plant roots can penetrate the soil. Thus,

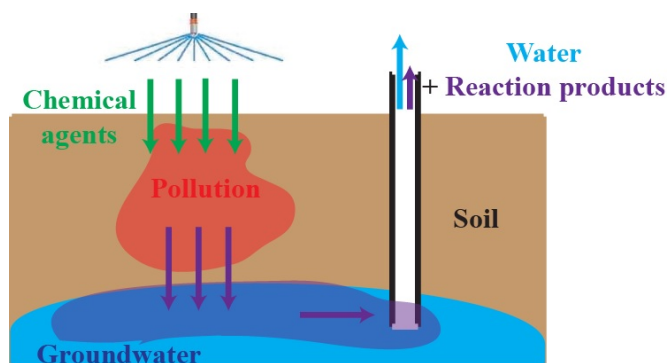


Figure 1.28: Remediation by chemical reactions.

the efficiency on bigger and deeper areas can be questioned. It also depends on the nature of the soil to allow plants to grow and spread.

1.3.2.2 What foams can improve...

Every conventional remediation technique has its advantages and its drawbacks. The main drawbacks are the cost, the area covered by the process and the post-treatment of the pollution. Foams could allow to solve some of these issues. Indeed, foams are a cheap product, since air is basically free. It does not require a lot of process and the material is light to transport. It would generate fewer by-products and less waste if the pollutants were to be absorbed and entrained by the foam. Besides, foams could carry chemical agents in the liquid phase and play the role of a transport agent into the porous soil. The transport of such agents is actually much more efficient with foams than with air or any newtonian liquids. Foams are able to span more polluted area and to invade all the defects and pores (providing that bubbles are small enough) thanks to their non-newtonian flow properties and their deformability. Therefore, such a flow allows foams to follow every direction. On the opposite, a pure cleaning solution would follow one direction lead by gravity and the injection pressure, with the capillary pressure preventing liquids from entering the smallest pores. Nuclear industry has already used foam processing to decommission old nuclear plants. The burning question of radioactive waste treatment obviously encourages research teams to find a method that generates less waste. In terms of efficiency, foams can decontaminate very complex structures, such as a nuclear tank and its related facilities. In this subject, the life expectancy of foams is also at stake to increase their efficiency and to use fewer surfactants (by the addition of plastifiers and stabilizing nanoparticles). More information on this subject of nuclear decommissioning by foams and other methods can be found in [51, 163]. Applying such processes to soil remediation appears very attracting, although the structure of a soil is more disordered and unknown than a tank.

1.3.3 Towards more energy supply: enhanced oil recovery

Soil remediation is a potential application to extract a material for people who would like to recycle or dispose of this material. However, extraction also means extracting resources that can be used in terms of energy. This is the case when one talks about enhanced oil recovery.

1.3.3.1 Processes of enhanced oil recovery

The extraction of oil (conventional and shale oil) is a research topic of considerable scope for the energy industry. We can describe the recovery of oil in three different stages [2].

First, one has the primary recovery. Once the extraction well is drilled into the oil reservoir, the high pressure of gas (which is often dissolved in the oil phase) enables oil to come out to the surface. A system of pumps can also allow to increase the difference of pressure between the reservoir and the surface. At the end of this stage, one extracts 10 to 20 % of the oil contained initially in the reservoir. While the reservoir is progressively emptied, the underground pressure decreases until being insufficient to push oil out of the reservoir. At this point, companies have to provide energy to the reservoir to extract the remaining oil. This is done by injecting different fluids into the soil to increase the pressure in the reservoir and push oil out. This is the secondary recovery. Fluids are water, natural gas and air. This technique is cost-effective, since energy needs to be provided to inject the aforementioned fluids. Meanwhile, the recovery rate is generally improved up to 35 to 45 %.

How about the remaining 55 to 65 %? This is the tertiary recovery or enhanced oil recovery. The idea is to increase the mobility of oil. The low recovery rate is essentially due to the high oil viscosity (1 to 10^8 Pa.s) and the existence of a high capillary pressure induced by the porous scale in the soil (see Eq. 1.1). One method consists in heating up the oil phase to decrease its viscosity and make it flow more easily. Water vapour is injected to increase the temperature. Burning oil (combustion) inside the reservoir is another heating technique.

The second well-known method to increase the mobility of oil is the injection of carbon dioxide. By doing so at high pressure and temperature, carbon dioxide goes to a supercritical state which is used as an organic solvent to dissolve and drag oil out. Then, the injection of water can also complement the process to extract the least viscous oil. With this technique, the recovery rate goes up between 40 and 60 %. We can cite two other techniques to improve the output of oil. Sometimes, micro-organisms are used to decompose oil into subproducts that are easier to extract. More frequently, surfactants are added to decrease the interfacial tension between water and oil and untrap oil from the porous matrix. This method is the one we are interested in. The question is: can we reach a better extraction efficiency above 60 %? This is where foams could help.

1.3.3.2 Surfactants, foams and the quest of oil

The injection of gas (especially carbon dioxide) and surfactants are two usual techniques to extract more oil. Why not combining both of them to inject aqueous foams inside the reservoir? This idea has come to the fore and promoted by oil research laboratories, such as the Institut Français du Pétrole Energies Nouvelles. Indeed, this could provide new opportunities:

- replace water by foams to push oil out. Like for soil remediation, we use fewer resources and make the most of the flow properties of foams,
- increase the mobility of oil by injecting gas,
- decrease the oil-water interfacial tension,
- ensure a better contact between oil and surfactants by co-transport with a gas phase. Hence, we use foams as a transport vector for chemical reactants.
- use foams as a direct agent to absorb oil.

Foams for enhanced oil recovery have been and are still the subject of some research on real soil systems and laboratory porous models. In particular, the injection of foams to push oil out of the porous matrix directly has been quantitatively studied [44, 66, 97, 144, 156, 166].

1.4 Conclusions

In this chapter, we have presented the different physical objects that will be part of the following chapters: surfactants, films, drops, foams and porous media. We have summed up their main properties and drawn the bond between all of them.

Surfactants are at the heart of the stability of air-water interfaces. They allow soap films to hold in time by putting them under “tension”. Short-range and electrostatic interactions, as well as interfacial tension gradients enhance the resistance of a film to deformation. This tension is quantified by the interfacial tension γ and the related interfacial energy E_I . This interfacial energy is proportional to the interfacial area. As a consequence, bubbles and drops appear when a film gets enclosed by minimizing the energy E_I and adopting a spherical shape.

The difference of pressure Δp_L through the air-liquid interface (bubbles in air) or the liquid-liquid interface (oil drops in water) is determined by the well-known Laplace law, which states that Δp_L is proportional to the interfacial tension and the main radii of curvature of the interface. The existence of an overpressure in a bubble due to this Laplace pressure maintains their shape. However, when bubbles flock together, they deform and form a dense assembly called foam.

Aqueous foams have a complex structure, potentially periodic for ordered bubbles, defined by

several typical features: films, Plateau borders at the bubbles' junction and vertices at the Plateau borders' junction. The geometry of foams gives astounding mechanical and physical properties. Among those, we can cite the osmosis effects that we will study in Chapter 2 and 5, the rheological behaviour similar to a yield stress fluid (either solid or liquid), the high interfacial rigidity (for specific surfactants) enabling foams to interact with other fluids, as we will see in Chapter 3, 5 and 6.

Combining these mechanical and physical properties offers huge opportunities in numerous daily and industrial applications from detergency to food industry. In manufacturing and civil engineering, foams represent the first stage to add air inclusions. In soil remediation and enhanced oil recovery, they contribute to extract more pollutants and oil. In these latter, the mechanisms at play involve the interactions between foams and immiscible fluids in a three-phase system.

Dynamical phenomena involving the three-phase system air, water and oil have been studied at the scale of a single Plateau border and an entire aqueous foam. In particular, some studies have shown that oil droplets can enhance foamability (how foams are generated) and foam stability (how foams can hold in time) [103, 161], although oil is known to be a good antifoaming agent. Such studies discuss about aqueous foams stabilized by emulsions, which are dispersions of oil in an aqueous phase. These kinds of foams are called "foamulsions" by Salonen et al. [161] and are characterized by the Plateau borders filled with oil droplets.

The situation we study is quite different. We want to use a naked foam as a liquid sponge in which oil is initially not present. Oil has to invade the foam while oil droplets play an active role in the formation of the foam for foamulsions. This idea of oil invasion is related to the work of Piroird et al. [137] on the propagation of an oil slug in a Plateau border and the simulations of an elongated oil droplet in a Plateau border by Neethling et al. [132]. Such studies have also been carried out for miscible liquids [39, 40].

However, oil has the peculiarity that it can interact with the external aqueous phase of the foam and destabilize the system. Thus, studying the hydrodynamics at the air-oil-water interface and the stability of oil-laden foams is the first step to understand how foams react to mechanical perturbations induced by the contact with an external oil phase and the possible invasion by this immiscible phase.

Chapter 2

Oil-foam interactions and stability

In our work, we try to understand how foams can transport immiscible liquids. Thus, studying how foams interact with these liquids and in particular how mechanically and physically stable this system can be are highly important. We need to consider the interaction between oil and every component of the foam at the local scale. In this chapter, we start by presenting the stability of soap films and Plateau borders, when put into contact with oil. Then, we discuss experimental results on the collapse of foams induced by oil. Unlike foams containing dispersed oil droplets, what happens if oil is directly put into contact with the foam after generation - by spongy absorption or forced injection? How do foams react to the invasion and the flow of oil afterwards? Is the oil-laden foam obtained with this experimental procedure stable?

Contents

2.1	Stability of a soap film towards oil	50
2.1.1	Liquid antifoams	50
2.1.2	Mechanisms of film rupture	51
2.1.2.1	Spreading fluid entrainment	52
2.1.2.2	Bridging-stretching and bridging-dewetting mechanism	52
2.2	Stability of oil-filled Plateau borders	55
2.2.1	In-situ interactions between oil and Plateau borders	55
2.2.1.1	Antifoaming action in Plateau borders	56
2.2.1.2	Criteria for antifoaming action between films and Plateau borders	57
2.2.2	Pseudoemulsion film and foam stability	58
2.2.2.1	Pseudoemulsion film and disjoining pressure	58
2.2.2.2	Pseudoemulsion film and stability mechanisms	59
2.3	Experimental study of the stability of oil-laden foams	60
2.3.1	Testing procedure	60
2.3.1.1	Observations of foam stability and collapse	61
2.3.1.2	Conditions increasing the stability of oil-laden foams	62
2.3.2	Morphology of gravitational imbibition into foams	63
2.3.2.1	Flow and collapse patterns	64
2.3.2.2	Analogy to forced drainage and flow in granular media	65
2.4	Conclusions	67

Specific variables

Variables	Parameters	Variables	Parameters
R_{ao}	Curvature radius of the air-oil interface	R_{ow}	Curvature radius of the oil-water interface
Q	Injection flow rate	h	Imbibition front
ϕ	Solid fraction	e	Film thickness
Δp_{ao}	Capillary pressure jump at the air-oil interface	Δp_{ow}	Capillary pressure jump at the oil-water interface

2.1 Stability of a soap film towards oil

In this section, we first look at the stability of a soap film when oil droplets are found inside the film. We highlight the different criteria that come into play to predict the antifoaming behaviour of an oil droplet or the stability of the film-oil system. We resort to classical thermodynamical arguments presented into great details in [56, 73], which do not actually describe the whole picture for foam stability. Meanwhile, different breaking mechanisms are presented if the soap film is destabilized by the presence of oil.

2.1.1 Liquid antifoams

As underlined in §1.1.5, destabilization mechanisms can occur in soap films due to drainage process and the fluctuations of the film thickness. The life expectancy of a film depends on the surfactant-induced rigidity of its interfaces, which can dampen any of these mechanisms. However, in most applications described in §1.3.1.2, one wants to break films and foams quickly (even before their generation). Thus, industries add liquid or solid antifoaming agents (oil-based and particle-based). Studying the different mechanisms explaining this antifoaming behaviour also allows us to understand what criteria are required to block this antifoaming action [56].

When a miscible liquid is injected into a film, two situations can occur. If the solution is a surfactant solution, the film generally remains stable and does not break, since interfaces are constantly saturated with surfactants. However, if a pure solution of water is injected, it is possible to induce a variation of interfacial concentration of surfactants by transfer to the bulk solution. Hence, one decreases the disjoining pressure, which can lead to film rupture [127].

Now, if immiscible liquids, typically oil and alkyl components (hexadecane, dodecane), are already dispersed into the foaming solution, they appear as small droplets in the film when these latters are generated, due to the oil-water interfacial tension [137]. This situation is drawn in Fig. 2.1a.

Then, two situations can appear. In one configuration, the oil droplet stays in the bulk phase. In the second configuration, it emerges at the air-water interface, as shown in Fig. 2.1a. This behaviour is controlled by the entry coefficient E . This coefficient compares the gain or the loss of interfacial energy between the first and the second configuration. From one configuration to the other, an air-water and an oil-water interface are replaced by an air-oil interface of the same area. Subsequently, the entry coefficient is defined as:

$$E = \gamma_{aw} + \gamma_{ow} - \gamma_{ao} \quad , \quad (2.1)$$

where γ_{aw} , γ_{ow} and γ_{ao} are, respectively, the air-water, the oil-water and the air-oil interfacial tensions. An oil droplet emerges at the air-water interface if $E > 0$ (loss of interfacial energy). On the opposite, if $E < 0$ (gain of interfacial energy), the droplet remains in the film, which does not break when invaded by an immiscible phase.

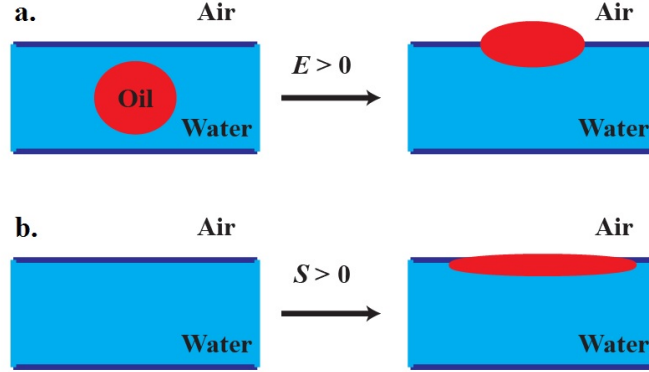


Figure 2.1: a. Emergence of oil at the air-water interface. b. Spreading of oil at the air-water interface.

If the droplet emerges at the air-water interface, it has two possibilities afterwards. The oil droplet can spread or not. The spreading behaviour depends on the spreading coefficient S which compares the difference of interfacial energy between a naked film and a film with oil at its air-water interface. From the non-spreading to the spreading configuration, the oil droplet loses an air-water interface but gains an oil-water and an air-oil interface of the same area. This transition is shown in Fig. 2.1b. The spreading coefficient is thus written as:

$$S = \gamma_{aw} - \gamma_{ow} - \gamma_{ao}. \quad (2.2)$$

If $S > 0$, it is energetically favourable for the oil droplet to spread onto the air-water interface. If $S < 0$, the oil droplet is unlikely to spread.

For antifoaming purpose, E must be positive since the oil droplet has to emerge at the air-water interface. Therefore, if $E < 0$, oil does not have any antifoaming activity and the film is stable, this is what we look for in our study. If $E > 0$, a film is more likely to break but it is also possible to have no film rupture, depending on the value of S .

2.1.2 Mechanisms of film rupture

In this section, we present the different mechanisms which destabilize the film according to the value of the thermodynamical coefficients E , S and B , and cause its rupture [56].

2.1.2.1 Spreading fluid entrainment

If $E > 0$ and $S > 0$, the oil droplet emerges and spreads at the air-water interface, as sketched in Fig. 2.2. The newly created air-oil interface does not contain any surfactants. Thus, attractive forces and mechanical fluctuations can destabilize the film. Moreover, the spreading of oil triggers the underlying flow of bulk aqueous phase by viscous entrainment. The bulk flow is ejected outwards, which thins the film and can eventually lead to rupture. The mechanism of spreading fluid entrainment has never been proven although this picture is commonly accepted. What has been observed is the existence of interfacial waves induced by the spreading of oil [56]. These waves destabilize and break the film. This is all the more true that the oil phase is able to sweep surfactants from the interface, which decreases the film elasticity and its resistance to the local deformations of the interface.

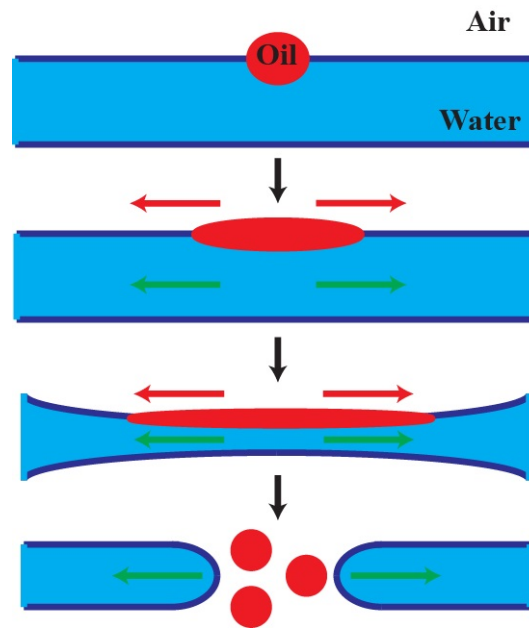


Figure 2.2: Spreading fluid entrainment mechanism. The red arrows indicate the oil spreading while the green arrows designate the outward flow of water inside the film.

2.1.2.2 Bridging-stretching and bridging-dewetting mechanism

When $E > 0$ and $S < 0$, the oil droplet emerges at the air-water interface but does not spread. As drawn in Fig. 2.3, the oil droplet bridges the film with the angle α_{ow} at the oil-water boundary. To determine if a bridge is stable, Garrett et al. [72] consider that the balance of capillary forces at the triple-phase contact line should be satisfied, as well as the pressure equilibrium beyond the

oil-water and the air-oil interfaces. Fig. 2.3 represents the geometry of the drop during the initial formation of the bridge.

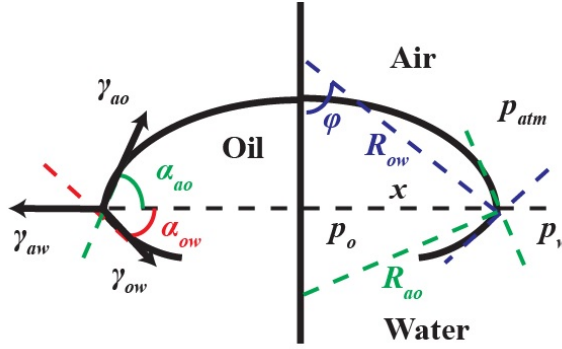


Figure 2.3: Geometry of the oil drop during bridge formation.

For the system to be in mechanical equilibrium, the capillary pressure jump across the air-oil interface $\Delta p_{ao} = p_o - p_{atm}$ and the oil-water interface $\Delta p_{ow} = p_o - p_w - \Pi$ should be equal (p_o , p_w and Π are the pressures in the oil phase, the aqueous phase and the disjoining pressure). From Garrett's notations, we introduce the curvature radii R_{ao} of the air-oil interface and R_{ow} of the oil-water interface, as well as ϕ the angle between the normal to the oil-water interface and the axis of revolution. The distance x is the distance to the axis of revolution. By using the Laplace law (see §1), we can estimate the capillary pressure jumps and the condition $\Delta p_{ao} = \Delta p_{ow}$ yields:

$$2 \frac{\gamma_{ow}}{R_{ow}} = 2 \gamma_{ow} \frac{\sin \phi}{x} = 2 \frac{\gamma_{ao}}{R_{ao}}. \quad (2.3)$$

Besides, one has to balance the capillary forces at the three-phase contact line with the Neumann relationship: $\gamma_{aw} + \gamma_{ao} + \gamma_{ow} = 0$. By projection on the vertical axis, one gets the following relationship:

$$\gamma_{ow} \sin \alpha_{ow} = \gamma_{ao} \sin \alpha_{ao}, \quad (2.4)$$

where α_{ao} is the angle made by the contact line with the air-oil interface. Using $x = R_d$, $\phi = \alpha_{ow}$ at the three-phase contact line - where R_d is the equivalent drop radius - $R_{ao} = R_d / \sin \alpha_{ao}$ and Eq. 2.4 in Eq. 2.3 gives the condition for mechanical equilibrium:

$$\frac{\sin \phi}{x} = \frac{\sin \alpha_{ow}}{R_d} = \frac{\gamma_{ao} \sin \alpha_{ao}}{\gamma_{ow} R_d}. \quad (2.5)$$

Eq. 2.5 is the equation of a series of spheres whose radius is $R_{ow} \propto 1 / \sin \alpha_{ow}$ and $\propto 1 / \sin \alpha_{ao}$.

Let us assume that $\alpha_{ow} < 90^\circ$. If α_{ow} decreases, $\sin \alpha_{ow}$ also decreases and R_{ow} should increase. At the same time, by volume conservation, α_{ao} and $\sin \alpha_{ao}$ have to increase. Thus, R_{ow} has to decrease. We have an incompatibility between both sides of Eq. 2.5.

Now if $\alpha_{ow} > 90^\circ$ and increases, $\sin \alpha_{ow}$ decreases and R_{ow} increases. By volume conservation, α_{ao} and $\sin \alpha_{ao}$ decrease and R_{ow} increases. This time, Eq. 2.5 can be verified. Therefore, an oil bridge exists when the oil-water interface is a spherical segment with $\alpha_{ow} > 90^\circ$. A bridge cannot be stable if $\alpha_{ow} < 90^\circ$. We relate this condition to the different interfacial tensions through the bridging coefficient B :

$$B = \gamma_{aw}^2 + \gamma_{ow}^2 - \gamma_{ao}^2. \quad (2.6)$$

It has been shown that the stability condition on α_{ow} is not fulfilled if $B > 0$ because $\cos \alpha_{ow} = (1 + (\gamma_{ow}/\gamma_{aw})^2 - (\gamma_{ao}/\gamma_{aw})^2)/2(\gamma_{ow}/\gamma_{aw})$ [72]. If $\alpha_{ow} > 90^\circ$ and $B < 0$, the oil bridge can be stable and the film does not break.

Fig. 2.4a describes the shape of the oil bridge when $\alpha_{ow} < 90^\circ$. We calculate Δp_{ao} and Δp_{ow} , which gives:

$$\Delta p_{ao} = 2 \frac{\gamma_{ow}}{R_{ao}}, \quad (2.7a)$$

$$\Delta p_{ow} = \gamma_{ow} \left(\frac{1}{R_{ao}} - \frac{1}{R_{ow}} \right). \quad (2.7b)$$

From Eq. 2.7a and Eq. 2.7b, $\Delta p_{ow} < \Delta p_{ao}$ (the capillary pressure jumps are not equal as expected) and $p_w = p_{atm} + \gamma_{ow} (1/R_{ao} + 1/R_{ow})$. Thus, the pressure in the film around the oil-water interface is higher than the pressure in the film far from the droplet ($\approx p_{atm}$). Then, a flow of water is induced inside the film from the droplet to the periphery of the film. The oil bridge is stretched, gets thinner from its edge to its center and eventually breaks into smaller oil droplets. The water film gets perforated and disappears. This is the bridging-stretching mechanism. This mechanism is summarized in Fig. 2.5b, along with experimental snapshots from [56]. It differs from the mechanism of spreading-fluid entrainment because the oil globule is eventually stretched and ruptures instead of the liquid film.

Another mechanism can also arise. If the oil droplet is not easy to deform (typically for high oil viscosities), the film dewets around the oil bridge until the triple-phase contact line is reached, which leads to rupture: this is the bridging-dewetting mechanism (see Fig. 2.5a). This mechanism competes with the bridging-stretching mechanism: one can assume that a comparison between

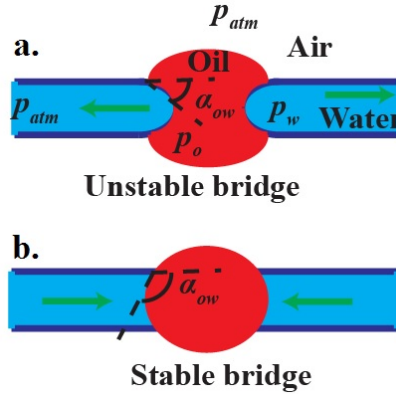


Figure 2.4: a. Unstable bridge: $\alpha_{ow} < 90^\circ$. b. Stable bridge: $\alpha_{ow} > 90^\circ$.

the characteristic time of dewetting and the time of oil deformation would give an idea on the mechanism at play. If the dewetting velocity is higher than the deformation velocity, then the bridging-dewetting mechanism is likely to occur. However, the bridging-stretching mechanism is encountered in most situations. This arises above all when films are covered with a predeposited layer of oil, which enhances oil wetting at the air-water interface by bringing more oil into the bridge.

For $\alpha_{ow} > 90^\circ$ (see Fig. 2.4b), we have $p_w = p_{atm} + \gamma_{ow}(1/R_{ao} - 1/R_{ow})$ with $R_{ow} < R_{ao}$. Thus, $p_w < p_{atm}$, which generates a flow of water from the film to the droplet and enhances the stability of the bridge.

2.2 Stability of oil-filled Plateau borders

Foams can collapse because oil-based antifoams (often coated with solid particles) are able to break films [120]. However, it is not the only location since oil can also be found in the Plateau borders. In fact, in the global picture of the conditions for which foams are unstable, the role of the different coefficients E , S and B , presented in §2.1.1, is still unclear.

2.2.1 In-situ interactions between oil and Plateau borders

Oil droplets can also be dispersed into Plateau borders. In this case, different mechanisms of rupture come into play. The shape of the oil phase is critical to understand how Plateau borders can resist to oil invasion.

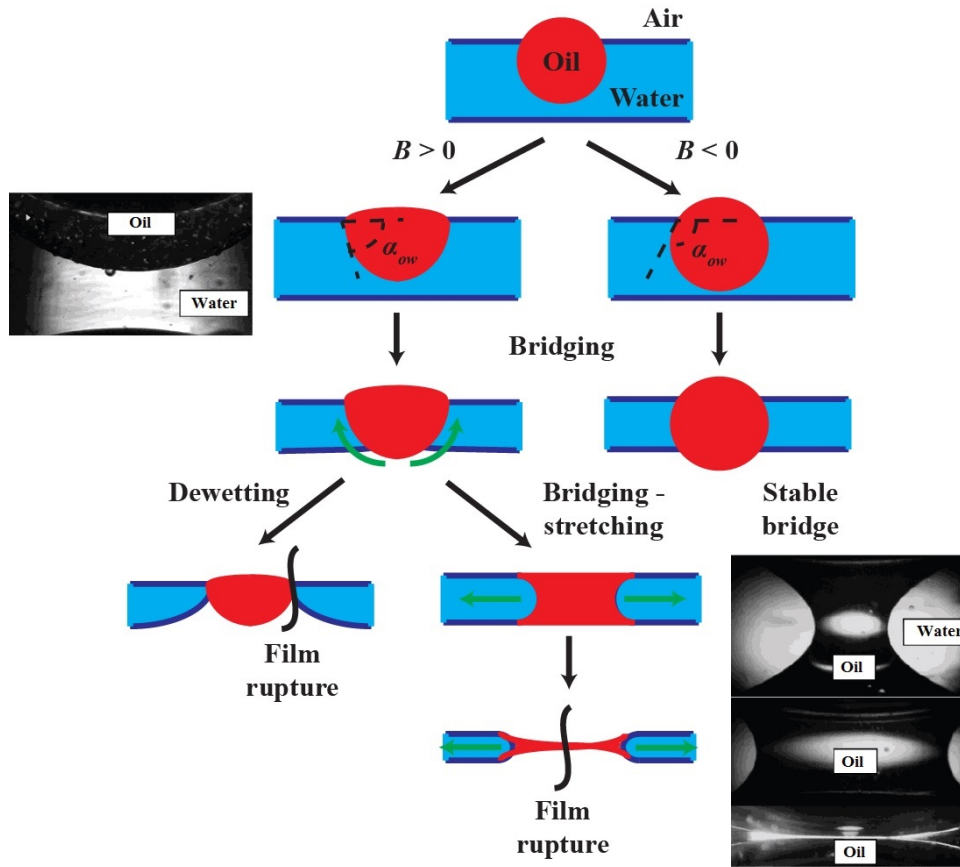


Figure 2.5: a. Bridging-dewetting mechanism. b. Bridging-stretching mechanism (black and white snapshots showing experimental observations [56]). c. Stable bridging.

2.2.1.1 Antifoaming action in Plateau borders

Any oil-induced antifoaming action starts by the emergence of oil drops at the air-water interface. This can happen in the films, as shown in §2.1.1, but also in the Plateau borders, as suggested by Koczó et al. [104].

When oil stays in the films and causes foam destruction by breaking them, it occurs very quickly after foam generation: this type of oil is a “fast” antifoam. Fast antifoams break the films by the bridging-dewetting or the bridging-stretching mechanism described in §2.1.2.2.

It is also possible to see oil drops being expelled from the films to the Plateau borders, as described in Fig. 2.6. Due to drainage, the film thickness can fluctuate with spots of larger thickness than the rest of the film, called dimples. These dimples can contain oil droplets. If the interfacial viscoelasticity is high, the dimple is unswollen symmetrically from both sides of the film. If the same viscoelasticity is small, the dimple is quickly expelled asymmetrically to the periphery of the film, due to the capillary suction. In both cases, dimples drive oil out of the film. Once oil is

expelled, the film reaches its equilibrium thickness ($e \approx 10$ nm from an initial thickness of $1 \mu\text{m}$).

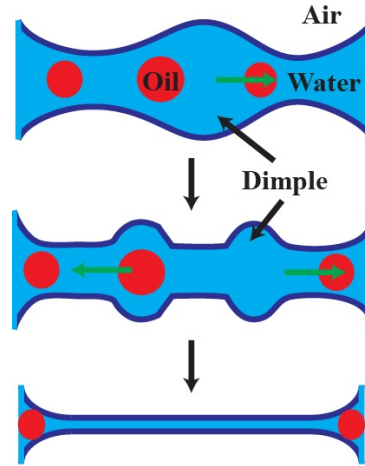


Figure 2.6: Stages of film thinning with oil droplets expelled to the Plateau border.

Due to foam drainage (i.e. liquid flow downwards owing to gravity), the Plateau borders get shrunk and the oil drops get compressed. By this compression, oil can emerge at the walls of the Plateau border and can induce rupture of the adjacent films by the generation of capillary waves, as shown in Fig. 2.7. When oil emerges at the wall of the Plateau border, it sweeps surfactants from the wall. Thus, the interfacial concentration of surfactants is lower in the Plateau border than in the connected films. There is an interfacial tension gradient from the film to the Plateau border, which generates a fluctuation of film thickness. This fluctuation creates capillary waves that can cause the rupture of films when the interfaces get closer. The timescale of foam destruction by slow antifoams is longer (typically minutes and hours) than foam destruction by fast antifoams (seconds). This difference is related to the drainage timescale in the films and the Plateau borders, as confirmed by a microgravity study [203].

2.2.1.2 Criteria for antifoaming action between films and Plateau borders

According to many studies and the conclusions from §2.1.1 and 2.2.1, oil spreading is not necessary to destabilize a foam through its films and its Plateau borders. Non-spreading oils and fast antifoams exhibit bridging mechanisms that do not require any spreading behaviour. However, oil spreading is very efficient to reduce the energy required to break the air-water interface and supply oil to the bridges.

The entry coefficient E and the spreading coefficient S do not determine the fast or slow character

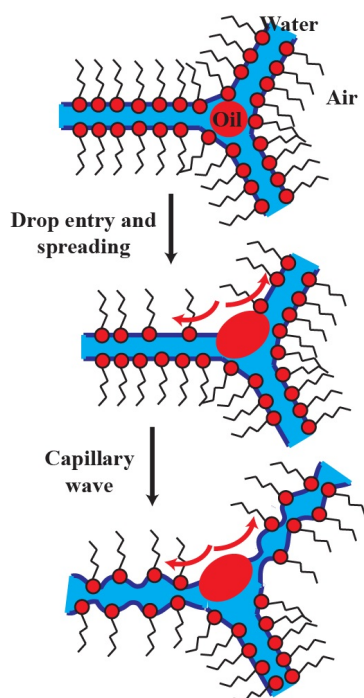


Figure 2.7: Spreading-wave generation.

of oil-based antifoams. Only the bridging coefficient B should be positive to have a destabilizing bridging mechanism. What determines such a character is the disjunction-related entry barrier which controls the entry of oil at the air-water interface. For fast antifoams, the entry barrier is low, below 15 Pa [56], since oil should easily enter the interface. Thus, solid-oil compounds are often considered as fast antifoams since solid particles decrease this entry barrier. For slow antifoams, the entry barrier is higher (above 15 Pa) and characteristic of many non particle-coated oil drops.

2.2.2 Pseudoemulsion film and foam stability

The entry barrier mentioned in §2.2.1.2 is related to the existence of a pseudoemulsion film between the air phase and the oil phase. This film has an important role in the stability of foams containing emulsified oil droplets.

2.2.2.1 Pseudoemulsion film and disjoining pressure

The pseudoemulsion film is a thin nanometric aqueous film formed between the air-water interface and an oil droplet in the Plateau border or in the film, as sketched in Fig. 2.8.

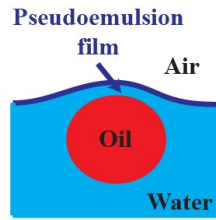


Figure 2.8: Pseudoemulsion film at the frontier between the oil phase and the air phase

Like naked foam films, a pseudoemulsion film can drain due to gravity and capillary suction. When drained, a pseudoemulsion film exhibits micellar structures which determines an oscillating disjoining pressure Π through the thickness of the film between the air-water interface and the oil-water interface [14, 15], as shown in Fig. 2.9. These oscillations originate from the surfactant structuring in both film and pseudoemulsion film, including the formation of micelles and bilayers. As the thickness decreases, these structures get closer and the repulsive forces get stronger, as well as the disjoining pressure.

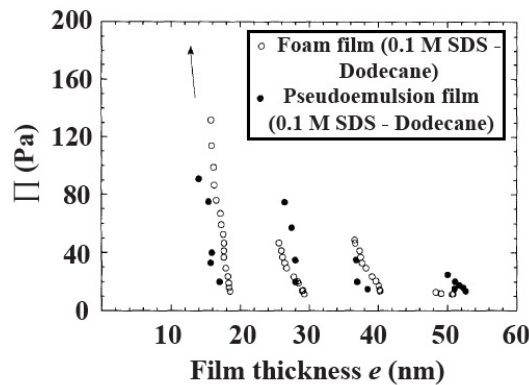


Figure 2.9: Disjoining pressure Π (Pa) as a function of film thickness e (nm) for SDS (concentration = 0.1 M) and dodecane [15].

2.2.2.2 Pseudoemulsion film and stability mechanisms

The disjoining force induced by the repulsive and attractive amphiphilic interactions, as well as the stratification of the pseudoemulsion film with micellar structures, enhances the stability of oil-filled Plateau borders and films. This happens when the entry coefficient E is negative and characteristic of repulsive interactions in the pseudoemulsion film .

To enable the destabilization of a Plateau border or a film, the oil droplet has to break the pseudoemulsion film when E is positive. However, the disjoining pressure, also characterized by the local entry barrier, can prevent oil from emerging. This is the case when this pressure overcomes

the capillary pressure driving the thinning of the pseudoemulsion film. If the capillary pressure is higher, the pseudoemulsion film breaks and oil can destabilize the foam structure [15].

Other mechanisms are involved when one looks at the foamability of foams with dispersed oil droplets at short times. A higher surfactant concentration increases the foamability. Due to the adsorption of surfactants at the surface of the oil droplet, the fewer surfactants are available, the more difficult the stabilization of the pseudoemulsion film. Oil droplets accumulate and block the Plateau borders, as shown in Fig. 2.10. This slows down drainage (Plateau borders and films thin due to gravity and capillary suction) and the thinning of the pseudoemulsion film, which reduces the probability of rupture [161].

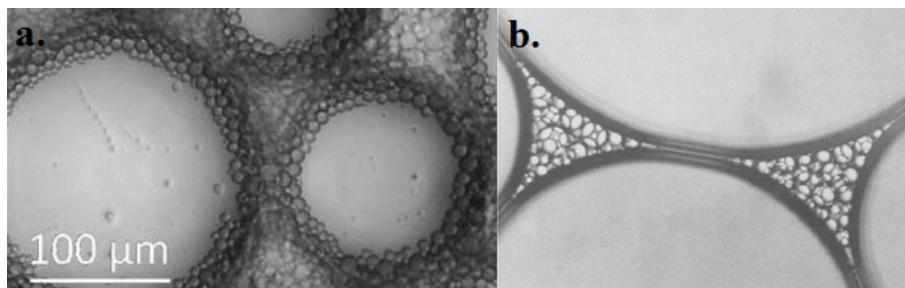


Figure 2.10: a. “Foamulsion” with rapeseed oil droplets - oil fraction: 70 % [161]. b. “Foamulsion” with octane droplets [103].

In the general case, foam stability is governed by the stability of the pseudoemulsion film. For dispersed oil droplets, the drainage dynamics drives its stability in Plateau borders and in films.

2.3 Experimental study of the stability of oil-laden foams

In §2.1.1, we present the stability of oil-laden foams through the stability of oil-filled films and thermodynamical coefficients. In §2.2.2.2, we consider the stability of emulsion-laden foams through the stability of the pseudoemulsion film. However, for imbibition into dry foams, the structures that are invaded by oil are the Plateau borders and the oil phase is continuous, so we can not really apply both theories. However, we would like to find a criterion that allows us to predict whether an aqueous foam would resist to oil invasion.

2.3.1 Testing procedure

In order to do so, we perform testing experiments to check the stability of oil-laden foams and to choose the appropriate oil-foaming solution for the rest of our work.

2.3.1.1 Observations of foam stability and collapse

To generate the foam, a slow flow of gaseous nitrogen is blown at imposed and constant pressure (0.7 Bar at the outlet of the gas tank) through a syringe needle (inner diameters vary from 0.6 to 0.8 mm depending on the bubble radii) into a 27 cm-high rectangular column with a 6 cm-wide square base filled with the foaming solution. The 5-cm high upper part of this column is removable, thus allowing us to extract foam samples at the top of the column. We use different syringe needles to obtain very monodisperse foams with an average bubble radius R_b of 0.5 mm, 1.8 mm or 2.5 mm and a polydispersity index of less than 2%. To measure the bubble size and check the monodispersity of the foam, we process an image of the foam taken near the column walls.

As shown in Fig. 2.11a, we deposit an oil droplet on a glass lamella. The oil droplet was previously covered by a surfactant film to facilitate the entry of oil into the foam. We also carry out the experiments without this covering procedure, which gives the same results presented in the following.

At time $t = 0$, we put this droplet into contact with a sample of dry aqueous foam and observe the response of the foam. We could have also imagined to deposit the oil droplet on top of a foam for our tests, as presented later in this chapter.

We use different oils and foaming solutions whose characteristics are summarized in Table 2.1. The CAPB-SLES-Mac solution, presented in Chapter 1, is a foaming solution of cosurfactants with a fatty acid, which gives a high interfacial viscoelasticity to the air-water interface. The foam generated by this solution can hold for many hours. Without Mac, the CAPB-SLES foam holds for a shorter time, but still higher than a few minutes. Saponin is a natural non-ionic surfactant which has the same properties as the CAPB-SLES-Mac surfactant, except that its air-water interfacial tension is exceptionally high (≈ 50 mN/m). The lifetime of SDS, TTAB-based foams is too short to be used in our experiments.

Three different scenarii are observed. First, in the case of sunflower oil/CAPB-SLES-Mac combination, oil is sucked up by the foam with a dynamics which will be described in Chapter 5. Oil is found in the network of the Plateau borders and very few breaking events occur. In that case, we can say that the foam is resistant to oil invasion. Second, in the case of silicon oil/CAPB-SLES-Mac combination, oil is also pumped through the Plateau borders. However, within less than 1 s, we observe many breaking events in the Plateau borders and the imbibed part of the foam has completely collapsed. Last, for sunflower oil/saponin couple, no imbibition occurs, the droplet is

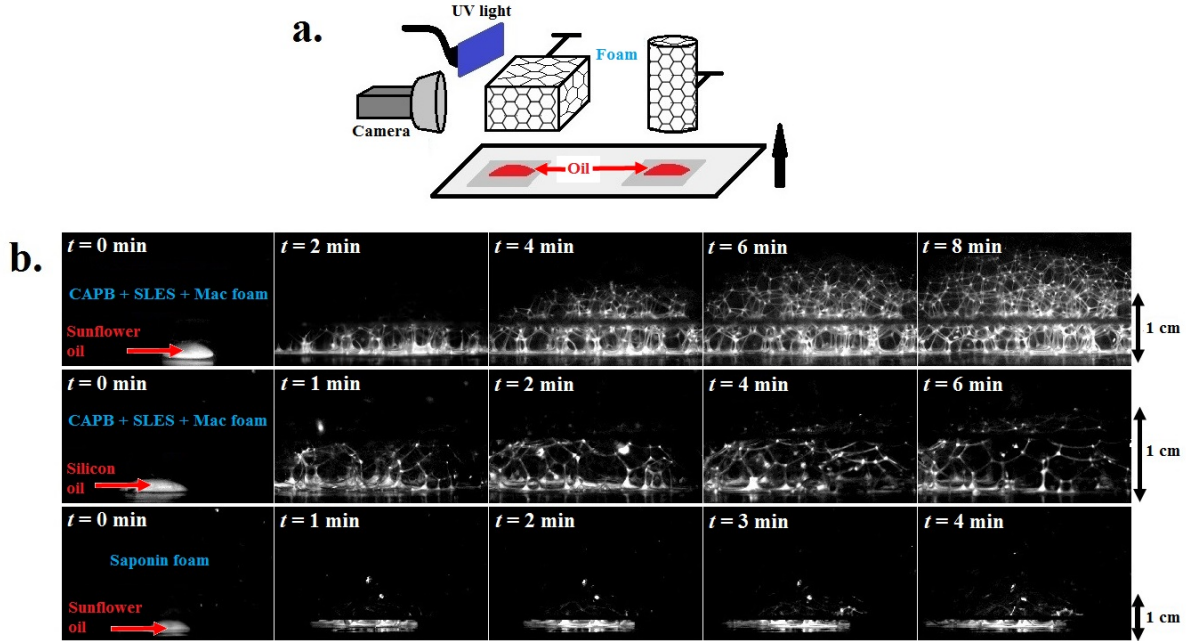


Figure 2.11: a. Experimental set-up for the stability experiments. b. Typical response of the foam to oil invasion for three different oil-foaming solution combinations: sunflower oil - CAPB+SLES+Mac, silicon oil - CAPB+SLES+Mac and sunflower oil - saponin (from top to bottom). Oil appears white due to a fluorescent agent (Yellow Black from Rohm and Haas).

Foaming solution	γ_{aw}	Oil	γ_{ao}	γ_{ow}	η_o	ρ_o	E	S	B	Stability
CAPB+SLES+Mac	23.7	Silicon oil	18.8	7	10	0.95	12	-2	257	Unstable
		Silicon oil	19.4	11	100	0.95	15	-7	305	Unstable
		Sunflower oil	32.5	4.5	55	0.92	-4	-13	-476	Stable
		Olive oil	30.8	3	61	0.92	-4	-10	-377	Stable
		Dodecane	21.8	4	0.88	0.75	6	-2	100	Unstable
		Hexadecane	27.3	4.9	3.13	0.77	1	-9	-165	Stable
CAPB+SLES	28.2	Silicon oil	18.8	3.6	10	0.95	13	6	457	Unstable
		Sunflower oil	32.5	2	55	0.92	-2	-6	-257	Unstable
Saponin	47.9	Silicon oil	18.8	11.7	10	0.95	17	17	2077	No invasion
		Sunflower oil	32.5	11.3	55	0.92	27	4	1364	No invasion
		Dodecane	21.8	10.9	0.88	0.77	37	15	1934	No invasion

Table 2.1: Oil and foaming solutions used for the characterization of the stability of oil-laden foams. The air-water γ_{aw} , air-oil γ_{ao} and γ_{ow} interfacial tensions (in mN/m) are given, as well as the entry E , spreading S and bridging B coefficient (in mN/m) defined in §2.1.1. We also indicate the oil viscosity η_o (mPa.s) and the oil density ρ_o .

only squeezed between the foam and the glass lamella without entering the foam.

2.3.1.2 Conditions increasing the stability of oil-laden foams

Let us compare our results to the stability theory developed for oil-filled films. In Fig. 2.12, we report the different oil-foaming solution combinations on a (B, E) diagram and a (S, E) diagram.

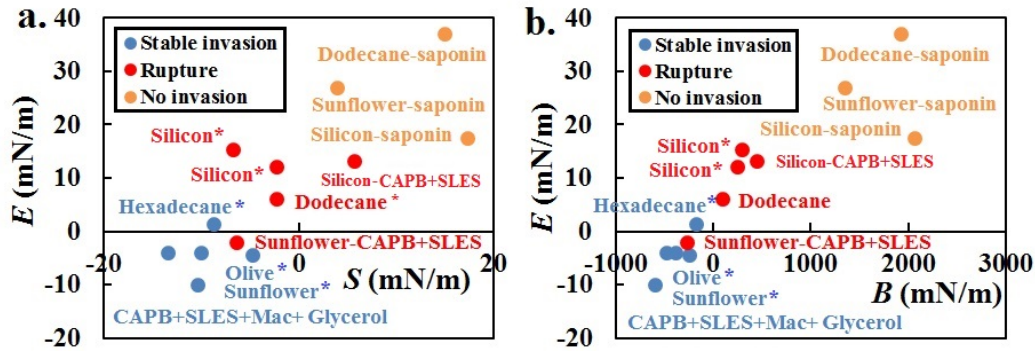


Figure 2.12: a. (S , E) diagram for the tested oils. b. (B , E) diagram for the tested oils. Two points correspond to miscible liquids: CAPB+SLES+Mac+Glycerol with $\eta_w = 10$ mPa.s and $\eta_w = 100$ mPa.s. The symbol * designates the surfactant CAPB-SLES-Mac.

Our experimental data shows a good correlation between the values of the coefficients E , S and B with the stable or unstable character of the oil-laden foams, except for two points. Fig. 2.12 shows that there are three different possibilities according to the values of E and S .

First, $E < 0$ (and $S < 0$ because $S < -2\gamma_{ow}$) means a stable invasion, this is especially the case for organic oils (olive, sunflower) and miscible liquids (glycerol+foaming solution). Second, $E > 0$ and $S \gg 0$ (and $B \gg 0$ since $B = (S + \gamma_{ow} + \gamma_{ao})^2 + \gamma_{ow}^2 - \gamma_{ao}^2$), as this is the case for the oil-saponin couples, means no invasion. Oil prefers to spread at the air-water interface, rather than invade the foam, this explains why a thin oil layer forms between the bottom of the foam and the glass lamella. Third, the foam collapse occurs for mineral oils which exhibit $E > 0$ and $S > 0$ (silicon oils/CAPB-SLES), and also $E > 0$, $S < 0$ and $B > 0$ (silicon oils/CAPB-SLES-Mac). Indeed, for $E > 0$ and $S < 0$, as it is the case also for hexadecane, the outcome of the oil-foam interaction is dictated by the value of B . In the unstable case, $B > 0$ but $B < 0$ in the stable case, which recalls the criterion for which an oil-laden film is stable. Stability theories for oil-laden foams and films seem in good agreement.

The case of the sunflower/CAPB-SLES couple is more intriguing. The entry coefficient E is negative but the oil droplet still destroys the foam. The static coefficients give indications on the stability of oil-laden foams but do not always describe the whole picture, especially when the entry coefficient is close to 0. The uncertainty around the values of interfacial tension ± 0.5 mN/m can make E either slightly positive, or slightly negative.

2.3.2 Morphology of gravitational imbibition into foams

Once the right oil-surfactant combination is found to have a stable oil-laden foam, we can visualize the flow of oil through the foam by a simple forced drainage. In this section, we provide

preliminary experimental results concerning the front pattern and velocity when oil is injected at the top of a foam sample at a given flow rate.

2.3.2.1 Flow and collapse patterns

For the experimental set-up, we use a cylindrical column of foam which is extracted by the same method as in §2.3. All the physical and chemical parameters are measured by the same procedure. We inject oil at the top of the sample, as shown in Fig. 2.13, by small capillary tubes. To obtain a uniform front throughout the width of the column, oil is flown throughout four injection points.

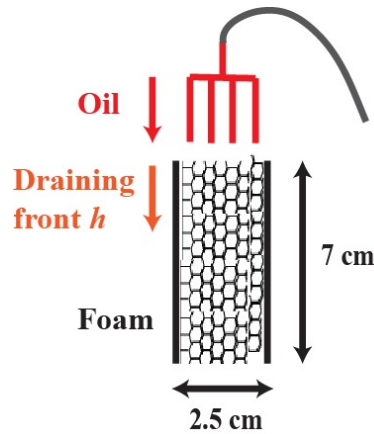


Figure 2.13: Experimental set-up for the forced drainage experiment.

We observe two types of flow pattern, as described in Fig. 2.14. For small flow rates, oil flows throughout the whole network of Plateau borders (see Fig. 2.14a), as observed in classical experiments of forced drainage when a foaming solution is injected at the top of the foam sample [28, 196]. For high flow rates, we observe a regime of “fracture”. The draining front flows downwards by following a straight path (see Fig. 2.14b).

To compare these two regimes quantitatively, we plot the position of the draining front h as a function of time t in Fig. 2.15. For the regime of “fracture”, the front propagation is linear with time. The draining velocity is constant and corresponds to the injection velocity. For the invasive regime at small flow rates, the front propagation slows down with time.

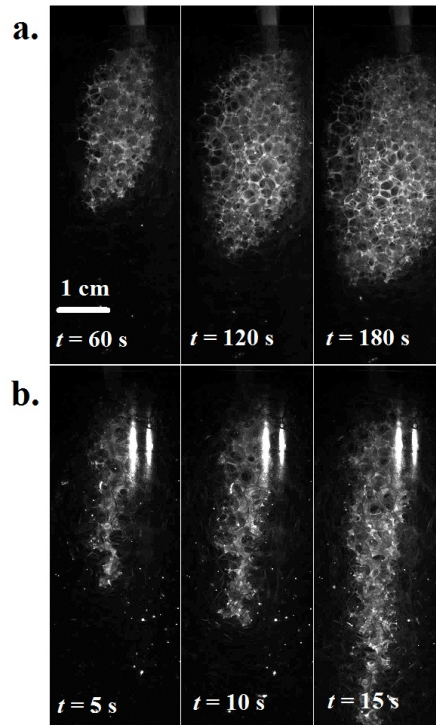


Figure 2.14: a. Invasive regime for $Q = 5$ mL/h (olive oil). b. "Fracture" regime for $Q = 20$ mL/h (sunflower oil).

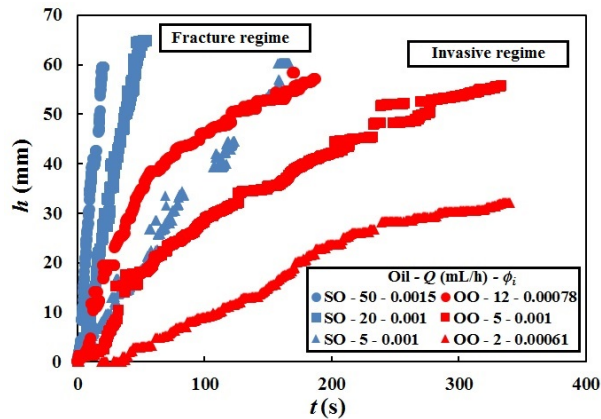


Figure 2.15: Draining front h as a function of time t for the forced drainage of olive oil (OO) and sunflower oil (SO). The injection flow rate Q (mL/h) and the initial liquid fraction ϕ_i are indicated in the legend.

2.3.2.2 Analogy to forced drainage and flow in granular media

The existence of different flow regimes is still an open question. However, we can try to make two analogies to explain our observations.

First, Weaire et al. [196] have shown the existence of a convective forced drainage above a flow velocity threshold. The convective drainage generates a motion of the bubbles upwards for wet foams. They report a threshold of 1 cm/s for a liquid fraction of 0.4-0.5. In our experiments, the

flow rate threshold is around 10 mL/h, which gives a velocity threshold of 5×10^{-4} cm/s for a liquid fraction of 10^{-3} . We have a difference of three orders of magnitude, which is probably due to the range of liquid fractions. The drier the foam, the easier it is to modify the structure of the foam at low flow rates.

However, we can make an analogy with air injection into a confined granular suspension. The injection of air into a water-immersed granular medium at a given flow rate exhibits different flow patterns presented in Fig. 2.16 [162]. Such regimes were also experimentally observed [35, 186, 187], as shown in Fig. 2.17.

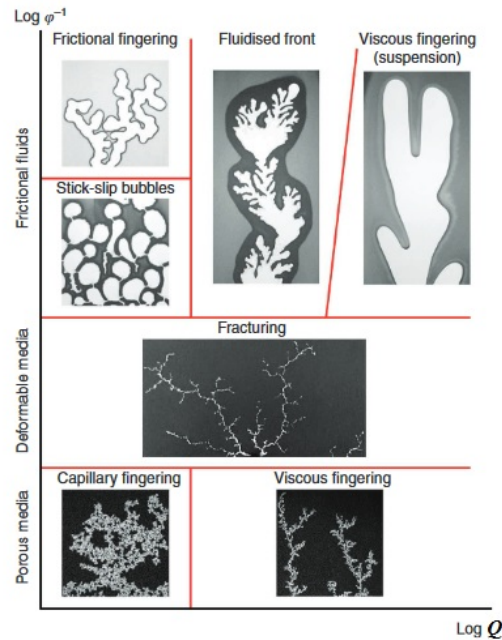


Figure 2.16: Flow morphology of a simple fluid flow (air) in a frictional fluid or granular mixture in a $(\log \phi^{-1}, \log Q)$ diagram where ϕ is the solid fraction and Q the injection flow rate. The figure is extracted from [162].

For granular suspensions, a phase diagram of the different flow morphology can be established by using the solid fraction and the injection flow rate as free parameters. For aqueous foams, equivalent free parameters (by considering the air fraction instead of the solid fraction) are also at stake. If we refer to Fig. 2.16 in the case of high air fractions (dry foams), we should observe capillary fingering at low flow rates and viscous fingering or fracturing at high flow rates, which is quite similar to our experimental observations. We did not systematically vary the liquid fraction of the foam, yet we observe similar features between dry foams (high air fraction) and confined granular suspensions with high solid fraction. In both cases, there is a transition at a critical flow rate for which the flow pattern evolves from a fracturing pattern to a more connected pattern.

Meanwhile, for granular suspensions, the regime of low flow rates is not exactly equivalent to the one we observe. Indeed, in aqueous foams, the permeability of all the paths is equivalent as long as the capillary forces are dominant. This is a consequence of the ability of the system to deform and to rearrange as needed. In granular suspensions, the system is more confined and the friction between all the grains induce heterogeneities in the different flow paths. Therefore, different flow paths are followed by the fluid as observed in Fig. 2.17a.

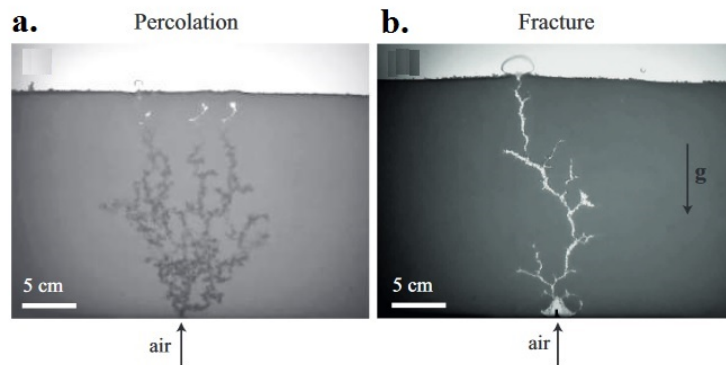


Figure 2.17: Experimental observations of air injection into a confined granular suspension. a. Percolation regime at low flow rate. b. “Fracture” regime at high flow rate. The pictures are extracted from [186].

2.4 Conclusions

Studying the hydrodynamics of oil-water interfaces is of considerable scope to understand the interactions between foams and immiscible oil-based liquids. Oil is often seen as an antifoaming agent which begets the breaking of soap films, and the possible collapse of foams. Especially in cleaning activities, if foams appear and hold for a long time, it means that greasy or oily impurities have completely vanished.

To start with, we have considered the stability of oil-filled films which is related to the values of the different interfacial tensions (air-water γ_{aw} , oil-water γ_{ow} and air-oil γ_{ao}) on which the different mechanisms of rupture also depend. One usually defines three coefficients: the entry coefficient E , the spreading coefficient S and the bridging coefficient B . To break a film, the oil droplet has to emerge at the air-water interface, which means $E > 0$. As soon as it does it, destabilization mechanisms arise when $S > 0$ (spreading-wave generation), or $S < 0$ and $B > 0$ (bridging-stretching and dewetting). On the opposite, if $E < 0$, or $E > 0$ and $B < 0$ (which gives $S < 0$ since $S < \sqrt{(\gamma_{ao} - \gamma_{ow})(\gamma_{ao} + \gamma_{ow})} - (\gamma_{ao} + \gamma_{ow})$), then the film does not break. This thermodynamical picture is in good agreement with our experimental observations, except

for one system.

We also have a global picture of oil invasion at the scale of several bubbles' layers in the case of forced imbibition. We highlight two different flow regimes according to the injection flow rate. These regimes of percolation and "tongues" recall observations made for air injection into a wet granular medium.

To go one step further in the next chapter, we focus on the oil-foam interaction in the specific geometry of a Plateau border.

Chapter 3

Plateau borders and oil: equilibrium shape and coalescence

As demonstrated in §2.1.1 and §2.2.1, oil drops are able to break films and Plateau borders. But they do not destabilize them in some physical conditions. Moreover, the study of the oil-induced stability is carried out for systems where antifoams are already present in the aqueous phase during foam generation. In our case, we consider a continuous oil phase forming long cylinders of oil inside the foam. These structures are also fragile and break when a film bursts.

Contents

3.1	Picture of oil invasion in Plateau borders by numerics	72
3.1.1	Oil slug in a Plateau border	72
3.1.1.1	Shape of the oil phase	72
3.1.1.2	Interactions between the oil phase and the pseudoemulsion film	73
3.1.2	Interfacial energy comparison with <i>Surface Evolver</i>	75
3.1.2.1	Numerical configurations	75
3.1.2.2	Comparison between numerics and experiments	76
3.2	Breaking dynamics in the oil-filled Plateau borders	77
3.2.1	The Rayleigh-Plateau instability	78
3.2.1.1	Breaking observations	78
3.2.1.2	Inertial regime	80
3.2.1.3	Viscous regime	81
3.2.2	Breaking of an emulsified viscous cylinder	81
3.2.2.1	Experiments	82
3.2.2.2	Instability wavelength	84
3.2.2.3	Size of the oil droplets	86
3.3	Conclusions	88

Specific variables

Variables	Parameters	Variables	Parameters
K	Interfacial tension ratio	r_o	Radius of oil droplet
Δp_f^*	Dimensionless pressure difference	r^*	Dimensionless droplet radius
r_c^*	Critical dimensionless radius	p_f^*	Dimensionless pressure in the pseudoemulsion film
p_w^*	Dimensionless pressure in the Plateau border	p_f	Pressure in the pseudoemulsion film
r_c	Cylinder radius	L_c	Cylinder length
S_c	Cylinder area	S_d	Droplet area
r_1	In-plane curvature radius in a bump	r_1^*	In-plane curvature radius in a hole
r_2	Transverse curvature radius in a bump	r_2^*	Transverse curvature radius in a hole
p_1	In-plane pressure in a bump	p_1^*	In-plane pressure in a hole
p_2	Transverse pressure in a bump	p_2^*	Transverse pressure in a hole
t_c	Characteristic time	k	Wave number
σ_{RP}	Growth rate of the Plateau-Rayleigh instability	η_c	Cylinder viscosity
γ^*	Interfacial tension between the inner and the outer fluid	η_f	Viscosity of the surrounding fluid
k_{max}	Wave number of maximum instability	λ_{max}	Wavelength of maximum instability
L_{oil}	Oil length	R_{oil}	Radius of the oil slug
N	Number of droplets for the breaking of a water jet	N^{foam}	Number of droplets from the rupture of a Plateau border
R_d^{foam}	Droplet radius from the rupture of a Plateau border	Ω_{PB}	Volume of a Plateau border
h_w	Humidity rate	P	Pressure
Bo	Bond number		

3.1 Picture of oil invasion in Plateau borders by numerics

As stated in §2.2.1, foam collapse can start from the Plateau borders with slow oil-based antifoams, non-coated with solid particles. The oil droplet has to emerge at the air-water interface. In §2.2.2, we consider the breaking of the pseudoemulsion as the triggering event for rupture of the Plateau border. However, we have highlighted mechanisms in which the Plateau border thins with the jamming of oil droplets. In our study, the configuration is quite different since the foam is already dry and imbibed with oil afterwards. In this situation, we need to understand how the oil phase is shaped inside the Plateau border. This was done by Neethling et al. by using *Surface Evolver* simulations [132].

3.1.1 Oil slug in a Plateau border

Neethling et al. [132] performed the numerical simulations of an oil slug elongated inside a Plateau border. Such configuration is similar to the configuration found in [137] in which Piroird et al. studied the elongation of an oil slug inside a Plateau border at imposed flow rate of oil or at imposed volume of oil.

3.1.1.1 Shape of the oil phase

In the case of film rupture by fast antifoams, we have seen that the entry coefficient E , the bridging coefficient B and the entry barrier are the three major factors that drive the stability of films macroscopically and locally. In particular, the entry barrier depends on the disjoining forces that appear in the air-water-oil pseudoemulsion film and how this film resists to the capillary suction. The pseudoemulsion film is a thin water film (nanometric) separating the squeezed oil phase from the air phase. This film has to break first to allow the bridge to be formed. If the entry barrier is too high, oil droplets are expelled towards the Plateau borders. They are trapped inside the Plateau border and the node with a pseudoemulsion film separating the oil phase from the air phase, as simulated in Fig. 3.2a.

Like for films, the rupture of the pseudoemulsion film is the first stage for the failure of Plateau borders, which could lead to foam collapse by the same aforementioned bridging mechanism or the spreading-wave generation (§2.2.1). A pseudoemulsion film breaks when the mechanical pressure exerted by the walls of the Plateau borders during drainage gets higher than the disjoining forces.

Neethling et al. [132] define different dimensionless parameters to characterize the shape of the droplet in the Plateau border and the subsequent stability of the pseudoemulsion film:

- the ratio K between the oil-water and the air-water interfacial tensions: $K = \gamma_{ow}/\gamma_{aw}$,
- the ratio r^* between the equivalent spherical radius of the oil droplet r_o and the curvature radius of the Plateau border r_{PB} (which is also the characteristic size of the Plateau border): $r^* = r_o/r_{PB}$,
- the ratio p^* between the different pressures P (pressure in the Plateau border, in the pseudoemulsion film and the oil phase) and the capillary pressure at the air-water interface: $p^* = (P - p_{atm})r_{PB}/\gamma_{aw}$.

Fig. 3.1 shows the three different configurations for the oil droplet in the Plateau border according to the size of the droplet.

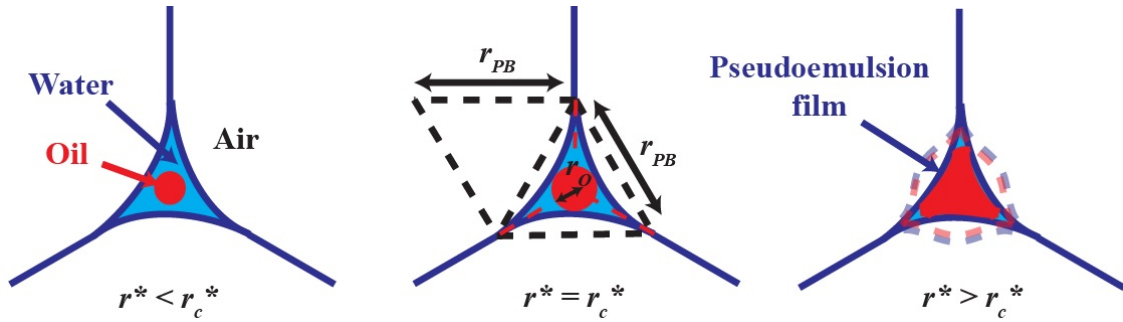


Figure 3.1: Configurations of the oil droplet in the Plateau border for different droplet sizes r^* , where $r_c^* = 2/\sqrt{3} - 1$ is the critical dimensionless radius for which the oil droplet first touches the walls of the Plateau border. In the far right image, the dotted lines indicate that oil can also swell the Plateau border and invert the curvature.

3.1.1.2 Interactions between the oil phase and the pseudoemulsion film

The size of the oil droplet r^* and the interfacial tension ratio K have a strong influence on the pressure p_f^* exerted in the pseudoemulsion film and the related pressure difference with the Plateau border $\Delta p_f^* = p_f^* - p_w^*$, where p_w^* is the dimensionless pressure in the Plateau border. Fig. 3.3 shows the evolution of Δp_f^* with respect to r^* . Small droplets and high interfacial tension ratios induce a stronger pressure on the pseudoemulsion film, due to the curvature of the oil droplet. Since $\Delta p_f^* > 1$ for most droplet sizes and interfacial tension ratios, the pseudoemulsion film is curved outwards (it swells the Plateau border). However when the interfacial tension ratio gets lower (≈ 0.1), $\Delta p_f^* < 1$. We have $\Delta p_f^* = 1 + (p_f - p_{atm})r_{PB}/\gamma_{aw}$ and $p_f - p_{atm} < 0$, thus the pseudoemulsion film is oriented inwards. As K goes to zero, the pseudoemulsion film remains curved inwards to follow the curvature of the Plateau border, i.e. $\Delta p_f^* = 0$ and $p_f - p_{atm} =$

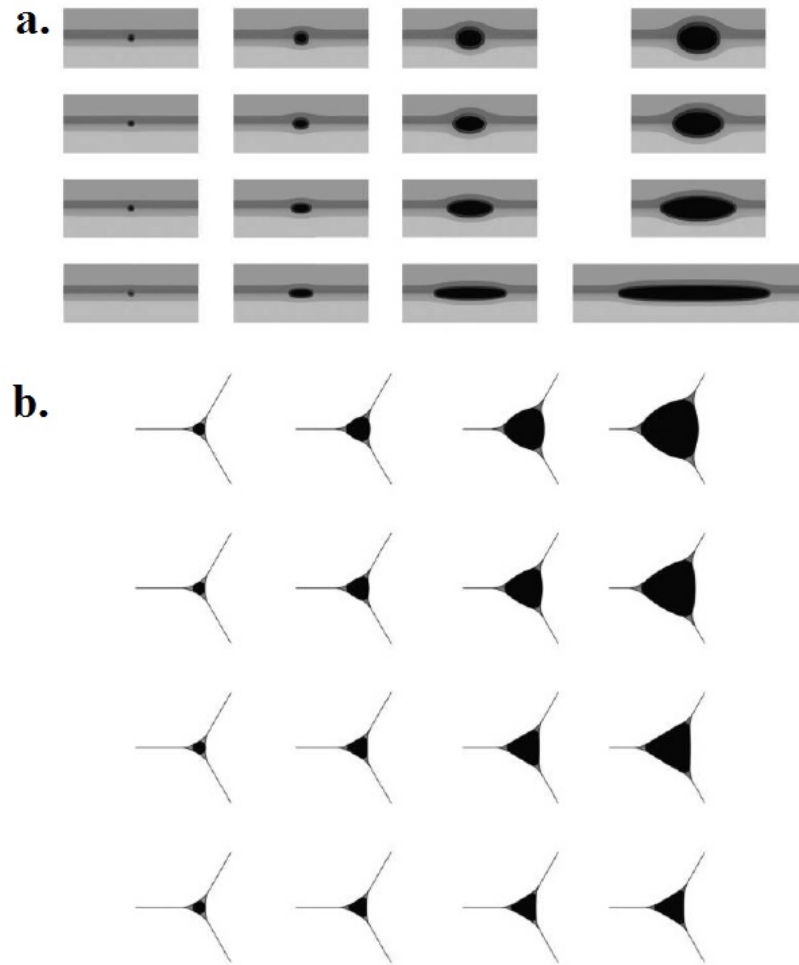


Figure 3.2: Oil droplets in Plateau borders [132]. a. Side-view. b. Cross-section. From top to bottom: $K = 1, 0.5, 0.2$ and 0.1 ; the oil-water interfacial tension γ_{ow} decreases. From left to right: $r^* = 0.2, 0.4, 0.7$ and 1 ; the volume of oil increases.

$-\gamma_{ow}/r_{PB}$. The oil effect is negligible with no interfacial tension, as though the Plateau border was empty.

As the interfacial tension ratio decreases, the pseudoemulsion film also gets larger. Indeed, for low K , it is easier to deform the droplet than to swell the Plateau border. The oil phase forms a long slug rather than an elongated droplet of cross-section bigger than the Plateau border's cross-section.

In Chapter 5, the oil-surfactant systems we use exhibit interfacial tension ratios $K \approx 0.1 - 0.25$. Thus, according to the simulations from Neethling et al. (see Fig. 3.2), the Plateau border keeps its initial shape (very slightly swollen) when invaded by oil and the oil phase is assumed to be

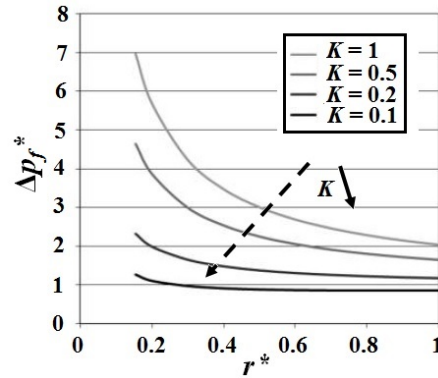


Figure 3.3: Dimensionless pressure difference between the pseudoemulsion film and the Plateau border Δp_f^* with respect to the dimensionless size of the oil droplet r^* [132].

entirely squeezed by the Plateau border to form a long slug. This assumption verified by numerics plays an important role in the model presented in Chapter 5.

3.1.2 Interfacial energy comparison with *Surface Evolver*

To help us complement the picture of oil inside a Plateau border in §2.3, we perform numerical simulations corresponding to the cases of stable invasion where $E < 0$ and $S < 0$ and no invasion where $S \gg 0$ and $E \gg 0$ by considering the geometry of the Plateau border with *Surface Evolver*. We would like to determine modified thermodynamical arguments taking the specific geometry of the Plateau borders into account.

3.1.2.1 Numerical configurations

The idea is to compare how oil distributes in the two configurations and calculate their interfacial energy:

- **the inner configuration:** a Plateau border is filled with an oil slug,
- **the outer configuration:** the oil slug lies at the junction between two adjacent bubbles when oil stays at the surface.

The preferred configuration is the one which has the lower interfacial energy. The simulations depend on the interfacial tensions and the ratio between the volume of oil V_o and the volume of water V_w in the Plateau border, which means the volume of oil compared to the volume of the pseudoemulsion film for the inner configuration. Fig. 3.4 shows the typical simulations for the inner and the outer configuration.

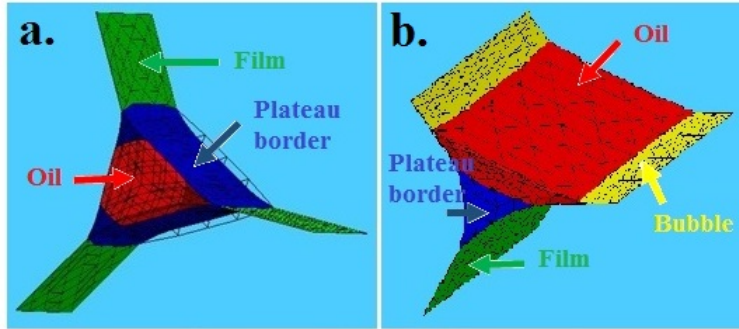


Figure 3.4: Simulations by *Surface Evolver*. a. Inner configuration. b. Outer configuration.

3.1.2.2 Comparison between numerics and experiments

For every configuration, we plot the amount of interfacial energy E_I as a function of the volume ratio V_o/V_w . Fig. 3.4 shows the different profiles for several oil-foaming solution systems presented in Table 2.1 and in Fig. 2.11. The ratio V_o/V_w starts at 1 because the oil slug does not touch and deform the walls of the Plateau border when $V_o/V_w < 1$.

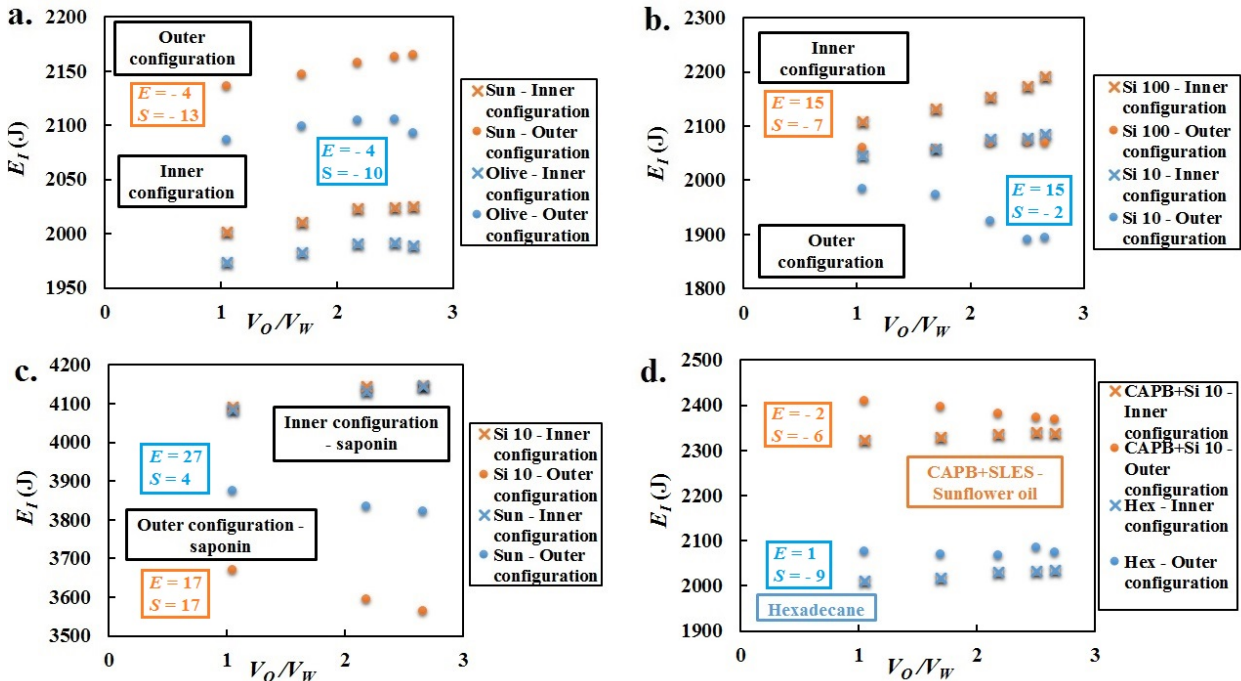


Figure 3.5: Energy calculations using simulations by *Surface Evolver*: total interfacial energy E_I as a function of the volume ratio V_o/V_w . a. Sunflower oil (Sun) and olive oil (Olive)-CAPB+SLES+Mac. b. Silicon oil with $\eta_o = 100$ mPa.s (Si 100) and silicon oil with $\eta_o = 10$ mPa.s (Si 10)-CAPB+SLES+Mac. c. Silicon oil with $\eta_o = 10$ mPa.s (Si 10) and sunflower oil (Sun)-CAPB+SLES+Mac. d. Silicon oil with $\eta_o = 10$ mPa.s (Si 10) and hexadecane (Hex)-CAPB+SLES.

For organic oils-CAPB+SLES+Mac combinations, E_I is lower for the inner configuration than the outer configuration (Fig. 3.5a). Thus, organic oils prefer to stay inside the Plateau border than to spread at the surface. On the contrary, silicon oils prefer to remain at the surface since E_I is higher for the inner configuration than the outer configuration (Fig. 3.5b). Oil is absorbed but quickly emerges and breaks the Plateau borders.

If we change the surfactant from CAPB+SLES+Mac to saponin, the difference of interfacial energy is very important (300 to 500 J) in favour of the outer configuration (Fig. 3.5c). So, oil strongly prefers to stay at the surface, which explains why oil invasion does not occur. Finally, for hexadecane for which the thermodynamical coefficients did capture the experimental observations with $B < 0$, E_I is indeed lower for the inner configuration, so numerics predicts the invasion of the Plateau border, in agreement with the experimental observations. For sunflower oil-CAPB+SLES, E_I is lower for the inner configuration, so sunflower oil should stay in the Plateau border (Fig. 3.5d), which is not what we observe experimentally. For this latter case, the numerics is also in discrepancy with the experimental observation. However, the interfacial energies in both configurations are really close and might overlap. Hence, a small variation of interfacial tension could modify the energy balance.

Numerics allows to take the equilibrium shape of the oil-filled Plateau border into account. A basic calculation of interfacial energy with the static coefficients E , S and B ignores this fact. Such calculations are valid for infinite films with vanishing curvatures whose shape does not change much with oil penetration. However, numerics is in good agreement with the coefficient-based estimations, providing that E is not too close to zero. Meanwhile, when the entry coefficient E is close to 0, a small variation of interfacial area and interfacial tension has a strong influence on the total interfacial energy and modifies the stability of the system. The entry barrier and the stability of the pseudoemulsion film might play in this case.

Here, oil appears as a long continuous slug in the foam. Drainage mechanisms for oil droplets do not come into play. The stability of the pseudoemulsion film is only governed by the molecular interactions between the oil phase and the air phase. Thermodynamical arguments seem to provide an accurate prediction for the stability of oil-laden foams, except for the smallest values of E where the system is metastable and the local interactions matter.

3.2 Breaking dynamics in the oil-filled Plateau borders

In §2.1.1 and §4.3, we show that oil could cause the collapse of foams by interacting with the air-water interfaces (bridging and spreading for instance). Now, let us imagine that the foam is stable in the presence of oil. Films are fragile structures that can break when an external force is

applied or when they change configurations (by T_1 event for instance). What consequences does this forced breaking of a film have on the adjacent oil-filled Plateau borders?

3.2.1 The Rayleigh-Plateau instability

As seen in Chapter 5, Plateau borders can drive oil inside a foam. When a film breaks, those oil-filled Plateau borders appear as long liquid cylinders. The question is: how does this cylinder evolve? The answer is similar to the fluid dynamics of liquid cylindrical threads, also known as the Rayleigh-Plateau instability.

3.2.1.1 Breaking observations

Everyone has noticed (at least once) that a water jet breaks into small droplets when one opens a tap [164]. Any liquid object wants to reduce its interfacial energy. To do so, the interfacial area has to decrease. This is what happens when a liquid cylinder breaks into small droplets. This instability is known as the Plateau-Rayleigh instability. Indeed, one can estimate the condition for which the interfacial area is smaller with drops than with cylinders. By volume conservation, the total volume of drops is equal to the volume of the cylinder [32]:

$$\pi r_c^2 L_c = \frac{4}{3} \pi r_d^3 N \quad , \quad (3.1)$$

where r_c , L_c , r_d and N are, respectively, the cylinder radius, the cylinder length, the droplet radius and the number of droplets.

By using Eq. 3.1, the ratio of interfacial area between the total area S_c of the cylinder and the total area S_d of the small droplets is written as:

$$\frac{S_c}{S_d} = \frac{2\pi r_c L_c}{4\pi r_d^2 N} = \frac{2r_d}{3r_c}. \quad (3.2)$$

For $r_d > 3r_c/2$, S_d is smaller than S_c . The bigger the droplets, the higher the loss of interfacial area.

The Rayleigh-Plateau instability is also observed when a fiber is wetted and surrounded by a liquid cylinder. The liquid film spontaneously undulates and breaks into small droplets. In this problem, gravity is negligible compared to the interfacial tension effects. Comparing the hydrostatic pressure $\rho_l g r_c$ and the Laplace pressure γ_{al}/r_c gives the Bond number $Bo = \rho_l g r_c^2 / \gamma_{al}$, introduced in §4.3.3. For $r_c = 100 \mu\text{m}$, $\gamma_{al} = 73 \text{ mN/m}$ and $\rho_l = 1000 \text{ g/L}$, $Bo \approx 0.001$ and gravity is negligible. Like the jet case, interfacial tension plays a dominant role and destabilizes

the cylindrical film.

In both situations (jet and liquid on fiber), a wavy cylinder is unstable. Indeed, we can look at the capillary pressure in the cylinder, presented in Fig. 3.6. The Laplace pressures are decomposed into two terms: one contribution from the curvatures $1/r_1$ and $1/r_1^*$ in the xy plane and one contribution from the curvatures $1/r_2$ and $1/r_2^*$ in the yz plane. From the first contribution, the pressure in the bumps is higher than in the holes ($p_1 > p_1^*$). Indeed, the curvature is positive in the first case and negative in the second one. However, from the second contribution, $r_2 > r_2^*$, thus $p_2^* > p_2$. A flow of liquid is driven from the hole to the bump, which enhances the instability. For the development of the instability, the unstable contribution has to be stronger than the stable one [140].

More precisely, if one considers a wave perturbation of wave number $k = 2\pi/\lambda$, the unstable capillary pressure is the strongest for $k \ll 1/r_c$ (see Appendix B). However, the growth rate σ_{RP} of the instability increases if the wavelength λ decreases (i.e. k increases). Indeed, $\lambda/2$ is the distance over which the flow of liquid from the hole to the bump occurs. The shorter this distance, the faster the transfer of fluid. Hence, there should be a maximum value of growth rate (and thus an optimal wavelength) for the strongest capillary pressure and the fastest transfer of liquid. This value depends on the dissipation origin: inertial or viscous-dominated regime.

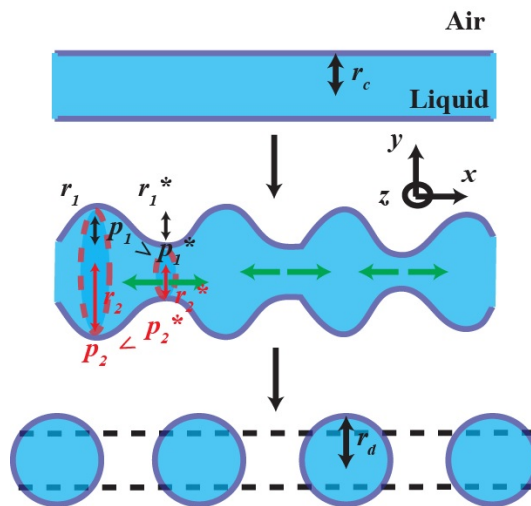


Figure 3.6: Mechanism of the Rayleigh-Plateau instability. From top to bottom: cylindrical thread, wave perturbation, breaking into small droplets.

3.2.1.2 Inertial regime

In this regime, the inertial forces are opposed to the destabilizing capillary forces because large volumes of liquid are difficult to move from the hole to the bump. These forces are dominant over the viscous forces [32, 147–149]. This is especially the case for low viscous fluids, such as water. We introduce the characteristic time t_c , the liquid density ρ_l , the cylinder radius r_c and the air-liquid interfacial tension γ_{al} . To determine the characteristic time of formation of the instability, one balances inertia $\rho_l r_c^2 / t_c^2$ with capillarity γ_{al} / r_c . One finds that:

$$t_c \sim \sqrt{\frac{\rho_l r_c^3}{\gamma_{al}}}. \quad (3.3)$$

The time t_c is very short, typically 3 ms for a millimetric cylinder radius. This is not surprising since a water jet impacts the bottom of a sink by small successive droplets that were formed very rapidly.

The growth rate of the instability σ_{RP} is proportional to $1/t_c$. More accurately, it also depends on the product between the wave number and the cylinder radius kr_c by the following relationship:

$$\sigma_{RP}^2 \approx \frac{k^2 r_c^2}{2t_c^2} (1 - k^2 r_c^2). \quad (3.4)$$

Eq. 3.4 is demonstrated in Appendix B. Fig. 3.7 shows the evolution of $\sigma_{RP} t_c$ as a function of kr_c . There is a maximum growth rate for $k_{max} r_c \approx 0.7$. This means that the wavelength of maximum growth is $\lambda_{max} = (2\pi/0.7)r_c \approx 9r_c$. Donnelly and Glaberson [61] have experimentally measured the growth rate and confirmed the result of Eq. 3.4.

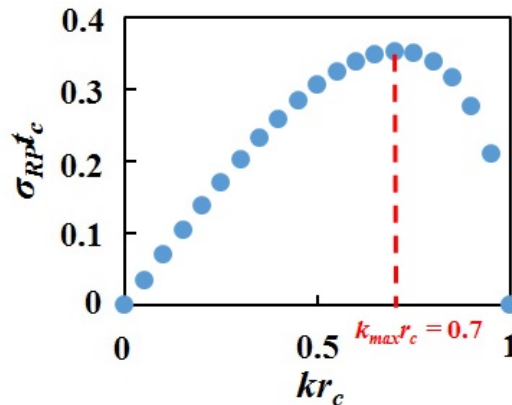


Figure 3.7: Growth rate $\sigma_{RP} t_c$ as a function of kr_c in the inertial regime. The maximum growth rate is obtained for $k_{max} r_c \approx 0.7$.

3.2.1.3 Viscous regime

In §3.2.1.2, we assume that inertial effects dominate viscous effects. However, what happens if water is replaced by oil whose viscosity can be 100 times higher? In this case, viscous effects cannot be neglected and get over the inertial effects [165, 183]. Moreover, Taylor [180] has noticed that the nature of the surrounding fluid, especially its viscosity, influences the development of the instability. In the viscous regime, the important parameter is the viscosity ratio between the viscosity of the cylindrical fluid η_c and the viscosity of the surrounding fluid η_f .

If $\eta_c/\eta_f \rightarrow +\infty$, the inner fluid is more viscous than the outer fluid. From the exact calculations summarized in Appendix B, the growth rate σ_{RP} of the instability can be expressed as:

$$\sigma_{RP} = \frac{\gamma^*}{2r_c\eta_c} \left(\frac{1 - k^2r_c^2}{k^2r_c^2 \frac{I_0(kr_c)^2}{I_1(kr_c)^2} - (1 + k^2r_c^2)} \right) \approx \frac{\gamma^*}{6r_c\eta_c} (1 - k^2r_c^2) \quad , \quad (3.5)$$

where γ^* is the interfacial tension between the inner and the outer fluid, I_0 and I_1 the modified Bessel functions. The characteristic time of instability growth is the viscous - capillary time $t_c = \eta_c r_c / \gamma^*$. Fig. 3.8 plots $\sigma_{RP} t_c$ with respect to kr_c . The growth rate is maximum when $k_{max} r_c = 0$, thus $\lambda_{max} \rightarrow +\infty$. The instability grows the fastest when the wavelength is very large.

If $\eta_c/\eta_f \rightarrow 0$, the inner fluid is less viscous than the outer fluid. The growth rate is given by:

$$\sigma_{RP} = \frac{\gamma^*}{2r_c\eta_f} \left(\frac{1 - k^2r_c^2}{k^2r_c^2 \frac{K_0(kr_c)^2}{K_1(kr_c)^2} - (1 + k^2r_c^2)} \right) \quad , \quad (3.6)$$

where K_0 and K_1 are other modified Bessel functions. Once more, as shown in Fig. 3.8, the growth rate is maximum for $k_{max} r_c = 0$ and $\lambda_{max} \rightarrow +\infty$. In the viscous regime, capillarity drives the choice of the wavelength of maximum growth, which is the largest possible.

3.2.2 Breaking of an emulsified viscous cylinder

In this section, we fill a Plateau border with oil and study the rupture of this Plateau border when an adjacent film is broken. By doing so, we mimic the situation where a broken film (due to antifoaming or mechanical perturbations) destabilizes the network of adjacent Plateau borders, potentially filled with immiscible liquids. When the oil-filled Plateau border is isolated, it can be assimilated to a long cylindrical thread which can break into small droplets. Thus, the similitude

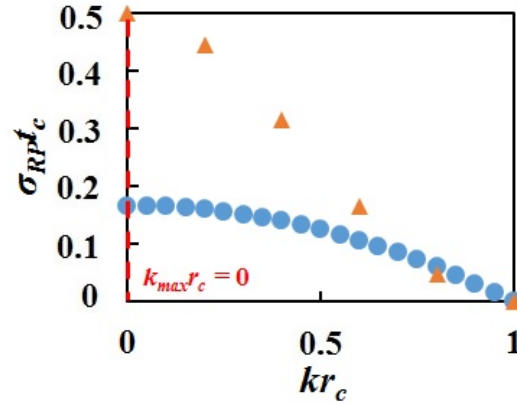


Figure 3.8: Dimensionless growth rate $\sigma_{RP} t_c$ as a function of $k r_c$ in the viscous regime. The blue round dots designate the case $\eta_c > \eta_f$, while the orange triangular dots designate the case $\eta_c < \eta_f$. In both cases, the maximum growth rate is obtained for $k_{max} r_c = 0$.

to the Rayleigh-Plateau instability is close. We model our experimental results with regard to the analysis on the Rayleigh-Plateau instability in §3.2.1.

3.2.2.1 Experiments

We perform the experiments with three different oils: paraffin oil (Sigma-Aldrich), olive oil (commercial) and hexadecane (Sigma-Aldrich). The oil characteristics are summarized in Table 3.1. The surfactant is the CAPB-SLES-Mac composition used in §2.3.1.2 with the air-water interfacial tension $\gamma_{aw} = 23.7$ mN/m.

Liquids	γ_{ao}	γ_{ow}	η_o	ρ_o	E	S	B
Paraffin oil	19.5	5.5	25.7	0.838	9.7	-1.3	212
Olive oil	30.8	3	61	0.92	-4	-10	-377
Hexadecane	27.3	4.9	3.1	0.77	1	-9	-165

Table 3.1: Characteristics of the different oils used to fill the Plateau border. The interfacial tensions γ_{ao} (air-oil), γ_{ow} (air-water)(mN/m), the oil viscosity η_o (mPa.s), the oil density ρ_o and the coefficients E , S and B (mN/m) are given.

Fig. 3.9 depicts the experimental set-up, which is also described in [137]. First, we generate a Plateau border by dipping a prism-like frame of length 15 cm and width 2 cm into the foaming solution. We gently pull the frame out of the surfactant bath. A slender Plateau border appears in the middle of the frame at the junction between three trapezoidal soap films. The frame is deposited horizontally between two supports in a closed box with saturated humidity: temperature $T = 23 - 25^\circ\text{C}$ and humidity rate $h_w = 90 - 95\%$. This reduces evaporation and increases the

lifetime of the Plateau border. We let the films drain for different durations. As the drainage time increases, the curvature radius of the Plateau border decreases: the system “dries”. This is very important if one studies the flow dynamics of oil in the Plateau border, which has been done by Piroird et al. [137]. In our case, a variation of curvature radius also allows to study the influence of the shape of the Plateau border in this problem.

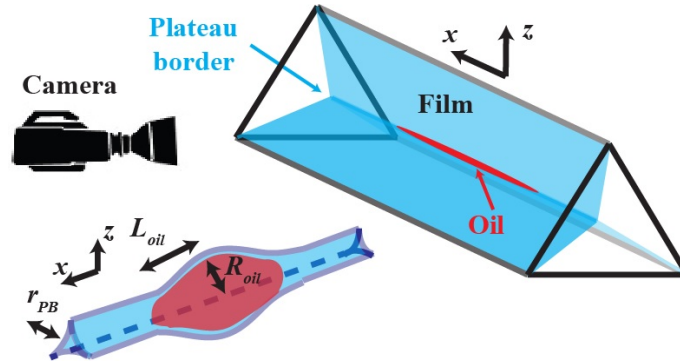


Figure 3.9: Experimental set-up presenting the slender Plateau border filled with oil at the junction between three soap films.

Oil is preemulsified by plunging a capillary tube containing the oil phase into the surfactant solution for 30 s. After the drainage period, we deposit this given volume of oil in the upper film to avoid any deformation of the Plateau border. The oil droplet slowly slides downwards due to gravity and enters into the Plateau border. At time $t = 0$, the oil phase forms a slug, aligned with the revolution axis of the Plateau border, and starts propagating symmetrically from the injection point due to the difference of pressure between the center and the tip of the slug. Indeed, the pressure at the center of the slug $p^+ = p_{atm} + (\gamma_{ow} + \gamma_{aw})/r_c$ is higher than the pressure at the tip $p^- = p_{atm} - \gamma_{aw}/r_{PB}$, which generates a capillary flow of oil outwards [137]. We wait for the oil slug to reach different lengths before breaking the lower rear film with a needle. We record the whole sequence from the propagation of oil to the breaking of the oil cylinder at 15 frames per second (camera AVT Marlin).

Fig. 3.10 presents a typical sequence of images after the film rupture. Once the film is broken, a single film is left with the oil slug right in the middle. However, in a fraction of seconds, this slug breaks into small emulsified oil droplets embedded within the remaining soap film. We can also observe some satellite droplets in-between the bigger droplets. In Fig. 3.11, we also illustrate the transverse view of the rupture of the oil-laden Plateau border.

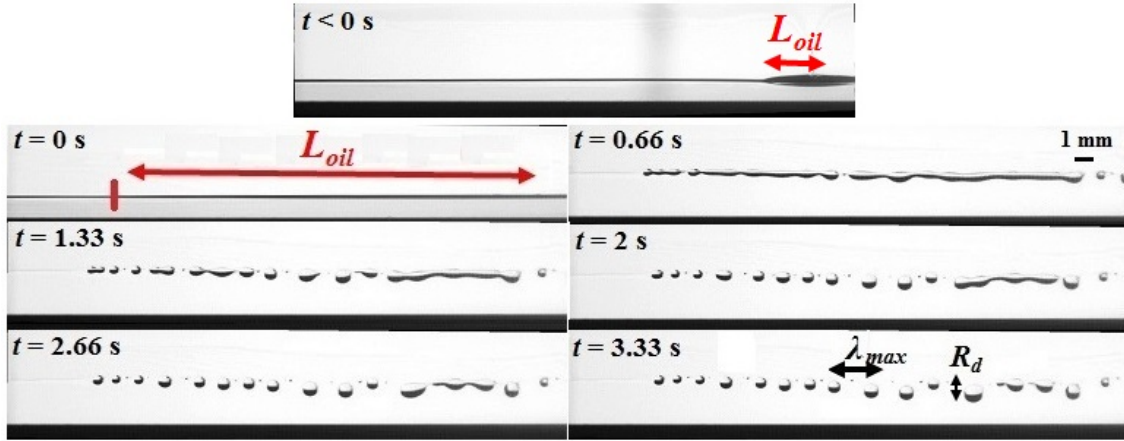


Figure 3.10: Snapshots of the breaking dynamics. Oil: olive oil; drop volume: $\Omega = 1.5 \mu\text{L}$.

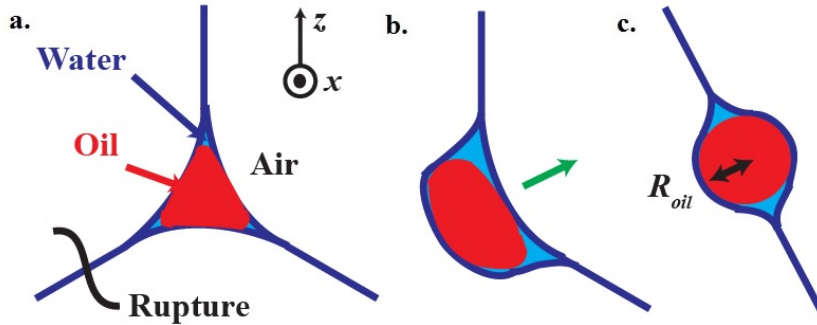


Figure 3.11: Side-view of the breaking process. a. Initial oil-filled Plateau border [137]. b. Breaking of the lower rear film. The Plateau border is ejected to the opposite direction. c. Oil-filled film before the Rayleigh-Plateau instability.

3.2.2.2 Instability wavelength

In the image sequence, we only shoot half of the oil slug to get more precision on the measured distances. We note L_{oil} the half-length of the oil slug at $t = 0$, Ω the half-volume of the oil droplet and R_{oil} , the radius of the oil slug that we assume uniform along the length L_{oil} . We also introduce the wavelength λ_{max} which is the average distance between two consecutive big droplets (i.e. we do not count the satellite droplets which appear due to pinch-off phenomena not discussed here), and R_d as the droplet radius. For each experiment, we calculate $R_{oil} = \sqrt{\Omega/\pi L_{oil}}$. We report λ_{max} with respect to R_{oil} in Fig. 3.12.

The experimental wavelength λ_{max} increases when the slug radius R_{oil} increases. We can try to compare the experimental data with the theoretical predictions deduced from the usual Rayleigh-Plateau instability. In the inertia-dominated regime (§3.2.1.2), λ_{max} is equal to $9R_{oil}$. This regime does not collapse with our data. We can also be in the viscous regime. The viscosity ratios

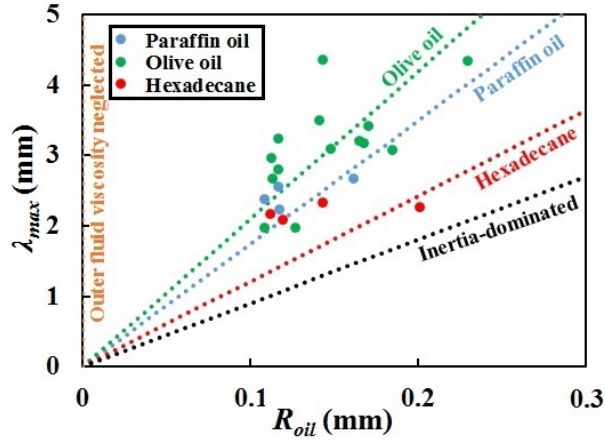


Figure 3.12: Wavelength λ_{max} as a function of the slug radius R_{oil} . The coloured dotted lines are the theoretical predictions [183]. The black dotted line is the prediction for the inertia-dominated regime [149] and the orange dotted line, the prediction for the viscous-dominated regime when the viscosity of the outer fluid is neglected.

between the oils and the foaming solution (of viscosity $\eta_w = 1.4$ mPa.s) are, respectively, 43.6, 18.4 and 2.2 for olive oil, paraffin oil and hexadecane. If we neglect the viscosity of the outer foaming solution, as shown in §3.2.1.3, λ_{max} should tend to $+\infty$. Yet, we obtain a finite wavelength in our problem. Therefore, we have to consider the viscosity of the outer fluid in the wavelength calculations. Tomotika [183] solves the whole Rayleigh-instability problem of a viscous cylinder in another viscous fluid (i.e. when the viscosity ratio η_o/η_w is finite). Fig. 3.13 gives the ratio λ_{max}/R_{oil} as a function of η_o/η_w . From this curve, we deduce the values of λ_{max} for our oil-foaming solution systems.

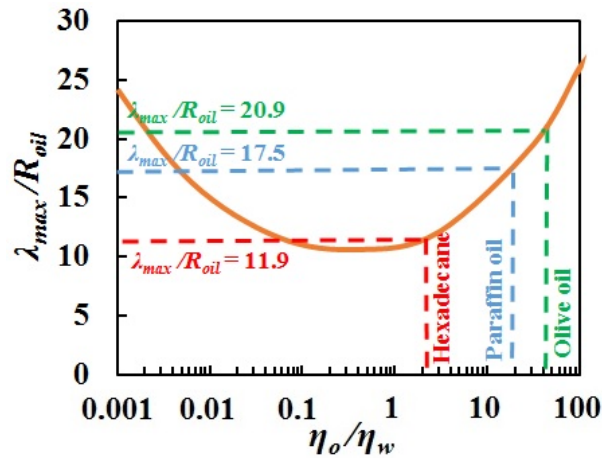


Figure 3.13: Theoretical ratio wavelength of maximum growth - cylinder radius λ_{max}/R_{oil} as a function of the viscosity ratio η_o/η_w [183]. The solutions for our oil-foaming solution systems are indicated with the same color code as in Fig. 3.12.

From the solutions indicated in Fig. 3.13, λ_{max} is linear with R_{oil} with different slopes according to the viscosity ratio. Fig. 3.12 shows a reasonable collapse (at least in terms of scaling order) between the experimental data and the predictions (dotted lines). Thus, by knowing the viscosity ratio and the cylinder radius (by the droplet volume and the slug length), we can predict the instability wavelength which is the distance between droplets.

3.2.2.3 Size of the oil droplets

If we know the wavelength and the cylinder radius, we can also predict the droplet radius R_d . Indeed, we have the total volume of oil $\Omega = N(4/3)\pi R_d^3$ where N is the number of droplets and we assume that the droplets are spherical. But $\Omega = L_{oil}\pi R_{oil}^2$. Thus, $R_d^3 = (3/4)(L_{oil}/N)R_{oil}^2$. By injecting $\lambda_{max} = L_{oil}/N$ into the previous equation, we find:

$$R_d = \left(\frac{3}{4}\right)^{1/3} (\lambda_{max} R_{oil}^2)^{1/3}. \quad (3.7)$$

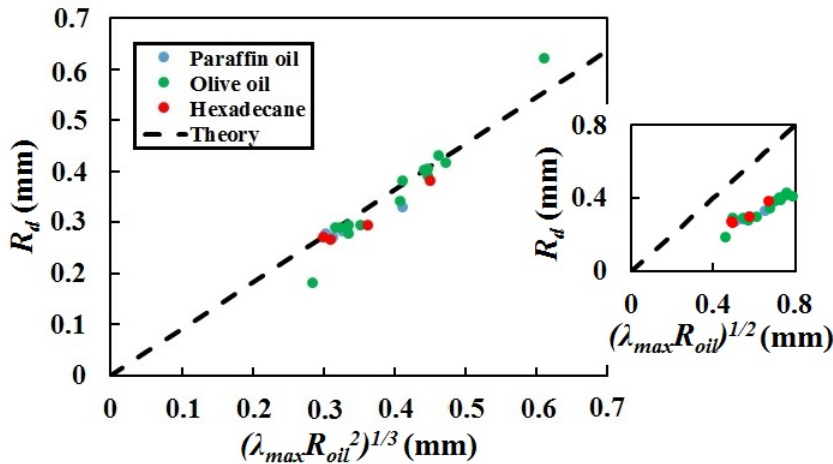


Figure 3.14: Theoretical radius of the oil droplet R_d as a function of $(\lambda_{max} R_{oil}^2)^{1/3}$ for paraffin oil, olive oil and hexadecane. The oil radius R_{oil} is deduced from the volume Ω of the oil slug. The black dashed line represents the theoretical prediction from Eq. 3.7. Inset: Theoretical radius R_d as a function of $(\lambda_{max} R_{oil})^{1/2}$ by assuming a pancake-like shape. The black dashed line is the theoretical prediction as detailed in the text. We observe that the agreement is not quantitative.

Fig. 3.14 plots R_d as a function of $(\lambda_{max} R_{oil}^2)^{1/3}$ for our experimental data. It shows a very good collapse with the theoretical prediction from Eq. 3.7. This result also confirms the assumption of spherical droplets. Indeed, we could have thought about a pill-like shape. In this case, $\Omega = N\pi R_d^2 R_{oil}$ by assuming a pill thickness equal to the cylinder radius R_{oil} . By the same calculations as the spherical shape, we find $R_d = (\lambda_{max} R_{oil})^{1/2}$. The inset of Fig. 3.14 presents the

collapse for the pill case and it does not clearly work. From these results, we can conclude that the film does not constrain the Rayleigh-Plateau instability and acts as a free deformable surface. This seems in contradiction at first glance with the assumption of §3.1 where we state that the presence of oil does not strongly modify the shape of the Plateau border. Yet, in this experiment, the two configurations are not obtained for the same film thickness. The films supporting the Plateau border at the beginning of the experiment are very thin, thus they induce an important capillary pressure which is sufficient to deform the oil slug. At the end of the experiment, there is a single film: the aqueous foaming solution initially contained within the Plateau border and the broken film have been redistributed. Therefore, the remaining soap film is thick and its disjoining pressure is not sufficient to deform the oil slug, which now adopts a cylindrical shape due to the non-zero value of the oil-water interfacial tension.

This result is very interesting if one thinks about the Rayleigh-Plateau instability at the scale of an oil-filled Plateau border inside a foam. From [183], we find that λ_{max} is uniquely determined by R_{oil} and η_o/η_w :

$$\lambda_{max} = R_{oil} \Phi \left(\frac{\eta_o}{\eta_w} \right) \quad , \quad (3.8)$$

with Φ the implicit function determined by Tomotika in [183]. The radius of the oil slug R_{oil} can be approximated by the curvature radius of the Plateau border $r_{PB} = 1.74\phi_l^{1/2}R_b$ for a dry foam in the case of low oil-water interfacial tensions. We have ϕ_l the liquid fraction of water and oil and R_b the bubble radius. Therefore, λ_{max} becomes a function of the liquid fraction and the bubble radius $\lambda_{max} \sim \phi_l^{1/2}R_b\Phi(\eta_o/\eta_w)$. Injecting this relationship and $R_{oil} \sim r_{PB}$ in Eq. 3.7 yield the radius of the oil droplet R_d^{foam} after the rupture of a Plateau border in a foam:

$$R_d^{foam} \sim \phi_l^{1/2}R_b\Phi \left(\frac{\eta_o}{\eta_w} \right)^{1/3} \quad . \quad (3.9)$$

Besides, the number of droplets N^{foam} can be predicted with $N^{foam} = L_{oil}/\lambda_{max}$. The length of the oil slug L_{oil} is equal to the length of a Plateau border $L_{PB} = (\pi/6\sqrt{2})^{1/3}R_b$ for a dry foam. Using 3.8 gives the number of droplets N^{foam} coming from the rupture of the Plateau border:

$$N^{foam} \sim \frac{1}{\phi_l^{1/2}\Phi \left(\frac{\eta_o}{\eta_w} \right)} \quad . \quad (3.10)$$

We can retrieve the volume of oil absorbed in the Plateau border (i.e. the volume of a Plateau border given that we approximate R_{oil} by r_{PB}) $\Omega_{PB} = (4/3)\pi N^{foam}(R_d^{foam})^3 \sim \phi_l R_b^3$ by multiplying Eq. 3.9 and Eq. 3.10. This result is coherent with the estimation deduced from the Kelvin

cell with the length of a Plateau border $L_{PB} = (\pi/6\sqrt{2})^{1/3}R_b$ and the volume $\Omega_{PB} \sim L_{PB}r_{PB}^2 \sim \phi_l R_b^3$.

However, as we will see in Chapter 4, the radius of the oil slug is not exactly constant and equal to the curvature of the Plateau border. It is actually a function of the local liquid fraction which depends on the position \mathbf{x} in the foam, so $R_d^{foam}(\mathbf{x}) \sim \phi_l(\mathbf{x})^{1/2}R_b\Phi\left(\frac{\eta_o}{\eta_w}\right)^{1/3}$. Hence, if we can measure R_d^{foam} experimentally by forcing the rupture of the oil-laden foam and recording the image sequence, we can actually determine the liquid fraction of oil and water at the position \mathbf{x} (or the average liquid fraction in a Plateau border whose center of revolution is located at the position \mathbf{x}). Knowing the initial liquid fraction of water ϕ_i , we can retrieve the profile of liquid fraction for the oil phase.

In this section, we try to understand the rupture of an oil-filled Plateau border into small emulsified droplets, owing to the rupture of an adjacent film. Our experimental data and theoretical analysis demonstrate that this problem can be studied under the light of the well-known Rayleigh-Plateau instability. We have to take the viscosity of the pseudoemulsion film into account to predict the wavelength of maximum growth of the instability. This problem presents all the conditions that allow to consider the Rayleigh-Plateau theory. The system is assimilated to a long cylindrical oil thread in an infinite outer fluid. This fluid is the foaming solution in the upper film which encircles the cylinder when the lower film is broken. The velocity components and the tangential stresses are continuous at the boundary between the oil phase and the pseudoemulsion film. The difference in normal stresses is only due to the oil-water interfacial tension γ_{ow} at the interface between the oil and the foaming solution. If we know the viscosity ratio η_o/η_w , the oil volume Ω and the length of the invaded region L_{oil} , we can thus predict the wavelength and the droplet size.

For a Plateau border in a foam, we can deduce the liquid fraction of oil at any position \mathbf{x} (for instance in case of imbibition process) by measuring the droplet radius after rupture and knowing the bubble radius and the viscosity ratio. This method does not require any external apparatus, such as light scattering [63] or conductimetry [67].

3.3 Conclusions

In this chapter, we have considered the local shape of an oil slug inside a Plateau border. In this situation, oil is encapsulated in the network of Plateau borders to form a three-phase system if the air phase in the bubbles is included in the whole picture.

In Chapter 2, we use the entry E , spreading S and bridging B coefficients to characterize the

ability of the foam to resist to oil invasion. To confirm our results, we resort to numerics to compare the interfacial energy in two different configurations: one where the oil is inside the Plateau border and the other one where the oil stays on top of a bubble and does not penetrate the foam. The simulations by *Surface Evolver* show a good agreement between the configuration of lower interfacial energy and the stability of oil-laden Plateau borders, providing that the error margin on the interfacial tension is small (this is critical for $E \approx 0$). Calculating the global interfacial energy for specific geometries (here an oil-filled Plateau border) is actually more relevant than reasoning on a simple flat geometry where two interfaces face each other. Our simulations confirm the calculations using the static coefficients. Locally, both Plateau borders and films exhibit the same configurations when oil emerges at the air-water interface.

However, what really governs the stability of oil-laden foams is the ability of the oil droplet to break the pseudoemulsion film, and thus to overcome the disjoining pressure. Energetical arguments are necessary but not always sufficient (for instance for particle-laden oils). The role of the pseudoemulsion film and the entry barrier is still an open question.

Finally, we have wondered what would occur when the oil-filled Plateau border breaks due to film bursting, bubble coalescence or rearrangements. We find that the Plateau border is decomposed into small emulsified droplets. This dynamics is analogous to the Rayleigh-Plateau instability. A viscous fluid cylinder is unstable because this object wants to reduce its interfacial area and can only do so by division into small droplets. We can retrieve the geometrical parameters of the instability, typically the decomposition wavelength λ_{max} , by considering the whole solution to the Rayleigh-Plateau instability, including the influence of the surrounding fluid. Studying this instability also allows us to retrieve the quantity of oil inside the foam by the evaluation of the liquid fraction.

Oil can come out of the Plateau border when this latter breaks but oil can also emerge at the air-water interfaces and spread on this interface, leading to the destabilization of the corresponding film or Plateau border.

Chapter 4

Soap films and oil: dynamics of rising oil droplets spreading at the air-water interface

The stability of oil-laden foams strongly depends on the ability of the oil phase to emerge at the air-water interfaces. Dispersed oil droplets that emerge are able to spread at the air-water interface. Such dynamics can destabilize films, as well as stabilize the formation of oil bridges [56]. We recall known theories on the spreading of oil droplets on solid surfaces before making the same analysis for the spreading on liquid surfaces. We study the spreading dynamics of rising oil droplets where oil is already encapsulated in the film, which is different from common situations where the oil layer is deposited onto the film by the air phase. We use a foam as a liquid sponge which absorbs oil through the Plateau borders. Hence, it seems logical to consider the spreading dynamics of oil droplets when they emerge from the aqueous phase.

Contents

4.1	Spreading of oil on solid surfaces	94
4.1.1	Wetting theory on solid surfaces	94
4.1.1.1	Surface energy and spreading coefficient	94
4.1.1.2	Partial wetting	95
4.1.1.3	Complete wetting	96
4.1.1.4	Pseudo-partial wetting	97
4.1.2	Dynamics of liquid spreading on air-solid interfaces	98
4.1.2.1	Precursor film	99
4.1.2.2	Capillarity-dominated regime	99
4.1.2.3	Gravity-dominated regime	100
4.2	Spreading of oil on air-water interfaces from the air phase	100
4.2.1	Liquid-liquid wetting	101
4.2.2	Regimes of oil spreading on air-water interfaces	102
4.2.2.1	Non-viscous to viscous oils	102
4.2.2.2	Very viscous oils	104
4.3	Spreading of oil rising from the aqueous phase at air-water interfaces	106
4.3.1	Experimental results	106
4.3.2	Short-time dynamics	108
4.3.2.1	Inertial-viscous-capillary regime	108
4.3.2.2	Collapse between experiments and theory at short times	110
4.3.3	Long-time dynamics	111
4.3.3.1	Transition to long-time dynamics for pure aqueous solutions	111
4.3.3.2	“Solid”-like spreading for surfactant solutions	112
4.4	Conclusions	116

Specific variables

Variables	Parameters	Variables	Parameters
S_S	Spreading coefficient for liquid-solid spreading	U	Mean velocity
a	Molecular size	H_k	Hamaker constant
θ_Y	Young contact angle	dE	Variation of interfacial energy
E_S	Energy of a film	E_{film}	Variation of the film energy
Ω	Film volume	e_{eq}	Equilibrium thickness
κ	Capillary length	γ_c	Critical interfacial tension
E_{film}	Film energy	e_{pp}	Pseudo-partial thickness
r	Spreading radius	F_{film}	Capillary force in the film
$F_{droplet}$	Capillary force in the droplet	θ_d	Dynamic contact angle
F_{cap}	Total capillary force	v	Horizontal velocity
τ_{ow}	Shear stress at the oil-water interface	v_r	Radial velocity
δ_d	Penetration depth	v_o	Velocity of the upper layer flow
d	Characteristic length	θ_{aw}	Air-water dynamic contact angle
θ_{ow}	Oil-water dynamic contact angle	θ_{eq}	Equivalent contact angle
γ_{eq}	Equivalent interfacial tension	\mathcal{D}	Viscous dissipation
Re_r	Reynolds number in the bulk flow	\mathcal{P}	Capillarity-induced power
C_{SDS}	SDS concentration	Oh	Ohnesorge number
Δp_C	Capillary pressure difference	R	Dimensionless spreading radius
T	Dimensionless time (capillarity)	T_{Oh}	Effective dimensionless time
Bo	Bond number	Oh_{eff}	Effective Ohnesorge number
T_{ST-LT}	Transition time between short-time and long-time regime	R_{ST-LT}	Transition radius between short-time and long-time regime
$T_{Oh-ST-LT}$	Effective transition time	T^*	Dimensionless time (gravity)
τ_g	Characteristic inertial-viscous-gravitational transition time	r_g	Characteristic inertial-viscous-gravitational transition radius
T_g^*	Dimensionless inertial-viscous-gravitational transition time	R_g	Dimensionless inertial-viscous-gravitational radius
T_c	Dimensionless inertial-viscous-capillary time	R_c	Dimensionless inertial-viscous-capillary radius
Ω_d	Droplet volume		

4.1 Spreading of oil on solid surfaces

We first recall some known results about the spreading theory on solid surfaces.

4.1.1 Wetting theory on solid surfaces

In this section, we present the basic notions about the wetting and the spreading of liquids on solid surfaces [115]. This allows us to introduce the case where the solid surface is replaced by its liquid counterpart.

4.1.1.1 Surface energy and spreading coefficient

More details for this subsection can be found in [79]. The wetting behaviour of a liquid film on a smooth solid surface is characterized by its energy E_S based on the interfacial interactions:

$$E_S = (\gamma_{sl} + \gamma_{al} + P(e)) \Sigma \quad , \quad (4.1)$$

where γ_{sl} , γ_{al} and Σ are, respectively, the solid-liquid, the air-liquid interfacial tensions and the film area. When the film thickness $e \rightarrow \infty$, we have a thick film and $P(\infty) = 0$, because we only have solid-liquid and air-liquid interfaces. When $e \rightarrow 0$, we obtain a free surface without film and only have an energy contribution from the solid-air interface. Thus, $P(0) = \gamma_{sa} - \gamma_{sl} - \gamma_{al} = S_S$ with γ_{sa} the solid-air interfacial tension and S_S the spreading coefficient for solid surfaces analogous to the spreading coefficient for air-oil-water interfaces S defined in §2.1.1.

The term $P(e)$ reflects the short-range and long-range interactions between the liquid and the solid phase and between the liquid molecules. More precisely, $P(e)$ is related to the disjoining pressure $\Pi(e)$ for films defined in §1.1.5: $\Pi(e) = -dP/de$. For e higher than the molecular size a but below 100 nm, long-range Van der Waals forces are dominant and $P(e)$ can be written as:

$$P(e) = \frac{H_k}{12\pi e^2} \quad , \quad (4.2)$$

where H_k is an effective Hamaker constant characteristic of the interactions between two charged interfaces ($|H_k| \approx 10^{-20}$ J). In this case, the disjoining pressure is written as:

$$\Pi(e) = \frac{H_k}{6\pi e^3} \quad (4.3)$$

The disjoining pressure is interpreted as the pressure to apply to prevent the film from being thickened by long-range forces.

Once the film is formed, E_S allows to relate the film thickness e to the wetting properties of the solid surface, as we will see in the following sections. For macroscopic films, we directly use the spreading coefficient S_S to evaluate the spreading ability of a liquid droplet deposited on a solid surface by comparing the interfacial energy between a dry and a wet surface:

$$S_S = \gamma_{sa} - \gamma_{sl} - \gamma_{al}. \quad (4.4)$$

If $S_S > 0$, a liquid droplet completely spreads on a solid surface: this is the complete wetting. If $S_S < 0$, a liquid droplet does not spread and form an angle θ_Y , called Young's equilibrium contact angle with the surface: this is the partial wetting. Glass and metallic oxides exhibit bonds of high energy (ionic, covalent and metallic, i.e. $\gamma_{sa} = 0.5-1$ N/m). These solid surfaces are easily wetted by most liquids. On the contrary, polymers, teflon and paraffin exhibit bonds of low energy (Van der Waals and hydrogen bonding, i.e. $\gamma_{sa} = 0.05$ N/m). Wetting can be complete or partial. The determination of the equilibrium shape of the spreading drop (film and/or spherical shape) is solved thanks to the evolution of the equilibrium parameters E_S and $P(e)$ with the film thickness e .

4.1.1.2 Partial wetting

In the partial wetting situation [77], $S_S < 0$ and the liquid takes a "pancake" shape by making a contact angle with the solid surface at equilibrium, the Young contact angle θ_Y , as sketched in Fig. 4.1 [205].

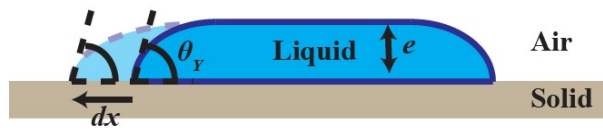


Figure 4.1: Liquid droplet on a solid surface in partial wetting.

The Young angle is related to the different interfacial tensions. One can consider a small displacement dx of the interface and the associated variation of interfacial energy dE . Per unit length in the transverse direction, $dE = (\gamma_{sl} - \gamma_{sa})dx + \gamma_{al} \cos \theta_Y dx$. At equilibrium, $dE/dx = 0$, which yields the well-known Young-Dupré relationship:

$$\cos \theta_Y = \frac{\gamma_{sa} - \gamma_{sl}}{\gamma_{al}} = 1 + \frac{S_S}{\gamma_{al}}. \quad (4.5)$$

This angle is only defined for $S_S < 0$. At $S_S = 0$, the transition to the complete wetting occurs

and $\theta_Y = 0^\circ$. The thickness e_{eq} of a liquid drop at equilibrium is determined by considering the balance between gravity, which tends to make the drop thinner, and the capillary forces, which hinder the thinning process to reduce the interfacial energy. The total mechanical energy of the puddle E_{puddle} is the sum of an interfacial capillary term and a gravitational term:

$$E_{puddle} = -S_S \Sigma + \frac{1}{2} \rho_l g \Sigma e^2 \quad , \quad (4.6)$$

where ρ_l is the liquid density and g the gravity acceleration. The volume of the puddle Ω is constant and $\Omega = \Sigma e$ by volume conservation, which gives $E_{puddle} = -S_S \Omega / e + (1/2) \rho_l g \Omega e$. The equilibrium thickness is given by $dE = 0$:

$$e_{eq} = \sqrt{\frac{-2S_S}{\rho_l g}} = 2\kappa \sin \frac{\theta_Y}{2} \quad , \quad (4.7)$$

where $\kappa = \sqrt{\gamma_{al} / \rho_l g}$ is the capillary length. This length reflects which forces are dominant between capillarity and gravity. If the drop size is higher than κ , then gravity forces are dominant and drags the drop thinning. For $\kappa \approx 2$ mm and $\theta_Y \approx 45^\circ$, one finds $e_{eq} \approx 1.5$ mm.

4.1.1.3 Complete wetting

If $S_S > 0$, it is favourable for the liquid drop to spread as a film, which means creating two interfaces (air-liquid and solid-liquid) instead of leaving the solid surface dry. This property generally concerns liquids with low air-liquid interfacial tension since it costs energy to create an air-liquid interface. Thus, liquids with surfactants are ideal candidates. Zisman [206] defined an empirical criterion that only depends on the nature of the solid material to determine whether a liquid completely wets a solid. This criterion is the critical tension γ_c . If $\gamma_{al} < \gamma_c$, the liquid spreads on the solid surface. For instance, plastic materials exhibit $\gamma_c = 30$ -40 mN/m. Thus, as shown in Table 1, most oils wet plastic, while water does not. For glass, $\gamma_c = 100$ mN/m. Thus, common liquids from oil to water spread on glass. However, most surfaces are not completely clean. Any dust and any greasy matter can decrease the value of γ_c and favour partial wetting.

The equilibrium thickness e_{eq} of the film in its final state is determined by the balance between the long-range forces and the capillary forces [77]. According to Eq. 4.2, the Van der Waals forces tend to thicken the film, since the energy potential decreases in $1/e^2$. But the capillary forces cause the thinning of the drop because $S_S > 0$. The variation of energy per unit area of the film E_{film} is written as $E_{film} = -S_S \Sigma + P(e) \Sigma$. Minimizing this energy ($dE_{film}/de = 0$) gives $S_S = e_{eq} \Pi(e_{eq}) + P(e_{eq}) = -(d(E_S/\Sigma)/de)_{e_{eq}} e_{eq} + P(e_{eq})$. This is the equation of the tangent crossing the points $(0, \gamma_{sa})$ and $(e_{eq}, E_S/\Sigma(e_{eq}))$ in the curves $(e, E_S/\Sigma)$ shown in Fig.

4.2. We deduce e_{eq} by using Eq. 4.2 and Eq. 4.3:

$$e_{eq} = \sqrt{\frac{H_k}{4\pi S_S}}. \quad (4.8)$$

For $H_k \approx 10^{-20}$ J and $S_S \approx 20$ mN/m, $e_{eq} \approx 0.1$ nm. This length is close to the molecular size and increases when one gets close to the transition between partial and total wetting for $S_S \rightarrow 0$.

4.1.1.4 Pseudo-partial wetting

Partial and total wetting characterize the spreading of a liquid drop on a solid surface. However, these two options are not the only possibilities. It has been demonstrated theoretically [24] and experimentally [170] that a third regime is possible: the pseudo-partial wetting [24]. Let us have a look at Eq. 4.1. For $H_k < 0$ and $S_S > 0$ or $S_S < 0$, E_S must have the profile depicted in Fig. 4.2a-b. Indeed, $P(e)$ is an increasing negative function and $P(e \rightarrow 0) = \gamma_{sa} > 0$. Thus, the profile must have a minimum at a value e_{pp} .

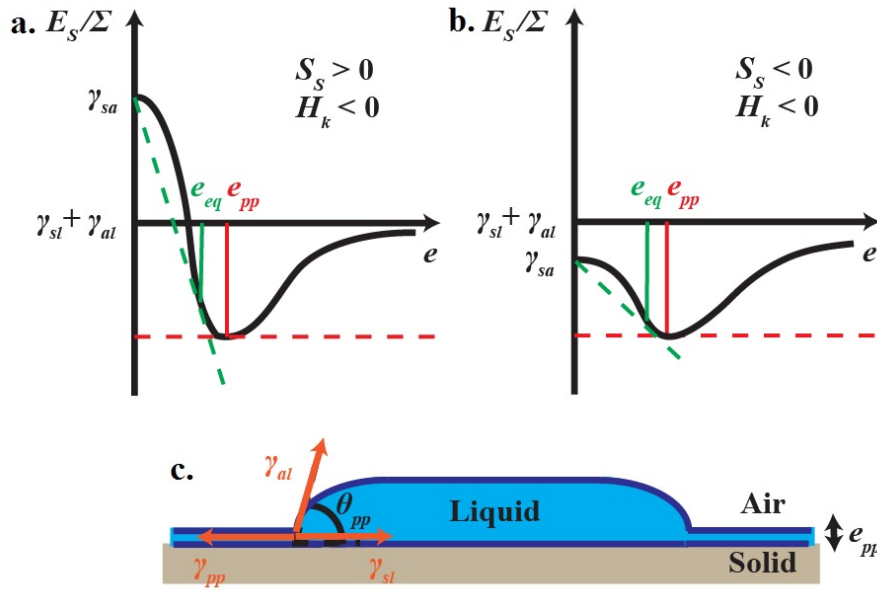


Figure 4.2: Energy of the film E_S as a function of the thickness e for pseudo-partial wetting.

We can draw a common horizontal tangent between the point $(e_{pp}, (E_S/\Sigma)(e_{pp}))$ and the point $(e \rightarrow \infty, \gamma_{al} + \gamma_{sl})$. Hence, the final equilibrium state is a liquid droplet sitting on a film of thickness e_{pp} , as depicted in Fig. 4.2c.

One can calculate the effective interfacial tension γ_{pp} of the pseudo-partial film. We have to

determine the variation of energy in the film when we vary its area at constant volume $d\Omega = (d\Sigma/\Sigma) + (de/e) = 0$. By differentiating Eq. 4.1 with e , we have $dE_S = (\gamma_{al} + \gamma_{sl} + P(e))d\Sigma - \Sigma\Pi(e)de$. We deduce $\gamma_{pp} = dE_S/d\Sigma$ as:

$$\gamma_{pp}(e) = \gamma_{al} + \gamma_{sl} + P(e) + e\Pi(e). \quad (4.9)$$

In Fig. 4.2c, the balance between horizontal forces yields:

$$\gamma_{pp}(e_{pp}) = \gamma_{sl} + \gamma_{al} \cos \theta_{pp} \quad , \quad (4.10)$$

where θ_{pp} is the equilibrium contact angle at the junction between the pseudo-partial film and the droplet. Let us also recall that e_{pp} and e_{eq} are respectively the thickness of the precursor film and the thickness of the total wetting film. Replacing the left term in Eq. 4.10 by Eq. 4.9, with $\Pi(e_{pp}) = -(d(E_S/\Sigma)/de)_{e_{pp}} = 0$ - because $(e_{eq}, (E_S/\Sigma)_{e_{eq}})$ is a minimum - gives the effective interfacial tension γ_{pp} :

$$\gamma_{pp}(e_{pp}) = \gamma_{sl} + \gamma_{al} \left(1 + \frac{P(e_{pp})}{\gamma_{al}}\right). \quad (4.11)$$

The pseudo-partial wetting is possible for droplets that are large enough to cover the whole solid surface. If not, a film of thickness e_{eq} is formed.

In summary, the wetting of liquid droplets on smooth solid surfaces can be decomposed in three different regimes:

- If $S_S > 0$ and $H_k > 0$, there is complete wetting with the formation of a thin film,
- If $S_S > 0$ or $S_S < 0$ and $H_k < 0$, there is pseudo-partial wetting with a droplet sitting on a wet solid,
- If $S_S < 0$ and $H_k > 0$, there is partial wetting with a droplet sitting on a dry solid.

4.1.2 Dynamics of liquid spreading on air-solid interfaces

The different wetting regimes for a liquid droplet on a solid surface are determined by considering an energy balance in a static configuration. In this section, we wonder how a liquid of spreading coefficient $S_S > 0$ spreads on the solid and reaches the shape of a film of thickness e_{eq} [115]. Driven by capillary and gravity forces, the spreading dynamics is divided into different regimes according to the value of the spreading radius r .

4.1.2.1 Precursor film

One could imagine that the driving force pulling the droplet is the spreading coefficient S_S . Yet, this is not the case since Hardy [85, 117] has shown that a precursor film of thickness e_{eq} quickly forms ahead of the droplet tip, as shown in Fig. 4.3. Due to the magnitude of S_S , a molecular liquid film rapidly spreads, as expected from §4.1.1.3. However, at the rear of this film, the droplet of thickness e still exists by making a dynamic contact angle θ_d between the air-liquid and the solid-liquid interfaces. This is what Tanner and Hoffmann first observe [90, 179]. Therefore, the capillary force per unit length exerted on the droplet has two components on the horizontal axis: one from the film $F_{film} = \gamma_{al} + \gamma_{sl}$ and one from the droplet $F_{droplet} = -\gamma_{sl} - \gamma_{al} \cos \theta_d$. Both contributions yield the global driving force F_{cap} :

$$F_{cap} = F_{film} + F_{droplet} = \gamma_{al} - \gamma_{al} \cos \theta_d. \quad (4.12)$$

For small angles, $F_{cap} \approx \gamma_{al} \theta_d^2 / 2$. In the following section, we use this approximation by considering the air-liquid interfacial tension only, with $\theta_d \approx e/r$.

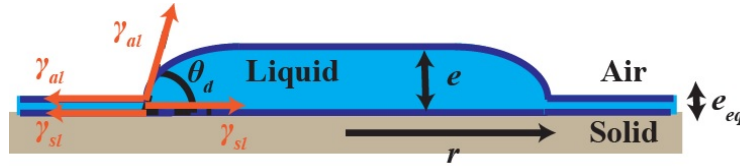


Figure 4.3: Spreading droplet and its precursor film.

4.1.2.2 Capillarity-dominated regime

In this regime, for thin films and droplets, we use the lubrication approximation in the Stokes equation. In cylindrical coordinates, the velocity v in the droplet only depends on the vertical coordinate z . The pressure p is only a function of the radial coordinate r . The Stokes equation is given by:

$$\eta_l \frac{\partial^2 v}{\partial z^2} = \frac{\partial p}{\partial r}, \quad (4.13)$$

with η_l the liquid viscosity and v the horizontal velocity. The boundary conditions are $v(0) = 0$ and $v(e) = U = (1/e) \int_0^e v dz$, with U the mean velocity along the cross-section of the droplet. This problem can be completely solved analytically and a demonstration is given in Appendix A [31]. Here, we choose to present the theoretical analysis in terms of scaling laws.

The tip of the droplet is in under pressure with the center of the droplet. Therefore, liquid is driven from the center to the tip and allows the liquid front to advance. Since $e \ll r$, we can approximate its curvature by the second derivative of the interface profile e/r^2 . The capillary pressure gradient is exerted on the spreading radius r . Thus, the pressure gradient is $\partial p/\partial r \sim \gamma_{al}e/r^3$. And the viscous dissipation is $\eta_l \partial^2 v/\partial z^2 \sim \eta_l U/e^2$. By volume conservation, the droplet volume is $\Omega_d \sim er^2$. By writing $U \sim dr/dt$ (t is the time) and injecting the different contributions into Eq. 4.13, one finds the following spreading law [82]:

$$r(t) \sim \Omega_d^{3/10} \left(\frac{\gamma_{al}}{\eta_l} t \right)^{1/10}. \quad (4.14)$$

As expected, the spreading rate is higher when the liquids are less viscous (less viscous friction) and the air-liquid interfacial tension is high (higher capillary pressure).

4.1.2.3 Gravity-dominated regime

The regime in $t^{1/10}$ is valid when the capillary forces are dominant over the gravity forces. Indeed, gravity can also drive the spreading process. Its volume contribution is $\rho_l g e/r$ since the hydrostatic pressure is applied on the surface of the spherical cap of the droplet. The spreading driving force changes as time goes by. Gravity dominates capillarity if $\rho_l g e/r > \gamma_{al}e/r^3$, which means $r > \kappa$, the capillary length. In that case, balancing the viscous dissipation with the gravity contribution gives the following spreading law [82]:

$$r(t) \sim \Omega_d^{3/8} \left(\frac{\rho_l g}{\eta_l} t \right)^{1/8}. \quad (4.15)$$

As time goes by, the spreading rate decreases. The viscous friction gets higher as the thickness of the drop decreases ($\propto 1/e^2$). The driving forces ($\propto e/r^3$ or e/r) get weaker since r also increases. As a result, a droplet of 1 cm^3 takes more than 1 year to reach a spreading radius $r = 10 \text{ cm}$. Fig. 4.4 shows the capillarity-driven and the gravity-driven regimes with the different transition times. Both capillarity and gravity-dominated spreading regimes are analytically solved in Appendix A.

4.2 Spreading of oil on air-water interfaces from the air phase

Now, what happens if the solid phase is replaced by a liquid phase that is immiscible with the liquid in the droplet? The wetting theory of liquid-liquid systems is similar to the wetting

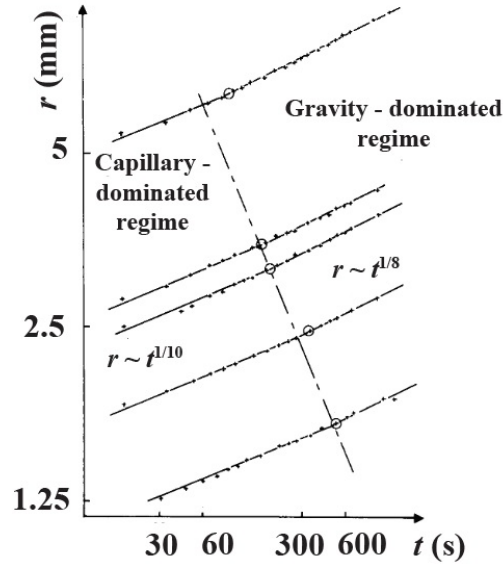


Figure 4.4: Spreading regimes for a liquid droplet on a solid hydrophilic surface for PDMS with $\eta_l = 1$ Pa.s. From top to bottom, $\Omega_d = 37.9, 5.8, 4.03, 1.35, 0.35$ μL . The data are extracted from [31].

predictions for liquid-solid systems. However, the spreading dynamics is completely different. Depending on the viscosity ratio η_o/η_w where η_o and η_w are the oil viscosity and the viscosity of the bulk fluid, two different regimes are observed for liquids in complete wetting.

4.2.1 Liquid-liquid wetting

An oil droplet breaks a film by emerging at the air-water interface if the entry coefficient $E > 0$ and transitions from a spherical shape to a lens shape. From this configuration, the droplet has three different options which depend on the value of the spreading coefficient $S = \gamma_{aw} - \gamma_{ow} - \gamma_{ao}$ already defined in §2.1.1. If $S < 0$, the oil lens remains as it is without contaminating the rest of the air-water interface. If $S > 0$, the oil lens has two possibilities:

- spread completely to form a thin film,
- keep its shape and spread on a thick film of oil (but non-macroscopic) or a solubilised film of oil.

These possibilities are summarized in Fig. 4.5 [5, 13, 100].

The value of S has to be taken at equilibrium, which means for a time scale longer than the diffusion and the adsorption of surfactants at the oil-water interface. Fig. 4.6 shows the evolution of the oil-water interfacial tension γ_{ow} for silicon oil (from Brookfield, oil viscosity $\eta_o = 100$ mPa.s) in a solution of SDS. It is clear that γ_{ow} decreases as time advances. The difference reaches

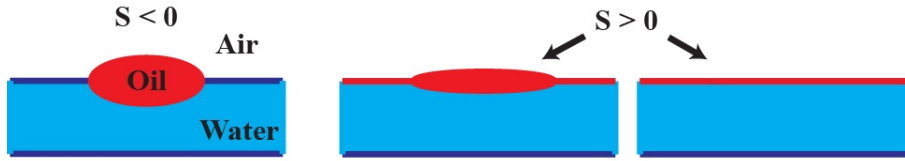


Figure 4.5: Topology of an oil lens spreading on a water surface in the limit where the gravity effects are negligible, i.e. the shape of the drops is only dictated by interfacial tension.

–4 mN/m over 24 hours. However, this decrease induces an increase of S . The equilibration of the value of the interfacial tension should actually enhance the spreading process.

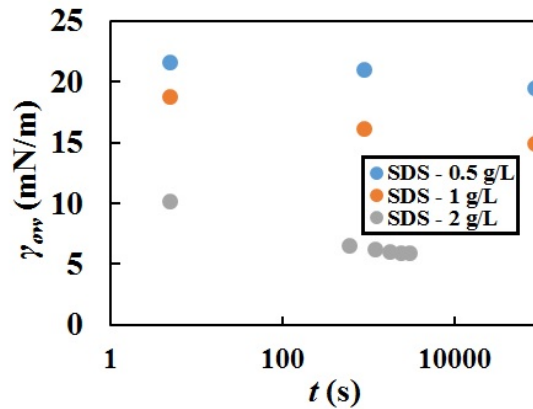


Figure 4.6: Oil-water interfacial tension γ_{ow} as a function of time t for the silicon oil ($\eta_o = 100$ mPa.s) - SDS system. The legend indicates the bulk concentration of surfactants.

4.2.2 Regimes of oil spreading on air-water interfaces

The theoretical and experimental studies of oil spreading at the surface of an aqueous bath with and without surfactants have been done for several systems [13, 27, 34, 48, 69, 175]. We can distinguish different regimes according to the viscosity of the oil phase.

4.2.2.1 Non-viscous to viscous oils

The theory developed here is found in [13]. But all the dynamical studies present the same theoretical arguments. For oil spreading to occur, S has to be positive. The driving force is the interfacial tension gradient along the spreading oil film. This force is resisted by the viscous force engendered by the underlying aqueous phase which is entrained by the film spreading. Fig. 4.7 depicts an oil lens of negligible thickness which spreads at the air-water interface.

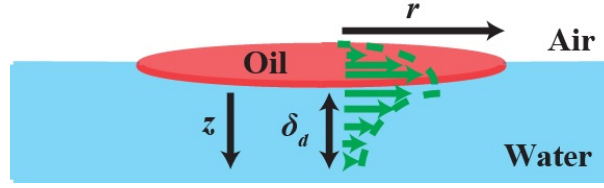


Figure 4.7: Oil lens spreading at the air-water interface.

Subsequently, we have the following balance of stresses:

$$\nabla\gamma + \tau_{ow} = 0 \quad , \quad (4.16)$$

where γ and τ_{ow} are, respectively, the interfacial tension and the shear stress at the oil-water interface. In the film, the variation of interfacial tension is given by S . The interfacial tension gradient varies over the radial spreading distance r . Thus, we have $\partial\gamma/\partial r \approx S/r$. We use an exponentially decaying profile for the velocity in the viscous boundary layer of the aqueous phase, as described in Fig. 4.7. The radial velocity v_r is written as $v_r = v_r(r, z = 0, t)e^{z/\delta_d} = (dr/dt)e^{z/\delta_d}$ where z is the vertical coordinate and δ_d the penetration length. According to the usual boundary layer theory for a laminar flow [10, 82, 113], $\delta_d = r/\sqrt{Re_r}$ where $Re_r = \rho_w v_o d/\eta_w$ is the Reynolds number for the density of the bulk fluid ρ_w , the viscosity of the bulk fluid η_w , the characteristic velocity of the upper layer flow v_o and d the characteristic length. In our case, for $d \approx r$, $v_o \approx r/t$. Thus, the penetration length is expressed as:

$$\delta_d = \sqrt{\frac{\eta_w t}{\rho_w}}. \quad (4.17)$$

The shear stress at the oil-water interface is $\tau_{ow} = \eta_w(\partial v_r/\partial z)_{z=0}$. Therefore, Eq. 4.16 with Eq. 4.17 yields:

$$\frac{S}{r} = \eta_w \left(\frac{\partial v_r}{\partial r} \right)_{z=0} = \frac{\eta_w}{\delta_d} \frac{dr}{dt} = \sqrt{\frac{\rho_w \eta_w}{t}} \frac{dr}{dt}. \quad (4.18)$$

Integrating Eq. 4.18 gives the following spreading law:

$$r = \left(\frac{4}{3} \right)^{1/2} \left(\frac{S}{\rho_w^{1/2} \eta_w^{1/2}} \right)^{1/2} t^{3/4}. \quad (4.19)$$

The power law in $t^{3/4}$ is completely different than the power laws in $t^{1/10}$ and $t^{1/8}$ found for the equivalent spreading of liquid on solid surfaces. This is due to the “moving” character of the liquid substrate, which causes the creation of a boundary layer flow. The dynamics for liquid-

liquid systems is faster than the dynamics for liquid-solid systems. It depends on the physical nature of the spreading liquid through the spreading coefficient S . The higher S , the stronger the driving force, the faster the spreading goes. It also strongly depends on the properties of the aqueous bath. In particular, if the water viscosity is high, the spreading rate is smaller. Indeed, the water substrate plays the role of a dampening layer. No geometrical parameter is involved, neither is the oil viscosity. The $t^{3/4}$ law is valid as long as $\delta_d < r$ but at short times, one might have $\delta_d > r$ since δ_d evolves as $t^{1/2}$. In that case, the penetration depth is r . One obtains a time-linear regime of spreading. The transition occurs for $\delta_d = r$. By equating Eq. 4.19 and Eq. 4.17, the transition time is $\eta_w^3/\rho_w S^2$. By considering $\eta_w = 10^{-3}$ Pa.s, $\rho_w = 10^3$ g/L and $S = 10^{-2}$ N/m, we find that the transition occurs around 10^{-8} s, which means instantaneously as the liquid starts spreading. The only observable regime is the $t^{3/4}$ regime. Fig. 4.8 shows the comparison between the theoretical predictions from Eq. 4.19 and some experimental results [13].

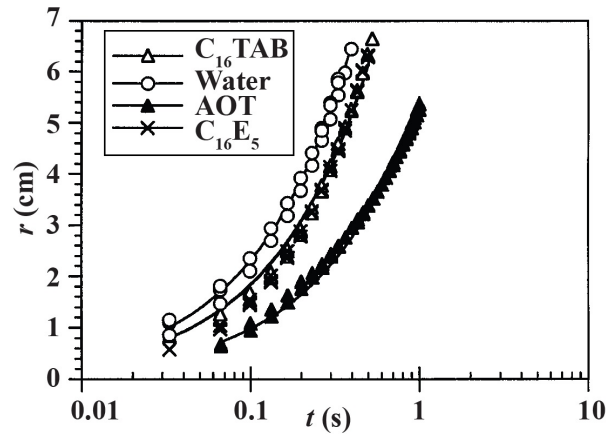


Figure 4.8: Spreading radius r as a function of time t for oil spreading on water-surfactants solutions [13]. Oil: PDMS (Polydimethylsiloxane $\eta_o = 100$ mPa.s). Aqueous bath: C₁₆TAB, Water, AOT (Dioctyl sulfosuccinate sodium) and C₁₀E₅. The black lines are the fit from Eq. 4.19.

In the calculations, one assumes that the interfacial tension is constant over the thickness of the oil droplet and that surfactant dynamics is negligible. If not, discrepancies from the expected law could arise [136].

4.2.2.2 Very viscous oils

These discrepancies can also appear when the oil phase is very viscous [6, 23]. In this case, the oil flow is described as a plug flow, as sketched in Fig. 4.9.

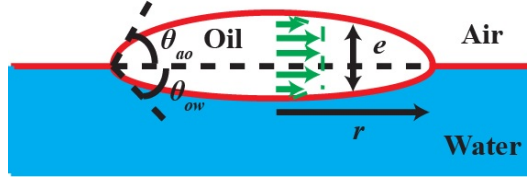


Figure 4.9: Viscous oil lens spreading at the surface of a water bath.

One also assumes that a precursor film is formed at the edge of the droplet. In the limit of small angles, the force balance at the leading edge is written as:

$$\frac{1}{2}\gamma_{ao}\theta_{ao}^2 + \frac{1}{2}\gamma_{ow}\theta_{ow}^2 = \frac{1}{2}\gamma_{eq}\theta_{eq}^2 \quad , \quad (4.20)$$

where θ_{ao} (respectively θ_{ow}) are the dynamic contact angles between the air-water (respectively the oil-water) interface and the horizontal axis. The contact angle θ_{eq} is the angle between the air-water and the oil-water interface. Both interfaces can be assimilated as an association of two springs in parallel. Thus, the equivalent interfacial tension γ_{eq} is deduced from $1/\gamma_{eq} = 1/\gamma_{ao} + 1/\gamma_{ow}$.

One considers the viscous dissipation \mathcal{D} in the droplet with the shear stress τ_{xy} and the shear rate $\dot{\epsilon}$:

$$\mathcal{D} = \int_{\Omega_d} \tau_{xy} \dot{\epsilon} d\Omega_d \approx \Omega_d \eta_o \left(\frac{\dot{r}}{r} \right)^2 \quad . \quad (4.21)$$

The capillarity-induced power \mathcal{P} is given by:

$$\mathcal{P} = \mathbf{F}_{cap} \cdot \dot{\mathbf{r}} = 2\pi r \frac{1}{2} \gamma_{eq} \theta_{eq}^2 \dot{r} \quad , \quad (4.22)$$

where \mathbf{F}_{cap} is the driving force deduced from Eq. 4.20. By volume conservation, we can write $e \approx \Omega_d/r^2$ and by the approximation of small angles, $\theta_{eq} \approx e/r$. Using these estimations and equating Eq. 4.22 to Eq. 4.21 yield the following spreading law:

$$r = \left(\frac{\gamma_{eq}}{\eta_o} \Omega_d \right)^{1/4} t^{1/4} \quad . \quad (4.23)$$

The power law in $t^{1/4}$ obviously gives a slower dynamics than the $t^{3/4}$ result for less viscous oils. Like the different laws presented before, increasing oil viscosity decreases the spreading rate, while higher interfacial tension has the opposite effect. The boundary between this regime and the $t^{3/4}$ regime is determined by equating the viscous dissipations from both cases. The $t^{1/4}$

regime dominates if $\Omega_d \eta_o (\dot{r}/r)^2 > \delta_d r^2 \eta_w (\dot{r}/\delta_d)^2 e^{z/\delta_d}$. For this latter term, the dissipation length is the width of the boundary layer δ_d and the volume is $\delta_d r^2$. We have $r \ll \delta_d = r/\sqrt{Re_r}$ with $Re_r \ll 1$ for a viscous flow. By setting $\delta_d \approx r$, one finds an upper limit for the regime separation:

$$\eta_o > \eta_o^* = \eta_w \left(\frac{r^3}{\Omega_d} \right). \quad (4.24)$$

For $\Omega_d = 0.1 \text{ cm}^3$, $r = 5 \text{ cm}$ and $\eta_w = 1 \text{ mPa.s}$, $\eta_o^* = 1.3 \text{ Pa.s}$, which is three orders of magnitude higher than the water viscosity. At high radius over the capillary length, the $t^{1/4}$ regime switches to a gravitational $t^{1/2}$ regime where the capillary force is replaced by the gravitational force [6].

4.3 Spreading of oil rising from the aqueous phase at air-water interfaces

In many situations, the oil phase emerges at the air-water interface from the aqueous phase: emulsified oil-water systems, froth flotation, underwater pollution and oil-laden aqueous foams [28, 56, 103, 128, 137]. The surrounding aqueous phase can affect the spreading dynamics, in comparison with the air phase which has a negligible role in previous spreading studies. This is all the more true that most relevant and real aqueous systems contain surfactants (or ionic agents acting as surfactants) which can also strongly modify the spreading behaviour.

We study the radial spreading of rising oil droplets at the surface of an aqueous bath containing soluble surfactants or not. We develop a model for short and long-time dynamics and compare with experimental results obtained with mineral and organic oils. We discuss our model with regard to existing spreading theories.

4.3.1 Experimental results

We perform spreading experiments with different oils whose characteristics are summarised in Table 4.1. The mineral oils are paraffin oil (Sigma-Aldrich) and different silicone oils (standard oils from Sigma-Aldrich or oils for rheometer calibration from Brookfield). All oils are dyed (1 wt% from Rohm and Haas) to enhance the contrast between the aqueous and the oily phase. The interfacial tensions are measured by the pendant drop method. For the aqueous phase, the surfactant is SDS (sodium dodecyl sulfate from Sigma-Aldrich) with concentrations C_{SDS} varying from 0.5 g/L to 10 g/L (5 times higher than the cmc). The aqueous phase is contained in a transparent polyacrylic box whose dimensions are variable (width: 10.7/9 cm - length: 15.5/9.5 cm - height: 3.7/9.7 cm).

Interfacial tension	Solution	Water	SDS - 0.5 g/L	SDS - 1 g/L	SDS - 2 g/L	SDS - 10 g/L
γ_{aw}	Air	73	58.8	52	39	36.9
Interfacial tensions	Oil	Par 25.7	Si 5	Si 20	Si 100	Si 350
	Solution	0.838	0.95	0.97	0.965	0.97
γ_{ao}	Air	19.5	20.9	19.1	19.6	19.1
γ_{ow}	Water	37.7	36.7	40.2	36.3	40.2
	SDS - 0.5 g/L	21.6		19.8	21.6	
	SDS - 1 g/L	16.7		14.6	18.8	
	SDS - 2 g/L	8.9		8.7	10.1	8.7
	SDS - 10 g/L	7.3		6.2	8.4	
$E - S$	Water	91.2	88.8	94.1	89.7	94.1
		15.8	15.5	13.7	17.1	13.7
	SDS - 0.5 g/L	60.9		59.5	60.8	
		17.7		20	17.6	
	SDS - 1 g/L	49.1		47.5	51.1	
		15.8		18.3	13.6	
	SDS - 2 g/L	28.4		28.6	29.5	28.6
		10.6		11.2	9.3	11.2
	SDS - 10 g/L	24.6		24	25.7	
		10.1		11.6	8.8	

Table 4.1: Interfacial tensions γ_{aw} , γ_{ao} and γ_{ow} (mN/m) with calculated entry E and spreading coefficients S_o of the oils and aqueous solutions. The dynamic viscosity η_o (mPa.s) and the density ρ_o (for each oil), and the surfactant concentration C_{SDS} (for each aqueous solution) are given.

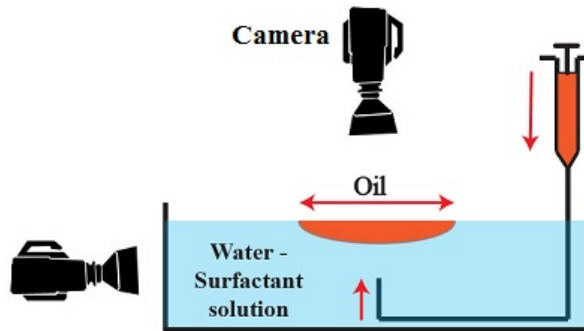


Figure 4.10: Experimental set-up. The oil droplet rises from the immersed needle and spreads at the bath surface.

As sketched in Fig. 4.10, the oil phase comes through a needle that is directed upwards and immersed inside the box. The tip of the needle can be located at different distances from the surface. First, the oil droplet is generated by a small injection rate (0.05 - 0.1 mL/min) and can remain attached or detached from the needle when it touches the surface. Before the touching time, we start recording the spreading dynamics at 7.5 frames per second for the standard camera

(AVT Marlin) and at 2000 or 2500 frames per second for the fast camera (Photron v9.7 and SA3). If the entry coefficient $E = \gamma_{aw} - \gamma_{ow} - \gamma_{ao} < 0$, the droplet remains spherical under the water surface and does not spread. If $E > 0$ but $S = \gamma_{aw} + \gamma_{ow} - \gamma_{ao} < 0$, the droplet breaks the surface and keeps a lens shape without spreading. Finally, if $E > 0$ and $S > 0$, within less than one second, the oil droplet breaks and penetrates the water surface before spreading radially. Fig. 4.11 summarizes these three possible configurations.

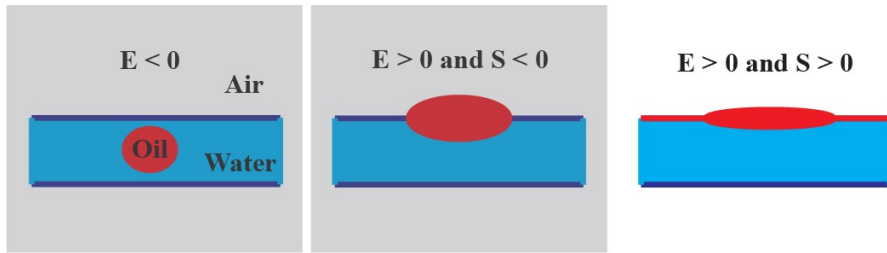


Figure 4.11: Configurations of an oil droplet at the air-water interface according to the values of the entry E and spreading S coefficient.

In our experiments, we do not encounter the cases $E < 0$ and $E > 0$ with $S < 0$ for which the droplet does not break the surface or spread at all. We focus on the case $E > 0$ and $S > 0$. Then, two possible evolutions are observed. Fig. 4.12 shows these two typical image sequences obtained from the spreading observations. With no surfactants in the aqueous bath, the oil droplet spreads completely in a fraction of seconds until forming a thin film at the bath surface (Fig. 4.12a). With surfactants, the oil droplet initially spreads until forming a lens (Fig. 4.12b), then keeps spreading slowly while holding the lens shape (Fig. 4.12c).

4.3.2 Short-time dynamics

Here, we consider the short-time dynamics of spreading by taking inertial, viscous and capillary effects into account.

4.3.2.1 Inertial-viscous-capillary regime

For the early stages of the no-surfactant and surfactant case, we can define a short-time spreading regime. When reaching the bath surface, the spherical oil droplet breaks the water surface in a “coalescence”-like scenario [134], as shown in the inset of Fig. 4.13. The driving force is the difference of capillary pressure Δp_C at the neck of the droplet. Using a parabolic shape at the

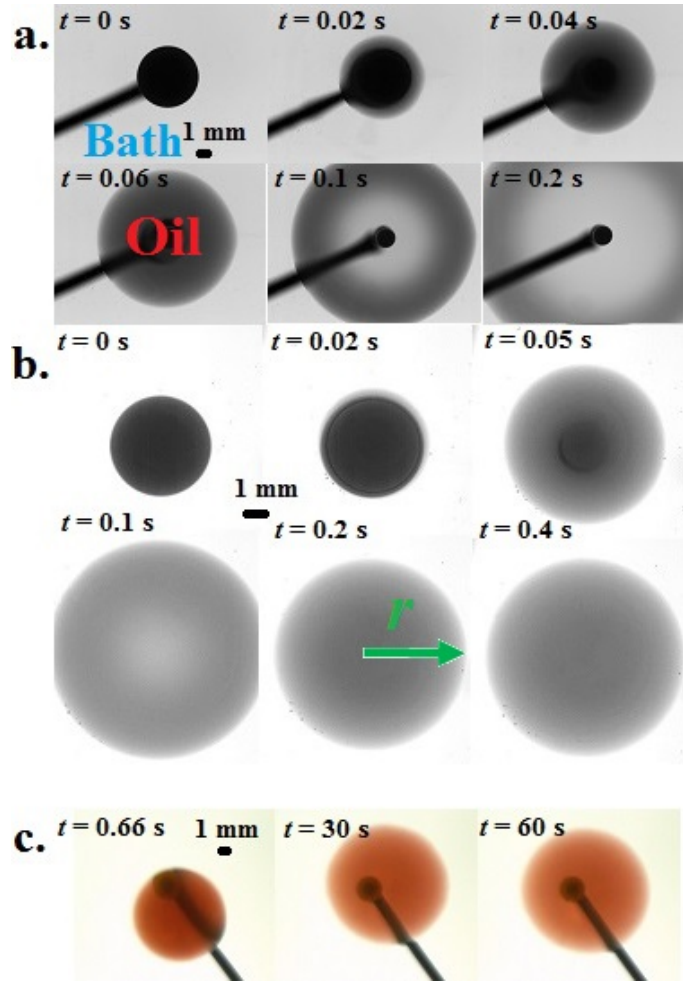


Figure 4.12: Snapshots of the spreading dynamics. a. No-surfactant case (aqueous solution = water and oil = silicon oil, $\eta_o = 5$ mPa.s); $R_d = 3.72$ mm and $Oh = 73.3$. b. Surfactant case in the short-time regime from $t = 0$ s to 0.4 s (aqueous solution = SDS solution, $C_{SDS} = 2$ g/L and oil = silicon oil, $\eta_o = 20$ mPa.s); $R_d = 2.84$ mm and $Oh = 7.7$. c. Surfactant case in the long-time regime from $t = 0.66$ s to 60 s (aqueous solution = SDS solution - $C_{SDS} = 2$ g/L and oil = silicon oil, $\eta_o = 20$ mPa.s); $R_d = 3.76$ mm and $Oh = 8.9$. The thick black line is the injection needle.

neck [64, 134], we can estimate $\Delta p_C = \gamma_{ow}(\kappa_2 - \kappa_1) \approx \gamma_{ow}R_d/r^2 + \gamma_{ow}/R_d \approx \gamma_{ow}R_d/r^2$, where R_d is the droplet radius and r the spreading radius. This pressure is balanced by the viscous stress with the velocity gradient over r , and the inertial pressure, which gives:

$$\gamma_{ow} \frac{R_d}{r^2} = \frac{\eta_o}{r} \frac{dr}{dt} + \rho_o \left(\frac{dr}{dt} \right)^2, \quad (4.25)$$

where η_o and ρ_o are, respectively, the oil dynamic viscosity and the oil density. By solving (4.25), we find that:

$$r(t) = \left(\frac{-\eta_o + \sqrt{\eta_o^2 + 4\rho_o\gamma_{ow}R_d}}{\rho_o} \right)^{1/2} t^{1/2}. \quad (4.26)$$

We non-dimensionalize r and t as $R = r/R_d$ and $T = t/(\eta_o R_d/\gamma_{ow})$. We also introduce the Ohnesorge number $Oh = \sqrt{\rho_o\gamma_{ow}R_d}/\eta_o$. Eq. (4.26) becomes:

$$R = \left(\frac{-1 + \sqrt{1 + 4Oh^2}}{Oh^2} \right)^{1/2} T^{1/2}. \quad (4.27)$$

4.3.2.2 Collapse between experiments and theory at short times

If $Oh \gg 1$ (non-viscous oil), we have an inertial-capillary regime and $R \sim (T/Oh)^{1/2}$, similar to [16] for the early spreading on a solid wall. On the opposite, if $Oh \ll 1$ (viscous oil), we have a viscous-capillary regime and $R \sim T^{1/2}$. We report the experimental data with the dimensionless spreading radius R as a function of $T_{Oh} = \left(\frac{-1 + \sqrt{1 + 4Oh^2}}{Oh^2} \right) T$ in Fig. 4.13. We obtain a good collapse between all curves for a short-time regime in the range of $T_{Oh} = 1$ to 5 ($t < 1$ s).

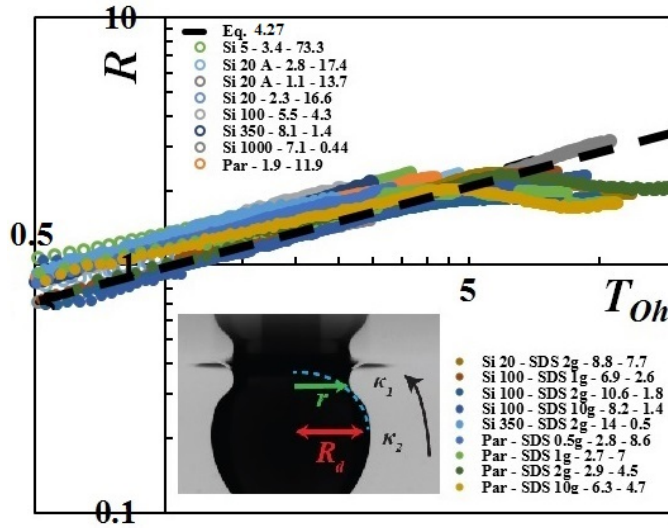


Figure 4.13: Dimensionless spreading radius R as a function of the dimensionless time T_{Oh} . The open dots correspond to a bath solution without surfactants and the close dots with surfactants. The type of oil - η_o (mPa.s) - C_{SDS} (per liter), Bo and Oh are indicated in this order in the legend. A corresponds to an attached droplet. The dashed line is Eq. 4.27. The black arrow in the snapshot indicates the direction of the oil movement.

The transition to the late stages is discussed in the following section.

4.3.3 Long-time dynamics

We also study the long-time spreading dynamics and the transition to multiple regimes for both pure aqueous and surfactant solutions in the bath phase.

4.3.3.1 Transition to long-time dynamics for pure aqueous solutions

For pure aqueous solutions in the bath, the aforementioned short-time diffusive regime transitions to the long-time regime in $t^{3/4}$ described in §4.2.2.1. This transition is shown in Fig. 4.14. Eq. 4.19 can be written in the dimensionless coordinates R and T :

$$R = \left(\frac{4}{3}\right)^{1/2} \frac{T^{3/4}}{Oh_{eff}^{1/2}}, \quad (4.28)$$

with the effective Ohnesorge number $Oh_{eff} = \sqrt{\rho_w R_d (\gamma_{ow}^{3/2} / S) / (\eta_o^{3/2} / \eta_w^{1/2})}$.

The transition time T_{ST-LT} and radius R_{ST-LT} between the short-time and the long-time regime are defined by equating Eq. 4.27 and Eq. 4.28, which gives:

$$T_{ST-LT} = \frac{Oh_{eff}^2}{f(Oh)^2} \quad \text{and} \quad R_{ST-LT} \approx \frac{Oh_{eff}}{f(Oh)^{3/2}}, \quad (4.29)$$

with $f(Oh) = Oh^2 / (-1 + \sqrt{1 + 4Oh^2})$.

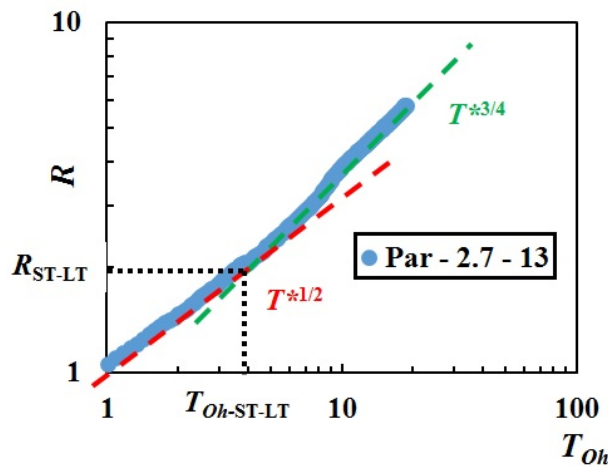


Figure 4.14: Dimensionless spreading radius R as a function of the dimensionless time T_{Oh} for the spreading of paraffin oil on water. Dimensionless numbers: $Oh = 13$, $Bo = 2.7$ and $Oh_{eff} = 3.6$. The transition time and radius are $T_{Oh-ST-LT} \approx Oh_{eff}^2 / f(Oh)^3 \approx 3.8$ and $R_{ST-LT} \approx Oh_{eff} / f(Oh)^{3/2} \approx 2$.

4.3.3.2 “Solid”-like spreading for surfactant solutions

However, with surfactants, the oil lens keeps spreading at a much slower spreading rate. Fig. 4.12c shows a typical sequence of spreading images for $t = 0.66$ to 60 s. Since $S > 0$, it is not surprising to observe a long-time spreading dynamics. Some studies [5, 24, 100] have shown the existence of a pseudo-partial wetting regime between the total wetting regime ($S > 0$) and the partial wetting regime ($S < 0$) for the spreading of liquid on a solid surface. In this regime, the liquid droplet keeps a lens shape and spreads onto a thin precursor film of liquid. Here, we assume the same situation, as shown in [24]. At the end of the short-time regime, the oil droplet reaches a lens shape. This lens is in equilibrium with a thin molecular film of oil and spreads upon it.

If $r > \kappa$ where $\kappa = \sqrt{\gamma_{ow}/(\rho_o g)}$, the capillary pressure gradient $\gamma_{ow}e/r^3$ is dominated by the gravity effects $\rho_o g e/r$, where e is the height of the lens (assuming a quasi-cylindrical shape). The hydrostatic pressure in the oil phase is only considered here. Indeed, the velocity field is radial in the droplet, thus the pressure is constant in the vertical direction (from the Stokes equation and the lubrication approximation) and equal to the oil hydrostatic pressure at $z = -e$. Using the volume conservation $R_d^3 \sim e r^2$ and balancing the gravity effects with the viscous dissipation $(\eta_o/e^2)dr/dt$, we find the spreading radius:

$$r(t) \sim \left(\frac{\rho_o g R_d^9}{\eta_o} \right)^{1/8} t^{1/8}. \quad (4.30)$$

We can non-dimensionalize r and t by $R = r/R_d$ and $T^* = t/(\eta_o/\rho_o g R_d)$ and we find $R = T^{*1/8}$ for $R > 1/Bo^{1/2}$ where $Bo = \rho_o g R_d^2/\gamma_{ow}$ is the Bond number.

However, if $r < \kappa$, the capillary pressure gradient dominates the gravity effects. Thus, in this range of radii, we find a spreading dynamics similar to the spreading of a microscopic droplet beyond a flat solid surface:

$$r(t) \sim \left(\frac{\gamma_{ow} R_d^9}{\eta_o} \right)^{1/10} t^{1/10}, \quad (4.31)$$

with $R = T^{*1/10}$ by non-dimensionalizing Eq. 4.31 for $R < 1/Bo^{1/2}$. For our experiments, $1/Bo^{1/2} < 1 < R$ (see Fig. 4.13) at the end of the short-time regime, we should transition to the viscous-gravitational regime. In Fig. 4.15, we plot the experimental data in the dimensionless coordinates (T^*, R) .

We find a good agreement with the model for all curves in Fig. 4.15. The plateau profile for $T^* <$

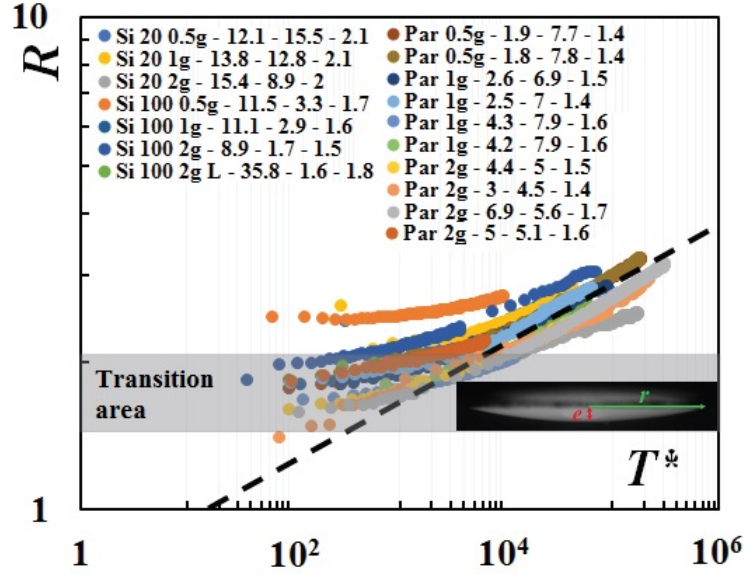


Figure 4.15: Dimensionless spreading radius R as a function of the dimensionless time T^* . The type of oil - η_o (mPa.s - C_{SDS} (per liter), Bo , Oh and R_g are indicated in this order in the legend. **L** in **Si100 2g L** is for a droplet attached to the needle for 1 h in the aqueous bath before spreading (in case surfactant dynamics matters). The dashed line is a guide line for the power law $T^{*1/8}$.

1000 corresponds to the transition between the short-time regime and the long-time dynamics. The crossover time between both dynamics is defined by the characteristic time τ_g^* and radius r_g . In the long-time dimensionless coordinates, τ_g^* and r_g are non-dimensionalized as T_g^* and R_g , in the viscous-gravitational regime. By equating Eq. 4.26 to Eq. 4.30, we find:

$$T_g^* \sim \left(\frac{BoOh^2}{-1 + \sqrt{1 + 4Oh^2}} \right)^{4/3}, \quad (4.32a)$$

$$R_g \sim \left(\frac{BoOh^2}{-1 + \sqrt{1 + 4Oh^2}} \right)^{1/6}. \quad (4.32b)$$

As reported in Fig. 4.15, a good correlation is found between the expected crossover time and the experimental transition to the long-time regime. If $Oh \gg 1$ (inertia-dominated short-time regime), $T_g^* = T_{i/g}^* \sim Bo^{4/3}Oh^{4/3}$ and $R_g = R_{i/g} \sim Bo^{1/6}Oh^{1/6}$. Yet, if $Oh \ll 1$ (viscous-dominated short-time regime), the crossover time and radius are, respectively, $T_{v/g}^* \sim Bo^{4/3}$ and $R_{v/g} \sim Bo^{1/6}$. For a viscous-capillary regime at long times, by equating Eq. 4.26 to Eq. 4.31, we find the dimensionless characteristic time $T_c \sim (Oh^2 / (-1 + \sqrt{1 + 4Oh^2}))^{5/4}$ and radius $R_c \sim (Oh^2 / (-1 + \sqrt{1 + 4Oh^2}))^{1/8}$. By reporting the transition radii, we build a phase diagram (Bo , R) which indicates the different regimes for a given Oh in Fig. 4.16.

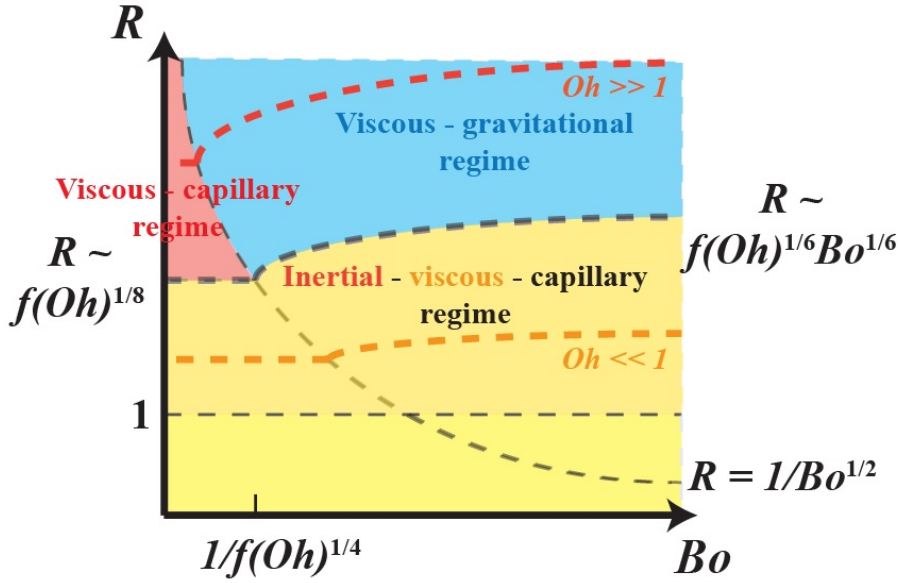


Figure 4.16: Phase diagram (Bo, R) for a given Oh in the surfactant case. The transitions for different values of Oh between the short-time and the long-time regimes are plotted in the red dashed line (for $Oh \gg 1$) and in the orange dashed line (for $Oh \ll 1$). We have $f(Oh) = Oh^2 / (-1 + \sqrt{1 + 4Oh^2})$. The curve $R = 1/Bo^{1/2}$ defines the transition between capillary and gravity-dominated regime (capillary length). The curves $R = f(Oh)^{1/6}Bo^{1/6}$ and $R = f(Oh)^{1/8}$ correspond to the transitions between the short-time and the long-time dynamics.

Our theoretical developments differ from previous studies who have shown that the spreading of an oil droplet upon a bath of aqueous liquid with and without surfactants follows a single regime in $t^{3/4}$ [13, 27]. At short times, the oil droplet coalesces with the bath by the air phase in previous works. Thus, as sketched in Fig. 4.17a, the viscous dissipation only occurs in the bath.

To evaluate this dissipation, an exponential decaying velocity profile is assumed in the bath, which allows to calculate the shear stress at the oil-water interface and leads to the aforementioned power law while balancing with the capillary pressure gradient. Yet, in our case, the dissipation occurs in the oil phase and the shear stress is zero at the air-oil interface. We estimate this dissipation by considering a velocity gradient in the coalescence neck along the radial direction, which yields the diffusive behaviour in $t^{1/2}$. From our study, we demonstrate that the initial location of the droplet with respect to the bath is critical and yields a different spreading power law for short-times. We retrieve a long-time regime in $t^{3/4}$ when the effect of the initial capillary pressure of the neck is lost and when the droplet switches to a lens shape.

Not only is the system configuration important, but the addition of surfactants causes a regime separation at long times. The spreading behaviour is similar to the spreading of an oil droplet on a solid surface with the development of a precursor film. In other studies, the addition of sur-

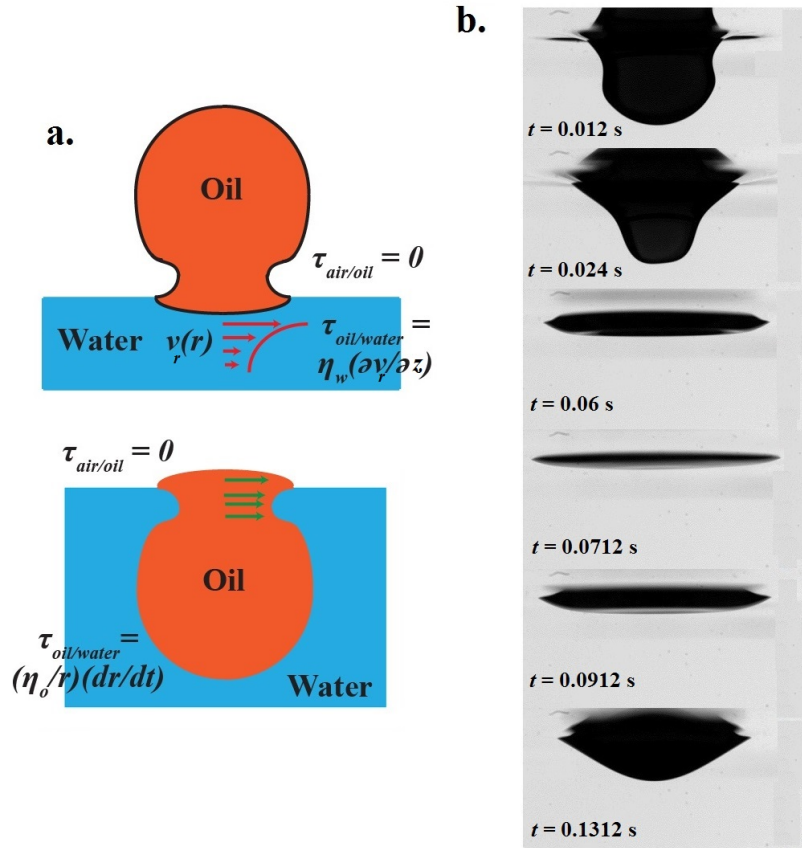


Figure 4.17: a. Schematic representation of the shear stress contributions at the air-oil interface $\tau_{air/oil}$ and at the oil-water interface $\tau_{oil/water}$ when the oil droplet initially spreads. b. Side-view of a typical short-time spreading dynamics (paraffin oil with surfactants) highlighting an oscillatory and a spring-like behaviour.

factants does not seem to impact the spreading law in $t^{3/4}$ where the dissipation in the aqueous bath is considered. Dynamics of surfactant adsorption leading to potential variations of S between the initial state and the final equilibrium state might play a role here. However, we carried out experiments after letting the oil droplet equilibrate with the bath from a few minutes to several hours. The oil-water interfacial tension only decreases, thus S increases and the spreading process should be more favourable.

A more consistent explanation comes from the existence of an interfacial stress that arises when the oil droplet spreads, as shown in Fig. 4.17b. The droplet can sweep surfactants from the air-water interface. Thus, the interfacial concentration of surfactants at the center is lower than the concentration at the edges. Hence, an interfacial tension gradient is created from the edges to the center and the air-water-oil interface behaves like a spring and slows down the spreading of the droplet. But a precursor film still propagates at the front of the droplet. From this configuration, we retrieve the long-time dynamics of a droplet sitting on a precursor film, as described in the

second part of this study. This happens more easily for mobile surfactants, such as SDS, than immobile surfactants with long polymeric chains like AOT and CTAB for instance. Molecular interactions between the surfactants and the oil might also be at stake and allow the system to find a configuration where a droplet coexists with a precursor film of molecular thickness.

In conclusion, we can describe the spreading of oil droplets coming from the aqueous phase by two regimes. The early stage is a fast diffusive regime in $t^{1/2}$ that occurs for bulk solutions with and without surfactants. In the case of pure aqueous phase, we transition to the common long-time regime in $t^{3/4}$. However, in the surfactant case, it is possible to find a transition to a long-time regime similar to the spreading of a liquid droplet on a solid wall: the air phase is replaced by the water phase and the solid phase by the air phase. It seems that this behaviour strongly depends on the nature of the oil phase and the type of surfactants.

4.4 Conclusions

The existence of oil-filled films is a question of emergence of oil droplets at the air-water interface. However, spreading issues are also important as it enhances the destabilization process. Therefore, we have studied the spreading dynamics of oil droplets at the air-water interface. Most studies have considered the deposition of oil droplets at the water surface by the air phase. In our case, we consider oil droplets that are already in the aqueous phase before rising to the surface, which is closer to the configurations of oil-filled films. Our results demonstrate the existence of a diffusive short-time dynamics - driven by capillarity and resisted by viscous and inertial forces - that joins the common spreading law in $t^{3/4}$ at long times for spreading on a pure aqueous surface. For surfactant-laden solutions, molecular dynamics at the oil-water interface gives results similar to the spreading of oil on solid surfaces. The motion of surfactants at the interfaces has a strong influence on the spreading dynamics.

In Chapter 2, 3 and 4, we have talked about oil-foam systems when oil is already present in the microstructures of the foam (stability in films and Plateau borders) and when oil seeks to come out of the foam (spreading dynamics, rupture instability). Now, the question is: how is oil absorbed into foams?

Chapter 5

Oil imbibition into aqueous foams

Dry aqueous foams can be seen as liquid porous media constituted by a network of liquid microchannels called Plateau borders at the bubbles' junctions, similarly to pores at the junction of granular beads that can be wicked by liquids. In this chapter, we study the dynamics of oil imbibition into aqueous foams. Different situations are considered: point-source of oil, oil slick and moving foam. We discuss our results with regard to known theories for liquid flows in foams and solid porous media.

Contents

5.1	Imbibition through liquid foams	121
5.1.1	1D Imbibition through solid porous media	121
5.1.1.1	Jurin's law	121
5.1.1.2	Lucas-Washburn's law	122
5.1.1.3	1D imbibition through an undeformable solid porous medium of variable pore size	124
5.1.1.4	1D imbibition through a deformable solid porous medium	125
5.1.2	Liquid flow in dry aqueous foams	126
5.1.2.1	Osmotic pressure and imbibition	126
5.1.2.2	Flow of liquid through a porous medium	128
5.1.2.3	Permeability models	130
5.1.2.4	Drainage equation	131
5.2	Point-source imbibition from an oil-filled pore	132
5.2.1	3D imbibition from a point-source for miscible liquids	132
5.2.1.1	Differential equation for the cross-sectional area A of a Plateau border	133
5.2.1.2	Solution to the partial differential equation (PDE)	133
5.2.2	3D imbibition from a point-source for immiscible liquids	135
5.2.2.1	Local picture of oil invasion	135
5.2.2.2	Effective interfacial tension	136
5.2.2.3	Driving equation for immiscible liquids	137
5.2.3	Experimental imbibition front	137
5.2.3.1	Experimental set-up	138
5.2.3.2	Imbibition picture	139
5.2.3.3	Time-dependence of the imbibition front	140
5.2.4	Comparison with experimental results	140
5.2.4.1	Collapse of the theory with the experiments	140
5.2.4.2	Analytical solution with $Bo = 0$	142
5.3	Capillary rise into aqueous foams for miscible and immiscible liquids	143

5.3.1	Oil absorption: characteristics and picture	144
5.3.2	Theoretical analysis	145
5.3.2.1	Time-dependent imbibition front	145
5.3.2.2	Comparison with the drainage theory	146
5.3.2.3	Scaling law	149
5.4	Oil recovery by a moving foam	154
5.4.1	Experimental configuration	154
5.4.2	Modelization of the imbibed moving foam	156
5.4.2.1	Imbibition profiles	156
5.4.2.2	Discretized model	157
5.5	Conclusions	161

Specific variables

Variables	Parameters	Variables	Parameters
I_S	Impregnation parameter	h_{max}	Maximum height
r_m	Curvature radius of the meniscus	p_m	Pressure in the meniscus
u	Velocity field in a pore	v_m	Mean rising velocity
m_l	Mass of liquid	m_{foam}	Mass of the foam sample
F_{cap}	Capillary force	$F_{viscous}$	Viscous force
P_W	Weight of the liquid column	Re	Reynolds number
v	Vertical velocity	r	Radial coordinate (or spreading radius)
r_{app}	Apparent radius	h	Imbibition height
Bo	Bond number	V_g	Volume of gas
e_W	Sheet thickness	ℓ_W	Sheet length
\mathcal{E}_{ec}	Elastocapillary number	B_{ec}	Bending stiffness per unit width of the wall
l_{ec}	Elastocapillary length	h_{foam}	Emptied distance in the U-tube
k_D	Darcy's permeability	k_{foam}	Foam permeability in the channel-dominated model
ℓ	Cylinder (Plateau border) length	β	Orientation angle
ξ	Transverse angle	u_{PB}	Velocity field in the Plateau border
A	Cross-sectional area	K_c	Permeability constant
u_{Darcy}	Darcy's velocity field	k	Permeability
Bq	Boussinesq number	η_s	Interfacial shear viscosity
V_n	Volume of the nodes	V_{PB}	Volume of the Plateau border
u_n	Velocity across a node	k_n	Foam permeability in the node-dominated model
V_{foam}	Volume of the foam sample	I	Fluorescence intensity
σ_I	Width of the intensity peak	α^*	Reduced length
t^*	Dimensionless time	Z_f	Dimensionless self-similar solution
τ	Dimensionless time	Z	Dimensionless vertical coordinate
R	Dimensionless radial coordinate	α	Dimensionless cross-sectional area
S_f	Area of the film surfaces	S_{PB}	Area of the Plateau border's surfaces
S_o	Oil-water interfacial area	S_w	Air-water interfacial area
γ_{eff}	Effective interfacial tension	ϕ_{ow}	Oil-water liquid fraction
z_f	Imbibition vertical front	ζ	Dimensionless self-similar variable
\bar{R}	Dimensionless spherical distance	ζ_f	Dimensionless self-similar front
Q	Injection flow rate	Q_o	Oil flow rate
V_o	Volume of oil	t_r	Experimental running time
U_f	Foam velocity	v_o	Elementary oil volume
d_t	Tube diameter	t_d	Contact time
U^*	Dimensionless foam velocity	Q^*	Dimensionless flow rate of oil
r^*	Characteristic radius of the Plateau border		

5.1 Imbibition through liquid foams

We first recall some results on the 1D imbibition into solid porous media (undeformable and deformable) and aqueous foams that are later used for comparison with our imbibition dynamics. Then, we present the main model to explain the flow of liquid in foams that we can assimilate as liquid porous media.

5.1.1 1D Imbibition through solid porous media

The 1D imbibition through undeformable and deformable solid porous media is a well-known subject. We present some of the main results.

5.1.1.1 Jurin's law

Let us consider an undeformable capillary tube of constant radius that we put into contact with an aqueous bath by the bottom of the tube. Liquid rises into the tube if the wet tube has an interfacial energy lower than the dry tube. By using the solid-liquid γ_{sl} and the solid-air γ_{sa} interfacial tensions, one defines the impregnation parameter I_S :

$$I_S = \gamma_{sa} - \gamma_{sl}. \quad (5.1)$$

If $I_S > 0$, capillary rise occurs in the tube. If $I_S < 0$, liquid goes down the tube. The criterion $I_S > 0$ is equivalent to the contact angle $\theta_Y < 90^\circ$ since $I_S = \gamma_{al} \cos \theta_Y$ by the Young-Dupré relationship (with γ_{al} the air-liquid interfacial tension).

Capillary rise lasts until the interfacial energy is balanced by the potential energy. Fig. 5.1 describes the liquid rising into the capillary tube. The energy \mathcal{E} of the liquid column can be written as:

$$\mathcal{E} = -2\pi r_t z I_S + \frac{1}{2} \pi r_t^2 z^2 \rho_l g, \quad (5.2)$$

where r_t is the tube radius, z the vertical coordinate and ρ_l the liquid density. In Eq. 5.2, the size of the meniscus is neglected, which is valid for $r_t \ll z$. Setting $d\mathcal{E}/dz = 0$ for the energy minimum and injecting $I_S = \gamma_{al} \cos \theta_Y$ yields the maximum height of capillary rise h_{max} :

$$h_{max} = \frac{2\gamma_{al}}{\rho_l g r_t} \cos \theta_Y. \quad (5.3)$$

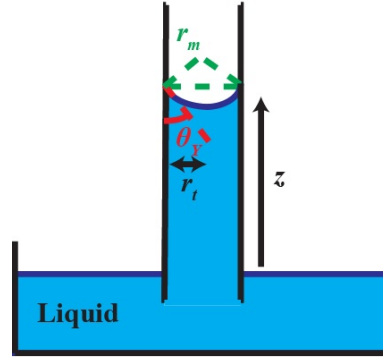


Figure 5.1: Liquid rising in a capillary tube.

Eq. 5.3 is known as the Jurin law [86, 99]. This height is maximum for $\theta_Y = 0^\circ$ (for a completely wetting droplet). The thinner the tube, the higher h_{max} . Indeed, if one thinks about the pressure balance at the spherical meniscus, the curvature radius r_m is $r_t / \cos \theta_Y$ and the pressure p_m is given by the Laplace relationship:

$$p_m = p_{atm} - 2 \frac{\gamma_{al} \cos \theta_Y}{r_t}. \quad (5.4)$$

This pressure is equilibrated with the hydrostatic pressure $p_o - \rho_l g h_{max}$. One finds again Eq. 5.3 and can understand that a smaller tube radius induces a higher capillary pressure, and thus a higher maximum height. For $\gamma_{al} = 70$ mN/m, $r_t = 10$ μm , $\rho_l = 1000$ g/L and $\cos \theta_Y = 0.5$, $h_{max} \approx 70$ cm. We have $r_t \ll h_{max}$ for micrometric tubes and Eq. 5.3 is valid.

5.1.1.2 Lucas-Washburn's law

Let us now describe the hydrodynamics of capillary rise. One can write Newton's momentum equation applied to the liquid column along the vertical direction e_z :

$$\frac{d(m_l v_m)}{dt} = F_{cap} - F_{viscous} - P_W, \quad (5.5)$$

where v_m is the mean rising velocity and the capillary force F_{cap} is resisted by the viscous force $F_{viscous}$ and the weight of the liquid column P_W . The capillary force is applied to the perimeter of the tube cross-section. Its value is proportional to the difference between the interfacial energy of the dry and the wet solid. Thus, F_{cap} is written as:

$$F_{cap} = 2\pi r_t I_S = 2\pi r_t \gamma_{al} \cos \theta_Y. \quad (5.6)$$

The weight P_W is equal to $\rho_l g \pi r_t^2 z$. The viscous force $F_{viscous}$ is determined by considering

a Poiseuille flow in the tube (see Appendix A). Indeed, the liquid rise is slow (the Reynolds number $Re = \rho_l v_m r_t / \eta_l \ll 1$) and the no-slip condition at the walls imposes a velocity gradient given by Stokes' equation. The vertical velocity $v(r)$ (r is the radial coordinate) across the cross-section of the tube is given by $v(r) = 2v_m(1 - (r/r_t)^2)$ (see Appendix A). Thus, we have $F_{viscous} = - \int_0^{2\pi} \int_0^z \eta_l (dv/dr)_{r=r_t} r_t d\beta dz$, where η_l is the liquid viscosity and $d\beta$ the elementary cross-sectional angle. After integration, one finds that:

$$F_{viscous} = 8\pi\eta_l v_m z. \quad (5.7)$$

Injecting the different force contributions in Eq. 5.5 gives:

$$\rho_l r_t^2 \frac{d(zv_m)}{dt} = 2r_t \gamma_{al} \cos \theta_Y - 8\eta_l v_m z - \rho_l g r_t^2 z. \quad (5.8)$$

We consider different cases. First, for $t \gg 0$, one can neglect the inertial term compared to the viscous term. As stated for the calculations of the viscous force, the flow of liquid is assimilated to a Poiseuille flow due to the low velocity and the no-slip condition at the wall. At the beginning of the capillary rise, the weight term can also be neglected providing that $z \ll \gamma_{al} / \rho_l g r_t$. As a consequence, we only balance capillary and viscous forces in the early stages of the capillary rise with $v_m = dz/dt$. Eq. 5.8 yields after integration:

$$z = \left(\frac{1}{2} \frac{\gamma_{al} r_t \cos \theta_Y}{\eta_l} t \right)^{1/2}. \quad (5.9)$$

Eq. 5.9 is known as the Lucas-Washburn law [122, 192]. The imbibition velocity decreases as a function of $1/\sqrt{t}$, which is typically observed when coffee is imbibed into a piece of sugar for instance. Eq. 5.9 also allows to determine the Young contact angle θ_Y for any porous material providing that the characteristic size of the pore r_t is known. The $t^{1/2}$ regime has been observed in many homogeneous porous media of unique length scale [112, 124, 177].

Now, when $t \rightarrow 0$, the imbibition velocity diverges, which is impossible. Thus, we have to consider the inertial term at very short times and balance this term with the capillary force only (since $z \rightarrow 0$). Integrating Eq. 5.8 yields [145]:

$$z = \left(\frac{2\gamma_{al} \cos \theta_Y}{\rho_l r_t} \right)^{1/2} t. \quad (5.10)$$

The imbibition velocity is constant and the inertial regime joins the Washburn regime for a characteristic time $\rho_l r_t^2 / \eta_l$, typically 10 ms to 1 s for standard micrometric and millimetric tubes and water.

Finally, for $t \rightarrow \infty$, the capillary height should reach its maximum h_{max} given by Eq. 5.3. Approximating $F_{viscous}$ by $8\pi\eta_l v_m h_{max}$ around $z = h_{max}$ yields a decreasing exponential relaxation towards h_{max} in Eq. 5.8.

The 1D model to explain imbibition into porous media is actually limited for several reasons. First, modelling a porous medium as an assembly of capillary tubes is limited as, generally speaking, a porous medium cannot be described by using a unique length scale (the tube radius). Indeed, other dynamics have also been reported: the capillary rise of water in a column of glass beads follows a $t^{1/4}$ regime for late times due to the rough surfaces of the glass beads or by a dynamical mechanism of wetting and depinning at the contact line between the invading meniscus and the solid beads [55, 112, 153, 168, 169]. Heterogeneities at a length scale much smaller than the pore size might therefore play a crucial role in the imbibition dynamics. The characteristic size of the porous medium can also vary with the height z , as observed in imbibition into corners and wedges and explained in §5.1.1.3. Last, the characteristic size of the medium can evolve with time as observed when using deformable porous media and seen in §5.1.1.4.

5.1.1.3 1D imbibition through an undeformable solid porous medium of variable pore size

This configuration is typically found for imbibition into open corners and imbibition into open wedges between two thin plates of height-dependent spacing, as sketched in Fig. 5.2.

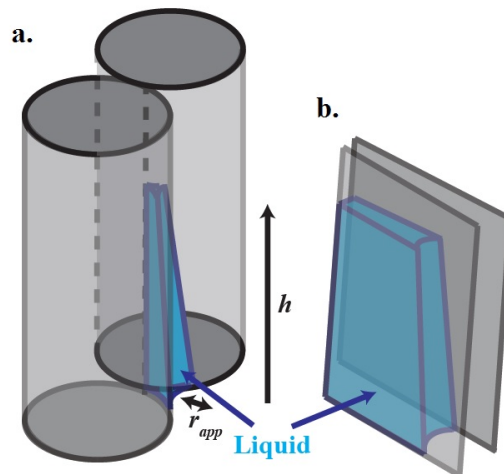


Figure 5.2: a. Imbibition in an open corner. b. Imbibition in an open wedge.

Tang et al. [178] and Ponomarenko et al. [141] have derived the imbibition dynamics in such geometries. As the imbibition height h increases, the apparent curvature radius of the meniscus

r_{app} decreases as one gets closer to the edge of the corner. When solving the dynamics by using a self-similar solution, the authors show that capillary forces are balanced by gravity, thus $r_{app} \sim \gamma_{al}/\rho_l g h$ at any position along the liquid column

The capillary rise in open corners and wedges is equivalent to the capillary rise in an undeformable tube of radius r_{app} . Replacing r_t by r_{app} in Eq. 5.9 gives the following time-dependent imbibition height:

$$h \sim \left(\frac{\gamma_{al}^2}{\rho_l g \eta_l} \right)^{1/3} t^{1/3}. \quad (5.11)$$

One can also directly use the Stokes equation $\eta_l (dh/dt)/r_{app}^2 \sim (\gamma_{al}/r_{app})/h$ to find Eq. 5.11. The dynamics in $t^{1/3}$ is slower than the diffusive Lucas-Washburn dynamics, due to the adaptability of the liquid column to the geometry of the corner or the wedge.

5.1.1.4 1D imbibition through a deformable solid porous medium

Now, what happens if the pores are deformable? Duprat et al. [62] and Cambau et al. [26] have studied this question by using flexible walls. They name the imbibition dynamics by the elastocapillary rise for a sufficiently high Bond number $Bo = \rho_l g e \ell_W / \gamma_{al}$ and high elastocapillary number $\mathcal{E}_{ec} = \gamma_{al} \ell_W^4 / B_{ec} e_W^2$ where ℓ_W , e_W and B_{ec} are, respectively, the height of the walls, the spacing between the walls where they are clamped and the bending stiffness per unit width of the wall. High Bo and \mathcal{E}_{ec} mean that capillarity and gravity are equally dominant and that the walls are very flexible.

Three different regimes are observable and depicted in Fig. 5.3.

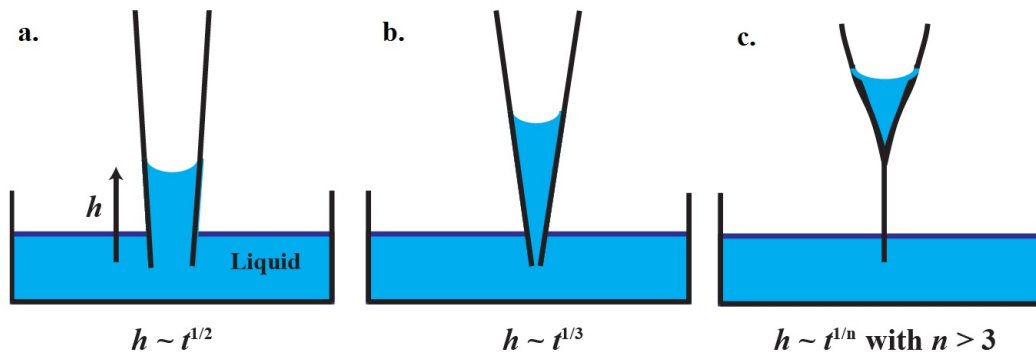


Figure 5.3: a. Diffusive Lucas-Washburn's regime. b. Wedge regime. c. Regime in a diverging channel.

At early times, the walls are slightly deflected. Gravity is negligible and capillary forces are not

important enough to pull and bend the walls. Imbibition is similar to the undeformable case. Thus, one finds the diffusive Lucas-Washburn dynamics in $h \propto t^{1/2}$ shown in §5.1.1.2. Then, when the capillary forces dominate the bending resistance of the sheets, the gap between the walls looks like a wedge and the sheets get closer at the bottom of the liquid column. Thus, the imbibition dynamics follows the $t^{1/3}$ power law defined in §5.1.1.3. The transition between the $t^{1/2}$ and the $t^{1/3}$ is defined for a height h equal to the elastocapillary length $\ell_{ec} = (B_{ec}e_W^2/\gamma_{al})^{1/4}$. For later times, the sheets touch at the bottom, which generates a new diverging geometry. Imbibition is slower in $t^{1/n}$ with $n > 3$ and gravity-dominated.

5.1.2 Liquid flow in dry aqueous foams

Imbibition in aqueous foams is a complex problem, as they encompass some of these features : evolution of pore size along the vertical axis due to gravity and deformability of channel walls. A dry aqueous foam (typically for a liquid fraction $\phi_l < 0.01$) can be assimilated to a porous medium with liquid pore walls. Indeed, a foam is a network of liquid microchannels called Plateau borders in which liquid can flow. In this section, we model the flow of liquid inside an aqueous foam with regard to common theories about flow in solid porous media. We first recall the driving pressure leading to imbibition, then we focus on modelling the flow of liquid through the foam.

5.1.2.1 Osmotic pressure and imbibition

In the case of liquid foams, the interfacial energy of a wet foam is lower than the interfacial energy of a dry foam since the bubbles are more spherical than in a dry foam. Thus, when an aqueous foam is put into contact with the same miscible liquid, liquid imbibition is driven by the reduction of interfacial energy that occurs when going from a dry to a wetter foam.

In other terms, the Plateau borders have a curvature creating a capillary underpressure in the liquid phase. For a dry foam, the pressure in the liquid phase is $p = P_b - \gamma_{aw}/r_{PB} \approx p_{atm} - \gamma_{aw}/r_{PB}$ by considering the pressure P_b in the bubbles equal to the atmospheric pressure p_{atm} (negligible overpressure in the bubbles). Due to the pressure difference with the outer environment at the atmospheric pressure, an aqueous foam has the ability to absorb liquids, similarly to a sponge.

To prevent liquid from being absorbed, a pressure Π_o called osmotic pressure in analogy with aqueous solutions has to be imposed:

$$\Pi_o = p_{atm} - p. \quad (5.12)$$

The osmotic pressure depends on the liquid fraction and this dependence has been quantified

by using a dedicated set-up with a membrane impermeable to the bubbles and permeable to the liquid only [88], as sketched in Fig. 5.4.

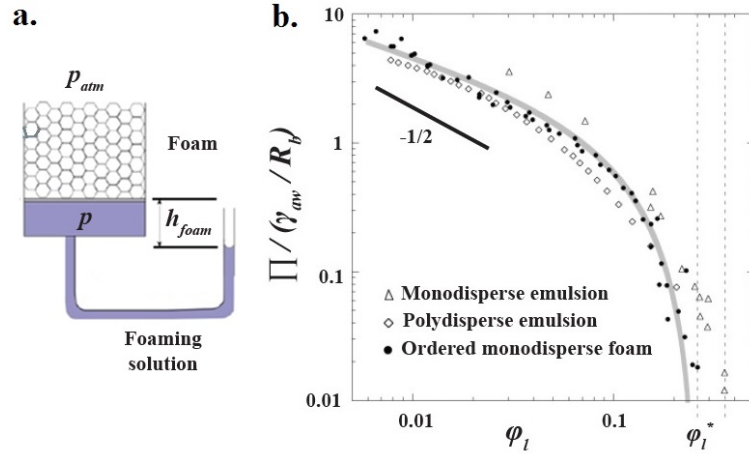


Figure 5.4: a. Osmotic cell: the pressure p in the foam is controlled by the distance h_{foam} between the membrane and the location of the meniscus in the U-tube. b. Dimensionless osmotic pressure measured from an osmotic cell as a function of the liquid fraction ϕ_l for a monodisperse, polydisperse emulsion (oil droplets in water) and an ordered monodisperse foam ($\phi_l^* = 0.26$) [88].

For dry foams, we have $\Pi_o = \gamma_{aw}/r_{PB} = \gamma_{aw}/(1.74R_b\phi_l^{1/2})$ [28]. More generally, the reduction of interfacial energy is used by the foam to pump a volume dV of liquid at the osmotic pressure Π_o . Thus, we have:

$$\Pi_o dV = -\gamma_{aw} d\Sigma, \quad d\Sigma < 0, \quad (5.13)$$

where γ_{aw} is the air-water interfacial tension and $d\Sigma$ the variation of the air-water interfacial area. However, dV is a function of the variation of liquid fraction $d\phi_l$:

$$d\phi_l = d\left(\frac{V}{V+V_g}\right) = \frac{(1-\phi_l)^2}{V_g} dV, \quad (5.14)$$

with V_g the volume of gas in the foam. Thus, Eq. 5.13 becomes:

$$\Pi_o = -\gamma_{aw} \frac{(1-\phi_l)^2}{V_g} \frac{d\Sigma}{d\phi_l}. \quad (5.15)$$

The osmotic pressure depends on the liquid fraction. The lower the liquid fraction, the higher the variation of interfacial area with the liquid fraction, the higher the osmotic pressure, the faster the imbibition process, as seen in Fig. 5.4 where data corresponding to the measurement

of the osmotic pressure as a function of ϕ_l has been reported for monodisperse and polydisperse emulsions and monodisperse foams.

5.1.2.2 Flow of liquid through a porous medium

Due to the osmotic pressure, liquid can invade a dry foam. Due to gravity, the liquid phase wants to pass below the air phase in the drainage process. In both cases, the liquid flows through the Plateau borders. How does it flow?

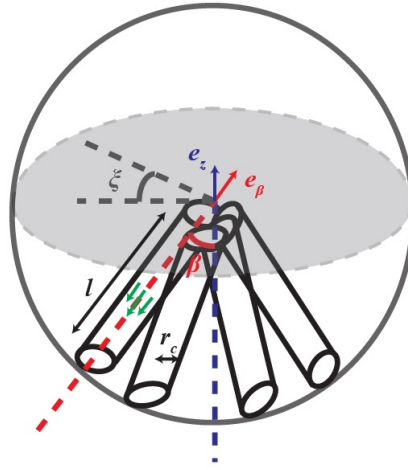


Figure 5.5: Porous model: network of cylindrical pores randomly oriented by the angle β .

We can consider the flow of liquid in a cylindrical pore, as depicted in Fig. 5.5. The velocity field \mathbf{u} of the liquid in the pore is $\mathbf{u} = u(r)\mathbf{e}_\beta$, where r is the radial coordinate in a pore. The unit vector \mathbf{e}_β is aligned with the revolution axis of the pore and directed towards the top. In this pore, the Reynolds number Re , which characterizes the dominance of inertia compared to viscous forces, is $Re = \rho_l u r_c / \eta_l$. We can estimate Re with the density $\rho_l = 1000$ g/L, the cylinder radius $r_c = 100$ μm , $\eta_l = 10^{-3}$ Pa.s and $u = 10^{-4}$ m/s, which gives $Re = 0.01 \ll 1$. Thus, we can use the Stokes equation to determine the velocity field:

$$\eta_l \Delta \mathbf{u} = \nabla p - \rho_l \mathbf{g}. \quad (5.16)$$

Projecting Eq. 5.16 on \mathbf{e}_β yields:

$$\eta_l \frac{1}{r} \frac{\partial}{\partial r} \left(r \frac{\partial u}{\partial r} \right) = \frac{dp}{dl} + \rho_l g \cos \beta. \quad (5.17)$$

Eq. 5.17 is solved into detail in Appendix A without gravity. The calculations give the mean velocity along the cross-section u_{PB} , also known as the Poiseuille law, as:

$$\mathbf{u}_{PB} = -\frac{A}{\eta_l} K_c \left(\frac{dp}{d\ell} + \rho_l g \cos \beta \right) \mathbf{e}_\beta \quad , \quad (5.18)$$

where A is the cross-sectional area of the pore and K_c the permeability coefficient. Eq. 5.18 can be generalized to a porous medium by averaging the velocity and the pressure over an elementary volume of pores. This is Darcy's law [52]. The average liquid velocity in the porous medium \mathbf{u}_{Darcy} is written as:

$$\mathbf{u}_{Darcy} = \phi_l \langle \mathbf{u}_{PB} \rangle = \frac{k_D}{\eta_l} (-\nabla p + \rho_l \mathbf{g}) \quad , \quad (5.19)$$

where $\langle \mathbf{u}_{PB} \rangle$ is the average velocity over the whole elementary volume and k_D the permeability (m^2). We can project Eq. 5.18 on the vertical direction \mathbf{e}_z , which gives:

$$u_{PB-z} = -\frac{A}{\eta_l} K_c \left(\frac{dp}{dz} + \rho_l g \right) \cos^2 \beta. \quad (5.20)$$

We can express $\langle u_{PB-z} \rangle = \int_0^{\pi/2} u_{PB-z} p(\beta) d\beta$ where $p(\beta)$ is the probability to find a pore between β and $\beta + d\beta$. This probability is equal to the ratio between the area covered by the pore between β and $\beta + d\beta$ and the area covered by the half-sphere, which gives:

$$p(\beta) d\beta = \frac{\int_0^{2\pi} \int_0^{\pi/2} \ell^2 \sin \beta d\beta d\xi}{\int_0^{2\pi} \int_0^{\pi/2} \ell^2 \sin \beta d\beta d\xi} = \frac{2\pi \ell^2 \sin \beta d\beta}{2\pi \ell^2} = \sin \beta d\beta. \quad (5.21)$$

Thus, the average vertical component of the velocity field is:

$$\langle u_{PB-z} \rangle = -\frac{A}{\eta_l} K_c \left(\frac{dp}{dz} + \rho_l g \right) \int_0^{\pi/2} \cos^2 \beta \sin \beta d\beta = -\frac{A}{\eta_l} \frac{K_c}{3} \left(\frac{dp}{dz} + \rho_l g \right). \quad (5.22)$$

Projecting Darcy's velocity \mathbf{u}_{Darcy} on the vertical direction \mathbf{e}_z from Eq. 5.19 yields:

$$\langle u_{PB-z} \rangle = \frac{u_{Darcy-z}}{\phi_l} = -\frac{k_D}{\eta_l \phi_l} \left(\frac{dp}{dz} + \rho_l g \right). \quad (5.23)$$

Identifying Eq. 5.22 and Eq. 5.23 gives:

$$k_D = \frac{A K_c \phi_l}{3}. \quad (5.24)$$

The permeability increases when the liquid fraction and the pore radius r_c increase since $A \propto r_c^2$. This is expected as bigger pores make flow easier. This relationship will be used in §5.2.

5.1.2.3 Permeability models

In the case of a dry foam for which the Plateau borders carry most of the liquid volume and have a length $\ell_{PB} \gg r_{PB}$ (their characteristic width), we can make an analogy with the solid porous media to evaluate the permeability of the foam: this is the channel-dominated model [189]. The cross-section of a Plateau border is $A = \delta_a r_{PB}^2$ with $\delta_a = \sqrt{3} - \pi/2$ and $r_{PB} = \delta_b R_b \phi_l^{1/2}$ with $\delta_b = 1.74$. Eq. 5.24 gives the permeability for a dry aqueous foam:

$$k_{foam} = \frac{\delta_a \delta_b^2 K_c}{3} R_b^2 \phi_l^2. \quad (5.25)$$

In Eq. 5.25, the coefficient K_c is unknown. For an undeformable cylindrical pore, $K_c = 1/8\pi$ (see Appendix A). However, we cannot use the same value for three major reasons. First, the structure of the foam is governed by the Plateau laws presented in §1.2.1.2. Second, the pores of the foam are liquid and deformable. Third, air-water interfaces are mobile. The bulk flow of liquid within the pores can entrain the air-water interface by tangential shear (so the boundary condition is a condition of interfacial stress and not a no-slip condition), which makes it difficult to evaluate the coefficient K_c , and thus the permeability k_{foam} .

Thus, to quantify the importance of the bulk viscous flow compared to the interfacial viscous flow, one defines the Boussinesq number $Bq = \eta_s / \eta_l r_{PB}$ where η_s is the interfacial shear viscosity and r_{PB} is the characteristic length of viscous dissipation of the bulk flow [42].

If $Bq \ll 1$, the interface is less “viscous” and offers less resistance to fluid entrainment. The interface is highly mobile and the velocity profile is a plug flow.

On the opposite, if $Bq \gg 1$, the interface offers enough resistance to the bulk flow to induce a strong velocity gradient, similar to a Poiseuille flow. Fig. 5.6 presents some typical velocity profiles in a Plateau border and the evolution of K_c with Bq . For very rigid interfaces, $Bq \rightarrow \infty$ and $K_c = 0.02$ [133].

Other permeability models exist, especially when the viscous dissipation in the vertices dominates the viscous dissipation in the Plateau borders (for big bubbles and mobile interfaces): this is the node-dominated model [106]. In this case, one has to consider the volume fraction of liquid in the vertices or nodes $V_n / (V_n + V_{PB}) = r_{PB} / (1 + \ell / r_{PB})$ with $V_n \propto r_{PB}^3$, the volume in the nodes, and $V_{PB} \propto r_{PB}^2 \ell$, the volume in the Plateau borders. For a dry foam, $r_{PB} \ll \ell$ and the

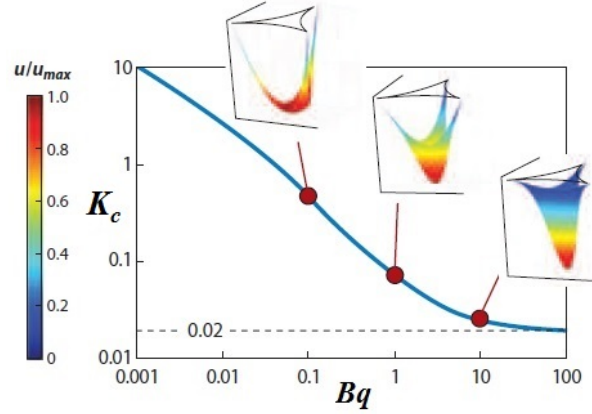


Figure 5.6: Coefficient K_c as a function of the Boussinesq number Bq for different velocity profiles [42].

volume fraction of liquid in the nodes is proportional to $\phi_l^{1/2}$. Balancing the viscous dissipation in volume in the nodes $\phi_l^{1/2} \eta_l < u_n > / r_{PB}^2$, where $< u_n >$ is the velocity across the node, by the pressure gradient in the node $\eta_l (< u_n > \phi_l) / k_n$, where k_n is the permeability in the node-dominated model, gives $k_n \propto R_b^2 \phi_l^{3/2}$.

More general models associate the dissipation in the Plateau borders and the nodes [42, 107, 121]. In the following experimental studies, we use rigid interfaces, for which $Bq \gg 1$ and $K_c = 0.02$, and we apply the channel-dominated model.

5.1.2.4 Drainage equation

For any flow of miscible liquid in a dry foam, there is a driving equation, called drainage equation, which describes the evolution of the liquid fraction ϕ_l with the time t and the spatial coordinates.

For dry foams, the osmotic pressure can be written as:

$$\Pi_o = p_{atm} - p \approx \frac{\gamma_{aw}}{r_{PB}} \approx \frac{\gamma_{aw}}{\delta_b R_b \phi_l^{1/2}}. \quad (5.26)$$

By combining Eq. 5.19, 5.26 and $k = k_{foam}$ with the unit vector \mathbf{e}_z directed upwards, we have:

$$\langle \mathbf{u}_{PB} \rangle = \frac{k_{foam}}{\eta_l \phi_l} \left(\nabla \left(\frac{\gamma_{aw}}{\delta_b R_b \phi_l^{1/2}} \right) - \rho_l g \mathbf{e}_z \right). \quad (5.27)$$

Then, we consider mass conservation in the Plateau border for the liquid phase, which is expressed as:

$$\frac{\partial \phi_l}{\partial t} + \nabla \cdot (\phi_l < \mathbf{u}_{PB} >) = 0. \quad (5.28)$$

Injecting Eq. 5.27 into Eq. 5.28 yields the comprehensive drainage equation for the liquid fraction ϕ_l :

$$\frac{\partial \phi_l}{\partial t} - \nabla \cdot \left(\frac{\gamma_{aw} k_{foam}}{2\delta_b R_b \eta_l \phi_l^{3/2}} \nabla \phi_l + \frac{k_{foam} \rho_l g}{\eta_l} \mathbf{e}_z \right) = 0. \quad (5.29)$$

Eq. 5.29 is the driving equation to study the flow of miscible liquids into a dry aqueous foam. Changing the boundary and the initial conditions changes the type of flow: flow downwards due to gravity for drainage issues, flow upwards due to the capillary underpressure for imbibition. We resort to Eq. 5.29 in the next sections §5.2 and §5.3.

5.2 Point-source imbibition from an oil-filled pore

The results presented in this section have been published in [129]. I am very grateful to Jesse T. Ault, PhD candidate at Princeton University, with whom I worked on this project.

The configuration we highlight in this section is the imbibition from a point-source, which requires to build a 3D model. Not surprisingly, imbibition for undeformable and deformable solid porous media in 2 and 3 dimensions have also been studied [126, 201]. Similar developments can be made for imbibition of dimensions in aqueous foams. In our case, we try to mimic the liquid extraction from a micropore. We develop a mathematical model and compare with experimental results for the radial imbibition from a point source (at imposed pressure). Also, we develop a model to explain why the imbibition of oil is possible in some cases despite the creation of new oil-water interfaces.

5.2.1 3D imbibition from a point-source for miscible liquids

We focus on a particular geometry where a point-source filled with liquid - immiscible with the foam or not - is placed below a dry foam. We recall the foam drainage equation [105, 188, 189], which describes foam imbibition and drainage. We make the following assumptions:

- We consider a dry foam with a constant mean bubble radius R_b and a low liquid fraction $\phi_w < 5 \times 10^{-3}$,
- The size of the point source is much smaller than the typical dimensions of the foam and the foam domain can be considered as an infinite space for imbibition,

- We assume isotropy of the foam. We use cylindrical coordinates (radial coordinate r and axial coordinate z).

5.2.1.1 Differential equation for the cross-sectional area A of a Plateau border

Like in §5.3, we consider rigid interfaces in the foam and use a channel-dominated model for the foam permeability k_{foam} [28, 42, 107, 132, 133]:

$$k_{foam} = \frac{\delta_a \delta_b^2 R_b^2 \phi_w^2}{150} \quad , \quad (5.30)$$

with ϕ_w the liquid fraction of water, $\delta_a = \sqrt{3} - \pi/2$, a numerical factor deduced from the cross-sectional area of a Plateau border $A = \delta_a r_{PB}^2$, and $\delta_b = 1.74$.

Combining Eq. 5.29 and Eq. 5.30 yields the time-space dependence of the liquid fraction ϕ_w :

$$\frac{\partial \phi_w}{\partial t} = \nabla \cdot \left(\frac{\gamma_{aw} \delta_a \delta_b R_b}{300 \eta_w} \phi_w^{1/2} \nabla \phi_w + \frac{\delta_a \delta_b^2 R_b^2 \rho_w g}{150 \eta_w} \phi_w^2 \mathbf{e}_z \right). \quad (5.31)$$

From Eq. 5.31, and $\phi_w = A/(\delta_a \delta_b^2 R_b^2)$, we deduce a non-linear partial differential equation for the time-space evolution of the cross-sectional area of a Plateau border [105]:

$$\frac{\partial A}{\partial t} = \frac{\gamma_{aw} \delta_a^{1/2}}{300 \eta_w} \nabla \cdot (A^{1/2} \nabla A) + \frac{\rho_w g}{150 \eta_w} \frac{\partial A^2}{\partial z}. \quad (5.32)$$

For the initial condition, we assume that the foam is dry, $\phi_w = 0$. For the boundary conditions, we assume that the liquid fraction and thus the cross-sectional area of a Plateau border far from the point-source is close to 0. At the point-source, $A = \delta_a R_b^2$, which is the cross-sectional area for the maximum packing of undeformed bubbles. Thus, we have the initial and boundary conditions:

$$\begin{aligned} A(r > 0, z > 0, 0) &= 0 & , & & A(r, z \rightarrow +\infty, t) &= 0 & , \\ A(r \rightarrow +\infty, z, t) &= 0 & , & & A(0, 0, t) &= \delta_a R_b^2 & , \end{aligned} \quad (5.33)$$

and the no-flux condition at $z = 0$: $\frac{\partial A}{\partial z} = -\frac{2\rho_w g}{\delta_a^{1/2} \gamma_{aw}} A^{3/2}$.

The no-flux condition is deduced from $\mathbf{u}_{Darcy} \cdot \mathbf{e}_z = \frac{\partial}{\partial z} \left(\frac{\gamma_{aw} \delta_a^{1/2}}{A^{1/2}} \right) - \rho_w g = 0$.

5.2.1.2 Solution to the partial differential equation (PDE)

We non-dimensionalize A , r , z and t as $\alpha = A/(\delta_a R_b^2)$, $R = r/R_b$, $Z = z/R_b$ and $\tau = (\delta_a/150)t/(\eta_w R_b/\gamma_{aw})$, and introduce the Bond number $Bo = \rho_w g R_b^2/\gamma_{aw}$, transforming Eq.

5.32 into:

$$\frac{\partial \alpha}{\partial \tau} = Bo \frac{\partial \alpha^2}{\partial Z} + \frac{1}{2} \left(\frac{1}{R} \frac{\partial}{\partial R} \left(R \alpha^{1/2} \frac{\partial \alpha}{\partial R} \right) + \frac{\partial}{\partial Z} \left(\alpha^{1/2} \frac{\partial \alpha}{\partial Z} \right) \right) , \quad (5.34)$$

with the initial and boundary conditions:

$$\begin{aligned} \alpha(R > 0, Z > 0, 0) &= 0 & , & & \alpha(R, Z \rightarrow +\infty, \tau) &= 0 & , \\ \alpha(R \rightarrow +\infty, Z, \tau) &= 0 & , & & \alpha(0, 0, \tau) &= 1 & , \end{aligned} \quad (5.35)$$

and the no-flux condition in $Z = 0$: $\frac{\partial \alpha}{\partial Z} = -2Bo\alpha^{3/2}$.

To solve Eq. 5.34 with the conditions 5.35, we use a discretization by finite differences on a 2D spatial mesh and solve the PDE with Matlab. The numerical solution gives $\alpha(R, Z, \tau)$, as shown in Fig. 5.7a. The front position is determined when $\alpha = 0$ as α decreases from the point source to the outer boundary of the mesh, which gives the front profile for different times and Bond numbers (Fig. 5.7b-d). The simulations show that the front profile flattens out as Bo and τ increase.

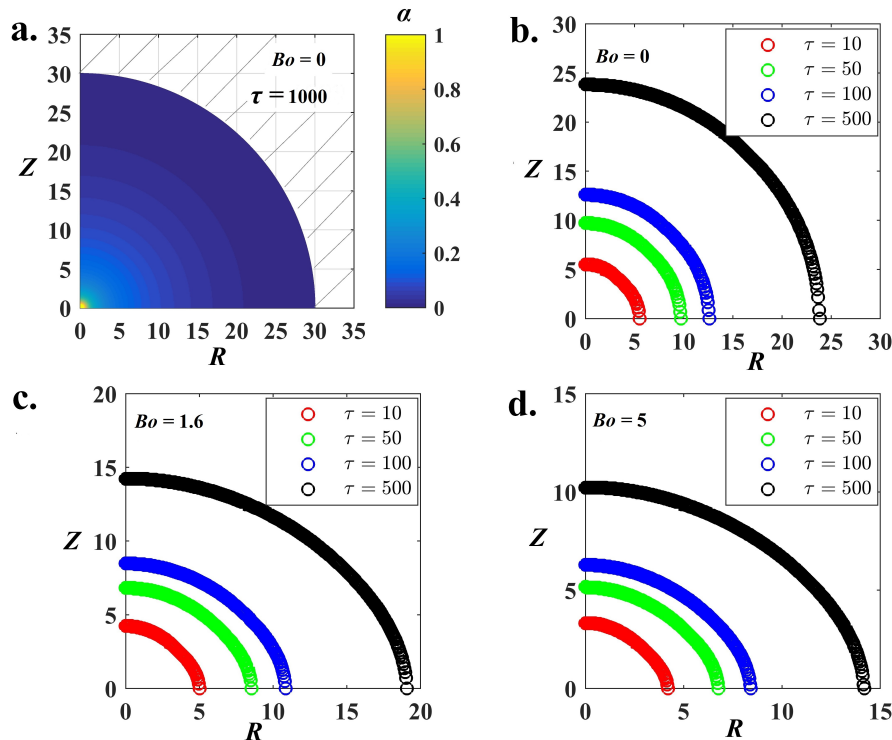


Figure 5.7: a. Typical numerical solution of Eq. 5.34 for the dimensionless Plateau border area α for $Bo = 0$ and $\tau = 1000$. b-d. Numerical solutions of the imbibition front for different times $\tau = 10, 50, 100$ and 500 with Bond numbers $Bo = 0, 1.6$ and 5 .

5.2.2 3D imbibition from a point-source for immiscible liquids

Now, let us describe the imbibition of immiscible liquids and the differences with miscible liquids.

5.2.2.1 Local picture of oil invasion

When a dry aqueous foam is wetted by a miscible liquid, the physical mechanism that enables the imbibition is the reduction of the surface area of the air-water interfaces inside the foam, i.e. the total energy of the system decreases [88]. The liquid flow swells the Plateau borders, creating more surface area. However, if we assume a constant volume of gas in the bubbles, the surface area of the films needs to decrease.

The reduction of interfacial energy is used by the foam to pump a volume dV of liquid at the osmotic pressure $\Pi_o = p_{atm} - p$. Thus, we have $\Pi_o dV = -\gamma d\Sigma$ (with $d\Sigma < 0$) where γ is the interfacial tension, $d\Sigma = dS_f + dS_{PB}$ is the variation of the air-water area, and S_f and S_{PB} are the film and Plateau border area, respectively (Fig. 5.8a).

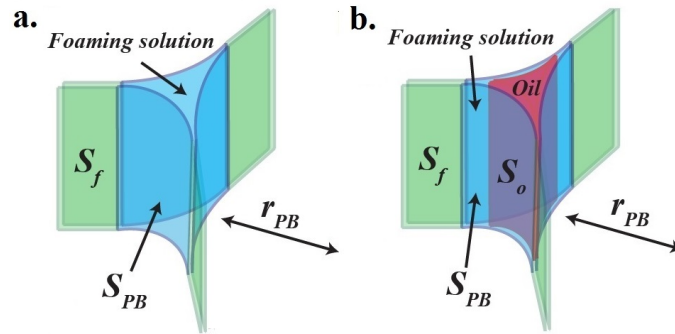


Figure 5.8: a. Cross-section of a Plateau border for a dry aqueous foam. b. Cross-section of a Plateau border filled with oil for a dry aqueous foam. S_{PB} and S_f , respectively, denote the areas of the side surfaces of the Plateau borders and the surface of the films that are connected to the Plateau borders. S_o represents the area of the oil-water interfaces.

For miscible liquids, the decrease of interfacial energy drives the imbibition into a dry aqueous foam. For immiscible liquids, such as organic oils, we sketch the liquid flow (in the dry limit) by an oil slug that penetrates the Plateau border, as shown in Fig. 5.8b; new air-water surfaces in the Plateau border are created and the surface area of the films decreases. However, new oil-water interfaces are also created, which are energetically costly. Therefore, we develop another model to add the influence of these oil-water interfaces.

5.2.2.2 Effective interfacial tension

Rewriting the osmotic pressure by using the interfaces dS_w and dS_o for the variations of the air-water and oil-water interfaces, respectively, yields:

$$\begin{aligned} \Pi_o dV &= -(\gamma_{aw} dS_w + \gamma_{ow} dS_o) \quad , \\ \text{with } dS_w &< 0 \quad \text{and} \quad dS_o > 0. \end{aligned} \quad (5.36)$$

Eq. 5.36 can also be expressed as:

$$\Pi_o dV = -\gamma_{aw} dS_w \left(1 + \frac{\gamma_{ow}}{\gamma_{aw}} \frac{dS_o}{dS_w} \right) = -\gamma_{eff} dS_w \quad , \quad (5.37)$$

with γ_{eff} an effective interfacial tension:

$$\gamma_{eff} = \gamma_{aw} \left(1 + \frac{\gamma_{ow}}{\gamma_{aw}} \frac{dS_o}{dS_w} \right). \quad (5.38)$$

For miscible liquids, $\gamma_{ow} = 0$, so $\gamma_{eff} = \gamma_{aw}$ and the osmotic pressure is related to the curvature of the Plateau borders by $\Pi_o \approx \gamma_{aw}/r_{PB}$. However, if $\gamma_{ow} \neq 0$, then γ_{eff} accounts for the oil-water interfacial tension and the creation of oil-water interfaces. The osmotic pressure becomes $\Pi_o = \gamma_{eff}/r_{PB} \approx \gamma_{eff}/(\delta_b R_b \phi_{ow}^{1/2})$ where ϕ_{ow} is the combined liquid fraction for oil and water. Since $dS_w < 0$, then $\gamma_{eff} < \gamma_{aw}$. With immiscible liquids, the osmotic pressure is reduced compared to miscible liquids, i.e., the driving force for imbibition is weaker. The value of γ_{eff} can be estimated. In particular, the variation of the air-water interfaces dS_w can be decomposed into two contributions, one from the films dS_f , and the other from the Plateau borders dS_{PB} (Fig. 5.8b).

Pitois et al. [139] and Hilgenfeldt et al. [89] provide estimates of the film and Plateau border surface areas with regard to the liquid fraction in the foam:

$$S_f \approx \frac{3.3}{R_b} V_{foam} (1 - \phi_{ow}) (1 - 1.52 \phi_{ow}^{1/2})^2 \quad , \quad (5.39a)$$

$$S_{PB} \approx \frac{V_{foam}}{1.5 R_b} \left(\frac{\pi}{\sqrt{3} \delta_a} \right) \phi_{ow}^{1/2} \quad , \quad (5.39b)$$

where V_{foam} is the volume of foam. Differentiating S_f and S_{PB} with respect to ϕ_{ow} in the dry limit yields:

$$dS_f \approx -\frac{V_{foam}}{R_b} \frac{(3.3)(3.04)}{2\phi_{ow}^{1/2}} d\phi_{ow} \quad , \quad (5.40a)$$

$$dS_{PB} \approx \frac{V_{foam}}{R_b} \frac{\pi}{3\sqrt{3}\delta_a\phi_{ow}^{1/2}} d\phi_{ow}. \quad (5.40b)$$

In the dry limit, we can assume as a first approximation that $dS_o \approx dS_{PB}$ and neglect the oil-water interface at the top of the oil slug (Fig. 5.8b). This assumption is in agreement with recent *Surface Evolver* simulations of the shape of an oil slug in a single Plateau border [132]. In our case, the ratio $\gamma_{ow}/\gamma_{aw} \approx 0.2$ is low and the ratio between the equivalent spherical radius for an oil slug embedded within the Plateau border and the radius of curvature of the Plateau border is close to 1 due to the very low liquid fraction. Thus, by using (5.40a) and (5.40b), we have:

$$\gamma_{eff} \approx \gamma_{aw} + \gamma_{ow} \frac{dS_{PB}}{dS_f + dS_{PB}} \approx \gamma_{aw} \left(1 - 3 \frac{\gamma_{ow}}{\gamma_{aw}} \right). \quad (5.41)$$

5.2.2.3 Driving equation for immiscible liquids

With this effective interfacial tension, the osmotic pressure is reduced by a factor that depends on the ratio between the oil-water and the air-water interfacial tensions. More precisely, the governing equation for A is the same as developed previously for aqueous liquids in (5.32) with A , the cross-sectional area of the Plateau border for both oil and water phases, γ_{eff} , instead of γ_{aw} , and η_o the oil viscosity:

$$\frac{\partial A}{\partial t} = \frac{\gamma_{eff}\delta_a^{1/2}}{300\eta_o} \nabla \cdot (A^{1/2} \nabla A) + \frac{\rho_o g}{150\eta_o} \frac{\partial A^2}{\partial z}. \quad (5.42)$$

We only use η_o because the viscous dissipation occurs predominantly in the oil phase as shown by Piroird et al. [137] in the limit of $\eta_o/\eta_w \gg 1$. Eq. 5.42 is identical to Eq. 5.32 and can be solved numerically, except with a smaller air-water interfacial tension. The smaller capillary pressure induced by the oil phase is in agreement with our imbibition experiments presented in the following: for the same elapsed time, the vertical front position of the oil is smaller than the aqueous case, as shown in Fig. 5.11.

5.2.3 Experimental imbibition front

Here, we present the imbibition experiments that we compare to the aforementioned theoretical developments. Most of the chemicals used in this section are similar to the chemicals presented in §2.3.1, as well as the generation of the foam.

5.2.3.1 Experimental set-up

The foaming solution we use is described in [9, 81, 137] and consists in a mixture of different components (cocoamidopropyl betaine, sodiumlaurylethyl sulfate, myristic acid and glycerol), already presented in §1.1.3 and §2.3. It provides rigid boundary conditions to the air-water interfaces due to the presence of the fatty myristic acid [9, 81]. The air-water interfacial tension, viscosity and density of this mixture are, respectively, $\gamma_{aw} = 23.7 \pm 1$ mN/m, $\eta_l = 1.4$ mPa.s and $\rho_l = 1026$ kg/m³.

As imbibing liquids, we use olive oil and two glycerol solution mixtures, whose wt.% of glycerol are different; the properties (oil-water surface tension, dynamic viscosity, density) are summarised in Table 5.1. We also add a small quantity of fluorescent dyes (1:50) to the imbibing liquid (Yellow Black from Rohm and Haas, Fluorescein from Sigma-Aldrich and Tracerline) to enhance the contrast between the foam and the imbibing liquid. We checked that the addition of dyes does not change the value of γ_{ow} .

Imbibing liquid	γ_{ow}	η	ρ	R_b	B
CAPB+SLES MAc+80% gly	0	64	1.21	1	0.5
CAPB+SLES MAc+65% gly	0	15	1.17	2	1.8
CAPB+SLES MAc+10% gly	0	1.4	1.016	2	1.7
Olive oil 1	6	61	0.88	1	1.5
Olive oil 2	6.2	68.5	0.88	2	5
Sunflower oil	4.5	55	0.91	2	3

Table 5.1: Characteristics of the imbibing liquids and foaming solution. γ_{ow} (mN/m) is the oil-water interfacial tension, η (mPa.s) the dynamic viscosity, ρ (g/cm³) the density, R_b (mm) the average bubble radius of the foam and B the Bond number defined in (5.34).

We generate foams with a well-controlled average bubble radius $R_b = 1 - 2$ mm by injecting nitrogen or compressed air through a needle into the foaming solution by the same procedure presented in §2.3.1. The rigid interfaces owing to the type of surfactants used yield a stable, monodisperse foam (deviations from the mean bubble radius remain below 5 %). After generating the foam in a 20 cm-high rectangular column with a 4.5 cm-wide square base, we let it drain and extract at random times at the top of the column a foam sample for which the volume V_{foam} and the weight m_{foam} are known. The sample is turned upside down to invert the drainage process. The initial liquid fraction of the foam sample is deduced from $\phi_i = m_{foam}/(\rho_w V_{foam})$, where ρ_w

is the density of the foaming solution.

For the imbibing reservoir, we use a polycarbonate plate into which a 1 mm-wide hole is drilled. A small capillary tube of 1 mm diameter is inserted into the hole and slightly displaced upwards into the foam to ensure complete contact between the foam and the reservoir. This capillary tube is connected to a 20 cm-long and a 2 mm-diameter PTFE tube (Fig. 5.9). This set of tubes is filled with the imbibing liquids, which completely wet the tubes. The bigger tube is attached to a motion controller that allows the adjustment of the input liquid level at the same height as the output liquid level while the liquid flows through the foam.

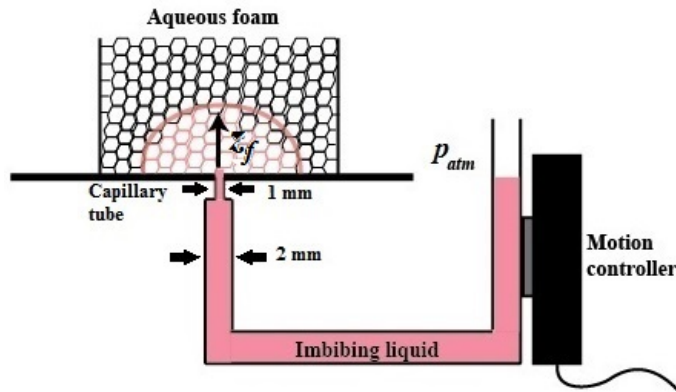


Figure 5.9: Experimental set-up. A 30 cm-long PTFE tube (2 mm-diameter) is filled with the imbibing liquid (mixtures of foaming solution-glycerol or oil) and terminated by a 1 cm-long capillary tube (1 mm diameter) that enables the connection with the foam. A motion controller allows maintenance of the pressure of the liquid phase input at atmospheric pressure p_{atm} .

This system sets a constant atmospheric pressure p_{atm} at the outlet of the capillary tube. We also use another system without feedback for comparison, by using a 5 cm-wide funnel for which the output level does not vary much when the liquid is imbibed. Both systems give the same results as shown below.

5.2.3.2 Imbibition picture

At time $t = 0$, the bottom of the foam touches the point source of the liquid. We record (at 24 frames per second for 3 to 4 minutes) foam imbibition by using fluorescent imaging. Fig. 5.10 shows a typical image sequence of the imbibition process.

The same experiment is repeated for the different imbibing liquids of Table 5.1. Thus, different liquids, different viscosities η , bubble radii R_b , air-water (γ_{aw}) and oil-water (γ_{ow}) interfacial ten-

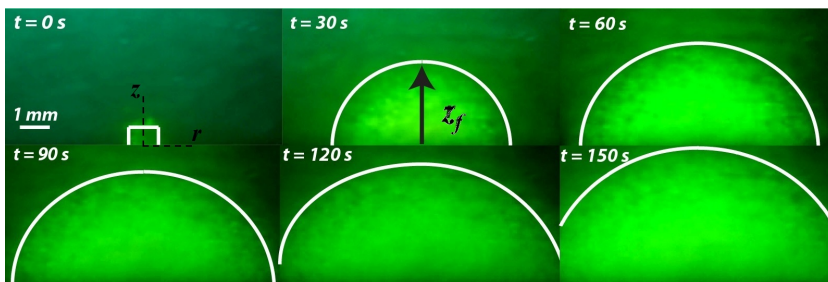


Figure 5.10: Snapshots of the imbibition front for a 30-second timescale. The imbibing liquid (glycerol-foaming solution) is fluorescent and the front is defined as the boundary between the brighter and darker fluorescent areas. The liquid-filled tube is displaced upwards by a millimeter in the first snapshot to ensure contact between the source and the foam.

sions, and initial liquid fractions ϕ_i are tested. We determine the imbibition front by applying a threshold at the boundary between the brighter and darker fluorescent areas. Using ImageJ software for image processing, we plot the maximum vertical position z_f with respect to time.

5.2.3.3 Time-dependence of the imbibition front

Fig. 5.11 shows two data sets for the evolution of the vertical front position $z_f(t)$. The experimental data for two different liquids typically have error bars of ± 0.5 mm, owing to the determination of the front, especially in the case of miscible liquids, where light diffusion by the films can create a small front width. For both types of liquid, the position of the front moves faster at short times and slows down as time increases. For similar viscosities, oil imbibition is slower than aqueous imbibition.

5.2.4 Comparison with experimental results

We now build a single comparison between the theory for miscible and immiscible liquids and make some remarks on the resolution of the PDE.

5.2.4.1 Collapse of the theory with the experiments

In Fig. 5.12, we rescale z_f by R_b and t by the capillary time $(150/\delta_a)\eta_{o/w}R_b/\gamma_{eff}$, which is the same scaling as in Eq. 5.34 written with γ_{eff} instead of γ_{aw} , and the viscosity of oil or aqueous solutions $\eta_{o/w}$. The log-log plot in the dimensionless variables displays a reasonable collapse between the experimental data and the numerical solution for all miscible and immiscible

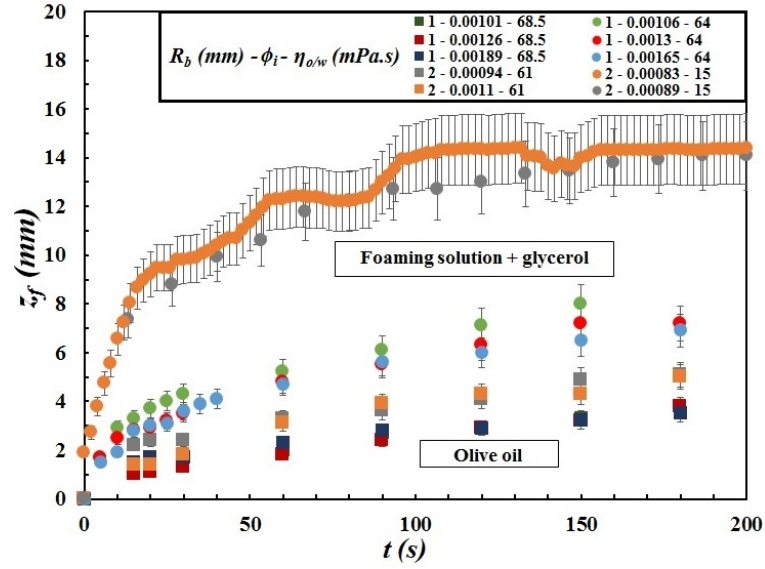


Figure 5.11: Evolution of the vertical front position z_f with respect to time t for two data sets. The round dots correspond to a glycerol-foaming solution and the square dots to olive oil. The bubble radius R_b , the initial liquid fraction ϕ_i , and the viscosity $\eta_{o/w}$ of the imbimbing oil or aqueous solution are indicated, respectively, in the legend.

imbibing liquids for the range of non-zero Bond numbers between 0.5 and 5. The collapse occurs at shorter τ for immiscible liquids, due to the smaller scaling in time induced by γ_{eff} .

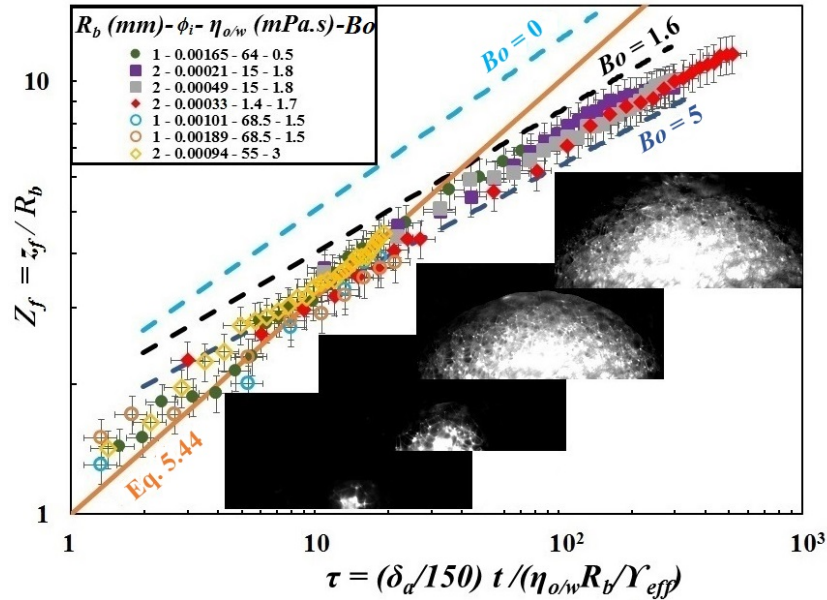


Figure 5.12: Vertical front position z_f with respect to time in dimensionless coordinates for immiscible oils (open dots) and miscible aqueous liquids (closed dots). The experimental curves are obtained for two $R_b = 1$ and 2 mm, different ϕ_i , $\eta_{o/w}$ and Bo . The numerical solutions of Eq. 5.34 for Bond numbers $Bo = 0$, 1.6 and 5 , deduced from Eq. 5.34, are plotted by the dashed lines. The self-similar power law evolution in $\tau^{1/2}$ in the no-gravity case (Eq. 5.44) is shown.

In both miscible and immiscible cases, the numerical solutions that include the capillary pressure gradient and gravity are comparable to the experimental data. The numerical solution with $Bo = 0$ largely deviates from the experimental data: gravitational effects flatten out the imbibition profiles very quickly as shown in Fig. 5.7. However, our numerical solution also deviates from the data at short times. Indeed when the front position is of the order of magnitude of one bubble size ($R^* < 2$), the Darcy model for the average velocity is not adequate, as imbibition occurs in individual Plateau borders. Also, $\phi_{ow} \neq 0$ around the point source.

The discrepancy between the numerical solution at $Bo = 0$ and the experimental data demonstrate that gravitational effects are comparable to the capillary pressure. Yet, our result differs from the $t^{1/3}$ power law developed by Xiao et al. [201] for radial imbibition in undeformable porous media with a constant permeability k_D . We account for the deformability of the Plateau borders (time variations and non-constant k_D) and the slope of the numerical solution depends on Bo in Fig. 5.12, which produces a non-constant power law from one Bond number to another. We assume that viscous dissipation occurs in the Plateau borders and adopt a channel-dominated model for the liquid flow through the foam. Also, we consider gravity effects, which are neglected in [201], since $Bo \ll 1$ due to the micron size of the glass beads in their porous matrix.

5.2.4.2 Analytical solution with $Bo = 0$

An analytical scaling for the front position in the no-gravity case ($Bo = 0$), which is encountered in microgravity conditions, can be found by assuming spherical symmetry with the dimensionless spherical distance \tilde{R} . We introduce the dimensionless self-similar variable $\zeta = \tilde{R}/\tau^{1/2}$. Substituting ζ into Eq. 5.34, written with γ_{eff} and $\eta_{o/w}$, we find that α is the solution of the ordinary differential equation:

$$\zeta^3 \frac{d\alpha}{d\zeta} + \frac{d}{d\zeta} \left(\zeta^2 \alpha^{1/2} \frac{d\alpha}{d\zeta} \right) = 0. \quad (5.43)$$

The first boundary condition is $\alpha(\zeta_f) = 0$, where $\zeta_f = \left(\frac{150\eta_{o/w}}{\gamma_{eff}\delta_\alpha R_b} \right)^{1/2} \frac{r_f}{t^{1/2}}$ is a constant which then yields the spherical front radius $r_f(t)$. A local analysis at the front provides a second boundary condition and uniquely determines the solution.

Setting $\zeta_f^4 \alpha^* = \alpha$ yields the same equation as (5.43) except with $\zeta_f = 1$. Therefore, we can take $\zeta_f = 1$ without loss of generality. The wetting front r_f is given by:

$$\frac{r_f(t)}{R_b} = \left(\frac{\delta_\alpha \gamma_{eff}}{150\eta_{o/w} R_b} t \right)^{1/2}. \quad (5.44)$$

This solution is plotted in Fig. 5.12. The $t^{1/2}$ power law result recalls the 1D diffusive imbibition in a Hele-Shaw cell observed in [29, 160]. However, the collapse between the PDE solution with $Bo = 0$ and the self-similar solution in $t^{1/2}$ occurs at long times for $\tau > 10^4$. Indeed, the solution to Eq. 5.43 has a singularity at the point source, where α diverges to $+\infty$ [38]. However, the solution to Eq. 5.34 has a finite boundary condition $\alpha = 1$ at the point source. Furthermore, the point source has the finite size of the inlet tip (half a bubble radius). Thus, the introduction of a source value and a length scale at the origin causes the lack of agreement between the PDE solution and the $t^{1/2}$ power law. Given sufficient time (beyond our experimental time) to lose the effect of the initial and boundary conditions, which is a classical condition in self-similar solutions enclosed in the structure of the solution itself, the collapse of both solutions should occur. The observed good agreement between experiments and the gravity-free analytical solution at short times is thus only a coincidence as this solution is only valid for $R^* > 2$. Moreover, due to the values of the Bond numbers from 0.5 to 5, the diffusive solution (and thus the no-gravity approximation) is not valid over our experimental range.

5.3 Capillary rise into aqueous foams for miscible and immiscible liquids

This study has been published in [128] and was presented at the *Eufoam 2014* and the *CMD 2014* conferences.

In §5.2, we have studied the 3D point-source imbibition into dry aqueous foams from an oil-filled pore for miscible and immiscible liquids. Here, we consider the 1D imbibition of an oil slick into an aqueous foam. This situation can be encountered when one would like to clean a surface where oil has been spilled or a surface polluted by an environmental catastrophe, such as black tides. In some sense, the oil slick can be considered as a multitude of small point-sources which converge towards each other to create a uniform 1D imbibition front. We can also notice that other configurations have also been studied theoretically and experimentally: pulsed imbibition at constant volumes and 2D foam drainage at constant flow rate [47, 93, 105, 108].

In this section, we experimentally study the 1D imbibition dynamics of miscible and immiscible liquids into a dry aqueous foam. The configuration is an aqueous or an oil slick absorbed into the foam. Our experimental set-up is the one used for the testing experiments in §2.3. We raise questions about the dynamics of imbibition in this geometry and compare our observations in the framework previously developed for the 3D imbibition from a point-source.

5.3.1 Oil absorption: characteristics and picture

The foaming solution is the CAPB-SLES-Mac-10% glycerol used in 5.2 and described in [9, 81, 137].

The characteristics of the imbibing liquids are summarized in Table 5.1 while the miscible liquids with a viscosity η_w ranging from 1.4 to 100 mPa.s are obtained by adding glycerol to the foaming solution. With our foaming solution and organic oils, such as olive oil or sunflower oil, both E and S exhibit negative values, as shown in Tab. 5.1. The viscosity η_o and the density ρ_o of the two oils are also displayed in Tab. 5.1. As in §5.2, after generation, we let the foam drain. During this drainage period, we extract the driest upper part of the foam at different times. Then, we reverse the foam sample to make the liquid fraction homogeneous and stop the drainage process in the sample. The volume V_{foam} and the mass m_{foam} of the sample are measured using a precision weighing scale. We deduce ϕ_i the liquid fraction of the sample from $\phi_i = m_{foam}/V_{foam}\rho_w$. Each time corresponds to a specific liquid fraction and typically $0.7 \times 10^{-4} < \phi_i < 1.2 \times 10^{-3}$. With this set-up, we can therefore vary independently ϕ_i and R_b . We also obtain the curvature radius of the Plateau border $r_{PB} = 1.74\phi_i^{1/2}R_b$ between 15 and 85 μm (see Fig. 5.13), in the limit where $\phi_i < 10^{-2}$.

Given that the contrast of optical indexes between the foam and the liquid is small or null, we still add a small quantity of liquid fluorescent dye to the imbibing liquid at a concentration of 10^{-2} g/g (fluorescein from Sigma-Aldrich for aqueous solutions and Yellow Black from Rohm and Haas for organic oils). Those fluorescent markers, which are trapped in the liquid, provide a means of visualizing the swollen part of the foam [138]. With this set-up and under illumination with excitation at 488 nm, the liquid is luminous while the aqueous foam - only constituted of air and foaming solution - is not visible. The fluorescence intensity is followed with a camera (AVT Marlin) recording at typically 6 frames per second.

Fig. 5.13 illustrates such an experiment where a dry dark foam is put into contact with a 20 μL fluorescent oil drop sitting on a solid surface. We first observe a lateral spreading of the oil drop, squeezed between the solid surface and the foam. Yet, after ten seconds, oil wicks into the foam, revealing the foam architecture and forming a complex oil-laden foam structure. After 5 minutes, oil has risen in the foam up to a height $h = 10$ mm. The foam film withstands without any problem the oil invasion: we barely observe any film break-up during the whole process. This suggests that the imbibition only occurs within the Plateau borders and the nodes and does not interfere with the fragile structure of the foam films as previously observed at the scale of a single Plateau border [137]. Yet, the structure of this oil-laden foam is not frozen: elementary

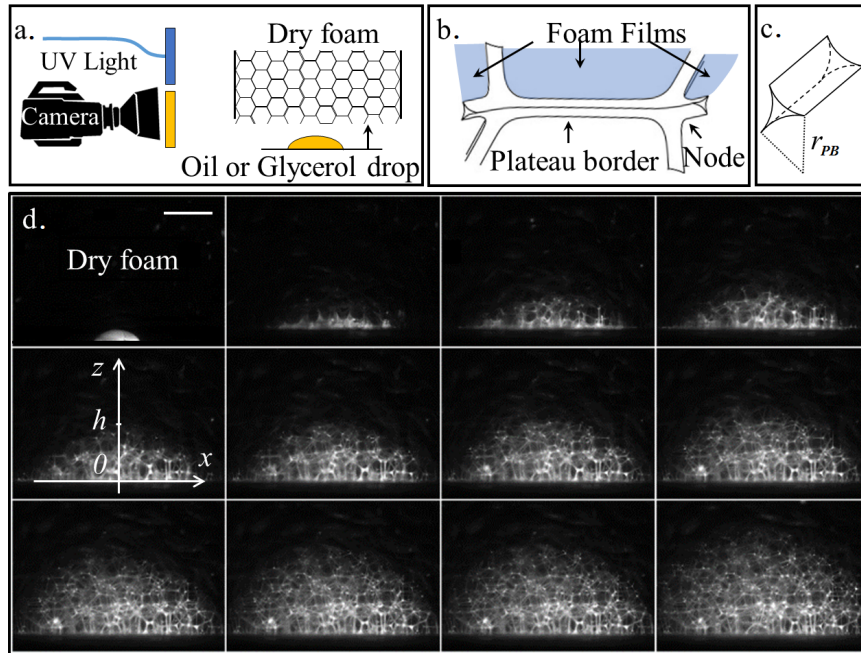


Figure 5.13: a. Experimental set-up. b. Geometrical elements of foams: vertices, Plateau borders and foam films. c. Slender Plateau border with a radius of curvature r_{PB} . d. Capillary rise of oil in a dry aqueous foam. The olive oil drop appears white thanks to a fluorescent dye and invades the network of Plateau borders. The time interval between each frame is 67 s. The scale bar is 3 mm.

topological changes known as T1 are frequently observed due to liquid redistribution [138].

5.3.2 Theoretical analysis

We present here the theoretical analysis by comparison with the drainage theory and the determination of a scaling law for the imbibition dynamics.

5.3.2.1 Time-dependent imbibition front

Our fluorescent set-up allows us to measure h , the upper boundary of the imbibition front in the foam as defined in the fifth frame of Fig. 5.13. Fig. 5.14 shows h as a function of time t , when a 20 μL olive oil drop is put into contact with foams at various liquid fractions. As classically observed in porous media, the early times dynamics is fast. Moreover, here, the drier the foam, the faster the early-time dynamics, a feature which underlines the importance of the liquid fraction of the foam prior to imbibition. When plotted in log-log scale, those curves do not exhibit a well-defined power law as it can be seen on the inset of Fig. 5.14. The data are well fitted by two different straight lines of different slopes corresponding to the $t^{1/2}$ early and

$t^{1/4}$ late-time dynamics. We also emphasize that for the driest foam, the front velocity is small: typically, $\dot{h} \sim 0.2$ mm/s at $t = 10$ s. Note that the imbibition of glycerol and sunflower oil exhibit the same trends.

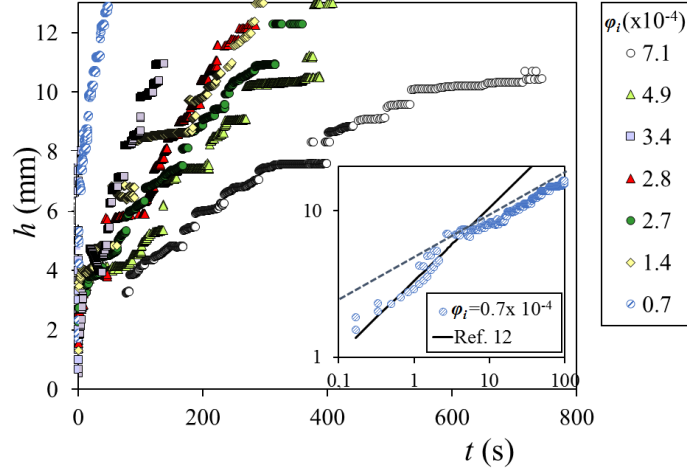


Figure 5.14: Height of the rising front for olive oil as a function of time for different initial liquid fractions and one mean bubble radius $R_b = 1.8$ mm. Inset: log-log scale of the data corresponding to $\phi_i = 0.7 \times 10^{-4}$. The plain line corresponds to the $t^{1/2}$ dynamics detailed in [29], while the dashed line illustrates the $t^{1/4}$ dynamics.

5.3.2.2 Comparison with the drainage theory

Foam drainage theory provides different scaling laws for foam imbibition, which can be confronted to our results. The foam drainage equations allow to study the time-space evolution of the liquid fractions for different configurations: free drainage (when a foam drains due to gravity), pulsed and forced drainage (when liquid is injected into a foam at constant volume and flow rate respectively). In particular, the diffusive regime of imbibition observed under microgravity conditions [29, 160] is in very good agreement with our data as it can be seen in the inset of Fig. 5.14 for very short times, thus underlining the negligible role of gravity when the foam is wet at the bottom.

We can write the drainage equation Eq. 5.45 with the permeability $k_{foam} = \delta_a \delta_b^2 R_b^2 K_c \phi_l^2 / 3$ in the channel-dominated model and the effective interfacial tension γ_{eff} found in §5.2:

$$\frac{\partial \phi_l}{\partial t} - \nabla \cdot \left(\frac{\gamma_{eff} \delta_a \delta_b R_b K_c \phi_l^{1/2}}{6\eta_l} \nabla \phi_l + \frac{\delta_a \delta_b^2 R_b^2 K_c \phi_l^2 \rho_l g}{3\eta_l} \mathbf{e}_z \right) = 0. \quad (5.45)$$

Projecting Eq. 5.45 on e_z yields:

$$\frac{\partial \phi_l}{\partial t} - \frac{\delta_a \delta_b R_b K_c}{3\eta_l} \frac{\partial}{\partial z} \left(\frac{\gamma_{eff} \phi_l^{1/2}}{2} \frac{\partial \phi_l}{\partial z} + \delta_b R_b \phi_l^2 \rho_l g \right) = 0. \quad (5.46)$$

We can rewrite Eq. 5.46 by replacing ϕ_l by the cross-sectional area $A = \delta_a \delta_b^2 R_b^2 \phi_l$, which gives:

$$\frac{\partial A}{\partial t} - \frac{\gamma_{eff} \delta_a^{1/2} K_c}{6\eta_l} \frac{\partial}{\partial z} \left(A^{1/2} \frac{\partial A}{\partial z} \right) - \frac{\rho_l g K_c}{3\eta_l} \frac{\partial A^2}{\partial z} = 0. \quad (5.47)$$

For the initial condition, we assume that the foam is dry, $\phi_l = 0 = A$. For the boundary conditions, we assume that the liquid fraction and thus the cross-sectional area of a Plateau border far from the bottom of the foam is close to 0. At the bottom, $A = \delta_a R_b^2$, which is the cross-sectional area for the maximum packing of undeformed bubbles. Thus, we have the following initial and boundary conditions:

$$\begin{aligned} A(0, t) &= \delta_a R_b^2, \\ A(z > 0, 0) &= 0, \quad A(z \rightarrow +\infty, t) = 0. \end{aligned} \quad (5.48)$$

We non-dimensionalize A , r , z and t as $\alpha = A/(\delta_a R_b^2)$, $R = r/R_b$, $Z = z/R_b$ and $\tau = (\delta_a K_c/3)t/(\eta_l R_b/\gamma_{eff})$, and introduce the Bond number $Bo = \rho_l g R_b^2/\gamma_{eff}$, transforming Eq. 5.47 into:

$$\frac{\partial \alpha}{\partial \tau} = Bo \frac{\partial \alpha^2}{\partial Z} + \frac{1}{2} \frac{\partial}{\partial Z} \left(\alpha^{1/2} \frac{\partial \alpha}{\partial Z} \right), \quad (5.49)$$

with the initial and boundary conditions:

$$\begin{aligned} \alpha(Z > 0, 0) &= 0, \\ \alpha(Z \rightarrow +\infty, \tau) &= 0, \quad \alpha(0, \tau) = 1. \end{aligned} \quad (5.50)$$

Fig. 5.15 plots α as a function of Z for $Bo = 0.4$ and different successive times. By finding the value of Z for which $\alpha = 0$, we deduce the imbibition front $Z_f = h/R_b$ as a function of time t .

At late times, analytical and numerical calculations for the imbibition of infinitely dry foams gives a self-similar solution for Z_f [105]:

$$Z_f = 12.1 \left(\frac{\tau}{Bo} \right)^{1/3}. \quad (5.51)$$

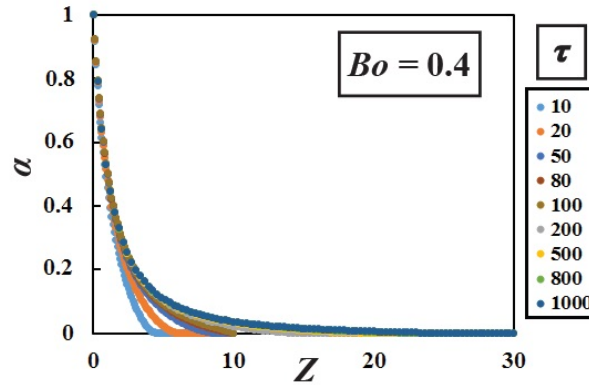


Figure 5.15: Drainage solution.

In dimensionalized parameters, Eq. 5.51 gives the evolution of the imbibition height h with the time t :

$$h = 1.24 \left(\frac{\gamma_{aw}^2}{\rho_l g \eta_l} \right)^{1/3} t^{1/3}. \quad (5.52)$$

Unfortunately, Eq. 5.52 neither captures the influence of ϕ_i nor R_b that is observed in the experiments. This can be understood by recalling that Equation 5.52 has been derived i) solving the Partial Differential Equation (PDE) ruling the evolution of $r(z, t)$ ii) assuming a foam with an initial liquid fraction equal to zero and iii) seeking for self-similar solutions of the PDE of the same form as in the free drainage case. This procedure is particularly useful to describe the asymptotic behavior of solutions in the limit where these no longer depend on the detail of the initial and boundary conditions. However, in our experiment, the foam sample is only 5-cm high, not infinitely dry and the time-scale is limited. Thus, the initial and boundary conditions are bound and cannot be neglected. Plus, the self-similar solution is found with a no-flux condition from free drainage at the top of the foam, which does not provide an appropriate boundary limit in this problem. Oil flows from the bottom of the foam and the flux condition is non-zero at $z = 0$. We thus never observe any convergence of the dynamics towards the $t^{1/3}$ regime. This is shown in Fig. 5.16 which exhibits the imbibition height h deduced from the self-similar solution (Eq. 5.52) and the exact solution calculated by solving Eq. 5.49. We cannot match our experimental data with the solution of the foam drainage equation (either self-similar solution or numerical solution for a given Bond number).

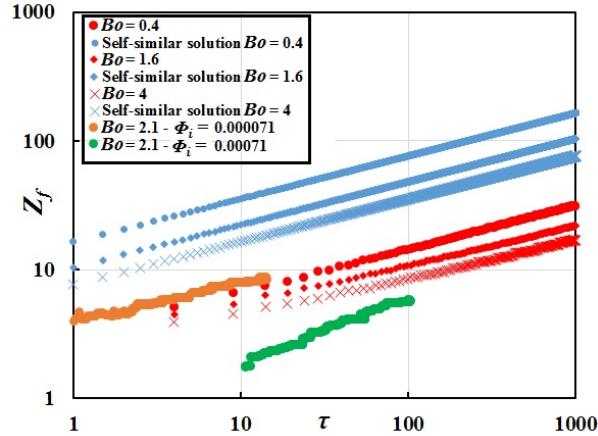


Figure 5.16: Dimensionless imbibition height Z_f as a function of the dimensionless time τ deduced from numerical resolution of Eq. 5.49 with the comparison to the self-similar solution given by Eq. 5.52 for different Bond numbers $Bo = 0.4, 1.6$ and 4 . Experimental data for $Bo = 2.1$ and two different initial liquid fractions ϕ_i are also plotted and do not converge towards a unique solution.

5.3.2.3 Scaling law

We try another approach to solve the problem by considering the flow of oil locally. For the length scale $d = 10 \mu\text{m}$, which is the typical width of a Plateau border, the Reynolds number is around $Re = \rho_l \dot{h} d / \eta_l \sim 10^{-11} \ll 1$. The rigid boundary conditions provided by the foaming solution and the small value of Re suggest that the fluid motion in the foam network corresponds to a Stokes flow where the capillary driving force is balanced with the viscous dissipation, as suggested in 5.1.2.2. In the limit where $\gamma_{ow} / \gamma_{aw} \ll 1$, recent experimental works at the scale of a single horizontal Plateau border have revealed the following features [39, 137]. On one hand, the driving capillary pressure that sustains the imbibition in the Plateau border is given by γ_{aw} / r_{PB} , where r_{PB} is the curvature radius of the Plateau border prior to imbibition.

On the other hand, the bulk viscous dissipation only occurs in the oil phase and scales as $\eta_o \dot{z} / r^{*2}(z, t)$, with the position z along the Plateau border and $r^{*2}(z, t)$ is proportional to the swollen Plateau border cross section $A = \delta_a r^{*2}$ with $\delta_a = 0.16$. In [137], the experiments were either driven at constant flow rate or constant volume of oil, thus $r^{*2}(z, t)$ is deduced from mass conservation [191], while here imbibition occurs from a large reservoir. In our case, the initial squeezing of the oil droplet, as shown in Fig. 5.13, creates an oil slick at the bottom of the foam and generates a reservoir of oil for the foam. The oil spreading is dynamically instantaneous compared to the initial rise of oil. Thus, we can assimilate our imbibition process to a quasi one-dimensional imbibition. This is all the more a good approximation that a change of oil volume from 20 to 80 μL does not involve any change in the imbibition pattern.

Moreover, in this experiment, the size of the oil slick - after it has been squeezed by the foam

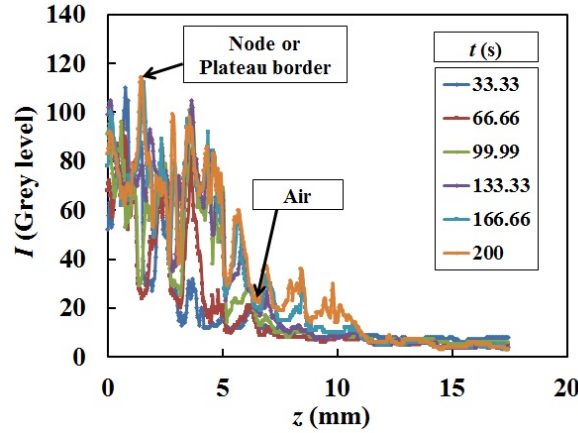


Figure 5.17: Typical profile of the fluorescence intensity I of a single node during olive oil imbibition as a function of the vertical coordinate z for different times t . A peak corresponds to an oil-filled node or an oil-filled Plateau border, a hole to air in the bubbles.

- is large compared to the size of the bubbles. This suggests that the imbibition simultaneously occurs from different points. The imbibition from each point source is symmetrical radially, yet since the upward velocity is identical in each point source, the front evolves towards a plane. To gain quantitative understanding of the spatial and temporal evolution of the Plateau border radius r^* , we take advantage of the fluorescence intensity of our images. Fig. 5.17 shows a typical intensity profile along the vertical axis z .

In Fig. 5.18, we report the spatial evolution of the fluorescence intensity of a single node located at $x = 1$ mm and $z = 7.9$ mm for different times.

The oil front reaches the height $z = 7.9$ mm at $t = 270$ s, thus the signal prior to $t = 270$ s corresponds to noise fluctuation. At $t = 274$ s, a peak in the fluorescence intensity is observed. The intensity of this peak grows until reaching a steady shape observed 100 s after the front has gone through the node, as it can be seen in the inset of Figure 5.18 where a saturation of the peak's width and amplitude is observed after $t = 400$ s. This suggests that for the foam below the oil front, the distribution of oil quickly reaches a steady-state profile. This steady-state profile must match the equilibrium profile given by a balance between capillarity and gravity [28, 193].

At late times and for $z < h$, r^* does not depend anymore on t and the corresponding steady-state curvature radius $r^*(z)$ is deduced from a balance between gravity and the vertical capillary pressure gradient $\nabla p = -\nabla\left(\frac{\gamma_{aw} + \gamma_{ow}}{r^*}\right)$, as observed in §5.1.1.3. We consider a small perturbation of order 1 at long times in Eq. 5.27 with the following relationship at order 0:

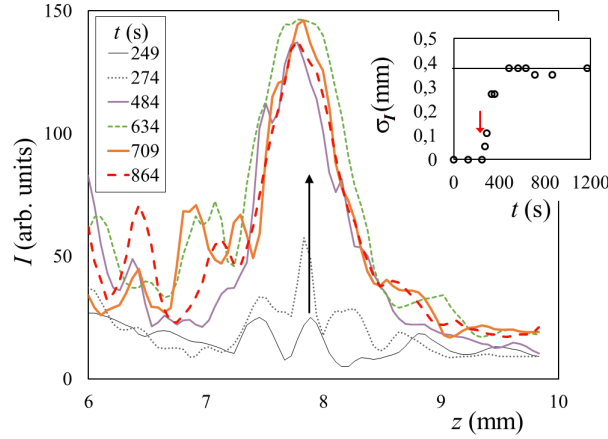


Figure 5.18: Typical evolution of the fluorescence intensity I of a single node during sunflower oil imbibition as a function of the node's vertical coordinate z . Initially, the node is located at $x = 1$ mm and $z = 7.9$ mm. The intensity of fluorescence is in arbitrary units and the different curves correspond to fluorescence intensity measurements taken at different times. The black arrow indicates the evolution of time. Inset: Width of the peak of intensity σ_I (defined at half of the maximum intensity) as a function of time t . The red arrow highlights the time at which the oil front has reached the node.

$$\rho \mathbf{g} - \nabla p = 0. \quad (5.53)$$

By projecting Eq 5.53 on the vertical direction \mathbf{e}_z and derivating $r^*(z)$ with respect to z , we find (with ρ the density of the immiscible or miscible liquid):

$$\frac{dr^*}{dz} + \frac{\rho g}{\gamma_{aw} + \gamma_{ow}} r^{*2} = 0. \quad (5.54)$$

Introducing the boundary condition $r^*(0, t) = R_b$ at the bottom of the foam yields:

$$r^*(z, t) = r^*(z) \sim \frac{R_b}{1 + \alpha^* z}, \quad (5.55)$$

where $\alpha^* = \frac{\rho g R_b}{\gamma_{aw} + \gamma_{ow}} \sim \frac{\rho g R_b}{\gamma_{aw}}$ has the dimension of an inversed length. This classic profile illustrates the complex multi-scale geometry of foam under gravity: for $z \ll 1/\alpha^*$, the curvature is only set by the bubble size $r \sim R_b$, while for $z \gg 1/\alpha^*$, $r \sim R_b/\alpha^* z$.

To describe the imbibition dynamics within the aqueous foam, we consider the flow throughout the slender Plateau borders below the front. We study the local flow dynamics by looking at one single average vertical Plateau border, sketched in Fig. 5.19 and use Eq. 5.22 with a permeability determined by the Plateau border cross-section:

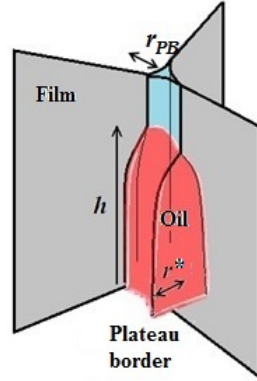


Figure 5.19: Oil imbibing a Plateau border.

$$v = -\frac{K_c \delta_a r^*(z)^2}{3\eta_l} \frac{dp}{dz}, \quad (5.56)$$

where $r^*(z)$ is given by Eq. 5.55 and v , η_l , K_c represent, respectively, the mean velocity of the imbibing liquid, the dynamic viscosity of the imbibing liquid and the permeability coefficient for infinite slender channels, $K_c = 0.02$ [133, 137], as already stated. We also use the cross-section of the Plateau border $A = \delta_a r^{*2}$. [42, 108, 133].

Then, we write mass conservation, which yields $v(z) = v(h)r^{*2}(h)/r^{*2}(z) = \dot{h}r^{*2}(h)/r^{*2}(z)$. At short times, the gravity effects are negligible (for $h \ll (\gamma_{aw} + \gamma_{ow})/\rho g$) but at late times, because of the equilibrium between capillarity and gravity, we consider that gravity only blocks the swelling of the Plateau border, as shown in Fig. 5.18, but does not affect the vertical flow of liquid upwards. Thus, we can use Darcy's equation for the whole time window.

Integrating Eq. 5.56 for $0 < z < h$ with the boundary conditions $p(z = 0) = p_o \approx p_{atm}$ at the bottom of the foam and $p(h) = p_o - \gamma_{aw}/r_{PB}$ at the imbibition front, and using Eq. 5.55 gives:

$$\dot{h} \left((1 + \alpha^* h)^3 - \frac{1}{(1 + \alpha^* h)^2} \right) = \frac{5\alpha^* \delta_a \gamma_{aw} K_c R_b^2}{3\eta_l r_{PB}}. \quad (5.57)$$

Eq. 5.57 is then integrated with the condition $h(t = 0) = 0$:

$$(1 + \alpha^* h)^4 + \frac{4}{1 + \alpha^* h} - 5 = \frac{2\delta_a}{15\sqrt{3}} \frac{\alpha^{*2} R_b \gamma_{aw}}{\sqrt{\phi_i} \eta_l} t. \quad (5.58)$$

At late times or for $\alpha^* h \gg 1$, Eq. 5.58 predicts an evolution of the rising front in $t^{1/4}$, while for $\alpha^* h \ll 1$, a second-order limited expansion of Eq. 5.58 gives $h^2 \sim R_b \gamma_{aw} t / \sqrt{\phi_i} \eta_l$, thus suggesting an early time dynamics of imbibition in $t^{1/2}$. These regimes intersect for $h \sim 1/\alpha^*$,

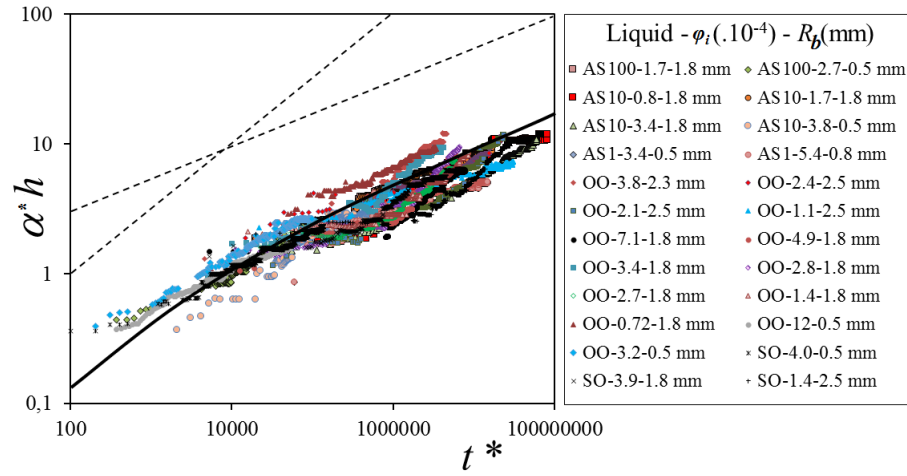


Figure 5.20: Normalized imbibition front α^*h as a function of normalized time t^* in log-log plot. In the legend, AS1, AS10 and AS100 respectively stand for Aqueous Solution with $\eta_l = 1.4, 10$ and 100 mPa.s, while OO and SO stands for Olive Oil and Sunflower Oil. The black line corresponds to $(1 + \alpha^*h)^4 + \frac{4}{1 + \alpha^*h} - 5 = b \frac{2\delta_a}{15\sqrt{3}} t^*$ with $b \sim 0.3$, while the two dashed lines represent the power laws: $t^{1/2}$ at early times and $t^{1/4}$ at late times.

the typical height for which the curvature radius of the Plateau borders changes from R_b to R_b/α^*h . Moreover, Eq. 5.58 suggests a collapse of the data using the dimensionless variables α^*h and $t^* = \frac{\alpha^{*2} R_b \gamma_{aw}}{\sqrt{\phi_i} \eta_l} t$, which is in reasonable agreement with our experimental results obtained for three different liquids, either organic or aqueous, and foams with various bubble diameters and initial liquid fractions, as can be seen in Fig. 5.20.

Furthermore, the data is reasonably fitted by $(1 + \alpha^*h)^4 + \frac{4}{1 + \alpha^*h} - 5 = b \frac{2\delta_a}{15\sqrt{3}} t^*$, with a coefficient b deduced from the experiments of $b \sim 0.3$. This coefficient may be related to the value of the pressure in the contact area between the foam and the oil. Since the foam squeezes the oil droplet initially to create an oil slick, the lower layer of bubbles is deformed. Thus, the pressure at the bottom that is critical in our model might not be the exact atmospheric pressure but a pressure that is lower, due to the concave curvature induced by this deformation. This will imply a shift in the pressure value (3 times as low as the atmospheric pressure according to the value of b), and thus a vertical shift downwards compared to the theoretical predictions.

In this context, our scaling law, where the topology of the foam is kept at its original value in the unwetted area, better captures the influence of R_b , ϕ_i and the long-term dynamics of the process than the numerical and analytical solution of the foam drainage equation. In [153], Reyssat et

al. have found a similar dynamics for the imbibition of a conical channel. The dimensional axial variations induce a modification of the usual Lucas-Washburn diffusive dynamics with a $t^{1/4}$ dynamics at long times. This configuration is similar to the case of a deformable and swelling Plateau border which self-adjusts during the whole imbibition process.

In this section, we quantify the 1D-imbibition dynamics of a dry aqueous foam by a miscible or immiscible liquid slick. To describe our experimental data, we use the framework of porous media considering steady-state solution and the initial liquid fraction of the foam. We exhibit a new late-time dynamics in $t^{1/4}$ in good agreement with the experiments. However, the dependence on the initial liquid fraction remains to be derived from the foam drainage theory. Moreover, we do not really know how oil behaves at the bottom of the foam (initial squeezing of the oil droplet). In the scaling law, we also assume that we can add up the contributions of every Plateau border connected to the oil droplet independantly, but collective phenomena can arise.

We can also notice that the scaling we find in this section is different from the resolution of the 3D problem. Here, we have a strong dependence on the initial liquid fraction, which is not the case for the pore imbibition. The difference probably comes from the imposed conditions. For the pore configuration, we impose the pressure, while the volume of oil is not completely infinite for the 1D configuration.

Despite this relatively slow dynamics at late times, the remarkable ability of dry aqueous foams to displace and drive upward an immiscible liquid highlighted in this section, should be of considerable interest in various industries such as soil remediation, detergency, shampoo industry, enhanced oil recovery and dismantling of nuclear power plants.

5.4 Oil recovery by a moving foam

In this section, we study the oil imbibition into the foam from a point-source with the foam moving over the extracting point. In §5.3 and §5.2, we have studied the 1D imbibition of an oil slick and the 3D static imbibition from a point-source. We go one step further by getting close to a real channel connected to a pore from which we need to remove the foam once it is oil-imbibed.

5.4.1 Experimental configuration

We use the experimental setup depicted in Fig. 5.21. First, we generate the foam with the system presented in §5.3 and §5.2. However, the removable part is here a 14.5 cm high and 2.5 cm width polycarbonate cylinder. This cylinder is blocked by a piston at the top. We fill the whole column and then wait for different times corresponding to different drainage times. Then, we

to 1000 mL/h (from 10 $\mu\text{m}/\text{min}$ to 3 cm/min). The foam advances into the column as a plug-like flow before touching the injection point. The cameras are started right before the touching time and record the imbibition dynamics at 24 frames per second. While imbibition occurs, the level of liquid in the U-tube is kept at its initial level by moving the tube upwards by incremental distance of 0.2 mm. The distance d by which the tube is moved allows to determine the volume V_o of liquid absorbed by the foam with $V_o = \pi r_t^2 d$ and $r_t = 1$ mm is the tube radius.

5.4.2 Modelization of the imbibed moving foam

From our experiments, we extract the imbibition profiles and try to model and predict the quantity of extracted oil.

5.4.2.1 Imbibition profiles

We observe the development of an imbibition front, as described in Fig. 5.22 and Fig. 5.23 for both imbibing oil and miscible liquids. Yet, here the front is axisymmetric towards the axis of the channel.

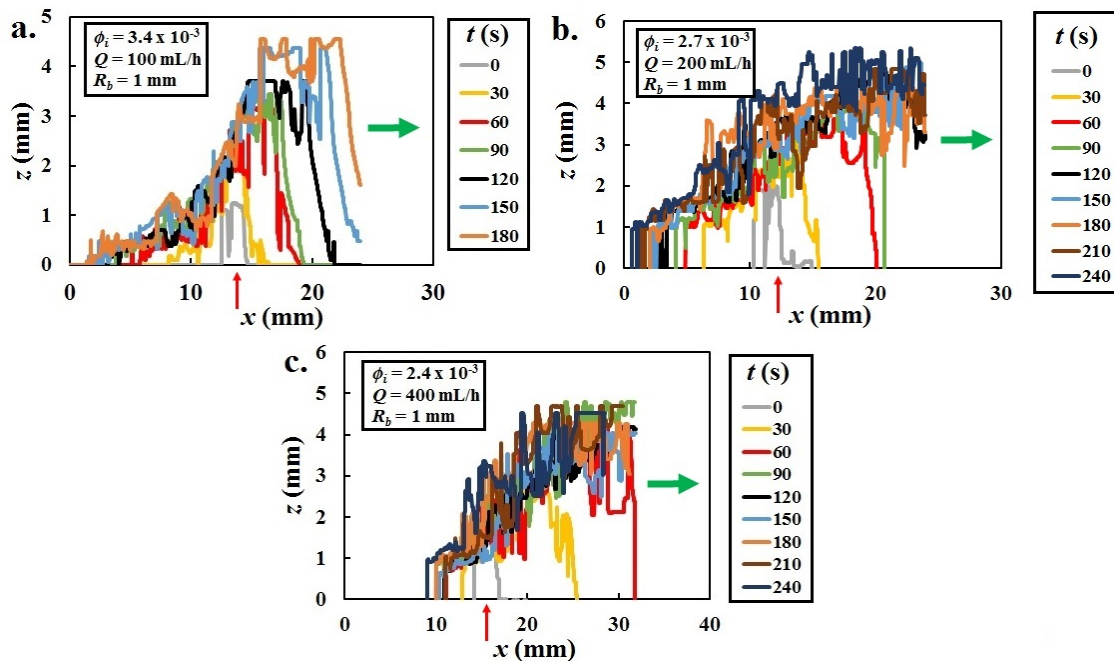


Figure 5.22: Imbibition profiles for immiscible liquids (olive oil) for successive times t . a. Initial liquid fraction $\phi_i = 3.4 \times 10^{-3}$, injection flow rate $Q = 100$ mL/h and bubble radius $R_b = 1$ mm. b. $\phi_i = 2.7 \times 10^{-3}$ and $Q = 200$ mL/h. c. $\phi_i = 2.4 \times 10^{-3}$ and $Q = 400$ mL/h. The red arrow indicates the extraction point and the green arrow the movement of the foam.

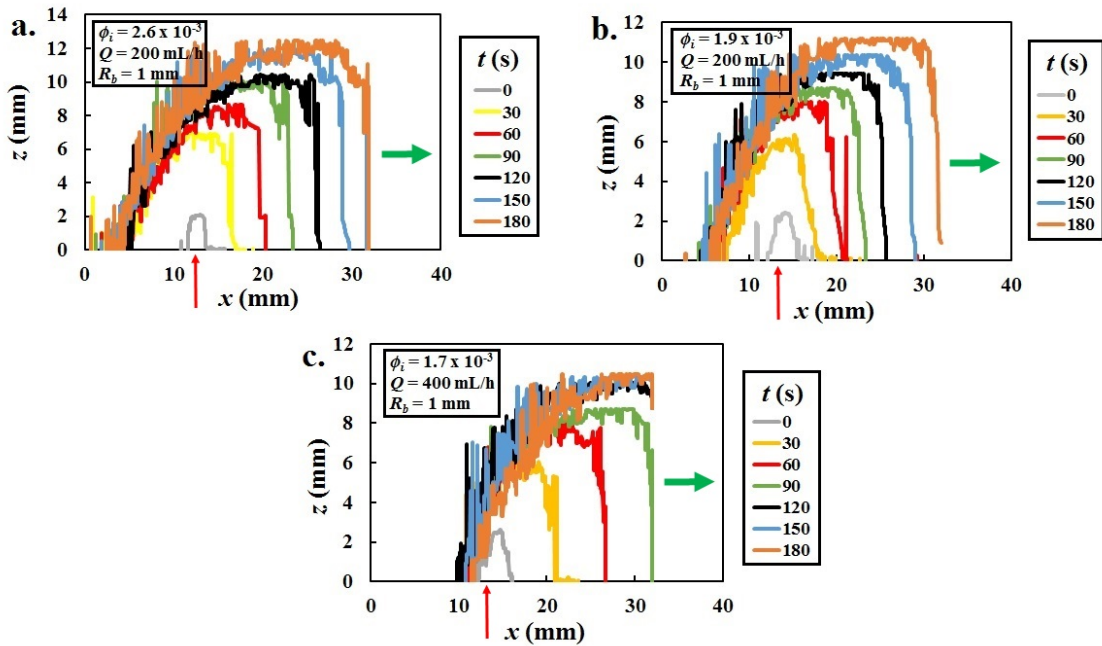


Figure 5.23: Imbibition profiles for miscible liquids (CAPB+SLES+Mac-glycerol) for successive times t . a. Initial liquid fraction $\phi_i = 2.6 \times 10^{-3}$, injection flow rate $Q = 200$ mL/h and bubble radius $R_b = 1$ mm. b. $\phi_i = 1.9 \times 10^{-3}$ and $Q = 200$ mL/h. c. $\phi_i = 1.7 \times 10^{-3}$ and $Q = 400$ mL/h. The red arrow indicates the extraction point and the green arrow the movement of the foam.

Fig. 5.24 also shows the mean flow rate of absorbed oil $Q_o = V_o/t_r$ as a function of the foam velocity $U_f = Q/\pi r_c^2$ (r_c is the column radius) for an experimental time frame between the touching time $t = 0$ and the final running time $t_r = 4$ min and 30 sec. What is surprising is that the volume decreases when the flow rate increases. Indeed, we could have imagined that bringing “fresh” foam would have brought more fresh connections between the extracting point and the foam, thus enhancing oil imbibition.

5.4.2.2 Discretized model

We try to explain the observed trend for the imbibition of immiscible liquids. We assume that the whole imbibition process is the sum of short static imbibitions every time a Plateau border encounters the extracting point.

We introduce the volume $v_o(t)$ of oil absorbed by a group of Plateau borders connected to the extracting point for a duration t . Indeed, the foam moves, so we have several Plateau borders that go through the pore and remain connected to the pore for a duration $t_d = d_t/U_f$ where $d_t = 2r_t = 1$ mm is the diameter of the capillary tube.

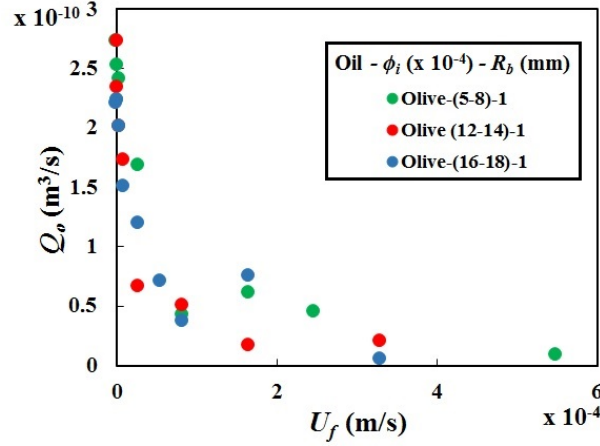


Figure 5.24: Mean extraction flow rate Q_o , for an injection time of 4 min and 30 s, as a function of the foam velocity U_f .

Then, we have two possible cases. If the experimental running time $t_r < t_d$, it means that one single Plateau border stays in touch with the extracting point within the injection time t_r . Thus, we are in the static case and the imbibed volume after a time t_r is $V_o(t_r) = v_o(t_r)$.

Now if $t_r > t_d$, several Plateau borders can successively be connected to the extracting point while the foam is moving. Hence, we can think about the simplest possible model where the total absorbed volume V_o is the sum of different volumes v_o absorbed every time a Plateau border is connected, which yields:

$$V_o(t) = F\left(\frac{tU_f}{d_t}\right) v_o\left(\frac{d_t}{U_f}\right) + v_o\left(t - F\left(\frac{tU_f}{d_t}\right) \frac{d_t}{U_f}\right), \quad (5.59)$$

where F is the floor function: given a a whole number and b a real number, if $a \leq b < a + 1$, then $F(b) = a$. In the first term of Eq. 5.59, $F(tU_f/d_t)$ is the number of times a Plateau border is connected and $v_o(d_t/U_f)$ is the absorbed volume during the contact time $t_d = d_t/U_f$. The second term is the residual volume for the last connection.

Then, we can express the mean flow rate $Q_o(t_r)$ over the running time t_r by:

$$Q_o(t_r) = \frac{V_o(t_r)}{t_r} = \frac{1}{t_r} \left[F\left(\frac{t_r U_f}{d_t}\right) v_o\left(\frac{d_t}{U_f}\right) + v_o\left(t_r - F\left(\frac{t_r U_f}{d_t}\right) \frac{d_t}{U_f}\right) \right]. \quad (5.60)$$

We need to determine an expression for $v_o(t)$ at short times, which corresponds to the time scale of one single static imbibition, close to the point-source. In Fig. 5.12, we showed that the experimental data are well-fitted at short times by a $t^{1/2}$ law even though we did not provide any modelling for this observed feature. We recall that the good agreement between the self-similar no-gravity solution from Eq. 5.43 and our data is a coincidence. The imbibition volume $v_o(t)$ is

determined by $v_o(t) = 4\pi \int_0^{r_f} \phi_o r^2 dr$ with the oil fraction ϕ_o . This integration gives the following dependence for $v_o(t)$:

$$v_o(t) \sim R_b^3 \left(\frac{\gamma_{eff} t}{\eta_o R_b} \right)^{3/2}, \quad (5.61)$$

where γ_{eff} , R_b and η_o are the only dimensionalizing parameters of our system.

In dimensionless coordinates Q^* for the dimensionless flow rate of oil and U^* for the dimensionless foam velocity, Eq. 5.60 gives:

$$\begin{cases} U^* = \frac{U_f t_r}{d} \\ Q^* = \frac{Q(t_r)}{R_b^3} \left(\frac{\eta R_b}{\gamma_{eff}} \right)^{3/2} \frac{1}{t_r^{1/2}} \\ Q^* \sim \frac{F(U^*)}{U^{*3/2}} + \left(1 - \frac{F(U^*)}{U^*} \right)^{3/2} \end{cases} \quad (5.62)$$

The log-log plot of Fig. 5.25 shows Q^* as a function of U^* for different experimental data with olive oil as the imbibing liquid. We can notice two different regimes. At low foam velocities U^* , Q^* is almost constant. However, as the foam goes faster, we transition to another regime for $U^* > 1$ where Q^* decreases when U^* increases. The faster we push the foam, the less oil we recover, as underlined before.

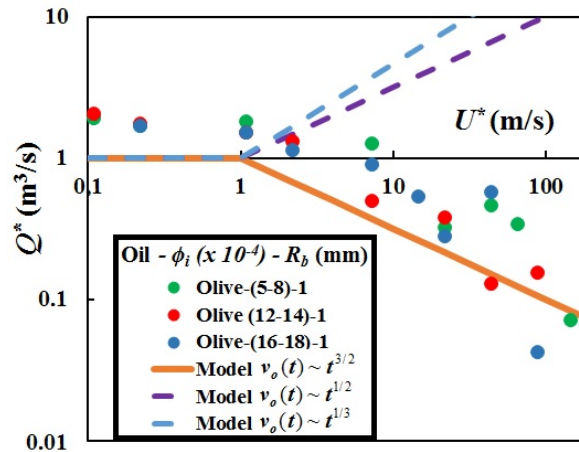


Figure 5.25: Dimensionless extraction flow rate Q^* as a function of the dimensionless foam velocity U^* for the imbibition of olive oil with different initial liquid fractions ϕ_i in the foam. The orange line is the fit with Eq. 5.62 and $v_o(t) \sim t^{3/2}$. The blue and the purple dashed lines are, respectively, the fits with $v_o(t) \sim t^{1/3}$ and $\sim t^{1/2}$ deduced from the numerical simulation from §5.2.

We retrieve this transition for $U^* = 1$ in our model. The boundary $U^* = 1$ means that one single Plateau border has managed to be in contact with the extracting point, like the static case. In Fig. 5.25, the fit is given for Eq. 5.62 and no multiplying coefficient. The collapse is not perfect. However, our model explains our experimental observations in scaling order. We therefore try to use the numerical solution developed for the static imbibition in §5.2. This solution deviates at short times and exhibits a power law behaviour for $v_o(t)$ from $t^{1/2}$ to $t^{1/3}$ (according to the Bond number) from the simulations, as seen in Fig 5.26. This actually suggests an increase of the imbibed volume with the foam velocity, which is not what is experimentally observed. The short-time dynamics around the point-source has to be taken into account. Obviously, adding up the contributions of successive imbibitions from the same pore is also a rough model that needs to be refined.

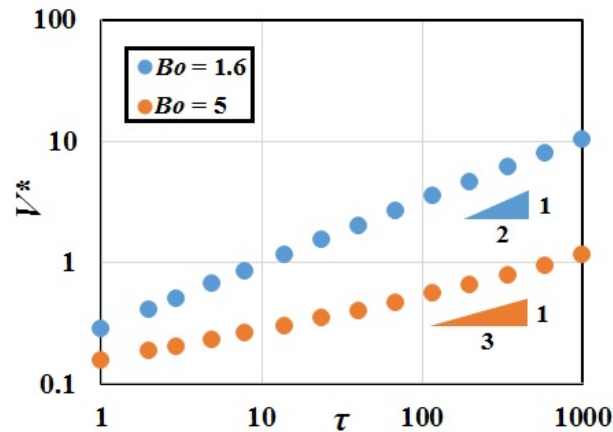


Figure 5.26: Log-log plot of the dimensionless imbibed volume $V^* = \int_0^{R_f} \int_0^{Z_f} \alpha(R, Z, \tau) R dR dZ$ (where $R_f = r_f/R_b$ and $Z_f = z_f/R_b$ are the dimensionless coordinates of the front) for the static imbibition of §5.2 as a function of the dimensionless time τ for two different Bond numbers $Bo = 1.6$ and 5.

But it is clear that injecting a foam at high flow rates is not the ideal situation to extract immiscible liquids from a connected pore. It makes sense because a Plateau border needs to be kept into contact with the extracting point as long as possible for the imbibition process to occur.

For miscible liquids, imbibition is quite fast, so the imbibing liquid invades the rear of the foam quite easily and the Plateau borders are already imbibed when they cross the extracting point, a discretized model is thus not really appropriate. Modelling this problem more accurately is still an open question.

5.5 Conclusions

In this chapter, we show that both miscible and immiscible liquids can be absorbed by an aqueous foam due to the capillary underpressure with the outer environment. We gradually travel from the imbibition of oil from a millimetric pore by a static foam to the 1D imbibition of an oil slick and the recovery of oil by a moving foam.

First, the radial imbibition from a point source (at imposed pressure) for different types of liquid into a dry aqueous foam has been studied theoretically, numerically and experimentally. Theory, numerics and experiments are in good agreement. The results demonstrate that gravitational effects are comparable to the capillary pressure. Moreover, we have identified two criteria that define the imbibition efficiency. The first one is the ratio between the oil-water and the air-water interfacial tension that predicts the imbibition strength. The resulting effective interfacial tension γ_{eff} allows to describe the local influence of the oil-water interface on the imbibition process. The second one is the Bond number Bo . The lower Bo , the less important gravity and the more liquid is imbibed. Decreasing the bubble radius is the main option for reducing Bo (apart from microgravity).

To go further, we consider a configuration where we have multiple point-sources to form an oil slick and a uniform propagating front of imbibition. To describe our experimental data in this case of a uniaxial vertical imbibition, we use the framework of liquid flow into porous media by considering a steady-state solution and the initial liquid fraction of foam. We exhibit a $t^{1/4}$ late-time dynamics in good agreement with the experiments and some observations made for imbibition into deformable solid porous media [153, 169]. Another study for imbibition into gellified foams [54] has reported a diffusive behaviour in $t^{1/2}$ by considering immobile air-water interfaces. All in all, our scaling remains to be derived from the foam drainage equation (see Eq. 5.29).

Finally, we have tried to build a system where a macroscopic channel is connected to a millimetric pore from which oil needs to be extracted. In the continuity of the static imbibition from a point-source, we have moved the foam on top of the extracting point-source and have looked at the volume of recovered oil. Our main result is that a low injection flow rate of foam is more favourable than high foam velocities because the foam needs to spend as much time as possible in contact with the pore to be efficient. Obviously, in terms of applications, a compromise has to be found between a better volume of absorption per foam unit and a fast injection process.

In conclusion, we have highlighted the remarkable ability of dry aqueous foams to displace and drive upwards immiscible and miscible liquids, as well as different dynamics according to the configurations of the oil reservoir. Actually, oil can also spontaneously penetrate wet foams due

to the dynamic decrease of the oil-water interfacial tension [172]. Macroscopic imbibition into aqueous foams is not the only mechanism enabling the extraction of liquids from a confined medium. At the microscopic scale, foams can also drag out liquids by interfacial interactions, as we see in Chapter 6.

Chapter 6

Foam - oil interactions in micropatterned structures

In this chapter, oil is confined and trapped in the roughness of a surface. We show how oil can be efficiently dragged out of the roughness by aqueous solutions containing surfactants and foams. To analyze our results, we use the framework developed by Wexler et al. [198], who studied how oil is dragged out of the roughness of a groove surface by using pure water. We compare the efficiency of the different liquids (surfactant solutions and foams versus pure water) and demonstrate that the volume of extracted oil is highly improved by using foams. We also refer to recovery issues from porous media trapping oil, where aqueous solutions and gas are injected to increase the efficiency of the recovery process. To some extent, we wonder how oil can be extracted from the roughness of a confined porous medium. This part was completed in collaboration with Dr. Jason S. Wexler in the Complex Fluids Group of Prof. Howard A. Stone at Princeton University.

Contents

6.1	Textured and liquid-infused surfaces	167
6.1.1	Wetting of rough surfaces	167
6.1.1.1	Wetting behaviour on rough surfaces: Wenzel model and hydrophilicity	167
6.1.1.2	Film impregnation	169
6.1.1.3	Hydrophobic textured surface	170
6.1.1.4	Generation of liquid-infused surfaces	171
6.1.2	Failure of textured surfaces	172
6.1.2.1	Transition from the Wenzel to Cassie-Baxter regime	172
6.1.2.2	Impalement of superhydrophobic surfaces	173
6.1.2.3	Shear-driven drainage of liquid-infused surfaces: scaling arguments	174
6.1.2.4	Shear-driven drainage of liquid-infused surfaces: analytical resolution	176
6.2	Surfactant-driven oil extraction from micropatterned channels	178
6.2.1	Materials	179
6.2.1.1	Characteristics of the textured surface and the tested fluids	179
6.2.1.2	Fluid injection	181
6.2.2	Experimental observations and results	182
6.2.2.1	Extraction patterns	182
6.2.2.2	Efficiency curves	182
6.2.3	Effect of surfactants on the extraction dynamics	183
6.2.3.1	Variations of the contact angle	185
6.2.3.2	Comparison between the predictions and the experimental results	187
6.2.4	Extraction instability	189
6.2.4.1	Instability of viscous stratification	189
6.2.4.2	Surfactant-induced instability	189
6.3	Foam-driven oil extraction from micropatterned channels	190
6.3.1	Controlled foam generation	191

CHAPTER 6: FOAM - OIL INTERACTIONS IN MICROPATTERNED STRUCTURES165

6.3.1.1	Flow-focusing	191
6.3.1.2	Foam calibration	192
6.3.2	Experimental results and discussion	193
6.3.2.1	Typical extraction pattern with foams	194
6.3.2.2	Shear modeling at the oil-water interface	195
6.3.2.3	Dissipation length and film thickness	196
6.4	Conclusions	198

Specific variables

Variables	Parameters	Variables	Parameters
θ^*	Apparent contact angle	dE	Variation of interfacial energy per unit length
r_S	Surface roughness	ϕ_S	Solid fraction of projected area
A_P	Projected area	r_ϕ	Texture roughness
P_d	Drop pressure	F_P	Pressure force
F_C	Capillary force	N_P	Number of posts
r_p	Post radius	Θ	Angle made by the air-liquid interface with the post
Θ	Advancing contact angle	P_{imp}^t	Impalement pressure for touch-down
P_{imp}^s	Impalement pressure for sliding	h	Post height
W	Channel width	H	Channel height
λ	Viscosity ratio	Q	Injection flow rate
w	Spacing between posts	θ	Receding contact angle
L	Retention length	L_o	Initial length of oil
r_{min}	Minimum radius of curvature	L_∞	Steady-state retention length
Re	Reynolds number	Bo	Bond number
u	Streamwise velocity	u_s	Shear-driven velocity
u_p	Pressure-driven velocity	q_s	Shear-driven flux
q_p	Pressure-driven flux	q_d	Drained flux
t_c	Characteristic time of extraction	\tilde{L}	Dimensionless retention length
\tilde{t}	Dimensionless time	V_d	Volume of extracted oil
V_0	Initial volume of oil	α	Extraction efficiency
Ca	Capillary number (with oil-water interfacial tension)	I	Fluorescence intensity
α_∞	Steady-state extraction efficiency	δ	Deflection of the oil-water interface
M	Marangoni number	C^*	Initial interfacial concentration of surfactants
γ_{ow}^*	Initial oil-water interfacial tension	q	Flow rate through the constriction
Δp_ℓ	Pressure difference through the constriction	T	Characteristic time of bubble break-up
q_g	Gas flow rate	l_c	Constriction length
w_c	Constriction width	w_o	Reservoir width
w_l	Width of the liquid channel	w_g	Width of the gas channel
V_b	Bubble volume	D	Film thickness at the wall
\tilde{Ca}	Apparent capillary number	α_{exp}	Experimental extraction efficiency
τ_{xy}^{foam}	Shear stress exerted by the foam	D^*	Dimensionless film thickness
τ_{xy}^{foam*}	Dimensionless shear stress	Ca^*	Outer capillary number (with air-water interfacial tension)
r_p	Pore radius	\mathcal{L}	Depth of the extraction well
ϕ	Porosity	d_g	Grain diameter

6.1 Textured and liquid-infused surfaces

In this chapter, oil is confined in the roughness of a confined medium. To realize this geometry experimentally, we use a microfluidic device constituted of a wide channel with a textured wall in which oil is confined due to a favourable wetting. We first recall some classical features concerning the wetting of rough surfaces and we show that these properties are enhanced when a lubricating film impregnates the cavities of the texture [146]. However, these surfaces can also lose their properties when the air-liquid interfaces are subject to external stresses.

6.1.1 Wetting of rough surfaces

Let us first discuss how a liquid interacts with a rough surface. It has indeed been shown that geometrical defects considerably modify the wetting properties of a surface. In the following, we discuss different results from the literature to relate the wetting properties to the roughness of the surface.

6.1.1.1 Wetting behaviour on rough surfaces: Wenzel model and hydrophilicity

A rough surface is a surface whose thickness varies locally due to the presence of defects. Shibuichi et al. [71] have shown that the apparent contact angle θ^* on a rough surface differs from the value of the Young static contact angle θ_Y on a smooth surface of the same chemical nature. Both configurations are sketched in Fig. 6.1. The same figure presents the variations of $\cos \theta^*$ with $\cos \theta_Y$. For hydrophilic smooth surfaces ($\theta_Y < 90^\circ$), the hydrophilicity is enhanced by the roughness. The apparent contact angle rapidly decreases when θ_Y decreases and gets close to a value of 0° . For hydrophobic smooth surfaces ($\theta_Y > 90^\circ$), the hydrophobicity is improved by the roughness. The apparent contact angle strongly increases when θ_Y increases.

How can we relate the apparent contact angle on a rough surface to the Young contact angle? In 1936, Wenzel was the first one to relate both angles [197]. He calculates θ^* by considering the horizontal displacement dx of the air-liquid contact line, as depicted in Fig. 6.1b. The total variation of interfacial energy dE is written as:

$$dE = r_S (\gamma_{sl} - \gamma_{sa}) dx + \gamma_{al} dx \cos \theta^* \quad , \quad (6.1)$$

where r_S is the surface roughness, γ_{sl} , γ_{sa} and γ_{al} the solid-liquid, the solid-air and the air-liquid interfacial tensions respectively. At equilibrium, $dE = 0$ and Eq. 6.1 yields the Wenzel state with:

$$\cos \theta^* = r_S \cos \theta_Y. \tag{6.2}$$

For a rough surface ($r > 1$), hydrophobicity and hydrophilicity are enhanced since $\cos \theta^* > \cos \theta_Y$ and $\theta^* < \theta_Y$ for $\theta_Y < 90^\circ$, and $\cos \theta^* < \cos \theta_Y$ and $\theta^* > \theta_Y$ for $\theta_Y > 90^\circ$. If $r = 1$ (smooth surface), one retrieves the Young contact angle.

Eq. 6.2 shows that it is possible to reach a complete wetting or a non-wetting state for a specific value of the roughness r_S^* . Indeed, this value is given by $r_S^* = 1/|\cos \theta_Y|$. One finds $r_S^* = 2$ for a value of $\theta_Y = 60^\circ$. This result is in contradiction with the experimental observations from Fig. 6.1 since the apparent contact angles never reach 180° and 0° .

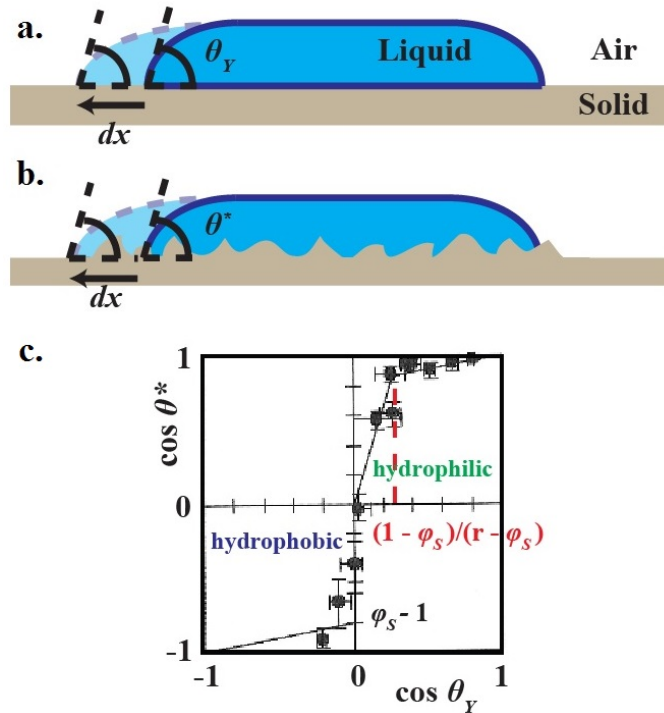


Figure 6.1: a. Wetting on a smooth surface with the Young contact angle θ_Y . b. Wetting on a rough surface with the apparent contact angle θ^* . c. Evolution of $\cos \theta^*$ with $\cos \theta_Y$ for a smooth and a rough surface of the same chemical nature [71]. The parameters ϕ_S and r_S are respectively the solid fraction and the roughness. The black plain line in the upper right part corresponds to Eq. 6.2.

The Wenzel model is indeed only valid for the linear part in the plot of Fig. 6.1 at small $\cos \theta_Y$. However, for $\cos \theta_Y$ and $\cos \theta^*$ close to 1 (complete wetting), a liquid film can escape from the droplet and invade the pores of the textured surface. This film creates a lubricating layer which gives a “smooth” character to the textured surface. As a consequence, the liquid droplet sits on a composite solid-liquid surface drawn in Fig. 6.2.

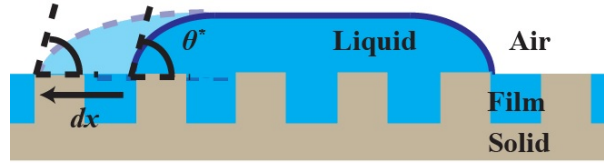


Figure 6.2: Liquid droplet sitting on a solid-liquid composite surface.

Let us calculate the apparent contact angle θ^* in this configuration. One considers a textured surface whose size pore and spacing between pores are uniform. We define ϕ_S as the solid fraction of projected area, which corresponds to the ratio between the areas at the top of every plot and the whole projected area A_P of the surface (see Fig. 6.3). When the air-liquid contact line moves by a distance dx over the solid-liquid area pattern, the virtual movement of the droplet covers the air-liquid interface of area per unit length $(1 - \phi_S)dx$ by the liquid phase and replaces the air-solid interface by a solid-liquid interface of area $\phi_S dx$. An air-liquid interface of area $\cos \theta^* dx$ is also created. Thus, the variation of interfacial energy dE is written as:

$$dE = dx (\phi_S(\gamma_{sl} - \gamma_{sa}) - (1 - \phi_S)\gamma_{al} + \gamma_{al} \cos \theta^*). \quad (6.3)$$

By injecting the Young-Dupré equation $\cos \theta_Y = (\gamma_{sa} - \gamma_{sl})/\gamma_{al}$ and setting $dE = 0$ at equilibrium in Eq. 6.3, one finds [17]:

$$\cos \theta^* = 1 - \phi_S + \phi_S \cos \theta_Y. \quad (6.4)$$

It is impossible to induce a complete wetting transition ($\cos \theta^* = 1$) since $\theta_Y \neq 0^\circ$ in a situation of partial wetting, which is supported by the experimental results.

6.1.1.2 Film impregnation

For Eq. 6.4 to be valid, a liquid film has to impregnate the roughness of the textured surface. For a sponge to impregnate liquid, the solid-liquid interfacial energy γ_{sl} has to be lower than the solid-air interfacial energy γ_{sa} , which means that $\theta_Y < 90^\circ$ by the Young-Dupré relationship. The case of textured surfaces is more complicated since air-liquid interfaces are created and increase the total interfacial energy of the system. Bico et al. [17] have calculated the condition for which a film impregnates a regular textured surface of uniform pore size, as sketched in Fig. 6.3.

One imposes a small horizontal displacement dx of the film over a repetitive solid-liquid composite interface. The wetted area per unit length is $(r_S - \phi_S)dx$ because the dry area at the top

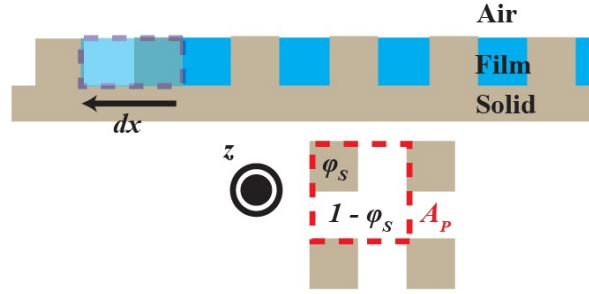


Figure 6.3: Impregnation of a film in a textured surface. The solid fraction ϕ_S and the projected area A_P are indicated in a subfigure.

of the plots is $\phi_S dx$. A free air-liquid area $(1 - \phi_S) dx$ is also created. The variation dE is given by:

$$dE = (r_S - \phi_S)(\gamma_{sl} - \gamma_{sa})dx + (1 - \phi_S)\gamma_{al}dx. \quad (6.5)$$

A film impregnates the textured surface if $dE < 0$ by loss of interfacial energy. By considering the Young-Dupré equation once more and Eq. 6.5, the condition $dE < 0$ means [17]:

$$\cos \theta_Y > \frac{1 - \phi_S}{r_S - \phi_S} = \cos \theta_c, \quad (6.6)$$

where θ_c represents the transition angle to the Wenzel state. Indeed, we have the following wetting behaviour on a hydrophilic textured surface:

- for $0 < \theta_Y < \theta_c$, which means $\cos \theta_Y > \cos \theta_c$, a liquid film impregnates the surface and the droplet sits on a solid-liquid composite surface. This corresponds to the upper right part of Fig. 6.1c and the curve is described by Eq. 6.4;
- for $\theta_Y > \theta_c$, which means $\cos \theta_Y < \cos \theta_c$, the wetting behaviour accurately follows the Wenzel model. The droplet follows the defects of the surface but the solid surface remains dry at the front of the droplet.

6.1.1.3 Hydrophobic textured surface

For a hydrophobic smooth surface, $\theta_Y > 90^\circ$ with $\gamma_{sa} < \gamma_{sl}$. The interfacial energy of the dry surface is lower than the interfacial energy of the wet surface. Providing that the Young-Dupré relationship is verified for every air-liquid-solid contact line, a textured surface can also be hydrophobic. In this situation, a liquid droplet sits on a solid-air composite surface by leaving air cushion in-between the pores. This configuration is sketched in Fig. 6.4.

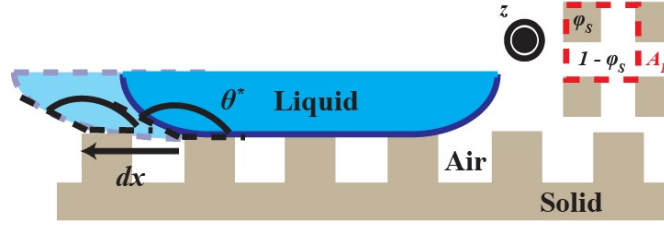


Figure 6.4: Liquid droplet sitting on a solid-air composite surface.

One can determine the apparent contact angle θ^* by considering once more the variation of interfacial energy dE when the air-liquid contact line advances by a small displacement dx . An air-solid interface of area $\phi_S dx$ is replaced by a solid-liquid interface of the same area. An air-liquid interface of area $(1 - \phi_S) dx$ is also created, as well as an air-liquid interface of area $\cos \theta^* dx$. The sum of these contributions gives:

$$dE = (\gamma_{sl} - \gamma_{sa})\phi_S dx + \gamma_{al}(1 - \phi_S) dx + \gamma_{al} \cos \theta^* dx. \quad (6.7)$$

Setting $dE = 0$ at equilibrium and using the Young-Dupré relationship yields:

$$\cos \theta^* = -1 + \phi_S (\cos \theta_Y + 1). \quad (6.8)$$

If one considers that the top of the plots is not flat, Eq. 6.8 becomes $\cos \theta^* = -1 + \phi_S (r_\phi \cos \theta_Y + 1)$, where r_ϕ is the texture roughness given by the ratio between the wetted area and the projected area at the top of a plot. This comprehensive equation is known as the Cassie-Baxter equation [123].

For any value of $\theta_Y > 90^\circ$, $\theta^* > 90^\circ$ and the surface is hydrophobic. Eq. 6.8 shows that $\cos \theta^*$ jumps to a value below $\phi_S - 1$ which can be close to -1, enhancing hydrophobicity.

6.1.1.4 Generation of liquid-infused surfaces

In §6.1.1.2, we have seen that a liquid is able to impregnate the roughness of the surface. By using an oil-based liquid of low air-liquid interfacial tension, we can indeed impregnate the texture to create a liquid-infused surface.

These liquid-infused surfaces, also known as SLIPS or LIPS, exhibit more interesting properties than common superhydrophobic surfaces, such as the non-pinning and the roll-off of liquid droplets (see Appendix D).

Eq. 6.6 gives the condition for which film impregnation occurs. A lubricating film appears if the

Young contact angle $\theta_Y < \theta_c$ where θ_c is determined by $\cos \theta_c = (1 - \phi_S)/(r_S - \phi_S)$. Playing on the roughness r_S and the solid fraction ϕ_S allows to find the right oil-texture combination. We always have $1/r_S > (1 - \phi_S)/(r_S - \phi_S)$, thus $\cos \theta_Y > 1/r_S$ is a sufficient condition to have film impregnation [111]. So the higher the roughness, the less constraining the condition for film impregnation, the easier the generation of liquid-infused surfaces for common types of oil (silicon oils, alkanes and siloxanes).

In our experiments, the equilibrium contact angles at the air-solid interface are pretty low below 20° and the roughness is 2 ($10 \mu\text{m} \times 10 \mu\text{m} \times 10 \mu\text{m}$ posts). The previous condition is always fulfilled and we can generate the desired liquid-infused surface.

6.1.2 Failure of textured surfaces

Owing to their repellent properties, textured surfaces are used in many applications from self-cleaning to drag reduction and biofouling (see Appendix D). However, because of failure mechanisms, they can lose their properties. In the case of superhydrophobic surfaces, we want to keep air pockets in the Cassie-Baxter regime, while for liquid-infused surfaces, we would like to keep the oil film impregnated in the texture. If one of these elements vanishes, textured surfaces lose their interest. The failure of both air and oil layers is mainly due to two types of stresses: normal and tangential.

6.1.2.1 Transition from the Wenzel to Cassie-Baxter regime

For Eq. 6.8 to be valid, air must be trapped in the pores of the textured surface. To determine the condition for which the trapping of air occurs, one writes the variation of interfacial energy dE for a unit area A_P between the configuration with air and the configuration without air under the liquid droplet, as described in Fig. 6.5.

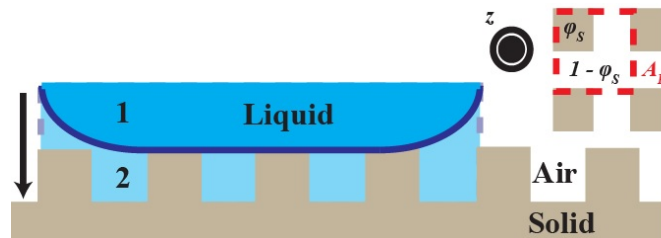


Figure 6.5: Transition from the regime of air cushion (1) to the Wenzel regime (2).

From one configuration to the other, an air-liquid interface of area $(1 - \phi_S)A_P$ disappears and

solid-liquid interfaces of area $(r_S - \phi_S)A_P$ replace solid-air interfaces of the same area. Thus, dE is given by:

$$dE = (\gamma_{sl} - \gamma_{sa})(r_S - \phi_S)A_P - \gamma_{al}(1 - \phi_S)A_P. \quad (6.9)$$

The regime of air cushion is favourable if $dE > 0$, which means that:

$$\cos \theta_Y < \cos \theta_c = \frac{\phi_S - 1}{r_S - \phi_S}. \quad (6.10)$$

Therefore, the wetting behaviour on hydrophobic textured surface is described by two regimes:

- when $\theta_c < \theta_Y < 180^\circ$, the regime of air cushion is stable and a liquid droplet sits on a solid-air composite surface. This corresponds to the lower left part of Fig. 6.1;
- when $90^\circ < \theta_Y < \theta_c$, the regime of air cushion is metastable and can transition to the Wenzel state although the Young angle is above 90° .

Indeed, in this latter case, the air-liquid interface can fail and fully wets the surface, as Eq. 6.9 suggests it. Calculations of interfacial energy actually provide a rough argument. Failure is rather induced by distortions of the air-liquid interface that can lead to its sagging. During a sagging event, the air-liquid interface can ultimately touch the bottom of the pores and transitions to a fully-wetted state. Sagging can be induced by an applied external pressure, the impact of a droplet or the mere Laplace pressure in the liquid droplet [185].

6.1.2.2 Impalement of superhydrophobic surfaces

The failure mechanisms for the sagging of superhydrophobic surfaces have been studied by Bartolo et al. [7]. They suggest that a drop pressure (due to the flow of liquid or a drop impact [152]) can push the air-liquid interface downwards. The drop pressure P_d has to overcome the capillary forces at the top of an array of posts for instance. The pressure force F_P is given by $F_P = P_d A_P (1 - \phi_S)$ where A_P is still the projected area of the post sample and ϕ_S the solid fraction. The capillary force is $F_C = N_P 2\pi \gamma_{ow} r_p |\cos \Theta|$ where $N_P = A_P \phi_S / \pi r_p^2$ for cylindrical posts of radius r_p is the number of posts and Θ the angle made by the air-liquid interface with the vertical axis in Fig. 6.6. The pressure P_d becomes:

$$P_d = \frac{2\phi_S}{1 - \phi_S} |\cos \Theta| \frac{\gamma_{ow}}{r_p}. \quad (6.11)$$

Then, two mechanisms are possible and presented in Fig. 6.6. The first one is the “touch down”

scenario. The curvature of the air-liquid interface increases with the pressure. The distance between the lowest point of the interface and the bottom of the cavity decreases up to zero. At this point, air pockets cannot be trapped any more and the superhydrophobic surface loses its repellent property. In Eq. 6.11, one can determine the critical contact angle Θ (which depends on the height h) for which the touchdown occurs, and thus deduce the pressure threshold for touchdown P_{imp}^t .

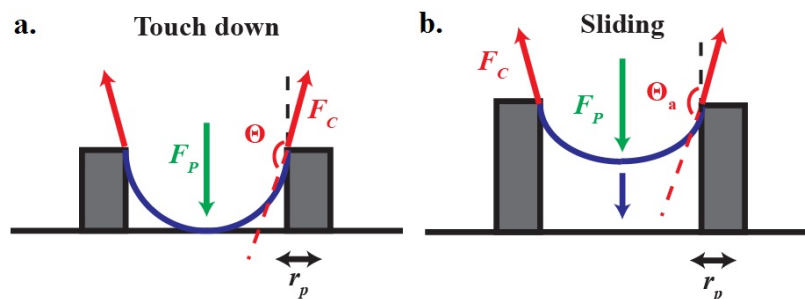


Figure 6.6: a. Touch down scenario [7]. b. Sliding scenario [7].

The second mechanism is the “sliding” scenario for higher posts. Due to the increasing pressure, the interface curves more and more downwards and the contact angle Θ increases until reaching the advancing contact angle Θ_a . When $\Theta = \Theta_a$, the air-liquid interface spontaneously slides downwards to the bottom of the cavity. Once more, by setting Θ_a as the threshold value of contact angle for impalement, one can determine a pressure threshold for sliding P_{imp}^s .

As a consequence, a criterion for the impalement of superhydrophobic surfaces is that the external pressure $P_d > \min(P_{imp}^t, P_{imp}^s)$.

6.1.2.3 Shear-driven drainage of liquid-infused surfaces: scaling arguments

The failure of superhydrophobic surfaces originates from potential normal stresses and contact angle hysteresis applied to the air-water interface in-between the roughness of the surface. As a consequence, air pockets are not sustainable and the surface gets fully wet. For liquid-infused surfaces, applying a normal stress to the lubricating layer deforms the air-oil interface downwards but would certainly not lead to the complete disappearance of the oil film.

However, liquid-infused surfaces are sensitive to another type of failure mechanisms that involves the tangential stresses exerted by the flow of an outer fluid in which they are immersed. This is what Wexler et al. [198] call the shear-driven drainage of liquid-infused surfaces. All the calculations stated in the following can be found in [198] and we summarize here the main ideas.

For experiments with a groove geometry (see Fig. 6.7), Wexler et al. explained the drainage dynamics of the oil film for pure aqueous solutions as the outer phase [198]. The ratio between the channel width W and height H is high, 40:1 or 20:1, and the channel is much deeper than the pattern ($H \gg h$). With the low viscosity ratio $\lambda = \eta_w/\eta_o \ll 1$ (η_w and η_o are respectively the water and the oil density) and the no-slip boundary condition, we can consider a parabolic velocity profile in the outer flow. This profile corresponds to a planar Poiseuille-like flow [167] (see Fig. 6.7a) for which the shear stress at the oil-water boundary is $\tau_{xy} \approx 6\eta_w Q/(WH^2)$, where Q is the injection flow rate. As sketched in Fig. 6.7, the external flow shears the oil-water interface and drags oil downstream out of the pattern. At short times, the tangential stresses in the water and the oil phase are equal, thus $\tau_{xy} \sim -\frac{\eta_o}{h} \frac{dL}{dt}$, where h is the height of the posts and L the retention length.

Locally, the applied shear deforms the oil-water interface, as sketched in Fig. 6.7 and Fig. 6.16. When the dynamic contact angle at this pinned interface reaches the receding contact angle θ , the interface slides to the bottom of the posts [7].

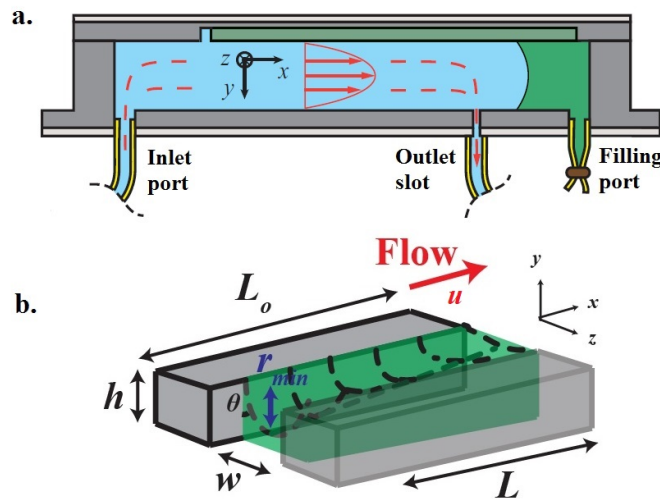


Figure 6.7: a. Shear-driven drainage of oil in a groove geometry [198]. b. Local configuration of the oil-water interface. The parameters L_o , $L(t)$, h , w , θ , r_{min} and u are, respectively, the length of the groove, the retention length, the height of the groove, the spacing in a groove, the receding contact angle, the minimal radius of curvature and the flow velocity.

The deformation of the liquid-liquid interface induces a difference of curvature between the upstream and the downstream ends for longer times. The capillary pressures are $\Delta p_C = p_w - p_o = \gamma_{ow}/r_{min}$ upstream (p_w and p_o are, respectively, the pressures in the outer fluid and the oil phase) and $\Delta p_C = 0$ downstream. The pressure gradient in the aqueous phase can be written as $dp_w/dx = -12Q\eta_w/WH^3$. Thus, the pressure difference Δp_w between the inlet and the out-

let of the channel of length $L_{channel}$ is $\Delta p_w \approx -12Q\eta_w L_{channel}/WH^3 \approx 4 \times 10^2$ Pa for $Q = 2$ mL/min. This value is small compared to the capillary pressure and the pressure difference in the oil phase is directly $\Delta p_o = \gamma_{ow}/r_{min}$. Thus, the pressure p_o in the trapped fluid is lower upstream than downstream and the pressure gradient drives an oil counterflow within the liquid trapped between the posts. Oil is being extracted so long as the shear-driven flux is higher than the capillary pressure-driven flux. The maximum retention length L_∞ is reached when the shear-driven flux is exactly balanced by the pressure-driven flux. In terms of stresses, $\tau_{xy}/h \sim (\gamma_{ow}/r_{min})/L_\infty$ and $L_\infty \sim h\gamma_{ow}/(r_{min}\tau_{xy})$ with r_{min} the minimum radius of curvature of the oil-water interface.

6.1.2.4 Shear-driven drainage of liquid-infused surfaces: analytical resolution

The comprehensive resolution of the shear-driven drainage, and particularly the time dependence, is done by solving the Stokes' equation. Indeed, the Reynolds number Re is low with $Re = \rho_o Qh/(WH\eta_o) \approx 0.01 \ll 1$ and the Bond number $Bo = w^2g(\rho_o - \rho_w)/\gamma_{ow} = 10^{-6}$ (ρ_o is the oil density and ρ_w the water density) is also low, so gravity is negligible. The flow is unidimensional along the x direction, so the streamwise velocity u is solution of:

$$\begin{aligned} \eta_o \Delta u &= -\frac{dp_o}{dx} \quad , \\ u(-\frac{h}{2}, z) &= 0 \quad , \quad u(y, -\frac{w}{2}) = 0 \quad , \\ u(y, -\frac{w}{2}) &= 0 \quad , \quad \eta_o \left(\frac{\partial u}{\partial y} \right)_{y=h/2} = \tau_{xy} \quad , \end{aligned} \tag{6.12}$$

where p_o is the pressure in the oil phase. We apply the no-slip condition at the side and bottom walls and the prescribed shear stress τ_{xy} at the oil-water interface. The velocity u is a superposition of two components, a shear-driven contribution u_s and a pressure-driven contribution u_p . Thus, we can solve the following system of equations for each component by separation of variables:

$$\begin{aligned} \eta_o \Delta u_s &= 0 \quad , \quad \eta_o \left(\frac{\partial u_s}{\partial y} \right)_{y=h/2} = \tau_{xy} \quad , \\ \eta_o \Delta u_p &= -\frac{dp_o}{dx} \quad , \quad \eta_o \left(\frac{\partial u_p}{\partial y} \right)_{y=h/2} = 0. \end{aligned} \tag{6.13}$$

We find the following solutions for the shear-driven oil flux q_s and the pressure-driven oil flux q_p :

$$\begin{aligned}
q_s &= c_s \frac{\tau_{xy} w h^2}{\eta_o} & \text{with} & & c_s &= \frac{1}{2} - \frac{4h}{w} \sum_{n=0}^{\infty} \frac{(-1)^n}{\lambda_n^4} \tanh\left(\frac{\lambda_n w}{2h}\right) , \\
q_p &= -c_p \frac{w h^3}{\eta_o} \frac{dp_o}{dx} & \text{with} & & c_p &= \frac{1}{3} - \frac{4h}{w} \sum_{n=0}^{\infty} \frac{(-1)^n}{\lambda_n^5} \tanh\left(\frac{\lambda_n w}{2h}\right) ,
\end{aligned} \tag{6.14}$$

where $\lambda_n = (n + 1/2)\pi$ are the eigenvalues deduced from the development in Fourier series. We also have $dp_o/dx \approx \Delta p/L = \gamma_{ow}/r_{min}L$, thus $q_p = -c_p w h^3 \gamma_{ow}/r_{min}L$.

By volume conservation, the sum of both fluxes q_s and q_p must be equal to the drained flux of oil q_d . The drained flux q_d is equal to dV/dt with V the volume of oil in the grooves and the time t . This volume is determined by integrating the cross-sectional area along the x direction and considering a linear variation of the curvature radius from $-1/r_{min}$ upstream to 0 downstream. We find that:

$$\begin{aligned}
q_d &= -c_d w h \frac{dL}{dt} , \\
\text{with} \quad c_d &= 1 - \frac{r_{min}}{h} \left(1 - \sqrt{\frac{1}{4} - \frac{w^2}{16r_{min}^2}} \right) + \frac{r_{min}^2}{wh} \csc^{-1} \left(\frac{2r_{min}}{w} \right) .
\end{aligned} \tag{6.15}$$

Equating Eq. 6.15 with the sum of q_s and q_p from Eq. 6.14 leads to the following dependence on the time t for the retention length $L(t)$:

$$\begin{aligned}
q_d &= q_s + q_p , \\
c_d w h \frac{dL}{dt} - c_p w h^3 \frac{\gamma_{ow}}{\eta_o r_{min}} \frac{1}{L} + c_s \frac{\tau_{xy} w h^2}{\eta_o} &= 0.
\end{aligned} \tag{6.16}$$

When $dL/dt = 0$, $q_s = q_p$ and we find the maximum retention length $L_\infty = \frac{c_p h \gamma_{ow}}{c_s r_{min} \tau_{xy}}$, which we have already demonstrated by scaling arguments. The retention length L is solution of:

$$L(t) = L_o - \frac{L_\infty}{t_c} t + \frac{L_\infty}{t_c} \ln \left(\frac{\frac{L_o}{L_\infty} - 1}{\frac{L}{L_\infty} - 1} \right) , \tag{6.17}$$

with the characteristic time of drainage $t_c = c_d c_p \eta_o \gamma_{ow} / (c_s^2 r_{min} \tau_{xy}^2)$. When $t \rightarrow 0$, $L \rightarrow L_o$, L is linear with time, as predicted by scaling law. Fig. 6.8 shows the dimensionless collapse between Eq. 6.17 and experimental measurements.

By looking at L_∞ , the retention of oil inside the textured surface can be controlled by playing on the oil-water interfacial tension, the contact angle (since $\cos \theta = w/2r_{min}$ when the interface does not touch the bottom of the cavities) and the aspect ratio w/h . It is typically easier to manipulate

the aspect ratio to design the most resistant liquid-infused surface. Ideally, the cavities should be high and large to get the smallest aspect ratio as possible.

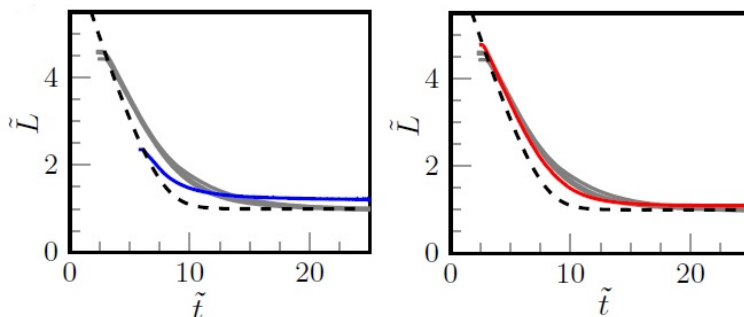


Figure 6.8: Dimensionless retention length $\tilde{L} = L/L_\infty$ as a function of the dimensionless time $\tilde{t} = t/t_c$. The blue, the red and the gray curves correspond to experimental results of drainage of silicon oils by water, respectively for oil viscosity $\eta_o = 42.7$ mPa.s and injection flow rate $Q = 1$ mL/min, $\eta_o = 201$ mPa.s and $Q = 2$ mL/min and $\eta_o = 42.7$ mPa.s and $Q = 2$ mL/min. The dotted lines are the theoretical predictions [198]. Both figures are extracted from [198].

6.2 Surfactant-driven oil extraction from micropatterned channels

The results concerning the surfactant and the foam-driven (next section) oil extraction from micropatterned channels have been submitted to the *Langmuir* journal [130]. They were presented at the *Droplets 2015* and *Eufoam 2016* conferences. This project was carried out with the help of Dr. Jason S. Wexler and Augustin Guibaud.

The properties of liquid-infused surfaces, highlighted in §D.2.1, depend on the robustness of the lubricating layer, similarly to the existence of air trapping for superhydrophobic textured surfaces. As shown in §6.1.2.3, the lubricating layer can be subject to an external shear flow when the surface is immersed in an another fluid environment (typically in drag reduction and bio-fouling). Subsequently, the impregnated film disappears and the surface loses its interest. In this section, we study the shear-driven extraction of oil from liquid-infused surfaces when surfactants - usually used in many extraction processes to decrease the oil-water interfacial tension - are added to the aqueous solutions. We use the framework of Wexler et al. [198] described in §6.1.2.3 and §6.1.2.4. To some extent, we also wonder how it is possible to extract oil from the roughness of a surface, which has potential applications in oil recovery issues. We are also aware that the nature of the interactions is only interfacial between the texture and the main shear flow. However, in the general context of oil recovery, the similitude to oil extraction is to be underlined.

6.2.1 Materials

We choose an array of microfabricated and equally-spaced posts as the texture to study the drainage of liquid-infused surfaces when the external shear flow contains surfactants. Compared to a groove geometry, cavities are connected to each other in the post geometry, which allows to look at collective phenomena within the posts. The patterned geometry is imprinted on the upper side of a microfluidic channel, as shown in Fig. 6.9. The system mimics an oil-filled porous microfracture where the assembly of posts represents a set of oil-filled and connected pores, which is a feature of randomly rough systems with open pores.

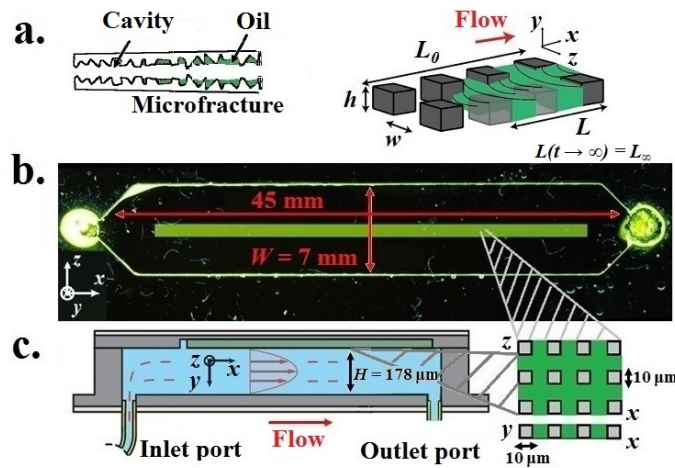


Figure 6.9: Geometry of the microfluidic channel with the liquid-infused micropattern imprinted on the upper side of the channel. a. Analogy between a real microfracture and a liquid-infused substrate. b. Top-view of the channel, with the oil fluorescing green-yellow. c. Side-view of the channel consisting of one wall with an array of posts.

6.2.1.1 Characteristics of the textured surface and the tested fluids

The materials and the microfabrication are the same as those used by Wexler et al. [198] and are sketched in Fig. 6.9b-c. The pattern consists of cubic posts ($w = h = 10 \mu\text{m}$ on a side), which are equally spaced at a distance of $10 \mu\text{m}$. The pattern is generated by depositing an epoxy adhesive on a PDMS (poly(dimethyl)siloxane) mold. We first etch a silicon wafer to draw the model for the texture. The etching is done inside the wafer by removing silicon. On this wafer, we deposit some PDMS that covers the cavities created by the etching. After baking, we obtain a mold of post pattern on which we deposit the epoxy.

The pattern and the channel, lying on black borosilicate glass, are molded in an epoxy adhesive (Norland Optical Adhesive 81) by the “sticker technique” [8]. The details of this technique is

described in Appendix C. The channels are 7 mm wide, 178 or 89 μm high, and 45 mm long. The channel has two ports: one inlet port at the upstream end and one outlet port at the downstream end. The 36 mm long and 1 mm wide pattern is located near the centerline of the channel and aligned with the inlet and outlet ports at a distance of 5 mm from both ports. The pattern consists of cubic posts (10 μm on a side), which are equally spaced at a distance of 10 μm , and ends with a 1 mm by 1 mm open well for flow entry (Fig. 6.9b).

The characteristics of the tested fluids are summarized in Table 6.1, with the dynamic viscosities measured in a rheometer (Anton-Paar) with a cone-plate geometry. The outer fluid is a surfactant solution. We use two types of surfactants: either SDS (sodium dodecyl sulfate) with different concentrations from 0.1 g/L to 10 g/L ($cmc \approx 2$ g/L), or a combination of co-surfactants, CAPB (cocoamidopropylbetaine), SLES (sodium laurylethyl sulfate), Mac (myristic acid) and 10 wt% glycerol, already presented in Chapter 2 and 5 [9, 81], with different surfactant concentrations from 0.005 wt% to 2 wt% (critical micellar concentration $cmc \approx 0.1$ wt%).

Aqueous solution - Oil	η_w	η_o
CAPB+SLES+MAc+10% glycerol - Olive oil (O)	1.4	68.5
CAPB+SLES+MAc+10% glycerol - Silicon oil 1 (PDM-7050 - S1)	1.4	201
CAPB+SLES+MAc+10% glycerol - Silicon oil 2 (PDM-7040 - S2)	1.4	42.7
SDS - Olive oil	1	68.5

Table 6.1: Characteristics of the aqueous solution - oil combinations. Here, η_w (mPa.s) and η_o (mPa.s) are, respectively, the shear viscosity of water and oil.

The lubricating oils, which initially fill the patterned substrate, are olive oil (commercial and Sigma-Aldrich) and two silicon oils (Gelest PDM - 7040 and 7050) containing a small amount of fluorescent dyes (from Tracerline) (1:100). In the following, all the interfacial tensions are measured by the pendant drop technique with a precision of ± 0.5 mN/m. Fig. 6.10 presents the variations of the equilibrium oil-water interfacial tension γ_{ow} with the surfactant concentration c . As expected, γ_{ow} decreases when c increases with the $cmc \approx 2$ g/L in both SDS-olive oil and CAPB-SLES-Mac-olive oil cases. As explained below, we clear the channel with the surfactant solution to leave oil trapped in the texture of the surface at a very slow velocity (0.002 mL/min). Thus, we give time for the system to equilibrate in terms of surfactant dynamics, which allows us to use the values presented in Fig. 6.10.

Table 6.2 summarizes the different values for the interfacial tensions and the entry E and S spreading coefficients defined in §2.1.1.

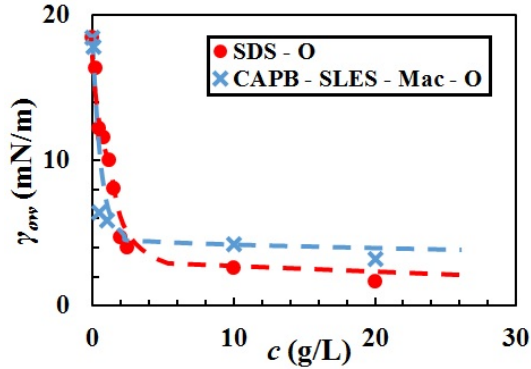


Figure 6.10: Equilibrium oil-water interfacial tension γ_{ow} (mN/m) as a function of the surfactant concentration c (g/L) for SDS-Olive oil (O) and CAPB-SLES-Mac-Olive oil (O) combinations. The blue and the red dashed lines are guide lines.

Interfacial tension	Solution	Water	CAPB-SLES-Mac 10% gly	SDS - 2 g/L
γ_{aw}	Air	73	23.7	39
Interfacial tensions	Oil Solution	Olive 68.5 0.92	Si 42.7 1.06	Si 201 1.09
γ_{ao}	Air	32.2	22.6	22.6
γ_{ow}	Water	24.8	29	28.2
	CAPB-SLES-Mac-10% gly	5.2	4.2	4.2
	SDS - 2 g/L	4.7		
$E - S$	Water	65.6 16	79.4 21.4	78.6 22.2
	CAPB-SLES-Mac-10% gly	-3.3	5.3	5.3
		-13.7	-3.1	-3.1
		11.5		
	SDS - 2 g/L	2.1		

Table 6.2: Interfacial tensions γ_{aw} , γ_{ao} and γ_{ow} (mN/m) with calculated entry E and spreading coefficients S of the oils and surfactant solutions. The dynamic viscosity η_o (mPa.s), the density ρ_o (for each oil), and the surfactant concentration C (for each surfactant solution) are given.

6.2.1.2 Fluid injection

At the start of an experiment, the channel is completely filled with oil from the downstream port. Then, the entire channel is cleared by the flow of the outer aqueous phase at a low injection rate (0.002 mL/min), which leaves oil trapped between the posts, while the oil in excess is evacuated to a reservoir from the outlet port. This procedure prevents oil extraction from being disturbed by an excess of oil. Once the main channel is cleared of oil, the outer fluid is injected at a constant flow rate between 0.05 mL/min and 8 mL/min, corresponding to average flow velocities.

6.2.2 Experimental observations and results

The experimental observations are made under UV or blue light (with a yellow filter from Tiffen in front of the camera objective) to ensure a strong contrast between the black glass background and the fluorescent oil trapped in the pores. Snapshots of the oil extraction process are taken every minute.

6.2.2.1 Extraction patterns

A typical time series of the oil extraction pattern is shown in Fig. 6.11. Depending on the flow rate Q and the oil-water interfacial tension γ_{ow} , the process shows two different patterns. In one case, for sufficiently low Q and high γ_{ow} , the draining front advances uniformly, as observed previously by Wexler et al. with pure aqueous solutions [198]. We define a retention length $L(t)$ (t is the time) and a steady-state retention length L_∞ (Fig. 6.9a). In a second case, for sufficiently high Q and low γ_{ow} , the draining front still propagates along the flow direction but is more irregular, leaving oil patches behind it. Since it is difficult to define a retention length in this second situation, we introduce the extraction efficiency α to quantify oil extraction from the porous substrate. Specifically, we define $\alpha = V_d/V_0$ which is the ratio between the volume of extracted oil V_d and the initial volume of oil V_0 between the posts. The parameter α varies from 0, when the pores are completely filled, to 1, when they are completely empty.

6.2.2.2 Efficiency curves

To measure $\alpha(t)$, we record the fluorescence intensity I in the pattern by using the sum of grey levels after image processing with ImageJ software. Neglecting photobleaching that occurs for a timescale longer than our experimental time, we assume that the fluorescence level is approximately proportional to the volume of the remaining oil $V_0 - V_d$, since the depth of the posts is small. Given that light conditions can change from one experiment to another, we only have access to $\alpha \approx 1 - I/I_0$, where I_0 is the initial fluorescence intensity between the posts for each experiment. In Fig. 6.12, we report α as a function of time t for the different liquids.

When varying one parameter (Q , γ_{ow} , η_o or the channel height H) during flow of a surfactant solution, α follows one typical evolution, as shown in Fig. 6.12. As time increases, α increases quickly before slowing down and eventually reaching a maximum value α_∞ at long times. For a given time and considering the different possible material properties, we find that oil recovery is more efficient if interfacial tension is low and the aqueous phase flow rate is high. Efficiency is

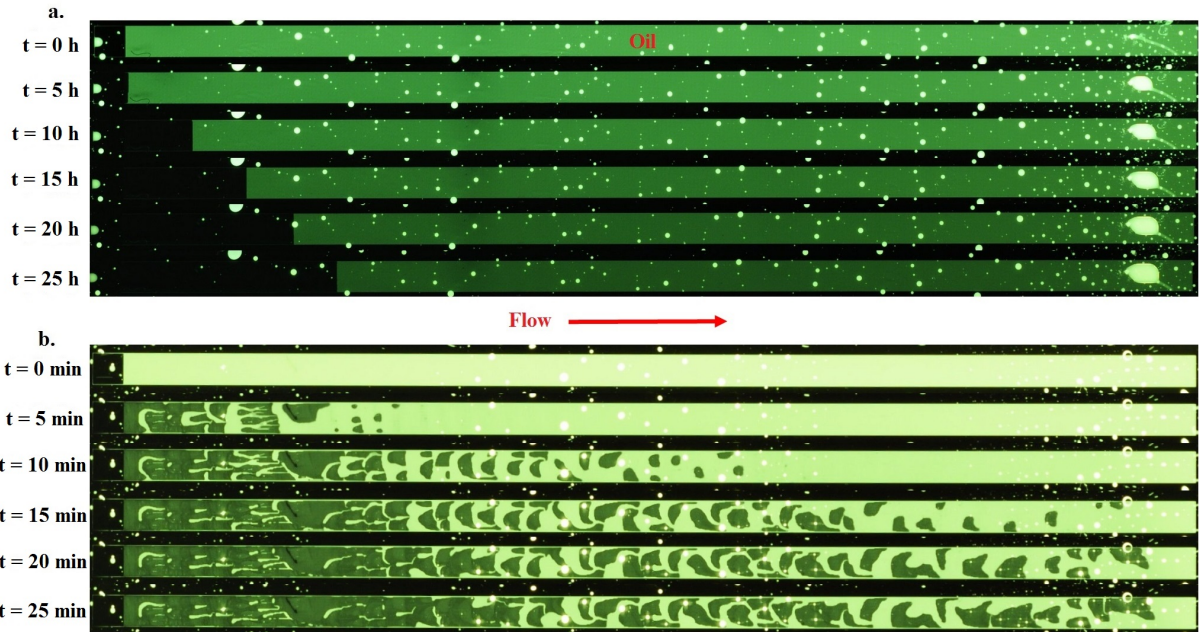


Figure 6.11: Top views of typical oil extractions (olive oil) by a surfactant solution (CAPB - SLES - Mac - 10 wt% glycerol). Fluorescent dyed oil appears green-yellow. The small green-yellow dots correspond to some oil droplets stuck on the epoxy surface when the channel was initially cleared of oil in the first place. The flow is from left to right. a. Extraction with a uniform front; $Q = 0.05$ mL/min and $\gamma_{ow} = 4.2$ mN/m, time interval: 5 h. b. Extraction with an unstable pattern; $Q = 5$ mL/min and $\gamma_{ow} = 4.2$ mN/m, time interval: 5 min.

also enhanced if the oil viscosity and channel height are low.

Next, we report α as a function of the injected volume Qt (Fig. 6.13). The data is organized by the capillary number $Ca = \eta_w Q / (WH\gamma_{ow})$, where W is the channel width. The six different data sets in Fig. 6.13 correspond to two capillary numbers $Ca \approx 0.005$ and $Ca \approx 0.015$. The experimental data, for a given capillary number, collapses on one single curve, suggesting that α depends on Qt and Ca .

6.2.3 Effect of surfactants on the extraction dynamics

We explain the experimental observations and results from §6.2.2 by developing and using the model introduced by Wexler et al. [198] in §6.1.2.3. We extend their work by considering aqueous liquids containing surfactants rather than pure aqueous solutions. This step builds upon earlier work by Jacobi et al. [95], who highlighted that traces of surfactants could induce unusual drainage behavior.

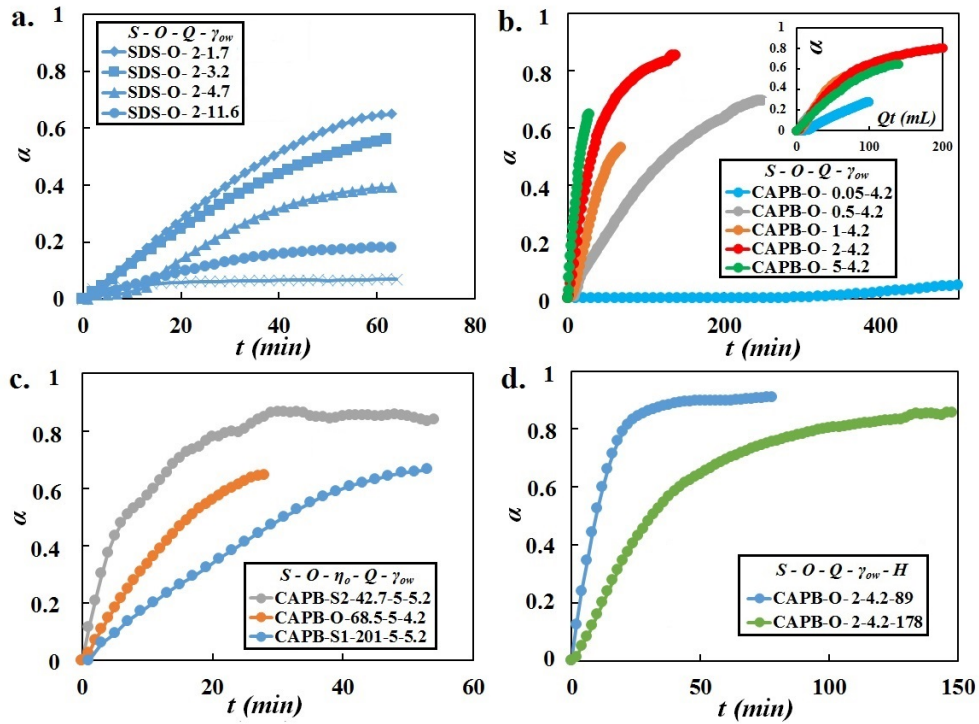


Figure 6.12: Extraction efficiency α as a function of time t for different draining liquid - oil combinations with the following variable parameters: a. γ_{ow} (mN/m). b. Q (mL/min) (Inset: α as a function of Qt). c. η_o (mPa.s). d. H (μ m). S and O are, respectively, the surfactant type, the oil type.

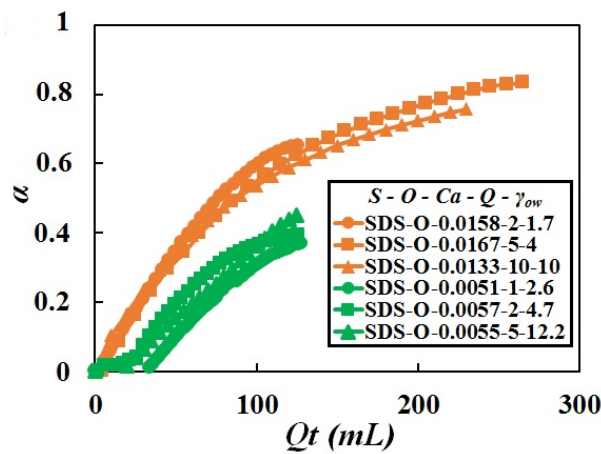


Figure 6.13: Extraction efficiency α as a function of the injected volume Qt for SDS - olive oil combination, with the capillary number $Ca \approx 0.015$ and 0.005 defined in Eq. 6.19b.

The comprehensive resolution of the shear-driven drainage, and particularly the time dependence, refers to §6.1.2.3 and is used in the following.

6.2.3.1 Variations of the contact angle

According to Wexler et al. [198], we can write the extraction efficiency $\alpha(t) = 1 - L(t)/L_o \sim \tau_{xy}ht/\eta_o$ for short times, where L_o is the length of the pattern (see Fig. 6.9) and $L(t)$ the residual length of oil in the pattern. We assume that the oil layer percolates through the connected posts. Thus, it is always possible to define a pressure path within the porous system. Oil is being extracted because the shear-driven flux is higher than the capillary pressure-driven flux. The maximum efficiency $\alpha_\infty = 1 - L_\infty/L_o$ is reached when the shear-driven flux is exactly balanced by the pressure-driven flux. Rewriting the complete steady-state solution of Wexler et al. [198], we find that:

$$\alpha_\infty = 1 - \frac{c_p h \gamma_{ow}}{c_s r_{min} \tau_{xy} L_o}, \quad (6.18)$$

where c_p and c_s are the numerical factors linked to the geometry of the channel, defined in Eq. 6.14.

The details of the comprehensive original time-dependent drainage theory explained in §6.1.2.4 allow to determine the efficiency $\alpha = 1 - L/L_\infty$ as a function of time t . Rewriting the time-dependent theory with $\alpha(t)$ and α_∞ as the main variables, we find:

$$\alpha + (1 - \alpha_\infty) \log \left(\frac{\alpha_\infty}{\alpha_\infty - \alpha} \right) = \frac{6c_s h \eta_w}{WH^2 c_d L_o \eta_o} Qt, \quad (6.19a)$$

$$\alpha_\infty = 1 - \frac{c_p H h \cos \theta}{3c_s L_o w Ca}, \quad (6.19b)$$

where c_d is the numerical factor depending on the receding contact angle θ at the oil-water interface (see Eq. 6.15). We also introduce the capillary number Ca and $\cos \theta = w/2r_{min}$. For $\cos \theta < 0$, $\theta > 90^\circ$ and the pressure-driven flux does not create a counterflow but enhances the flow downwards, which leads to a complete oil extraction. For our experiments, $w = h$. Thus, c_d can be expressed as:

$$c_d = 1 - \frac{1}{2 \cos \theta} \left(1 - \frac{1}{2} \sqrt{1 - \cos^2 \theta} \right) + \frac{1}{4 \cos^2 \theta} \csc^{-1} \left(\frac{1}{\cos \theta} \right). \quad (6.20)$$

Subsequently, we deduce θ from the confocal microscope measurements of the interface deflection at different points along the porous substrate, when the pinned oil-water contact line starts receding. A local close-up on the oil-water interface is shown in Fig. 6.14.

We relate the curvature radius r_{min} to the deflection δ by the following geometrical relationship:

$$r_{min} = \delta + \sqrt{r_{min}^2 - \left(\frac{w}{2}\right)^2}. \quad (6.21)$$

Solving Eq. 6.21 yields $r_{min}^2 = (1/2\delta)^2((w/2)^2 - \delta^2)^2 + (w/2)^2$. We finally find that:

$$r_{min} = \frac{\delta}{2} \left(1 + \left(\frac{w}{2\delta}\right)^2 \right). \quad (6.22)$$

Thus, $\cos \theta = w/2r_{min}$ enables to determine θ from Eq. 6.22.

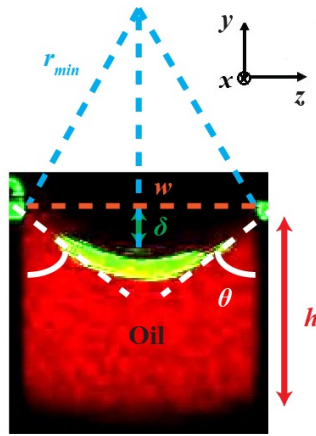


Figure 6.14: Confocal snapshot of the oil-water interface in the texture cavity. The geometrical parameters are indicated on the picture: δ is the deflection.

We report the values of θ with respect to Ca in Fig. 6.16 and we notice a systematic variation of θ between 0° and 90° . Such a variation has been observed when the contact line is perpendicular to the flow direction and moves streamwise with the flow: this is the well-known Tanner-Hoffmann law [77, 79, 90, 179] which relates the variation of the dynamic contact angle θ_d at an air-liquid interface moving across a solid substrate with respect to the capillary number with the finding that $\theta_d \propto Ca^{1/3}$.

For liquid-liquid interfaces, Fermigier et al. [68] have observed the same kind of variation and use the Cox law [46, 92] to model the movement of a glycerin-silicone contact line in a capillary tube, which depends on Ca and the viscosity ratio $\lambda = \eta_w/\eta_o$, as sketched in Fig. 6.15a. In our case, it is difficult to apply the aforementioned model since the contact line recedes transversely to the main flow and θ is defined in the post and flow cross-section, as sketched in Fig. 6.15b.

The velocity profile in the vicinity of the contact line is unknown and might not be parallel to the motion of the contact line. However, from our contact angle observations and measurements, a

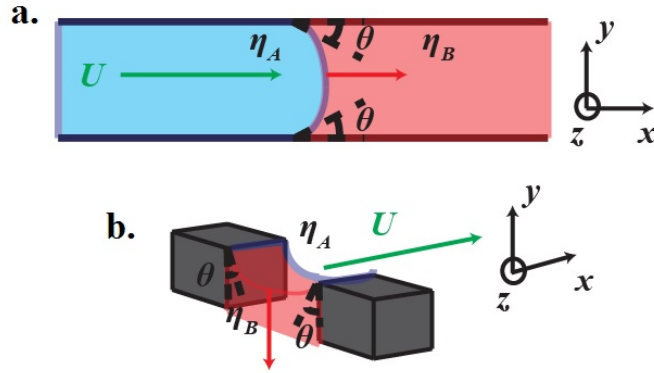


Figure 6.15: a. Movement of the A - B interface parallel to the flow of mean velocity U with the viscosity ratio $\eta_B/\eta_A > 1$. b. Movement of the same A - B interface for our post pattern with the interface receding perpendicular to the main flow of mean velocity U .

dependence of θ on Ca can be similarly reported.

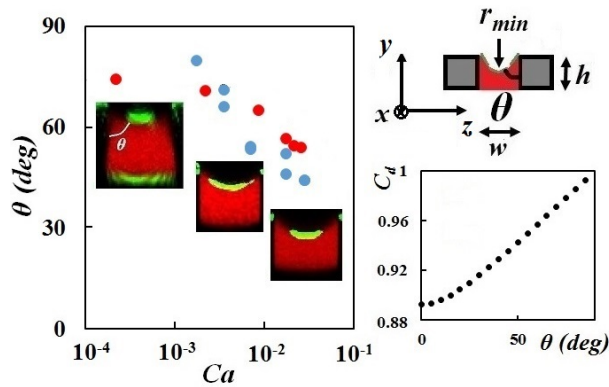


Figure 6.16: Measurements of the receding contact angle θ as a function of Ca for CAPB - olive oil (red dots) and CAPB - silicon oil 1 (blue dots) combinations. Oil appears red in the confocal microscope and the green line is the laser reflection between the glass and the aqueous phase. Lower right: Evolution of the numerical factor c_d with respect to θ .

6.2.3.2 Comparison between the predictions and the experimental results

The coefficient c_d does not change very much, from 0.893 to 0.993, when θ varies from 0° to 90° . Considering the small variations of c_d , Eqs. (6.19a - 6.19b) are in good agreement with our experimental observations in terms of the dependence in Fig. 6.12: α depends on Qt , η_o , the geometry of the channel and Ca . With the measured values of θ and the theoretically deduced numerical factors $c_s = 0.0764$, $c_p = 0.0573$, which enable the calculation of α_∞ in Eq. (6.19b) and c_d from Eq. (6.20), we rescale the data sets. In Fig. 6.17a, we represent the experimental efficiency

α_{exp} as a function of $g(t) = \frac{6c_s h \eta_w}{WH^2 c_d L_0 \eta_o} Qt$, which is the right-hand side of Eq. (6.19a), with CAPB-SLES-Mac as the outer phase and three different oils as the inner phases. All curves collapse onto a master curve for $\alpha_{exp} < 0.4$ and $g(t) < 0.5$, which suggests that the theory reasonably predicts the linear time dependence of extraction dynamics at short times. To go further, Fig. 6.17b shows the collapse between $f(\alpha_{exp}) = \alpha_{exp} + (1 - \alpha_\infty) \log\left(\frac{\alpha_\infty}{\alpha_\infty - \alpha_{exp}}\right)$ and $g(t)$ for the entire time frame. The predictions of Wexler et al. [198] account for the observed dynamics if we consider a variation of the receding contact angle due to the addition of surfactants, which was not observed with pure solutions.

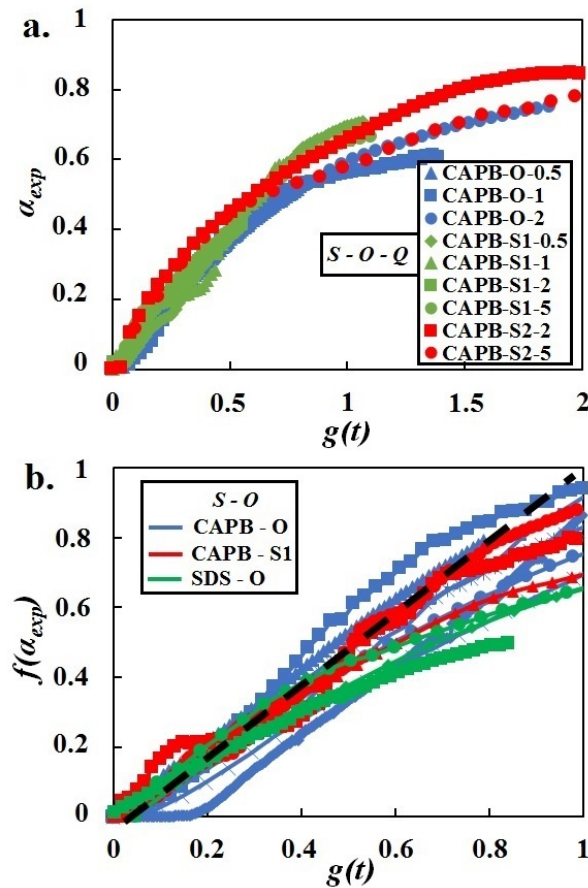


Figure 6.17: a. Experimental efficiency α_{exp} as a function of $g(t)$ for CAPB - olive oil, CAPB - silicon oil 1 and CAPB - silicon oil 2 combinations. b. $f(\alpha_{exp})$ as a function of $g(t)$ for different surfactant-oil combinations. The black dashed line is the theoretical prediction (Eq. (6.19a))

6.2.4 Extraction instability

As seen in Fig. 6.11b, the drained front loses its uniformity as Q increases and γ_{ow} decreases, leaving patches of oil between the posts. Fig. 6.19a shows the instability for both connected posts and independent grooves, indicating that this instability occurs for multiple types of surface texture.

6.2.4.1 Instability of viscous stratification

The appearance of these stable and unstable regimes, reported in Fig. 6.19b, could be caused by the flow of two superposed layers of fluids of different viscosities (the aqueous solution and the underlying oil layer trapped in-between the posts). Indeed, it has been long known that such a two-fluid shear flow can be unstable [33, 91, 204]. In particular, when gravity and interfacial tension are neglected, Yih [204] and Hooper et al. [91] have shown that the inertial terms of the Navier-Stokes equations are responsible for the development of the instability, even in the limit of low Reynolds numbers. Instabilities appear because of the jump in the slope of the velocity profile at the interface between both fluids. The discontinuity engenders the development of velocity disturbances, i.e. inertia-related vorticities that disturb the interface from the base flow. Long-wave and short-wave instabilities appear if $\eta_o > \eta_w$ and $h < H - h$.

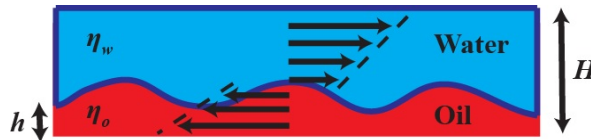


Figure 6.18: Unstable two-layer Couette flow with layers of different viscosities η_w and η_o and different thickness h and $H - h$.

6.2.4.2 Surfactant-induced instability

However, in our case, the capillary number is low, so we expect that interfacial tension plays a significant role. The destabilizing role of surfactants on the interface recalls the work of Frenkel et al. [70] and Blyth et al. [18] who showed that the presence of insoluble surfactants at the interface can trigger the growth of interfacial waves in a two-layer channel flow, even in the absence of inertia, provided that shear flow occurs. From their calculations, a surfactant-free system is stable, which corresponds to the system used by Wexler et al. [198] where the extracting front remains uniform along the section of the post pattern. In the two-layer geometry, the growth rate of the instability increases with the Marangoni number $M \propto C^*/\gamma_{ow}^*$ where C^* and γ_{ow}^* are,

respectively, the initial interfacial concentration of surfactants and the initial oil-water interfacial tension. We also observe that very low capillary numbers can be stable as the range of unstable wavenumbers is reduced [18]. But the instability is amplified for very low interfacial tension, like in our experimental observations. Thus, this would be the first experimental observation of the destabilizing role of surfactants in a two-layer channel flow. Yet, other types of two-fluid instabilities can also be considered, such as the fingering instabilities [184] appearing in the transverse direction to the flow for the displacement of a thin film by body or shear forces.

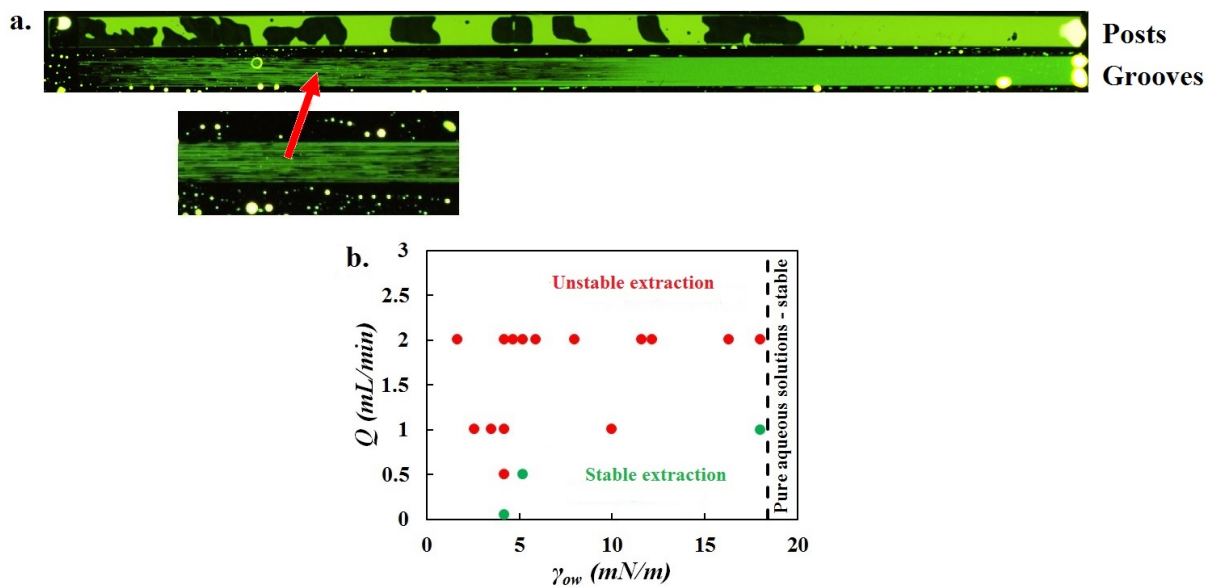


Figure 6.19: a. Typical unstable extraction pattern for posts and grooves with the same height and width. The surfactant solution - oil combination is SDS (2 g/L) - olive oil; $Q = 2$ mL/min and $t = 60$ min. Contrast is enhanced in the snapshots. b. Phase diagram where each point (γ_{ow}, Q) represents an experiment with the CAPB - olive oil, the CAPB - silicon oil 1 and the SDS - olive oil combinations. Unstable extraction is represented by red dots and stable extraction by green dots. The dashed black line defines the stable regime for pure aqueous solutions - olive oil (the silicon oil 1 case is further to the right of the diagram).

6.3 Foam-driven oil extraction from micropatterned channels

In §6.2.3, we study oil extraction when surfactants are added to the external phase. In this section, we investigate the case where gas is co-injected with surfactants, thus creating an aqueous foam, which also acts to extract the infused liquid during flow.

6.3.1 Controlled foam generation

We first generate the aqueous foam through a flow-focusing device by building a microfluidic system.

6.3.1.1 Flow-focusing

The flow-focusing technique allows to control the bubble size by co-injecting nitrogen gas at a given pressure p and the liquid phase (CAPB - SLES - Mac described for surfactant solutions) at a given flow rate q through a constriction [74, 75].

The flow-focusing device is fabricated by soft photolithography. Photolithography is the basic technique to build microfluidic devices [176]. Fig. 6.20 depicts the whole process. First, we need a black film through which the pattern of the device is imprinted: the film is transparent where the channels of the microfluidic device are. Then, the film is deposited on a photoresisting material lying on a silicon wafer. UV light is flashed through the film and the composite surface. The photoresisting material is reticulated where the film is transparent and the channels are drawn. The dissolution of the non-reticulated part leaves blocks of photoresist of precised thickness (depending on the quantity of initial deposited photoresist). The silicon wafer with these polymer blocks on top of it is our mold. Afterwards, PDMS is poured onto the mold and baked. By removing the mold, we obtain a negative of the mold etched in the PDMS with channels of controlled thickness. We close the channels by sticking a glass lamella.

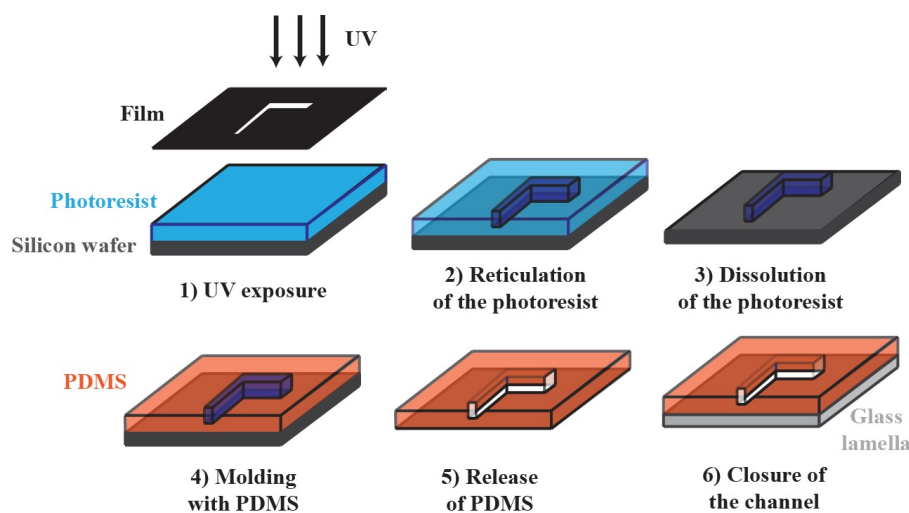


Figure 6.20: Description of the microfluidic fabrication by photolithography. Colors are here to distinguish each component. They do not correspond to a physical reality.

6.3.1.2 Foam calibration

To slow down bubble coarsening, gas is blown through a solution of tetradecafluorohexane (C_6F_{14}) [159] before entering the device because fluorinated gas is insoluble in water. We calibrate the mean bubble radius R_b as a function of the liquid flow rate q and the gas pressure p . The characteristics of the flow-focusing device are summarised in Fig. 6.21.

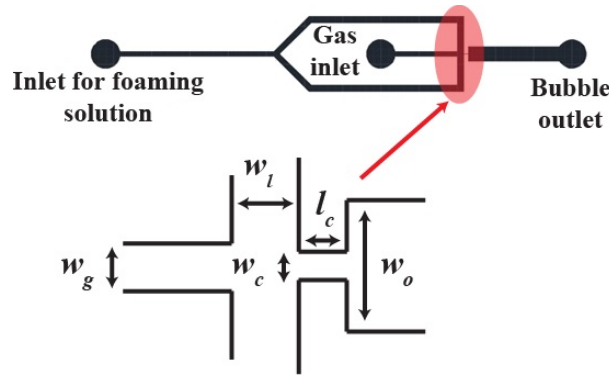


Figure 6.21: Flow-focusing device with the main geometrical features: $w_g = 200 \mu\text{m}$, $w_l = 300 \mu\text{m}$, $w_c = 60 \mu\text{m}$, $l_c = 100 \mu\text{m}$ and $w_o = 500 \mu\text{m}$. The height H of the channel is $27 \mu\text{m}$ or $72 \mu\text{m}$.

Garstecki et al. [74, 75] have followed the first steps of bubble formation. First, the gaseous thread enters the constriction and the liquid phase is squeezed within a thin film between the gas phase and the wall. For a Poiseuille-like viscous flow, the liquid flow rate q is proportional to $\Delta p_\ell e^4$ where Δp_ℓ is the pressure difference between the upstream and the downstream end of the liquid flow, and e is the characteristic width of the flow, as shown by scaling arguments in §1.1.5. In the constriction, e decreases. Thus, to maintain a constant q , Δp_ℓ has to increase. The increase of pressure gradient induces the squeezing of the liquid-gas interface, leading to the break-up of the thread and the formation of bubbles. The characteristic time of break-up is $T \approx 1/q$ which corresponds to the time the liquid phase needs to fill the constriction. The bubble volume is $V_b \approx q_g T$ where q_g is the gas flow rate. This flow rate q_g is given by the Poiseuille equation and $q_g \propto p H^4 / (\eta_w l_c)$ where H and l_c are the channel height and the constriction length. Using this expression and the volume estimation, one finds that V_b scales as:

$$V_b \propto \frac{p}{\eta_w q}. \quad (6.23)$$

Fig. 6.22 reports the correlation between V_b and p/q . With this plot, we can build a calibration curve that determines the bubble volume and radius for each couple (p, q) . We typically generate bubbles with $R_b \approx 30 \mu\text{m}$ by setting $p = 7 \text{ Psi} = 48.3 \text{ kPa}$ and $q = 10 \mu\text{L/s}$.

Other methods, such as T-junction [76] and step emulsification [119], could have been used. Nevertheless, flow-focusing is an easy method to implement that gives a polydispersity index (standard deviation of the bubble volume) below 2 %. This allows a good reproducibility in our experiments. It is also important to notice that the change of bubble size also induces a change of liquid fraction (identical to T-junction systems but not to step emulsification).

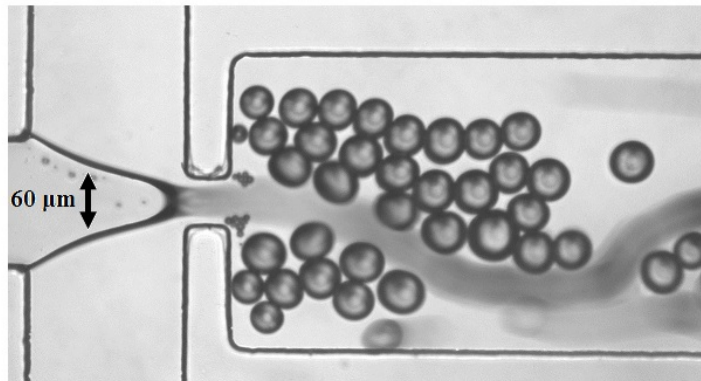
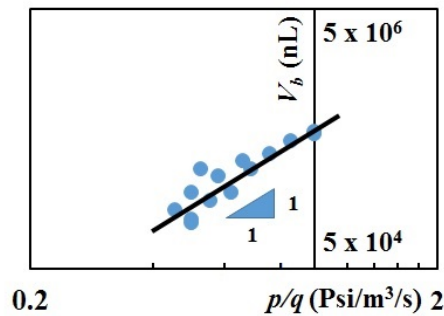


Figure 6.22: Bubble volume V_b (nL) as a function of the ratio pressure-flow rate p/q ($\text{Psi}/\text{m}^3/\text{s}$). Below: bubbles (radius $R_b \approx 30 \mu\text{m}$) accumulating in the outlet reservoir.

6.3.2 Experimental results and discussion

Once the bubbles are generated, the downstream reservoir of the flow-focusing device is connected to a 12 or 24 mL syringe with a 0.3 mm diameter PTFE tube. Bubbles accumulate in the syringe, which is capped at its end. Then, the piston is added at the top of the filled syringe. By weighing the syringe and measuring the foam volume, we deduce the foam liquid fraction ϵ which varies from 0.15 to 0.25.

For the injection stage, we use the pre-generated foam cartridge on the experimental set-up presented in the first section. We reproduce the same protocol with a range of foam flow rates Q

between $15 \mu\text{L}/\text{min}$ ($0.9 \text{ mL}/\text{h}$) and $1000 \mu\text{L}/\text{min}$ ($60 \text{ mL}/\text{h}$). We also use the same oils in the porous substrates, as well as the same channel geometry.

6.3.2.1 Typical extraction pattern with foams

We report a typical time series of the extraction process by an aqueous foam in Fig. 6.23. We observe a non-uniform extraction front for all of our experiments. In Fig. 6.24, we represent α as a function of Qt by varying Q , R_b and H .

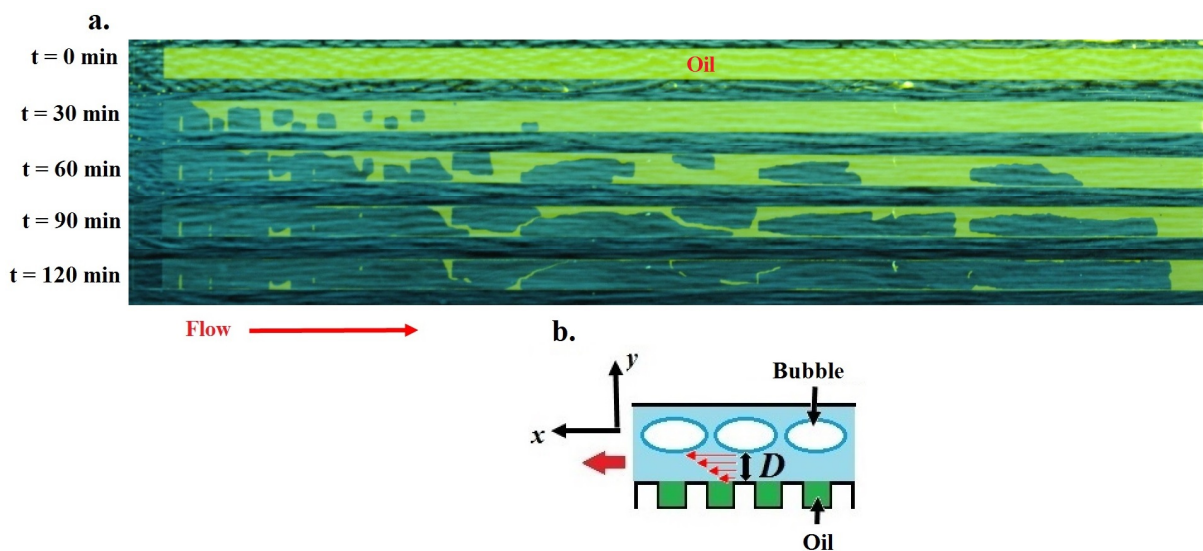


Figure 6.23: a. Top-view of olive oil extraction by an aqueous foam with $R_b = 100 \mu\text{m}$ and $Q = 50 \mu\text{L}/\text{min}$. Fluorescent dyed oil appears green-yellow. The flow is from left to right. b. Foam flow in the channel with D , the film thickness between the substrate and the bubbles.

In particular, in Fig. 6.24a-b, we report a surprising feature: an increase of flow rate engenders a decrease of α for a given injected volume with all other parameters constant. In other words, the slower the injection, the more efficient the oil extraction, which is a feature characteristic of extraction by foams. Moreover, Fig. 6.24c shows that the bubble radius has no influence on the extraction profile. If we compare α in the foam-driven case to the surfactant-driven case (Fig. 6.24d), α is higher in the foam case for a given injected volume. This result is all the more surprising as the injection flow rates Q used for the aqueous foams are one to two orders of magnitude lower than those used for surfactant solutions.

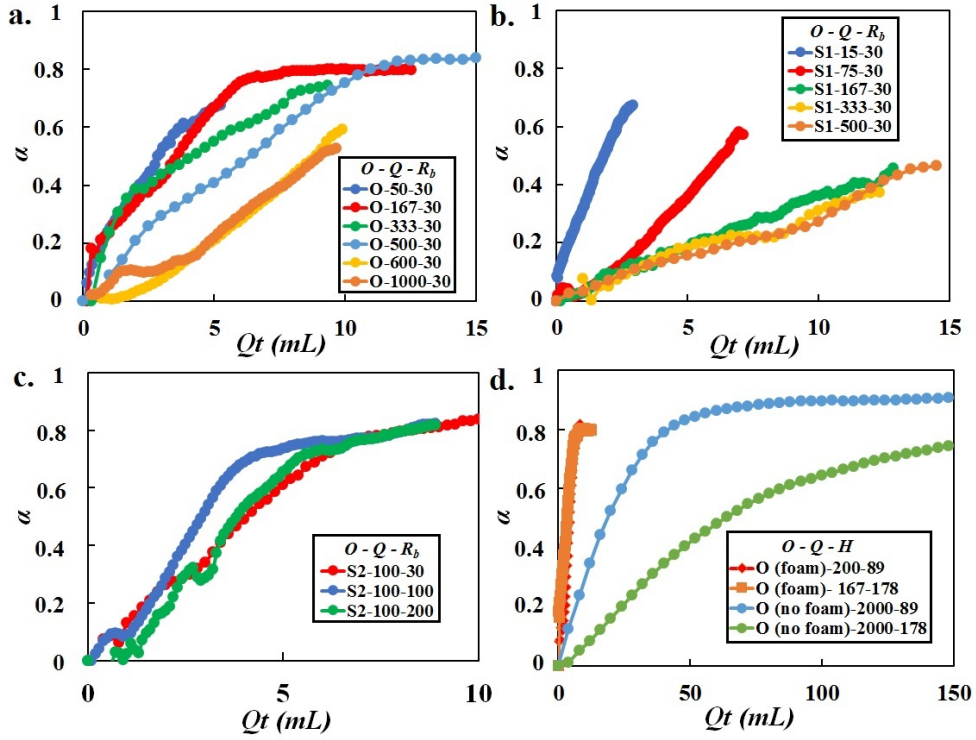


Figure 6.24: Efficiency α as a function of the injected volume Qt . a. Olive oil extraction by a foam with $R_b = 30 \mu\text{m}$. b. Silicon oil 1 extraction by a foam with $R_b = 30 \mu\text{m}$. c. Extraction for silicon oil 2 and $R_b = 30, 100$ and $200 \mu\text{m}$, and $H = 179 \mu\text{m}$. d. Comparison between surfactant solutions and foams with a varying channel height (89 or 178 μm). In the legend, O , Q ($\mu\text{L}/\text{min}$), R_b (μm) and H (μm) are, respectively, the oil type, the injection flow rate, the mean bubble radius and the channel height.

6.3.2.2 Shear modeling at the oil-water interface

To understand these results, we note that with aqueous foams, the applied shear stress is higher than with surfactant solutions. Indeed, as sketched in Fig. 6.23b, the existence of a thin film between the foam bubbles and the underlying oil layer creates a higher shear stress, since the velocity gradient does not apply on the channel height H but rather occurs over the film thickness D . Owing to their chemical composition, the bubbles have rigid air-water interfaces [81] that act as a rigid wall for the oil layer. Thus, we model the shear stress exerted by the foam on the oil phase as $\tau_{xy}^{foam} = \eta_w Q / (WHD)$. Replacing τ_{xy} in Eqs. (6.19a - 6.19b) with τ_{xy}^{foam} , we obtain a new expression for $\alpha(t)$:

$$\alpha + (1 - \alpha_\infty) \log \left(\frac{\alpha_\infty}{\alpha_\infty - \alpha} \right) = \frac{c_s h}{WHD L_o} \frac{\eta_w}{\eta_o} \frac{1}{c_d} Qt \quad , \quad (6.24a)$$

$$\alpha_\infty = 1 - \frac{2c_p D}{c_s} \frac{D}{L_o} \frac{h \cos \theta}{w Ca} \quad . \quad (6.24b)$$

In order to use Eqs. (6.24a - 6.24b), we measure θ and use D as an adjustable parameter. Again, like for surfactant solutions, θ depends on Ca . More precisely, as shown in Fig. 6.25a, we can collapse all the angle measurements from surfactants and foams on the same plot by introducing a new capillary number $\tilde{Ca} = Ca(H/\ell)$ where ℓ is the characteristic length for viscous dissipation. If $\ell = H$ as it is the case for surfactant solutions, then $\tilde{Ca} = Ca$. However, for foams, $\ell = D$. Fig. 6.25b-c compares α_{exp} and $f(\alpha_{exp})$ to $G(t) = \frac{c_s h}{WHDLo} \frac{\eta_w}{\eta_o} \frac{1}{c_d} Qt$. We are able to obtain good agreement between Eqs. (6.24a - 6.24b) and our data sets.

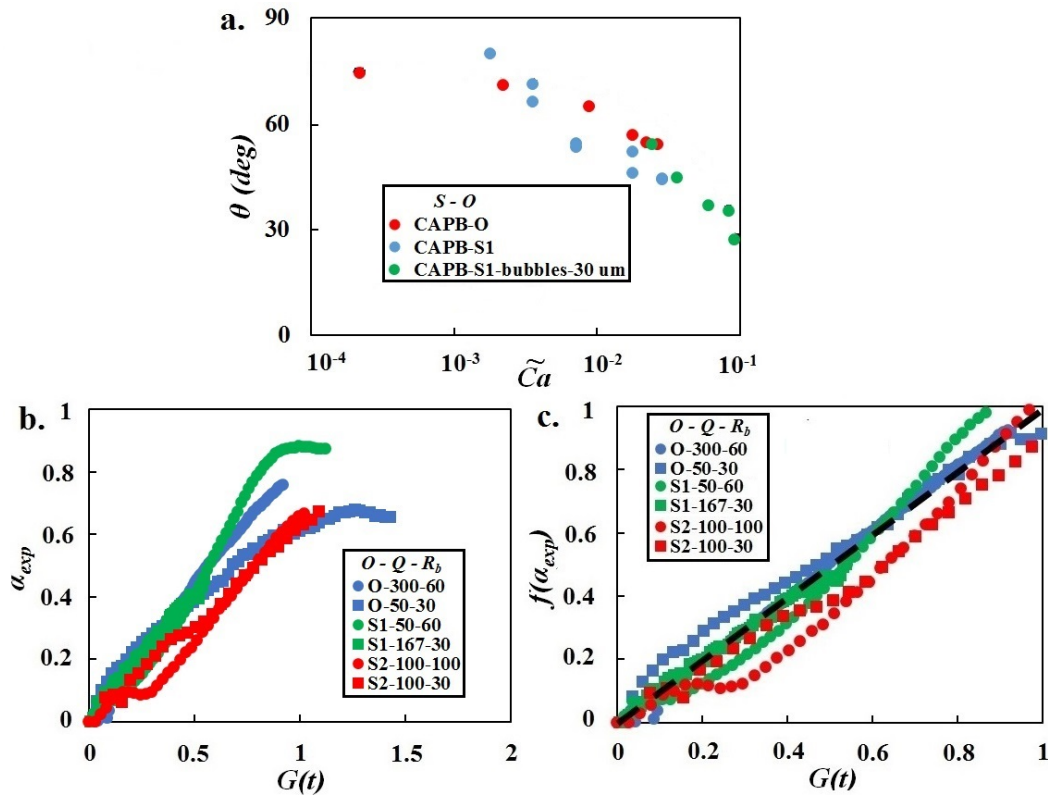


Figure 6.25: a. Measurements of the receding contact angle θ as a function of \tilde{Ca} . b. Experimental efficiency α_{exp} as a function of $G(t) = \frac{c_s h}{WHDLo} \frac{\eta_w}{\eta_o} \frac{1}{c_d} Qt$ for some oils, Q ($\mu\text{L}/\text{min}$) and R_b (μm). c. $f(\alpha_{exp})$ as a function of $G(t)$ for the same parameters. $f(\alpha_{exp}) = G(t)$ is represented by the black dashed line.

6.3.2.3 Dissipation length and film thickness

The fitting parameter D is found to vary between $1 \mu\text{m}$ and $7 \mu\text{m}$, as shown in the inset of Fig. 6.26a. The values of D are in reasonable agreement with common orders of magnitude found for a bubble moving across a solid wall [28, 57–59, 131]. Also, we notice that D and τ_{xy}^{foam} do not depend strongly on R_b , since $\alpha(Qt)$ maintains the same profile when we increase R_b by 10 times (Fig. 6.24c). Thus, we choose to introduce the dimensionless film thickness $D^* = D/H$

and the dimensionless applied shear stress $\tau_{xy}^{foam*} = \tau_{xy}^{foam} H / \gamma_{aw}$ by non-dimensionalizing D and τ_{xy}^{foam} , respectively, by H and by γ_{aw} / H . In Fig. 6.26, we plot D^* and τ_{xy}^{foam*} as a function of the outer capillary number $Ca^* = \eta_w Q / (WH\gamma_{aw})$ that differs from Ca by replacing γ_{ow} by the air-water interfacial tension γ_{aw} . We compare the results to the estimates of film thickness provided by mathematical studies of the liquid meniscus at a solid wall. We find a good collapse with the exact solution for wet foams, made with the combination of surfactants and fatty acids used in our experiments, as developed by Denkov et al. [57–59]. We use two channel heights $H = 89$ and $178 \mu\text{m}$ and different Ca^* for two orders of magnitude from 10^{-5} to 10^{-3} . In their study, they find:

$$D^* = Ca^{*1/2} \quad , \quad (6.25a)$$

$$\tau_{xy}^{foam*} = 4.63\xi(\epsilon)Ca^{*1/2} + 7.35\chi(\epsilon)Ca^{*2/3} \quad , \quad (6.25b)$$

where ξ and χ are functions of the liquid fraction ϵ .

Common surfactant-based foams with poor rigidity and shorter lifetime, such as SDS or TTAB, exhibit the classical Bretherton theory [22] for $D \propto Ca^{*2/3}$ on a bubble moving in a channel of comparable size. This scaling can be derived by balancing the pressure gradient in the meniscus at the bubble front with the viscous dissipation at the wall. In the exact calculations, friction is neglected in the central area of the film. However, the calculations by Denkov et al. are based on the assumption of rigid tangentially immobile interfaces, which means that the velocities of the upper film surface and the wall are different and creates friction. Thus, it gives a difference of power laws (Eqs. (6.25a - 6.25b)). While they consider the bubble radius R_b and the capillary pressure in the bubbles γ_{aw} / R_b as the rescaling parameters, we use H as the characteristic length. This is quite surprising but one possible reason is that the confinement of the bubbles in the channel sets a different and unique characteristic length, which is the channel height H .

Since D is smaller when Ca^* decreases, this explains why smaller flow rates are more favourable to drain oil out for a given injected volume (see Eq. (6.24a)). A similar trend is observed when oil is removed from a macroscopic channel by imbibition, as described in Chapter 5, due to a longer contact time between the foam and the lubricating liquid when injection is slow.

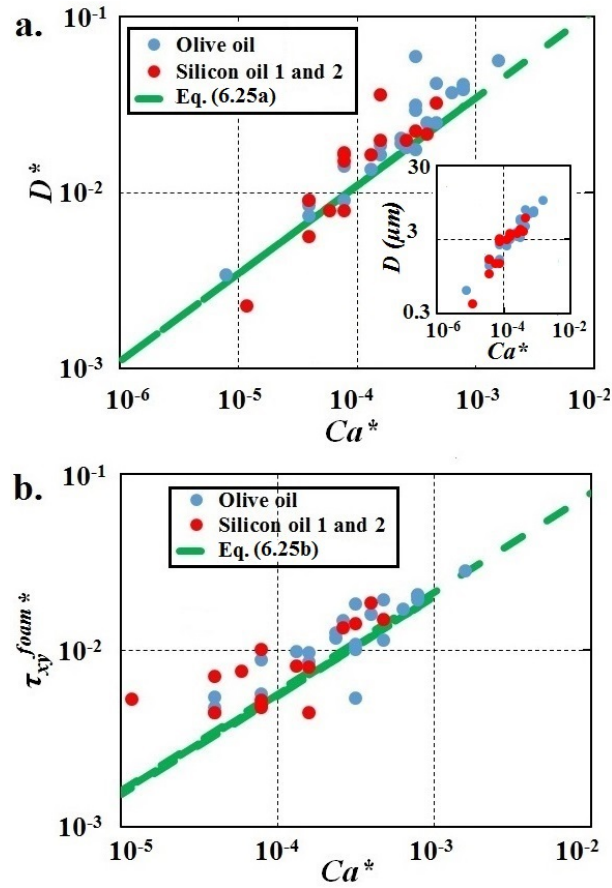


Figure 6.26: a. Dimensionless film thickness $D^* = D/H$ as a function of the outer capillary number Ca^* for all data sets. Inset: Film thickness D as a function of Ca^* for the same data set. b. Dimensionless applied shear stress $\tau_{xy}^{foam*} = \tau_{xy}^{foam} H / \gamma_{aw}$ as a function of Ca^* for all data sets. The green dashed line represents the values predicted by Denkov et al. [57] with H as a rescaling length for a liquid fraction $\epsilon = 0.2$.

6.4 Conclusions

Liquid-infused surfaces are rough and patterned surfaces, in which a lubricating liquid is infused. Like superhydrophobic textured surfaces, they have been studied for their amazing properties: omniphobicity, biofouling or drag reduction. These properties vanish if the trapping of air (for superhydrophobic surfaces) or oil (for liquid-infused surfaces) into the cavities is lost. The failure of such surfaces is thus at stake. For superhydrophobic surfaces, an external applied pressure, normal to the air-liquid interface can lead to the sagging of this interface. For liquid-infused surfaces, a tangential stress induced by the shear flow of pure aqueous fluids can drag oil out of the cavities [198]. This failure mechanism also occurs when the nature of the outer fluid is changed. We have shown that surfactants in the outer phase adsorb at the oil-water interface. Thus, they change the dynamics of the contact line between the posts that make up the porous

substrate. They actually enhance extraction compared to pure water. Then, the adsorption of surfactants can trigger long-wave and short-wave instabilities at the oil-water interface, leading to the non-uniform propagation of the extraction front.

Furthermore, using aqueous foams in the outer phase enhances the failure dynamics drastically. The existence of a thin water film between the foam and the oil phase increases the shear exerted by the outer phase. For comparable volumes of sheared oil, the volume of products used from pure solutions to foams is reduced by a factor 10 to 20. It also decreases by up to two orders of magnitude the typical injection flow rates required to drag oil completely out of the channel. The decreasing value of the film thickness when the outer capillary number $Ca^* = \eta_w Q / (WH\gamma_{aw})$ is reduced also means that lower flow rates increase the efficiency of oil extraction for a given injected volume of foam.

The failure of liquid-infused surfaces induced by surfactants and aqueous foams can be related to recovery issues if one imagines that oil is trapped within the roughness at the surface of a rock layer. Rocks are often fractured and have a porosity (larger than the typical size of the roughness) with a high specific surface area from which oil can be difficult to extract because of the high capillary pressure. In this case, surfactants are often injected into the porous soil to reduce the interfacial tension with the oil phase, which causes a decrease of the capillary pressure and enhances oil recovery. Moreover, surfactants are often co-injected with gas, such as carbon dioxide, which is a transport agent. The higher mobility of the resulting foam enables the injected materials to span more areas in the porous soil than a single aqueous phase [109]. In both cases, industrials apply a normal stress on the pores and the oil phase by increasing the extracting pressure (which can also lead to fracking issues) [118].

From our work, we show that it is also possible to use the tangential shear at the wall to extract oil confined in the roughness. We model the microporous and rough rock layer by a microfluidic liquid-infused surface. However, the chemical and physical nature of the external flow modifies the dynamics of the receding contact line and/or the nature of the applied shear stress. In both cases, we account for these effects by introducing a modified dependence on the capillary numbers $Ca = \eta_w Q / (WH\gamma_{ow})$ and $Ca^* = \eta_w Q / (WH\gamma_{aw})$. For recovery efficiency, it is more beneficial to increase the interfacial capillary number Ca when surfactant solutions are used, especially by the reduction of the oil-water interfacial tension, as expected. In the foam case, it is more beneficial to decrease Ca^* for a given injected volume of foam. In other words, extraction efficiency is maximized if the injection flow rate is reduced. In both cases, we suggest a model that can predict the quantity of oil and pollutant that can be extracted.

To compare with, we can evaluate the range of capillary numbers Ca and Ca^* for real soil systems. By the Darcy's law, $Ca = \eta_l u_{Darcy} / \gamma_{ow} = k_D / (r_p \mathcal{L})$ where u_{Darcy} is the mean flow velocity,

r_p the typical pore radius, \mathcal{L} the depth of the extraction well and k_D the permeability. We can approximate k_D by using the Carman-Kozeny model [30, 110]. For an assembly of spherical grains: $k_D = \phi^3 d_g^2 / (180(1 - \phi)^2)$ where ϕ and d_g are the porosity and the grain diameter. We can take $\phi = 0.4$ and $d_g \approx 100 \mu\text{m}$, which gives $k_D \approx 4 \times 10^{-11} \text{ m}^2$. Given that $r_p \approx 10 \mu\text{m}$ and $\mathcal{L} \approx 1 \text{ km}$ [50], we find that $Ca \approx 4 \times 10^{-9}$ and $Ca^* = (\gamma_{ow}/\gamma_{aw})Ca \approx 4 \times 10^{-10}$. This is definitely well below our experimental Ca and Ca^* (10^{-5} to 10^{-3}). Yet, in both cases, the physics is mainly ruled by capillarity. We thus believe that the understanding gained in this chapter should still be valid for ranges of flow rates and velocities more compatible with soil extraction.

Conclusions and future work

We present here the main conclusions of this thesis and suggest ideas for future work and progress.

Concluding remarks

In this thesis, we study how aqueous foams interact with immiscible and oily liquids at different scales:

- microscopic scale: size of a surface roughness,
- millimetric scale: soap films and Plateau, borders
- centimetric scale: macroscopic foam samples.

We understand our experimental results by a static and dynamical theoretical analysis. In every part of this thesis, we play on the chemistry and the physical parameters of our experimental systems, including the nature of the foam phase and the oil phase.

In Chapter 1, we show how the physical and the mechanical properties of aqueous foams offer wide opportunities in many applications where one would like to find an alternative method to extract a liquid phase from a confined medium (soil remediation, enhanced oil recovery). Foams are light, have a very little water content and offer a high specific surface area, which generates less waste, less energy supply and requires easier processes.

In Chapter 2, we study the different criteria on which the stability and the collapse of foams in contact with oil depends. Common examples of oil interaction with foams refer to the incorporation of oil droplets (emulsified droplets) during foam generation to generate “foamulsions”. Here, we consider the case where oil is directly absorbed by the foam due to the capillary underpressure. As a consequence, oil appears as long slugs invading the Plateau borders of a dry foam. Oil-laden foams do not collapse if the entry coefficient E , the spreading coefficient S and the bridging coefficient B are all negative, similarly to common theories on antifoaming action induced by oil droplets in soap films. However, for values of the coefficients close to 0 (and considering the error margins on the interfacial tension measurements), the correlation between the coefficient values and the foam stability is less clear. The destabilization of a Plateau border starts by the breaking of the pseudoemulsion film which is the thin aqueous film between the air phase and the oil phase. This can only happen if the entry of the oil phase at the air-water interface overcomes an entry barrier related to the pressure required to thwart the disjoining pressure in the pseudoemulsion film. The relationship between the entry barrier and the static coefficients is still an open question.

In Chapter 3, we try to understand how oil locally behaves when propagating inside a Plateau border. Numerical simulations and results on the capillary flow of oil inside a Plateau border show that the oil slug swells the Plateau border and that the viscous dissipation is determined by the oil phase. We compare the interfacial energies of configurations where oil remains in the Plateau border and spreads out of the Plateau border. Our results confirm the stability analysis

and the experimental tests from Chapter 2. When an adjacent film breaks, the oil-filled Plateau border breaks into small emulsified droplets. The breaking dynamics can be understood as the Rayleigh-Plateau instability of a viscous fluid in another viscous fluid. We can predict the size of the droplets from the volume of oil, the length of the oil slug and the wavelength of maximum instability growth.

In Chapter 4, we study locally how oil interacts with the air-water interface by spreading experiments. We consider a configuration where the oil phase rises to the air-water interface by the aqueous phase to reproduce the entry conditions of oil droplets at the air-water interface of soap films. At short times, we determine a comprehensive time-dependent dynamics for the spreading radius for viscous and non-viscous oil droplets. For pure aqueous phases and surfactant-laden phases, this dynamics follows a $t^{1/2}$ behaviour. However, we observe a difference at long times for both types of aqueous phases. For pure water, the short-time regime joins a long-time regime in $t^{3/4}$ already found for spreading at liquid-liquid interfaces, based on the existence of a viscous boundary layer between oil and water. However, for surfactant solutions, we observe a solid-like spreading dynamics driven by gravity in $t^{1/8}$, which still raises questions. Potential molecular interactions and adsorption dynamics might be at stake with surfactants.

In Chapter 2, 3 and 4, we study the consequences of oil-foam interactions at different scales. In Chapter 5, we determine how oil is absorbed into foams, and thus how oil-foam interactions can occur. Due to the capillary underpressure (or osmotic pressure) in the foam, oil can be imbibed into aqueous foams, providing that the conditions defined in Chapter 2 are fulfilled. We consider three different configurations. First, we study the 3D imbibition from a point-source at imposed atmospheric pressure to reproduce oil extraction from a pressure-controlled pore. In this case, we numerically solve the drainage equation in cylindrical coordinates. We include the effect of gravity and the creation of oil-water interfaces (through the Bond number B) in our resolution by introducing an effective interfacial tension. The higher the Bond number, the slower the imbibition dynamics. the 1D imbibition of an oil slick. The rising oil front follows a $t^{1/4}$ dynamics at very long times. The initial liquid fraction of the foam plays an important role as it determines the driving pressure difference for the oil slug to invade the Plateau borders. Then, we consider the 1D imbibition of an oil slick. The rising oil front follows a $t^{1/4}$ dynamics at very long times. The initial liquid fraction of the foam plays an important role as it determines the driving pressure difference for the oil slug to invade the Plateau borders. Finally, we move the foam on top of the extracting point to simulate a recovery process. Our preliminary results show that a slow injection rate is more favourable to extract oil for a given volume of oil. This can be related to a longer contact time between the Plateau border and the oil reservoir, although this remains to be proven.

In Chapter 6, we trap oil in the roughness of a microfracture. To model this microporous system, we use liquid-infused surfaces. The lubricating layer of oil can be sheared out of the texture by injecting a pure aqueous phase through a microfluidic channel, on one side of which the textured pattern is imprinted. In our case, we study how surfactant solutions and foams can also drag oil out of the texture by comparison with the theory developed by Wexler and al. [198] for the shear-induced failure of liquid-infused surfaces. For a given volume of injected fluid, surfactants enhance oil extraction and induce a variation of the dynamic contact angle with the capillary number Ca . Oil extraction is also improved with foams. These latter require a lower injection flow rate and a lower injected volume to extract as much oil as with pure aqueous solutions. This is due to an increase of the shear stress at the oil-water interface. Indeed, the viscous dissipation occurs upon the length scale of a film thickness, which is much smaller than the length scale of the channel height, thus the shear stress is higher for foams than for pure water. The film thickness we deduce is in good correlation with theoretical estimations for a liquid film with rigid interfaces lying at the wall.

In this work, we combine different aspects and approaches of the hydrodynamics of foams in contact with oil. We model the multiphase system constituted by the air, the water and the oil phase locally and we try to understand the interplay between the different phases and its consequences on the dynamical phenomena at stake in oil-laden foams. We hope that this study could be an interesting starting point for global studies at the scale of bigger foam volumes and macroscopic soil samples. In particular, soil remediation, enhanced oil recovery and any application involving the extraction of a non-aqueous phase might be concerned.

Perspectives and outcomes

The results presented in this thesis ask for more developments and suggest new leads to a better understanding of the interactions between aqueous foams and immiscible liquids.

First, finding a comprehensive argument to predict whether a foam will be destabilized by the oil phase needs to be completed. This requires to understand the behaviour of the air-water-oil pseudoemulsion film, which strongly depends on the competition between the disjoining pressure and the pressure distributions in the flowing oil phase.

Second, the effect of surfactants on the spreading of oil on a liquid surface is still an open question. Surfactant dynamics certainly play a role and a microscopic and molecular analysis at the contact line could complete the work done so far.

Third, imbibition studies were conducted for a defined foam sample and an open reservoir. What will happen in the case of a real soil system, whose pores trap oil? The same question arises

for the extraction from micropatterned surfaces. We model an ideal system with a controlled roughness and produce a theoretical explanation based on well-defined parameters. How does it change when the surface configuration is more random and involve different features for which it is difficult to define a unique length scale?

In this situation, we would need to carry out recovery experiments and injection tests in porous models (glass beads) and macroscopic soil samples that are oil-laden beforehand. In-situ observations can be made by MRI (Magnetic Resonance Imaging) for example. MRI is a non-destructive technique that traces the spin resonance of the hydrogen protons in a molecule. An electromagnetic wave impulsion is applied and changes the magnetization of the system. At the end of the impulsion, the magnetization relaxes to its initial position. Depending on the chemical environment, the relaxation time (T_1 and T_2 relaxation) changes. Preliminary results have shown that it is possible to distinguish the oil phase from the aqueous phase by this technique. By recording the relaxation time and measuring the size of the relaxation peak for each phase, one can map the quantity of oil and water in the system, and thus deduces the quantity of oil left and extracted. A typical T_1 signal given by nuclear magnetic resonance for an oil-laden foam is given in Fig. 6.27. Yet, due to the lack of time, we could not perform a systematic study using MRI.

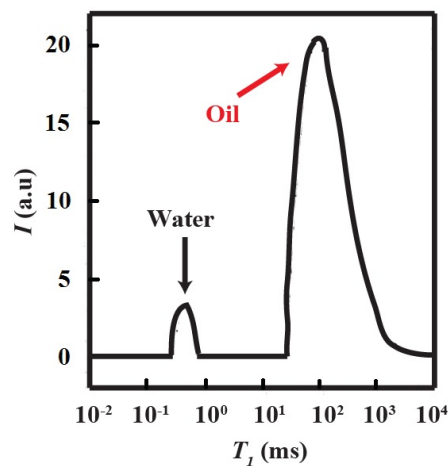


Figure 6.27: Typical NMR spectrum for an oil-laden foam with the intensity I as a function of the relaxation time T_1 . The relaxation times are $T_1 \approx 0.5$ ms for water in foams and $T_1 \approx 100$ ms for oil. We use gadolinium as a contrasting agent (and EDTA as a chelating agent). Gadolinium is able to shorten the T_1 - typically for a pure water solution from 2 s to 10 ms according to the concentration of gadolinium.

In our study, we use basic types of oil (organic and mineral). We can wonder whether other types of oils and immiscible liquids give the same results. For instance, tar oils are closer to industrial applications. Oil can also carry small particles that might have some effect on the foam stability. Combining the effect of particles and oils is an interesting question. Studies have been carried out

for particle-laden foams [83, 84] but the subject of “foamulsions” with particles at the air-water interfaces is still open.

Finally, in this work, we look for a stable oil-laden foam for which oil does not exhibit an antifoaming activity. An interesting question is to study the antifoaming mechanisms and in particular the breaking avalanches when an oil droplet is deposited at the top or inside an aqueous foam.

Appendix A

Examples of flow dynamics by resolution of Stokes' equation

We give two examples of exact calculations describing the flow dynamics based on Stokes' equation. First, we derive the dynamics for the capillarity and gravity-driven spreading of a liquid drop on a solid surface. Second, we analytically solve the laminar pressure-driven flows in circular and rectangular infinite pipes.

A.1 Spreading dynamics of a liquid droplet on a solid surface

We solve the spreading dynamics of a liquid droplet on a solid surface in the capillarity and gravity-dominated regimes.

A.1.1 Lubrication approximation

We consider the viscous spreading of a thin film on a plane surface (Reynolds number $Re = \rho_l u r / \eta_l \ll 1$), sketched in Fig. A.1 with the spreading radius r very small compared to its width h - u is the velocity field, ρ_l the liquid density and η_l its viscosity.

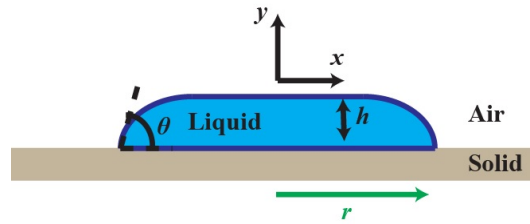


Figure A.1: Spreading a liquid droplet on a solid surface.

Mass conservation gives $\nabla \cdot \mathbf{u} = 0$ for the velocity field $\mathbf{u} = u\mathbf{e}_x + v\mathbf{e}_y$ and thus:

$$\frac{\partial u}{\partial x} + \frac{\partial v}{\partial y} = 0. \quad (\text{A.1})$$

From Eq. A.1, we have $v \sim (e/r)u$. Thus, since $e \ll r$, v is negligible compared to u . The Stokes' equation with gravity negligible compared to capillarity is given by (with the pressure p):

$$\eta_l \Delta \mathbf{u} = \nabla p. \quad (\text{A.2})$$

Projecting Eq. A.2 on \mathbf{e}_x and \mathbf{e}_y , we find:

$$\begin{cases} -\frac{\partial p}{\partial x} + \eta_l \frac{\partial^2 u}{\partial y^2} = 0 \\ \frac{\partial p}{\partial y} = 0. \end{cases}, \quad (\text{A.3})$$

The pressure p only depends on the coordinate x and using the boundary condition $u(x, 0, t) = 0$

(t is the time) at the wall (no-slip condition) and the free surface condition $\left(\frac{\partial u}{\partial y}\right)_{h(x,t)} = 0$ yields:

$$u(x, y, t) = \frac{1}{2\eta_l} \frac{dp}{dx} y (y - 2h(x, t)). \quad (\text{A.4})$$

A.1.2 Thin film equation

Then, we can write the advancing velocity $U = (1/h) \int_0^h u dy$, which gives:

$$\eta_l U = -\frac{1}{3} h^2 \frac{dp}{dx}. \quad (\text{A.5})$$

Mass conservation gives the following relationship:

$$\frac{\partial h}{\partial t} + \frac{\partial (hU)}{\partial x} = 0. \quad (\text{A.6})$$

The pressure gradient close to the edge of the spreading front is given by the Laplace pressure $p = -\gamma_{al} \partial^2 h / \partial x^2$, where γ_{al} is the air-liquid interfacial tension. Injecting this pressure in Eq. A.5 and Eq. A.6 give the thin film equation:

$$\frac{\partial h}{\partial t} - \frac{\gamma_{al}}{3\eta_l} \frac{\partial}{\partial x} \left(h^3 \frac{\partial^3 h}{\partial x^3} \right) = 0. \quad (\text{A.7})$$

The asymptotic solution of Eq. A.7 is [31]:

$$h = \left(\frac{9\eta_l U}{\gamma_{al}} \right)^{1/3} x \log^{1/3} k, \quad (\text{A.8})$$

where $k = 10^4$ is an integration constant in the vicinity of the contact line. Considering a small dynamic contact angle $\theta \approx h/x$, we deduce the well-known Tanner-Hoffmann's law:

$$\theta = (9Ca)^{1/3} \log^{1/3} k. \quad (\text{A.9})$$

This law describes the variation of the dynamic contact angle with the capillary number Ca and thus the velocity U of the contact line.

A.1.3 Spreading laws

We introduce the spreading radius r . We find the spreading velocity $U = dr/dt$. The volume of the spreading drop is $\Omega_d = (\pi/4)\theta r^3$. From Eq. A.9, we deduce that:

$$\frac{dr}{dt} = \frac{\gamma_{al}}{\eta_l} \frac{1}{9 \log k} \left(\frac{4\Omega_d}{\pi r^3} \right)^3. \quad (\text{A.10})$$

By integrating [A.10](#), we finally find that:

$$r(t) = \left(\frac{10}{9} \frac{\gamma_{al}}{\eta_l \log k} \left(\frac{4\Omega_d}{\pi} \right)^3 \right)^{1/10} t^{1/10}. \quad (\text{A.11})$$

We use [Eq. A.11](#) in Chapter 4 to describe our long-time spreading regime for liquid-liquid interfaces.

When gravity dominates capillarity, [Eq. A.7](#) is replaced by:

$$\frac{\partial h}{\partial t} - \frac{\rho_l g}{3\eta_l} \frac{\partial}{\partial x} \left(h^3 \frac{\partial h}{\partial x} \right) = 0. \quad (\text{A.12})$$

Mass conservation gives the drop volume $\Omega_d = 2\pi \int_0^r h(x, t) x dx$. [Eq. A.12](#) can be non-dimensionalized by the variables $H = h/\Omega_d^{1/3}$, $X = x/\Omega_d^{1/3}$ and $T = t/(3\eta_l/\rho_l g \Omega_d^{1/3})$:

$$\frac{\partial H}{\partial T} - \frac{\partial}{\partial X} \left(H^3 \frac{\partial H}{\partial X} \right) = 0, \quad (\text{A.13})$$

with the mass conservation equation written as $1 = 2\pi \int_0^{X_f=r/\Omega^{1/3}} H(X, T) X dX$. One can look for a self-similar solution of the form $H(X, T) = T^\alpha H^*(X/T^\beta) = T^\alpha H^*(\mu)$ with μ the dimensionless self-similar variable. Injecting the self-similar solution in [Eq. A.13](#) and mass conservation, one finds that $\alpha = -1/4$ and $\beta = 1/8$ for non-dimensionalization. One deduces that the spreading radius r is written as:

$$r(t) = \mu_f \left(\frac{\rho g \Omega^3}{3\eta_l} \right)^{1/8} t^{1/8}, \quad (\text{A.14})$$

where μ_f is a constant determined by studying the asymptotic behaviour at the spreading front of [Eq. A.13](#). [Eq. A.7](#) could also have been solved by self-similarity. [Eq. A.14](#) is also used in Chapter 4 but deduced by scaling arguments.

A.2 Poiseuille flow

We assume a steady laminar pressure-driven flow in the following two examples.

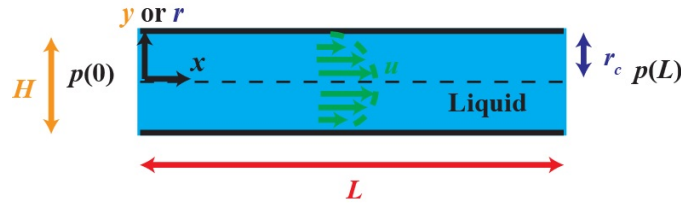


Figure A.2: Poiseuille flows in circular and rectangular pipes.

A.2.1 In a cylindrical tube

We consider that the velocity field \mathbf{u} is uniaxial and has the form $\mathbf{u} = u(r)\mathbf{e}_x$. This problem is invariant by rotation (coordinate θ) and translation (coordinate x). Eq. A.2 becomes in cylindrical coordinates (r, θ, x) :

$$\frac{dp}{dx} = \frac{\eta}{r} \frac{d}{dr} \left(r \frac{du}{dr} \right). \quad (\text{A.15})$$

We have the following boundary conditions: $u(0)$ is bounded and $u(r_c) = 0$ (no-slip condition) where r_c is the cylinder radius. Integrating A.15 yields a solution $u = (1/4\eta)r^2 dp/dx + A_1 \ln r + A_2$. From the boundary conditions, we have $A_1 = 0$ and $A_2 = -(1/4\eta)r_c^2 dp/dx$. But $dp/dx = -\Delta p/L$ where L is the length of the cylinder, so the axial velocity u is given by:

$$u(r) = \frac{r_c^2}{4\eta} \frac{\Delta p}{L} \left(1 - \frac{r^2}{r_c^2} \right). \quad (\text{A.16})$$

We can deduce the flow rate $Q = \int_0^{2\pi} \int_0^{r_c} u(r)r dr d\theta$ from Eq. A.16, which yields the well-known Hagen-Poiseuille flow rate in a cylindrical tube:

$$Q = \frac{\pi r_c^4 \Delta p}{8 \eta L}. \quad (\text{A.17})$$

Eq. A.17 can be rewritten in a more general form $Q = AK_c \Delta p / \eta L$ where A is the cross-sectional area and K_c the permeability constant. For the laminar flow in a cylindrical pipe, $K_c = 1/8\pi$ (for a Plateau border, $K_c = 1/50$). Eq. A.17 is used in Chapter 1 and 6 (but demonstrated by scaling arguments).

A.2.2 Between two plates

Here, we consider the steady laminar pressure-driven flow between two parallel plates separated by a distance H . Once more, the velocity field is uniaxial and $\mathbf{u} = u(y)\mathbf{e}_x$. We have the

following projected Stokes' equation:

$$\frac{dp}{dx} = \eta_l \frac{d^2u}{dy^2} \quad , \quad (\text{A.18})$$

with the boundary conditions $u(0) = 0$ and $u(H) = 0$ (no-slip condition). The solution u has the form $u = (1/2\eta_l)(dp/dx)r^2 + A_1r + A_2$. One finds that $A_2 = 0$ and $A_1 = -(1/2\eta_l)(dp/dx)H$. Thus, u is given by:

$$u(y) = \frac{\Delta p}{2\eta_l L} r (H - r) \quad , \quad (\text{A.19})$$

where we have replaced dp/dx by $-\Delta p/L$.

We can determine the flow rate $Q = \int_0^H \int_{-W/2}^{W/2} u(y) dy dz$ by integrating the velocity field beyond the cross-section of a wide rectangular channel of width W . One finds that:

$$Q = \frac{WH^3}{12} \frac{\Delta p}{\eta_l L}. \quad (\text{A.20})$$

Moreover, we can deduce the shear stress at the wall $\tau_{xy} = \eta_l(\partial u/\partial y)_{y=0}$:

$$\tau_{xy} = \frac{\Delta p H}{2L}. \quad (\text{A.21})$$

Finally, by using Eq A.20 to find an expression for $\Delta p/L$ as a function of Q , one finds that:

$$\tau_{xy} = \frac{6\eta_l Q}{WH^2}. \quad (\text{A.22})$$

Eq. A.22 is the exerted shear stress in the microfluidic channel used in Chapter 6.

Appendix B

Rayleigh-Plateau instability of a viscous fluid in another viscous fluid

We explicit the comprehensive solution of the Rayleigh-Plateau instability in the case of the inertia-dominated regime and give some indications to solve the whole problem in the case of a viscous-dominated regime.

B.1 Inertia-dominated regime

First, we explain why the maximum instability wavelength λ_{max} is $9r_c$ (r_c is the cylinder radius) in the case of an inertia-dominated regime.

We consider an axisymmetric jet of sinusoidal shape defined by its local radius $r_2(x, t)$ depicted in Fig. B.1:

$$r_2(x, t) = r_c + \epsilon(t) \cos(kx) \quad , \quad (\text{B.1})$$

with k the wave number and a small modulation of the interface $\epsilon \ll r_c$ and $dr_2/dx \ll 1$.

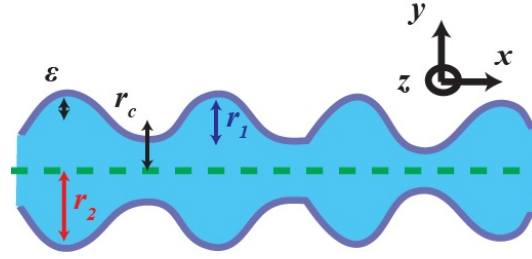


Figure B.1: Geometry of the axisymmetric unstable jet.

The capillary pressure $p - p_{atm}$ is given by the in-plane r_1 and the transverse r_2 curvatures of the air-water interface (γ_{aw} is the air-water interfacial tension), which gives:

$$p - p_{atm} = \gamma_{aw} \left(-\frac{\partial^2 r_1}{\partial x^2} + \frac{1}{r_c + \epsilon(t) \cos(kx)} \right) = \gamma_{aw} \epsilon(t) \cos(kx) \left(k^2 - \frac{1}{r_c^2} \right) \quad , \quad (\text{B.2})$$

by derivating the first term and developing at first order the second term with $\epsilon \ll r_c$.

Then, we use the Navier-Stokes equation by neglecting the viscous effects and considering a uniform pressure gradient and axial velocity v_x along the transverse direction e_x , which yields the momentum equation (ρ_l is the liquid density):

$$\rho_l \frac{dv_x}{dt} = -\frac{dp}{dx} \quad (\text{B.3})$$

Integrating Eq. B.3 along the cross-section of the jet and using Eq. B.2 to express the pressure gradient gives the flow rate $Q(x, t)$:

$$\frac{\partial Q(x, t)}{\partial t} = \frac{\pi \gamma \epsilon(t) r_c^2}{\rho_l} k \sin(kx) \left(k^2 - \frac{1}{r_c^2} \right). \quad (\text{B.4})$$

Mass conservation gives (by assuming once more that $\epsilon \ll r_c$):

$$-\frac{\partial Q(x, t)}{\partial x} = \frac{d}{dt} (\pi (r_c + \epsilon(t) \cos(kx))^2) \approx 2\pi r_c \cos(kx) \frac{d\epsilon(t)}{dt}. \quad (\text{B.5})$$

Derivating Eq. B.4 and Eq. B.5 with respect to x and t , and equating them, gives the following time-dependence for $\epsilon(t)$:

$$\frac{d^2 \epsilon}{dt^2} \approx \frac{\gamma}{2\rho_l r_c^3} k^2 r_c^2 (1 - k^2 r_c^2) \epsilon(t). \quad (\text{B.6})$$

This second-order equation has an exponential solution of the form $\exp(\sigma t)$ with σ given by:

$$\sigma^2 \approx \frac{\gamma}{2\rho_l r_c^3} k^2 r_c^2 (1 - k^2 r_c^2). \quad (\text{B.7})$$

We find the expression presented in 3.2.1.2, for which the maximum growth rate corresponds to $k_{max} = 0.697/r_c$ and $\lambda_{max} = 2\pi/k_{max} \approx 9r_c$.

B.2 Viscous-dominated regime

Here, we study the Rayleigh-Plateau instability of a viscous fluid in another viscous fluid. We need to solve the complete Navier-Stokes equation in both inner cylindrical fluid and outer fluid. We give some hints for the resolution. The comprehensive problem has been solved by Tomotika et al. and more details can be found in [183].

We consider the flow dynamics in one of the fluids in cylindrical coordinates and the motion is symmetrical around the axis x . Thus, we introduce the velocity field $\mathbf{U}_1 = u_1 \mathbf{e}_r + w_1 \mathbf{e}_x$. (u_1 , w_1) are solutions of the Navier-Stokes equations:

$$\frac{\partial u_1}{\partial t} + u_1 \frac{\partial u_1}{\partial r} + w_1 \frac{\partial u_1}{\partial x} = -\frac{1}{\rho_1} \frac{\partial p}{\partial r} + \frac{\eta_1}{\rho_1} \left(\frac{\partial^2 u_1}{\partial r^2} + \frac{1}{r} \frac{\partial u_1}{\partial r} - \frac{u_1}{r^2} + \frac{\partial^2 u_1}{\partial x^2} \right), \quad (\text{B.8a})$$

$$\frac{\partial w_1}{\partial t} + u_1 \frac{\partial w_1}{\partial r} + w_1 \frac{\partial w_1}{\partial x} = -\frac{1}{\rho_1} \frac{\partial p}{\partial x} + \frac{\eta_1}{\rho_1} \left(\frac{\partial^2 w_1}{\partial r^2} + \frac{1}{r} \frac{\partial w_1}{\partial r} + \frac{\partial^2 w_1}{\partial x^2} \right). \quad (\text{B.8b})$$

Due to fluid incompressibility, mass conservation is given by:

$$\frac{\partial u_1}{\partial r} + \frac{u_1}{r} + \frac{\partial w_1}{\partial x} = 0. \quad (\text{B.9})$$

We introduce the Stokes' current function Ψ which satisfies the following relationships and Eq. B.9:

$$u_1 = \frac{1}{r} \frac{\partial \Psi}{\partial x} \quad \text{and} \quad w_1 = -\frac{1}{r} \frac{\partial \Psi}{\partial r}. \quad (\text{B.10})$$

We rewrite Eq. B.8a and Eq. B.8b with Ψ and neglect the squares and products of the velocity components for small perturbations, thus Ψ is solution of:

$$\left(\mathcal{D} - \frac{\rho_1}{\eta_1} \frac{\partial}{\partial t} \right) \mathcal{D}\Psi = 0 \quad , \quad (\text{B.11})$$

where \mathcal{D} is the differential operator $\mathcal{D} = \frac{\partial^2}{\partial r^2} - \frac{1}{r} \frac{\partial}{\partial r} + \frac{\partial^2}{\partial x^2}$, ρ_1 and η_1 are the density and the viscosity of one fluid.

One can decompose Ψ into two subfunctions Ψ^* and Ψ^{**} for which the general solution is:

$$\begin{aligned} \Psi &= \Psi^* + \Psi^{**} \\ &= (A_1 r I_1(kr) + B_1 r K_1(kr) + A_2 r I_1(k_1 r) + B_2 r K_1(k_1 r)) e^{i(\sigma t + kx)} \quad , \end{aligned} \quad (\text{B.12})$$

where a sinusoidal solution in $e^{i(\sigma t + kx)}$ is considered with the wave number k_1 satisfying $k_1^2 = k^2 + \frac{i\eta_1 \sigma}{\rho_1}$. The functions I_1 and K_1 are Bessel functions.

Then, we need boundary conditions to find the values of the constants A_1 , B_1 , A_2 and B_2 in both inner and outer fluids. The following conditions are considered:

- Continuity of the velocity components at the interface between both fluids in $r = r_c$:

$$\left(\frac{1}{r} \frac{\partial \Psi_2}{\partial x} \right)_{r=r_c} = \left(\frac{1}{r} \frac{\partial \Psi_1}{\partial x} \right)_{r=r_c} \quad \text{and} \quad \left(\frac{1}{r} \frac{\partial \Psi_2}{\partial r} \right)_{r=r_c} = \left(\frac{1}{r} \frac{\partial \Psi_1}{\partial r} \right)_{r=r_c}. \quad (\text{B.13})$$

- Continuity of the tangential stress at the interface between both fluids in $r = r_c$:

$$\eta_2 \left(\frac{\partial^2 \Psi_2}{\partial r^2} - \frac{1}{r} \frac{\partial \Psi_2}{\partial r} - \frac{\partial^2 \Psi_2}{\partial x^2} \right)_{r=r_c} = \eta_1 \left(\frac{\partial^2 \Psi_1}{\partial r^2} - \frac{1}{r} \frac{\partial \Psi_1}{\partial r} - \frac{\partial^2 \Psi_1}{\partial x^2} \right)_{r=r_c}. \quad (\text{B.14})$$

- The difference of normal stresses is given by the interfacial tension:

$$(\sigma_{rr}^1)_{r=r_c} - (\sigma_{rr}^2)_{r=r_c} = - \left((p_1 - p_2) + 2\eta_2 \frac{\partial u_2}{\partial r} - 2\eta_1 \frac{\partial u_1}{\partial r} \right)_{r=r_c} = \gamma \kappa. \quad (\text{B.15})$$

Solving this whole set of equations allows to find a relationship between the growth rate σ and the wave number k , which especially depends on the viscosity ratio η_2/η_1 and to deduce the different relationships presented in §3.2.1.

Appendix C

Microfluidic fabrication: the “sticker technique”

We describe how the microfluidic channels in Chapter 6 are built, by using the “sticker technique” [8].

C.1 Fabrication of the channel

The microfluidic channel is synthesized by using polymeric stickers.

C.1.1 Fabrication of the sticker

A sticker is a layer of polymer material of controlled size. The polymer we use is the thiolene-based resin NOA 81 (Norland Optical Adhesive). NOA is more resistant to swelling than PDMS (polydimethylsiloxane used for most microfluidic chips) and has an elastic modulus higher than PDMS, which allows to reduce the deformation of the polymer when an external force is applied. We first generate a mold of our channel by curing PDMS over a silicon wafer on which the channel pattern is drawn. We deposit a drop of NOA on the resulting PDMS stamp and we press the liquid polymer with a black borosilicate glass lamella. PDMS is permeable to air, which allows to obtain a thin polymer film with no trapped air bubbles. Then, we cure the polymer by UV light through the transparent PDMS stamp before removing the PDMS stamp. We obtain the black glass with the epoxy stucked to it and representing the main channel.

We also punch holes beforehand through the black glass and the PDMS stamp for the inlet and the outlet ports. Afterwards, we treat the channel under plasma to oxydize the surface of the channel and make it hydrophilic.

C.1.2 Fabrication of the pattern

The mold for the pattern is created by soft photolithography. We deposit small droplets of epoxy on the mold. We cover the polymer with a thin glass lamella and let trapped air leave the epoxy through the PDMS stamp during 2 hours at least. Then, we cure the epoxy to print the pattern in the epoxy material. We stick the pattern to the top of the channel by curing once more under UV.

C.2 Sketch of the microfabrication

In Fig. C.1, a sketch summarizing the microfabrication process is presented. The pictures in Fig. C.2 depict three different components of the “sticker technique”.

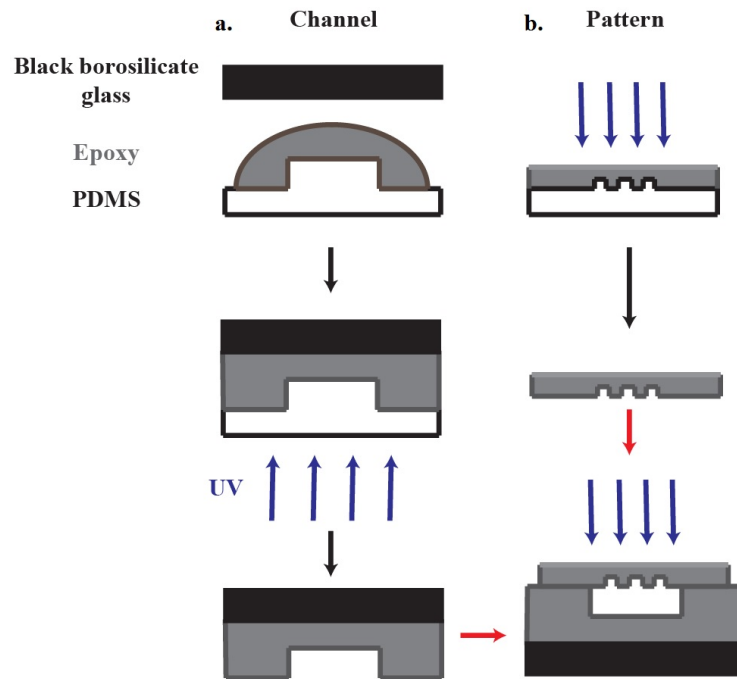


Figure C.1: a. Fabrication of the microfluidic channel. b. Fabrication of the textured pattern.

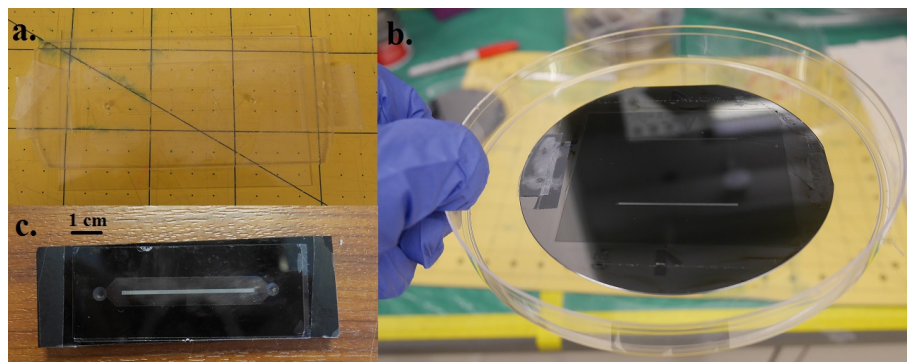


Figure C.2: a. PDMS mold for the main channel. b. Negative of the textured pattern on a silicon wafer. c. Microfluidic channel ready for experiments.

Appendix D

Properties of textured surfaces

We come back on the main properties of superhydrophobic and liquid-infused surfaces and how to tune their properties. By doing so, we underline their great interest and why the understanding of failure mechanisms in Chapter 6 is of considerable scope.

D.1 Properties of superhydrophobic surfaces

D.1.1 Self-cleaning

The roughness of a surface enhances its hydrophobicity. This property is well-described in the regime of air cushion (also known as the Cassie-Baxter regime) where air pockets are trapped under the deposited liquid droplet. The hydrophobicity is characterized by the apparent contact angle θ^* whose value is higher than the Young contact angle θ_Y , as shown in Fig. 6.1.

Thus, on a textured surface, it is possible to reach a superhydrophobic state for which θ^* is close to 180° . Such a property is very common in nature. We can cite two examples pictured in Fig. D.1. The first one is the duck feather. The feather can be assimilated as a fiber textured surface that allows ducks to remain “dry” in spite of the wet environment. The second one is the lotus leaf which is covered by a multitude of bumps of micrometric size. These microstructures give a self-cleaning character to the leaf. Subsequently, water droplets deposited on a lotus leaf roll over the leaf.

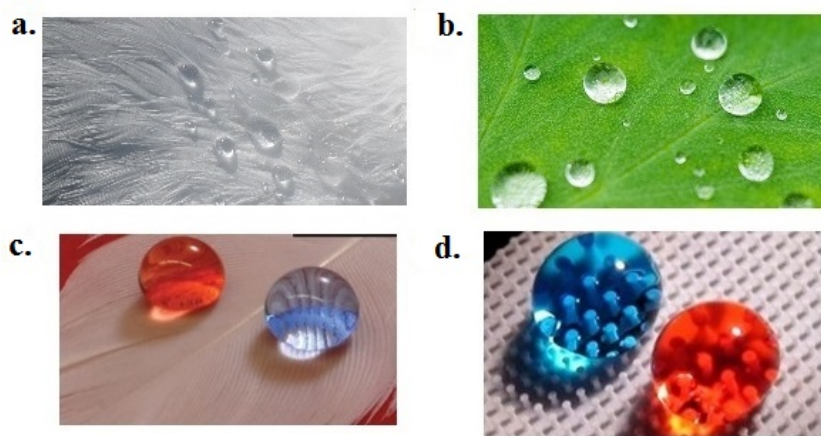


Figure D.1: a. Gull feather repelling water (Source: *matthewwills.com*). b. Water droplets rolling down a lotus leaf (Source: *Hydrobead*). c. Water (in blue - $\gamma_{aw} = 72.1$ mN/m) and rapeseed oil (in red - $\gamma_{aw} = 35.5$ mN/m) on a shelduck feather dip-coated in a solution of 50/50 fluorodecyl POSS/Tecnoflon [173]. d. Water (blue) and octane (red) droplets on a textured surface (Source: *Scientific American*).

D.1.2 Controlling the hydrophobicity

To control the hydrophobicity, one can think about increasing the Young contact angle, which means playing on the chemical properties of the liquid droplet. Another interesting solution consists in increasing the roughness of the surface. The ideal configuration is to trap air pockets

in the textured surface and avoids the transition to the Wenzel state, as underlined in §6.1.1.3. In order to do so, the main idea is to sharpen the defects and increase the number of discontinuities. Fig. D.2 shows the transition of an air-liquid contact line moving in the vicinity of a solid defect. Before reaching the defect, the contact line makes the Young contact angle θ_Y with the solid surface. While reaching the defect, the contact angle can take any value between θ_Y and $\pi - \Psi + \theta_Y$, where Ψ is the opening angle of the defect. This phenomenon is called canthotaxia: the contact line is anchored at the defect and sweeps every value in the interval mentioned above.

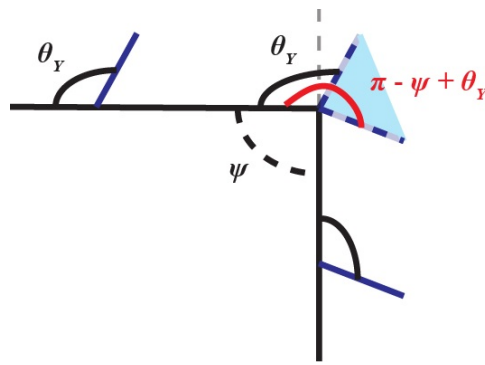


Figure D.2: Anchored air-liquid contact line around a defect on a solid surface.

For instance, let us consider the case of the plot structure presented in the calculations of §6.1.1. In this situation, $\Psi = 90^\circ$ and the contact angle varies from θ_Y to $\pi/2 + \theta_Y$. Given that $\theta_Y > 90^\circ$ for hydrophobic surfaces, the contact angle can reach a value of 180° and remains anchored. Thus, increasing the roughness of the surface creates more sharp discontinuities and is favourable to trap air pockets, as well as to improve the hydrophobicity. Shapes, such as spikes, mushrooms and fibers, are all well-studied and used, as shown in Fig. D.3.

D.1.3 Tuning the oleophobicity

The superhydrophobicity of textured surfaces (θ^* close to 180°) is induced for water droplets exhibiting a non-wetting behaviour on a smooth surface with $\theta_Y > 90^\circ$. However, other liquids with low air-liquid interfacial tensions, such as oils, exhibit an oleophilic behaviour ($\theta_Y < 90^\circ$) and wet most surfaces. According to §6.1.1.2, the textured surface should also present an oleophilic (oil-attractive) character and a fully-wetted surface. However, one can wonder whether it is possible to tune the textured surface and make it oleophobic (oil-repellent) by trapping air pockets in a Cassie-Baxter regime.

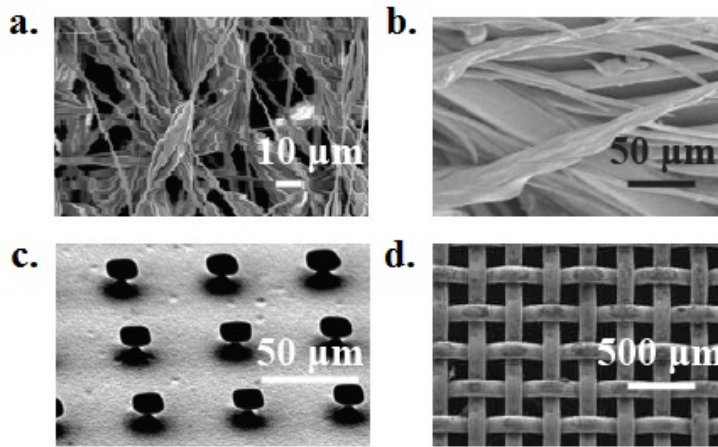


Figure D.3: Different texture geometries enhancing hydrophobicity and oleophobicity (images from Scanning Electron Microscopy). a. Electrospun fibers of PMMA (poly(methyl) methacrylate)-fluorodecyl POSS [185]. b. Barbules of a duck feather dip-coated in fluorodecyl POSS/Tecnoflon [37]. Electrospun beads on strings of fluorodecyl POSS [185]. d. Mesh geometry dip-coated in fluorodecyl POSS/Tecnoflon [36].

The answer is positive if one plays again on the geometry of the texture. Fig. D.4 presents two possible geometries.

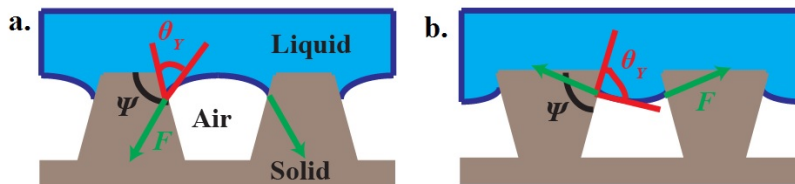


Figure D.4: a. Texture without any reentrant curvature: $\Psi > 90^\circ$ and $\theta_Y < \Psi$. b. Texture with a reentrant curvature: $\Psi < 90^\circ$ and $\theta_Y > \Psi$ [185].

In Fig. D.4a, $\theta_Y < \Psi$ where $\Psi > 90^\circ$ is the opening angle of the texture. As a result, the total force exerted on the air-liquid interface is directed downwards and tends to pull the interface to the bottom of the pore and the fully-wetted regime. On the contrary, in Fig. D.4b, $\theta_Y > \Psi$. This situation corresponds to a re-entrant texture curvature for which $\Psi < 90^\circ$. The total force exerted on the air-liquid interface is directed upwards and tends to lift the interface to the top of the plots. This allows to trap air pockets under the liquid droplet with $\theta^* > 90^\circ$ even though $\theta_Y < 90^\circ$. Thus, for wetting oils, textured surfaces must have a re-entrant curvature $\Psi < 90^\circ$ to be oleophobic. For instance, beads on strings and meshes create such configurations. The Cassie-Baxter regime is metastable and the air-oil interfaces can also be subject to local sagging.

D.2 Properties of liquid-infused surfaces

D.2.1 Rolling and pinning effects on liquid-infused surfaces

The wetting of liquid droplets can be considerably modified on liquid-infused surfaces compared to smooth and common textured surfaces. In particular, liquid-infused surfaces have a strong influence on the contact angle hysteresis.

On an ideal smooth surface, a liquid droplet makes the Young equilibrium contact angle θ_Y with the solid surface. However, when chemical (difference of chemical treatment) or physical (roughness) defects appear, the static contact angle can take different values. The droplet is pinned on the defect. If one swells the droplet, the contact angle increases without any movement of the contact line. Above a certain threshold value θ_a , the contact line advances: θ_a is called the advancing contact angle. On the opposite, if one unswells the droplet, the contact angle decreases without any movement of the contact line. Below a certain threshold value θ_r , the contact line recedes: θ_r is the receding contact angle. The difference between the advancing and the receding contact angle is the contact angle hysteresis: $\Delta\theta = \theta_a - \theta_r$ [96].

We are able to observe the effect of $\Delta\theta$ by tilting the solid surface. Due to the capillary forces (for millimetric droplets) induced by this hysteresis, the droplet does not fall with gravity. However, as depicted in Fig. D.5, when the contact angle at the head of the droplet reaches θ_a and the contact angle at the tail of the droplet reaches θ_r , the droplet slides down the inclined surface. Therefore, the contact angle hysteresis allows to characterize the ability of a droplet to slide or to remain stuck to a surface. The lower $\Delta\theta$, the more easily it slides. The higher $\Delta\theta$, the more easily it remains stuck.

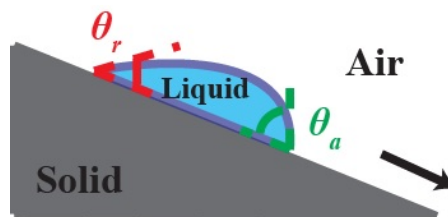


Figure D.5: Liquid drop sliding down an inclined surface.

As shown in Fig. D.6, liquid droplets deposited on a liquid-infused surface exhibit a very small contact angle hysteresis ($\Delta\theta < 3^\circ$), while usual wetting on superhydrophobic textured surfaces exhibit $\Delta\theta > 10^\circ$.

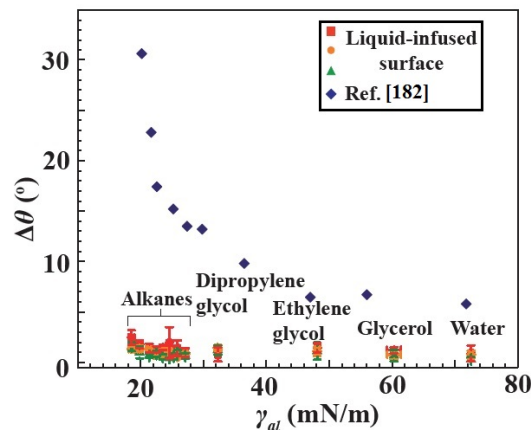


Figure D.6: Contact angle hysteresis $\Delta\theta$ ($^{\circ}$) as a function of the air-liquid interfacial tension γ_{al} (mN/m) [199]. The red squares, the orange rounds and the green triangles correspond to three different liquid-infused surfaces (fluorinated lubricant and teflon/epoxy material). The blue diamonds refer to measurements on omniphobic surfaces in [185].

Due to the small contact angle hysteresis, it is very easy for an immiscible liquid droplet to roll off a liquid-infused surface without leaving a lot of residual liquid behind it. For smooth and omniphobic surfaces, the droplet remains pinned on the defects or the texture and leaves a stain when sliding down a tilted surface [199].

D.2.2 Conditions for slippery surfaces

The hysteresis $\Delta\theta$ is small providing that the droplet floats on the liquid-infused surface. If it sinks, pinning can arise and the slippery character is lost. One can determine the condition for which pinning does not happen. Wong et al. [199] and Lafuma et al. [111] have suggested to compare the interfacial energy of a droplet sitting on the liquid-infused surface and a droplet sinking to the bottom of a texture cavity, as sketched in Fig. D.7.

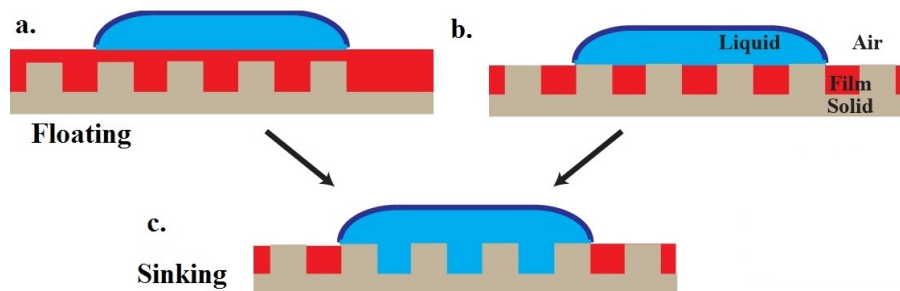


Figure D.7: a. Immiscible droplet floating on the lubricant layer covering the whole texture (complete wetting). b. Immiscible droplet floating on the liquid-infused surface. c. Sinking of the droplet towards the bottom of the cavities.

Fig. D.7 shows two possible initial configurations: with and without the lubricating film covering the top of the texture. This latter is possible if the lubricant completely wets the solid surface. We introduce the solid-droplet γ_{s2} , the solid-film γ_{s1} and the film-droplet γ_{12} interfacial tensions. From Fig. D.7a to the final state (Fig. D.7c), one finds that the loss of interfacial energy is $r\gamma_{s1} + \gamma_{12}$ (respectively $(r - \phi_S)\gamma_{s1} + (1 - \phi_S)\gamma_{12}$ when we start from Fig. D.7b). The gain of interfacial energy is $r\gamma_{s2}$ (respectively $(r - \phi_S)\gamma_{s2}$). The variation of interfacial energy ΔE from the floating to the pinning configuration is written as:

$$\Delta E = r(\gamma_{s2} - \gamma_{s1}) - \gamma_{12} \quad \text{or} \quad \Delta E = (r - \phi_S)(\gamma_{s2} - \gamma_{s1}) - (1 - \phi_S)\gamma_{12}. \quad (\text{D.1})$$

We can write the Young relationships $\gamma_{s2} - \gamma_{s1} = \gamma_{a1} \cos \theta_1 - \gamma_{a2} \cos \theta_2$ where γ_{a1} and γ_{a2} are the air-film and air-droplet interfacial tensions, with θ_1 and θ_2 the Young's contact angles for both film and droplet. Setting $dE > 0$ for floating droplets yields the following condition from Eq. D.1:

$$\gamma_{a1} \cos \theta_1 - \gamma_{a2} \cos \theta_2 > \frac{\gamma_{12}}{r} \quad \text{or} \quad \gamma_{a1} \cos \theta_1 - \gamma_{a2} \cos \theta_2 > \frac{(1 - \phi_S)\gamma_{12}}{r - \phi_S}. \quad (\text{D.2})$$

This condition for floating droplets and thus slippery surfaces can be fulfilled if the lubricant exhibits a complete wetting ($\theta_1 \approx 0$) with the solid surface being hydrophobic ($\theta_2 > 90^\circ$) towards the immiscible droplet. Decreasing the interfacial tension between the lubricant and the droplet, as well as increasing the roughness of the texture are also necessary conditions.

The no-pinning character of liquid-infused surfaces is considerably useful in many applications [3, 25, 65, 102, 171, 202]. The slippery nature of the surface allows to remove stains and to reduce drag. The small contact angle hysteresis hinders the well-known coffee ring effect for the evaporation of particle-laden liquid droplets [53]. When liquid evaporates, particles accumulate where the contact line is pinned. However, on liquid-infused surfaces, particles accumulate uniformly at the center of the evaporating droplet because the receding air-liquid contact line cannot pin the deposition surface. This is particularly useful if one wishes to concentrate particles in small aggregates (for chemical synthesis for instance).

Unlike omniphobic textured surfaces, liquid-infused surfaces cannot fail by sagging phenomena. They are robust to any pressure-driven distortions. Yet, liquid-infused surfaces can lose their properties when they interact dynamically with an external flow dragging the lubricating film out of the texture. In the following sections, we focus on the shear-driven failure of these surfaces with the aim to understand how impregnated oil can be extracted from a micropatterned porous medium.

Bibliography

- [1] A. W. Adamson. *Physical Chemistry of Surfaces*. John Wiley and Sons, 1976. [17](#)
- [2] V. Alvarado and E. Manrique. Enhanced oil recovery: An update review. *Energies*, 3:1529–1575, 2010. [43](#)
- [3] S. Anand, A. T. Paxson, R. Dhiman, J. D. Smith, and K. K. Varanasi. Enhanced condensation on lubricant-impregnated nanotextured surfaces. *ACS Nano*, 6:10122–10129, 2012. [229](#)
- [4] A. S. Aronson, V. Bergeron, M. E. Fagan, and C. J. Radke. The influence of disjoining pressure on foam stability and flow in porous media. *Col. Surf. A*, 83:109–120, 1997. [21](#)
- [5] R. Aveyard, B. P. Binks, P. D. I. Fletcher, T. G. Peck, and C. E. Rutherford. Aspects of aqueous foam stability in the presence of hydrocarbon oils and solid particles. *Adv. Col. Int. Sci.*, 48: 93–120, 1994. [101](#), [112](#)
- [6] L. Bacri, , G. Debrégeas, and F. Brochard-Wyart. Experimental study of the spreading of a viscous droplet on a nonviscous liquid. *Langmuir*, 12:6708–6711, 1996. [104](#), [106](#)
- [7] D. Bartolo, D. Bouamrène, E. Verneuil, A. Buguin, P. Silberzan, and S. Moulinet. Bouncing or sticky droplets: Impalement transitions on superhydrophobic micropatterned surfaces. *Europhys. Lett.*, 74:299–305, 2006. [xxiii](#), [173](#), [174](#), [175](#)
- [8] D. Bartolo, G. Degré, P. Nghe, and V. Studer. Microfluidic stickers. *Lab On a Chip*, 8:274, 2008. [179](#), [219](#)
- [9] E. Basheva, D. Ganshev, N. D. Denkov, K. Kasuga, N. Satoh, and K. Tsujii. Role of betaine as foam booster in the presence of silicone oil drops. *Langmuir*, 16:1000, 2000. [138](#), [144](#), [180](#)
- [10] G. K. Batchelor. *An Introduction to Fluid Dynamics*. Cambridge Univ. Press, 1967. [103](#)
- [11] V. Bergeron. Disjoining pressures and film stability of alkyltrimethylammonium bromide foam films. *Langmuir*, 13:3474–3482, 1997. [31](#)

- [12] V. Bergeron. Forces and structure in thin liquid soap films. *J. Phys.: Cond. Matter*, 11:R215, 1999. [21](#)
- [13] V. Bergeron and D. Langevin. Monolayer spreading of polydimethylsiloxane oil on surfactant solutions. *Phys. Rev. Lett.*, 76:3152–3155, 1996. [xix](#), [31](#), [101](#), [102](#), [104](#), [114](#)
- [14] V. Bergeron and C. J. Radke. Equilibrium measurements of oscillatory disjoining pressures in aqueous foam films. *Langmuir*, 8:3020–3026, 1992. [59](#)
- [15] V. Bergeron and C. J. Radke. Disjoining pressure and stratification in asymmetric thin-liquid films. *Col. Polym. Sci.*, 273:165–174, 1996. [xvii](#), [31](#), [59](#), [60](#)
- [16] A. L. Biance, C. Clanet, and D. Quéré. First steps in the spreading of a liquid droplet. *Phys. Rev. E*, 69:016301, 2004. [110](#)
- [17] J. Bico, C. Tordeux, and D. Quéré. Rough wetting. *Europhys. Lett.*, 55:214–220, 2001. [169](#), [170](#)
- [18] M. G. Blyth and C. Pozrikidis. Effect of surfactants on the stability of two-layer channel flow. *J. Fluid Mech*, 505:59–86, 2004. [189](#), [190](#)
- [19] A. Bonfillon and D. Langevin. Viscoelasticity of monolayers at oil-water interfaces. *Langmuir*, 9:2172–2177, 1993. [24](#)
- [20] K. A. Brakke. The Surface Evolver. *Exp. Math.*, 1:141–165, 1992. [xv](#), [15](#), [16](#)
- [21] K. A. Brakke. The Surface Evolver and the stability of liquid surfaces. *Philos. Trans. Roy. Soc. A.*, 354:2143–2157, 1996. [xv](#), [16](#), [32](#)
- [22] F. P. Bretherton. The motion of long bubbles in tubes. *J. Fluid Mech.*, 10:166, 1961. [197](#)
- [23] F. Brochard-Wyart, G. Debrégeas, and P. G. De Gennes. Spreading of viscous droplets on a non viscous liquid. *Col. Polym. Sci.*, 274:70–72, 1996. [104](#)
- [24] F. Brochard-Wyart, J. M. Di Meglio, D. Quéré, and P. G. De Gennes. Spreading of nonvolatile liquids in a continuum picture. *Langmuir*, 7:335–338, 2011. [97](#), [112](#)
- [25] A. Busse, N. D. Sandham, G. McHale, and M. I. Newton. Change in drag, apparent slip and optimum air layer thickness for laminar flow over an idealised superhydrophobic surface. *J. Fluid. Mech.*, 727:488–508, 2013. [229](#)
- [26] T. Cambau, J. Bico, and E. Reyssat. Capillary rise between flexible walls. *Europhys. Lett.*, 96:24001, 2011. [125](#)

- [27] D. W. Camp and J. C. Berg. The spreading of oil on water in the surface-tension regime. *J. Fluid. Mech.*, 184:445, 1987. [102](#), [114](#)
- [28] I. Cantat, S. Cohen-Addad, F. Elias, F. Graner, R. Höhler, O. Pitois, F. Rouyer, and A. Saint-Jalmes. *Foams: Structure and Dynamics*. Oxford Press, 2013. [22](#), [24](#), [27](#), [30](#), [64](#), [106](#), [127](#), [133](#), [150](#), [196](#)
- [29] H. Caps, S. Cox, H. Decauwer, D. Weaire, and N. Vandewalle. Capillary rise in foams under microgravity. *Col. Surf. A*, 261:131, 2005. [xxii](#), [143](#), [146](#)
- [30] P. C. Carman. Fluid flow through granular beds. *Trans. Inst. Chem. Eng.*, 15:150–166, 1937. [200](#)
- [31] A. M. Cazabat and M. A. Cohen Stuart. Dynamics of wetting on smooth and rough surfaces. *Prog. Col. Polym. Sci.*, 74:69–75, 1987. [xix](#), [99](#), [101](#), [209](#)
- [32] F. Charru. *Instabilités Hydrodynamiques*. CNRS Editions, 2007. [78](#), [80](#)
- [33] F. Charru and E. J. Hinch. “Phase diagram” of interfacial instabilities in a two-layer couette flow and mechanism of the long-wave instability. *J. Fluid Mech.*, 414:195–223, 2000. [189](#)
- [34] Y. Cheng, X. Yel, and H. R. Ma. Solidlike spreading of a liquid/liquid system. *App. Phys. Lett.*, 89:181906, 2006. [102](#)
- [35] C. Chevalier, A. Lindner, M. Leroux, and E. Clément. Morphodynamics during air injection into a confined granular suspension. *J. Non-Newt. Fluid Mech.*, 158:63–72, 2009. [66](#)
- [36] S. S. Chhatre, W. Choi, A. Tuteja, K. C. Park, J. M. Mabry, G. H. McKinley, and R. E. Cohen. Scale dependence of omniphobic mesh surfaces. *Langmuir*, 26:4027–4035, 2009. [xxvii](#), [226](#)
- [37] W. Choi, A. Tuteja, S. S. Chhatre, J. M. Mabry, R. E. Cohen, and G. H. McKinley. Fabrics with tunable oleophobicity. *Adv. Mat.*, 21:2190–2195, 2009. [xxvii](#), [226](#)
- [38] I. Christov and H. A. Stone. Resolving a paradox of anomalous scalings in the diffusion of granular materials. *Proc. Natl. Acad. Sci. USA*, 10:1073, 2012. [143](#)
- [39] A. Cohen, N. Fraysse, J. Rajchenbach, M. Argentina, Y. Bouret, and C. Raufaste. Inertial mass transport and capillary hydraulic jump in a liquid foam microchannel. *Phys. Rev. Lett.*, 112:218303, 2014. [45](#), [149](#)
- [40] A. Cohen, N. Fraysse, and C. Raufaste. Drop coalescence and liquid flow in a single plateau border. *Phys. Rev. E*, 91:053008, 2015. [45](#)

- [41] S. Cohen-Addad and R. Höhler. Rheology of foams and highly-concentrated emulsions. *Cur. Op. Col. Int. Sci.*, 19:536–548, 2014. [35](#)
- [42] S. Cohen-Addad, R. Höhler, and O. Pitois. Flow in foams and flowing foams. *Ann. Rev. Fluid Mech.*, 45:241–267, 2013. [xxi](#), [130](#), [131](#), [133](#), [152](#)
- [43] S. Colombano, A. Saada, V. Guerin, P. Bataillard, G. Bellenfant, S. Beranger, D. Hube, C. Blanc, C. Zornig, and I. Girardeau. *Quelles Techniques pour quel Traitements - Analyse Coûts-Bénéfices*. BRGM, 2010. [40](#)
- [44] C. Conn, K. Ma, G. J. Hirasaki, and S. Biswal. Visualizing oil displacement with foam in a microfluidic device with permeability contrast. *Lab on a Chip*, 14:3968, 2014. [44](#)
- [45] P. Coussot. *Rheophysics - Matter in All States*. Springer, 2014. [32](#), [33](#)
- [46] R. G. Cox. The dynamics of the spreading of liquids on a solid surface. Part 1. Viscous flow. *J. Fluid Mech.*, 168:169–194, 1986. [186](#)
- [47] S. J. Cox, D. Weaire, and G. Verbist. Comment on “Foam imbibition in microgravity. an experimental study” by H. Caps, H. Decauwer, M. L. Chevalier, G. Soyvez, M. Ausloos and N. Vandewalle. *Eur. Phys. J. B*, 40:119, 2004. [143](#)
- [48] R. V. Craster and O. K. Matar. On the dynamics of liquid lenses. *J. Col. Int. Sci.*, 303:503–516, 2006. [102](#)
- [49] F. E. C. Culick. Comments on a ruptured soap film. *J. Appl. Phys.*, 31:1128, 1960. [27](#)
- [50] L. P. Dake. *Fundamentals of Reservoir Engineering*. Elsevier, 1978. [200](#)
- [51] C. Dame, C. Fritz, O. Pitois, and S. Faure. Relations between physicochemical properties and instability of decontamination foams. *Col. Surf. A.*, 263:210–218, 2005. [42](#)
- [52] H. Darcy. *Les fontaines publiques de la ville de Dijon: exposition et application des principes à suivre et des formules à employer dans les questions de distribution d’eau*. Victor Dalmont, 1856. [129](#)
- [53] R. D. Deegan, O. Bakajin, T. F. Dupont, G. Huber, S. R. Nagel, and T. A. Witten. Capillary flow as the cause of ring stains from dried liquid drops. *Nature*, 389:827–829, 1997. [229](#)
- [54] R. Deleurence, T. Saison, F. Lequeux, and C. Monteux. Time scales for drainage and imbibition in gellified foams: application to decontamination processes. *Soft Matter*, 11:7032–7037, 2015. [161](#)

- [55] T. Delker, D. B. Pengra, and P. Z. Wong. Interface pinning and the dynamics of capillary rise in porous media. *Phys. Rev. Lett.*, 76:2902–2905, 1996. [124](#)
- [56] N. D. Denkov. Mechanisms of foam destruction by oil-based antifoams. *Langmuir*, 20: 9463–9505, 2004. [xvii](#), [5](#), [50](#), [51](#), [52](#), [54](#), [56](#), [58](#), [91](#), [106](#)
- [57] N. D. Denkov, V. Subramanian, D. Gurovich, and A. Lips. Wall slip and viscous dissipation in sheared foams: Effect of surface mobility. *Col. Surf. A*, 263:129–145, 2005. [xxvi](#), [37](#), [196](#), [197](#), [198](#)
- [58] N. D. Denkov, S. Tcholakova, K. Golemanov, V. Subramanian, and A. Lips. Foam-wall friction: effect of air volume fraction for tangentially immobile bubble surface. *Col. Surf. A*, 282:329–347, 2006.
- [59] N. D. Denkov, S. Tcholakova, K. Golemanov, K. P. Ananthpadmanabhan, and A. Lips. The role of surfactant type and bubble surface mobility in foam rheology. *Soft Matter*, 5:3389–3408, 2009. [196](#), [197](#)
- [60] B. Dollet and C. Raufaste. Rheology of foams. *C. R. Physique*, 15:731–737, 2014. [35](#)
- [61] R. J. Donnelly and W. Glaberson. Experiments on the capillary instability of a liquid jet. *Proc. Roy. Soc A*, 290:547–556, 1966. [80](#)
- [62] C. Duprat, J. M. Aristoff, and H. A. Stone. Dynamics of elastocapillary rise. *J. Fluid Mech.*, 679:641, 2011. [125](#)
- [63] D. J. Durian, D. A. Weitz, and D. J. Pine. Multiple light-scattering probes of foam structure and dynamics. *Science*, 252:686–688, 1991. [88](#)
- [64] J. Eggers, J. R. Lister, and H. A. Stone. Coalescence of liquid drops. *J. Fluid Mech.*, 401: 293–310, 1999. [109](#)
- [65] A. K. Epstein, T. S. Wong, R. A. Belisle, E. M. Boggs, and J. Aizenberg. Liquid-infused structured surfaces with exceptional anti-biofouling performance. *Proc. Natl. Acad. Sci. USA*, 109:13182, 2012. [229](#)
- [66] R. Farajzadeh, A. Andrianov, R. Krastev, G. J. Hirasaki, and W. R. Rossen. Foam-oil interaction in porous media: Implications for foam assisted enhanced oil recovery. *Adv. Col. Int. Sci.*, 183:1–13, 2012. [44](#)
- [67] K. Feitosa, S. Marze, and A. Saint-Jalmes. Electrical conductivity of dispersions: from dry foams to dilute suspensions. *J. Phys.: Condens. Matter*, 17:6301–6305, 2005. [88](#)

- [68] M. Fermigier and P. Jenffer. An experimental investigation of the dynamic contact angle in liquid-liquid systems. *J. Col. Int. Sci.*, 146:226–241, 1991. [186](#)
- [69] J. G. E. M. Fraaije and A. M. Cazabat. Dynamics of spreading on a liquid substrate. *J. Col. Int. Sci.*, 133:452, 1989. [102](#)
- [70] A. L. Frenkel and D. Halpern. Stokes-flow instability due to interfacial surfactant. *Phys. of Fluids*, 14:45–48, 2002. [189](#)
- [71] G. C. Frye, T. Onda, N. Satoh, and K. Tsujii. Super water-repellent surfaces resulting from fractal structures. *J. Col. Int. Sci.*, 100:19512–19517, 1996. [xxiii](#), [167](#), [168](#)
- [72] P. R. Garrett. Preliminary considerations concerning the stability of a liquid heterogeneity in a plane-parallel liquid film. *J. Col. Int. Sci.*, 76:587–590, 1980. [5](#), [52](#), [54](#)
- [73] P. R. Garrett. *Defoaming: Theory and Industrial Applications*. CRC, 1992. [50](#)
- [74] P. Garstecki, I. Gitlin, W. DiLuzio, G. Whitesides, E. Kumacheva, and H. A. Stone. Formation of monodisperse bubbles in a microfluidic flow-focusing device. *App. Phys. Lett.*, 85:13, 2004. [191](#), [192](#)
- [75] P. Garstecki, H. A. Stone, and G. Whitesides. Mechanism for flow-rate controlled breakup in confined geometries: a route to monodisperse emulsions. *Phys. Rev. Lett.*, 94:164501, 2004. [191](#), [192](#)
- [76] P. Garstecki, M. J. Fuerstmann, H. A. Stone, and G. Whitesides. Formation of droplets and bubbles in a microfluidic T-junction—scaling and mechanism of break-up. *Lab on a chip*, 6:437–446, 2006. [193](#)
- [77] P. G. De Gennes. Wetting: Statics and dynamics. *Rev. Mod. Phys.*, 57:827–863, 1985. [95](#), [96](#), [186](#)
- [78] P. G. De Gennes. Young soap films. *Langmuir*, 17:2416, 2001. [21](#)
- [79] P. G. De Gennes, F. Brochard-Wyart, and D. Quéré. *Capillarity and Wetting Phenomena: Drops, Bubbles, Pearls and Waves*. Springer, 2004. [13](#), [94](#), [186](#)
- [80] J. W. Gibbs. *Transactions of the Connecticut Academy of Arts and Sciences*. 1875. [20](#)
- [81] K. Golemanov, N. D. Denkov, S. Tcholakova, M. Vethamuthu, and A. Lips. Surfactant mixtures for control of bubble surface mobility in foam studies. *Langmuir*, 24:9956–9961, 2008. [xvi](#), [37](#), [138](#), [144](#), [180](#), [195](#)

- [82] E. Guyon, J. P. Hulin, L. Petit, and C. Mitrescu. *Physical Hydrodynamics*. Oxford Univ. Press, 2001. [100](#), [103](#)
- [83] B. Haffner, Y. Khidas, and O. Pitois. Flow and jamming of granular suspensions in foams. *Soft Matter*, 10:3277, 2014. [206](#)
- [84] B. Haffner, Y. Khidas, and O. Pitois. The drainage of foamy granular suspensions. *J. Col. Int. Sci.*, 458:200–208, 2015. [206](#)
- [85] W. B. Hardy. III. The spreading of fluids on glass. *Philo. Mag.*, 38:49–55, 1919. [99](#)
- [86] F. Hauksbee. An account of an experiment touching the ascent of water between two glass planes, in an hyperbolic figure. *Philo. Trans. Roy. Soc. Lond.*, 27:539–540, 1712. [122](#)
- [87] B. Herzhaft, S. Kakadjian, and M. Moan. Measurement and modeling of the flow behavior of aqueous foams using a recirculating pipe rheometer. *Col. Surf. A*, 263:153–164, 2005. [xvi](#), [34](#)
- [88] R. Höhler, Y. Yip Cheung Sang, E. Lorenceau, and S. Cohen-Addad. Osmotic pressure and structures of monodisperse ordered foam. *Langmuir*, 24:418–425, 2008. [xxi](#), [127](#), [135](#)
- [89] S. Hilgenfeldt, S. Koehler, and H. A. Stone. A generalized view of foam drainage. *Phys. Rev. Lett.*, 86:4704, 2001. [136](#)
- [90] R. L. Hoffman. A study of the advancing interface: I. Interface shape in liquid-gas systems. *J. Col. Int. Sci.*, 50:228–241, 1974. [99](#), [186](#)
- [91] A. P. Hooper and W. G. C. Boyd. Shear-flow instability at the interface between two viscous fluids. *J. Fluid Mech.*, 128:507–528, 1983. [189](#)
- [92] C. Huh and L. E. Scriven. Hydrodynamic model of steady movement of a solid/liquid/fluid contact line. *J. Col. Int. Sci.*, 35:85–101, 1971. [186](#)
- [93] S. Hutzler, S. J. Cox, and G. Wang. Foam drainage in 2D. *Col. Surf. A*, 263:178, 2005. [27](#), [143](#)
- [94] J. Israelashvili. *Intermolecular and surface forces*. Academic Press, 1985. [18](#)
- [95] I. Jacobi, J. S. Wexler, and H. A. Stone. Overflow cascades in liquid-infused substrates. *Phys. of Fluids*, 27:082101, 2015. [183](#)
- [96] R. E. Johnson and R. H. Dettre. Contact angle hysteresis. III. Study of an idealized heterogeneous surface. *J. Phys. Chem.*, 68:1744–1750, 1964. [227](#)

- [97] S. A. Jones, B. Dollet, N. Slosse, Y. Jiang, S. J. Cox, and F. Graner. Two-dimensional constriction flows of foams. *Col. Surf. A*, 382:18–23, 2011. [44](#)
- [98] F. Almgren Jr and J. E. Taylor. The geometry of soap films and soap bubbles. *Sci. Am.*, 235:82, 1976. [29](#)
- [99] J. Jurin. An account of some experiments shown before the Royal Society; with an enquiry into the cause of some of the ascent and suspension of water in capillary tubes. *Philo. Trans. Roy. Soc. Lond.*, 30:739–747, 1718. [122](#)
- [100] H. Kellay, J. Meunier, and B. P. Binks. Wetting properties of n-alkanes on AOT monolayers at the brine-air interface. *Phys. Rev. Lett.*, 69:1220–1223, 1992. [101](#), [112](#)
- [101] S. Khan, C. A. Schnepper, and R. C. Armstrong. Foam rheology: III. measurement of shear flow properties. *J. Rheo.*, 32:69, 1988. [xvi](#), [34](#)
- [102] P. Kim, T. S. Wong, J. Alvarenga, M. J. Kreder, W. E. Adorno-Martinez, and J. Aizenberg. Liquid-infused nanostructured surfaces with extreme anti-ice and anti-frost performance. *ACS Nano*, 6:6569, 2012. [229](#)
- [103] K. Koczó, L. A. Lobo, and D. T. Wasan. Effect of oil on foam stability: Aqueous foams stabilized by emulsions. *J. Col. Int. Sci.*, 150:2, 1991. [xvii](#), [45](#), [60](#), [106](#)
- [104] K. Koczó, J. K. Koczóne, and D. T. Wasan. Mechanisms for antifoaming action in aqueous systems by hydrophobic particles and insoluble liquids. *J. Col. Int. Sci.*, 166:225–238, 1994. [56](#)
- [105] S. Koehler, H. A. Stone, M. P. Brenner, and J. Eggers. Dynamics of foam drainage. *Phys. Rev. E*, 58:2097, 1998. [132](#), [133](#), [143](#), [147](#)
- [106] S. Koehler, S. Hilgenfeldt, and H. A. Stone. Liquid flow through aqueous foams: the node-dominated foam drainage equation. *Phys. Rev. Lett.*, 82:4232–35, 1999. [130](#)
- [107] S. Koehler, S. Hilgenfeldt, and H. A. Stone. A generalized view of foam drainage: Experiment and theory. *Langmuir*, 16:6327–6341, 2000. [131](#), [133](#)
- [108] S. Koehler, S. Hilgenfeldt, and H. A. Stone. Foam drainage on the microscale - I. Modeling flow through single Plateau borders. *J. Col. Int. Sci.*, 276:420–438, 2004. [143](#), [152](#)
- [109] K. G. Kornev, A. V. Neimark, and A. N. Rozhkov. Foam in porous media: Thermodynamic and hydrodynamic peculiarities. *Adv. Col. Int. Sci.*, 82:127–187, 1999. [199](#)

- [110] J. Kozeny. Über kapillare Leitung des Wassers im Boden. *Sitzungsber. Akad. Wiss. Wien*, 136:271–306, 1927. [200](#)
- [111] A. Lafuma and D. Quéré. Slippery pre-suffused surfaces. *Europhys. Lett.*, 96:56001, 2011. [172](#), [228](#)
- [112] M. Lago and M. Araujo. Capillary rise in porous media. *J. Col. Int. Sci.*, 234:35–43, 2001. [123](#), [124](#)
- [113] L. D. Landau and E. M. Lifshitz. *Fluid Mechanics*. Pergamon Press, 1987. [103](#)
- [114] P. S. Laplace. *Traité de Mécanique Céleste*. 1805. [15](#)
- [115] L. Léger and J. F. Joanny. Liquid spreading. *Rep. Prog. Phys.*, pages 431–486, 1992. [94](#), [98](#)
- [116] J. G. Leidenfrost. *Traité sur Certaines Propriétés de l'Eau - De aquae communis nonnullis qualitatibus tractatus*. 1756. [15](#)
- [117] M. D. Leelah and A. Marmur. Spreading kinetics of drops on glass. *J. Col. Int. Sci.*, 82:518–525, 1981. [99](#)
- [118] R. Lenormand, C. Zarcone, and A. Sarr. Mechanisms of the displacement of one fluid by another in a network of capillary ducts. *J. Fluid Mech.*, 135:337–353, 1983. [199](#)
- [119] Z. Li, A. M. Leshansky, S. Metais, L. M. Pismen, and P. Tabeling. Step-emulsification in a microfluidic device. *Lab On a Chip*, 15:1023–1031, 2015. [193](#)
- [120] L. Lobo and D. T. Wasan. Mechanisms of aqueous foam stability in the presence of emulsified non-aqueous-phase liquids: structure and stability of the pseudoemulsion film. *Langmuir*, 9:1668–1677, 1993. [55](#)
- [121] E. Lorenceau, N. Louvet, F. Rouyer, and O. Pitois. Permeability of aqueous foams. *Eur. Phys. J. E*, 28:293–304, 2009. [131](#)
- [122] R. Lucas. Über das Zeitgesetz des kapillaren Aufstiegs von Flüssigkeiten. *Kolloid Z.*, 23:15, 1918. [123](#)
- [123] A. Marmur. Wetting on hydrophobic rough surfaces: To be heterogeneous or not to be? *Langmuir*, 19:8343–8348, 2003. [171](#)
- [124] A. Marmur and R. D. Cohen. Characterization of porous media by the kinetics of liquid penetration: The vertical capillaries model. *J. Col. Int. Sci.*, 189:299–304, 1997. [123](#)

- [125] T. G. Mason, M. D. Lacasse, G. S. Grest, D. Levine, J. Bibette, and D. A. Weitz. Osmotic pressure and viscoelastic shear moduli of concentrated emulsions. *Phys. Rev. E*, 56:3150, 1997. [32](#)
- [126] S. Mendez, E. M. Fenton, , G. R. Gallegos, D. N. Petsev, S. S. Sibbett, H. A. Stone, Y. Zhang, and G. P. Lopez. Imbibition in porous membranes of complex shape: Quasi-stationary flow in thin rectangular segments. *Langmuir*, 26:1380, 2009. [132](#)
- [127] R. Mensire, K. Piroird, and E. Lorenceau. Coalescence of dry foam under water injection. *Soft Matter*, 10:7068–7072, 2014. [50](#)
- [128] R. Mensire, K. Piroird, and E. Lorenceau. Capillary imbibition of aqueous foams by miscible and nonmiscible liquids. *Phys. Rev. E*, 92:053014, 2015. [106](#), [143](#)
- [129] R. Mensire, J. T. Ault, E. Lorenceau, and H. A. Stone. Point-source imbibition into dry aqueous foams. *Europhys. Lett.*, 113:44002, 2016. [132](#)
- [130] R. Mensire, J. S. Wexler, A. Guibaud, E. Lorenceau, and H. A. Stone. Surfactant and aqueous foam-driven oil extraction from micropatterned surfaces. *Langmuir*, 2016. [178](#)
- [131] M. Le Merrer, R. Lespiat, R. Höhler, and S. Cohen-Addad. Linear and non-linear wall friction of wet foams. *Soft Matter*, 11:368–381, 2015. [196](#)
- [132] S. J. Neethling, G. Morris, and P. R. Garrett. Modeling oil droplets in Plateau borders. *Langmuir*, 27:9738–9747, 2011. [xviii](#), [45](#), [72](#), [74](#), [75](#), [133](#), [137](#)
- [133] A. V. Nguyen. Liquid drainage in single Plateau borders of foam. *J. Col. Int. Sci.*, 249:194–199, 2002. [130](#), [133](#), [152](#)
- [134] J. D. Paulsen, R. Carmignani, A. Kannan, J. Burton, and S. Nagel. Coalescence of bubbles and drops in an outer fluid. *Nature Comm.*, 2014. [108](#), [109](#)
- [135] P. C. Petit, M. Le Merrer, and A. L. Biance. Holes and cracks in rigid foam films. *J. Fluid Mech.*, 774:R3, 2015. [27](#)
- [136] N. D. Di Pietro, C. Hull, and R. G. Cox. Dynamics of spreading on a liquid substrate. *J. Fluid Mech.*, 84:529, 1978. [104](#)
- [137] K. Piroird and E. Lorenceau. Capillary flow of oil in a single foam microchannel. *Phys. Rev. Lett.*, 111:234503, 2013. [xix](#), [45](#), [50](#), [72](#), [82](#), [83](#), [84](#), [106](#), [137](#), [138](#), [144](#), [149](#), [152](#)
- [138] K. Piroird, E. Lorenceau, and A. L. Biance. Oil repartition in a foam film architecture. *Soft Matter*, 10:7061, 2014. [144](#), [145](#)

- [139] O. Pitois, E. Lorenceau, N. Louvet, and F. Rouyer. Specific surface area model for foam permeability. *Langmuir*, 25:97, 2009. [136](#)
- [140] J. A. F. Plateau. *Statique Expérimentale et Théorique des Liquides Soumis aux Seules Forces Moléculaires*. Gauthier-Villard, 1873. [29](#), [79](#)
- [141] A. Ponomarenko, D. Quéré, and C. Clanet. A universal law for capillary rise in corners. *J. Fluid Mech.*, 666:146–154, 2011. [124](#)
- [142] H. M. Princen. Rheology of foams and highly concentrated emulsions. *J. Col. Int. Sci.*, 105:150–171, 1984. [37](#)
- [143] H. M. Princen and A. D. Kiss. Osmotic pressure of foams and highly concentrated emulsions. 2. Determination from the variation in volume fraction with height in an equilibrated column. *Langmuir*, 3:36–41, 1987. [31](#), [32](#)
- [144] N. Quennouz, M. Ryba, J-F. Argillier, B. Herzhaft, Y. Peysson, and N. Pannacci. Microfluidic study of foams flow for enhanced oil recovery (EOR). *Oil and Gas Sci. Tech.*, 69:457–466, 2014. [44](#)
- [145] D. Quéré. Inertial capillarity. *Europhys. Lett.*, 39:533–538, 1997. [123](#)
- [146] D. Quéré. Wetting and roughness. *Ann. Rev. Mater. Res.*, 38:71–99, 2008. [167](#)
- [147] Lord Rayleigh. On the instability of jets. *Proc. Lond. Math. Soc.*, 10:4, 1879. [80](#)
- [148] Lord Rayleigh. On the capillary phenomena of jets. *Proc. Roy. Soc.*, 29:71, 1879.
- [149] Lord Rayleigh. On the instability of a cylinder of viscous liquid under capillary force. *Philo. Mag.*, 34:145, 1892. [xix](#), [80](#), [85](#)
- [150] D. A. Reinelt and A. M. Kraynik. Simple shearing flow of a dry Kelvin soap foam. *J. Fluid Mech.*, 311:327–343, 1996. [35](#)
- [151] D. A. Reinelt and A. M. Kraynik. Simple shearing flow of dry soap foams with tetrahedrally close-packed structure. *J. Rheo.*, 44:453, 2000. [35](#)
- [152] M. Reyssat, A. Pépin, F. Marty, Y. Chen, and D. Quéré. Bouncing transitions on microtextured materials. *Europhys. Lett.*, 74:306–312, 2006. [173](#)
- [153] M. Reyssat, L. Courbin, E. Reyssat, and H. A. Stone. Imbibition in geometries with axial variations. *J. Fluid Mech.*, 615:335–344, 2008. [124](#), [153](#), [161](#)

- [154] E. Rio and A. L. Biance. Thermodynamic and mechanical timescales involved in foam film rupture and liquid foam coalescence. *ChemPhysChem*, 15:3692–3707, 2014. [25](#), [27](#)
- [155] O. I. Del Rio and A. W. Neumann. Axisymmetric drop shape analysis: Computational methods for the measurement of interfacial properties from the shape and dimensions of pendant and sessile drops. *J. Col. Int. Sci*, 196:136–147, 1997. [17](#)
- [156] W. R. Rossen. *Foams in enhanced oil recovery*. Surfactant Sci. Series, 1996. [44](#)
- [157] J. Rowlinson and B. Widom. *Molecular Theory of Capillarity*. Oxford Univ. Press, 1982. [13](#)
- [158] J. F. Sadoc and N. Rivier. *Foams and Emulsions*. Col. Surf. A, 2010. [27](#)
- [159] A. Saint-Jalmes. Physical chemistry in foam drainage and coarsening. *Soft Matter*, 2:836–849, 2006. [192](#)
- [160] A. Saint-Jalmes, S. Marze, H. Ritacco, D. Langevin, S. Bail, J. Dubail., L. Guingot, G. Roux, P. Sung, and L. Tosini. Diffusive liquid propagation in porous and elastic materials: The case of foams under microgravity conditions. *Phys. Rev. Lett.*, 98:058303, 2007. [143](#), [146](#)
- [161] A. Salonen, R. Lhermerout, E. Rio, D. Langevin, and A. Saint-Jalmes. Dual gas and oil dispersions in water: production and stability of foamulsion. *Soft Matter*, 8:699–706, 2012. [xvii](#), [45](#), [60](#)
- [162] B. Sandnes, E. G. Flekkoy, H. A. Knudsen, K. J. Maloy, and H. See. Patterns and flow in frictional fluid dynamics. *Nature Comm.*, 2:288, 2011. [xviii](#), [66](#)
- [163] S. Sarrade, S. Faure, B. Fournel, and F. Lemont. *Pour des Déchets et des Effluents plus Propres*. CEA, 2010. [42](#)
- [164] F. Savart. *Annales de Chimie*. 1833. [78](#)
- [165] S.Chandrasekhar. *Hydrodynamic and Hydromagnetic Stability*. Dover Publications Inc., 1981. [81](#)
- [166] L. L. Schramm. *Foams: Fundamentals and Applications in the Petroleum Industry*. Am. Chem. Soc., 1994. [44](#)
- [167] R. K. Shah and A. L. London. *Laminar Flow Forced Convection in Ducts*. Academic Press, 1978. [175](#)
- [168] Y. Shikhmurzaev and J. Sprittles. Anomalous dynamics of capillary rise in porous media. *Phys. Rev. E*, 86:016306, 2012. [124](#)

- [169] J. I. Siddique, D. M. Anderson, and A. Bondarev. Capillary rise of a liquid into a deformable porous material. *Phys. Fluids*, 21:013106, 2009. [124](#), [161](#)
- [170] P. Silberzan and L. Léger. Evidence for a new spreading regime between partial and total wetting. *Phys. Rev. Lett.*, 66:185–188, 1991. [97](#)
- [171] J. D. Smith, R. Dhiman, S. Anand, E. Reza-Garduno, R. E. Cohen, G. H. McKinley, and K. K. Varanasi. Droplet mobility on lubricant-impregnated surfaces. *Soft Matter*, 9:1772–1780, 2013. [229](#)
- [172] J. Sonoda, T. Sakai, and Y. Inomata. Liquid oil that flows in spaces of aqueous foam without defoaming. *J. Phys. Chem. B*, 118:9438–9444, 2014. [162](#)
- [173] S. Srinivasan, S. S. Chhatre, J. O. Guardado, K. C. Park, A. R. Parker, M. F. Rubner, G. H. McKinley, and R. E. Cohen. Quantification of feather structure, wettability and resistance to liquid penetration. *J. Roy. Soc. Int.*, 11:20140287, 2014. [xxvi](#), [224](#)
- [174] P. Stevenson. *Foam Engineering: Fundamentals and Applications*. John Wiley and Sons, 2012. [27](#), [38](#)
- [175] T. F. Svitova, R. M. Hill, and C. J. Radke. Spreading of aqueous dimethyldidodecylammonium bromide surfactant droplets over liquid hydrocarbon substrates. *Langmuir*, 15:7392–7402, 1999. [102](#)
- [176] P. Tabeling. *Introduction to Microfluidics*. Oxford Univ. Press, 2006. [191](#)
- [177] G. K. Tampy, W. J. Cen, M. E. Prudich, and R. L. Savage. Wettability measurements of coal using a modified Washburn technique. *Energy & Fuels*, 2:782–786, 1988. [123](#)
- [178] L. H. Tang and Y. Tang. Capillary rise in tubes with sharp grooves. *J. Phys. II*, 4:881, 1994. [124](#)
- [179] L. H. Tanner. The spreading of silicone oil drops on horizontal surfaces. *J. Phys. D*, 12:1473, 1992. [99](#), [186](#)
- [180] G. I. Taylor. The formation of emulsions in definable fields of flow. *Proc. Roy. Soc.*, 146:501, 1934. [81](#)
- [181] G. I. Taylor. The dynamics of thin sheets of fluid. Part III: Disintegration of fluid sheets. *Proc. Roy. Soc. Lond. A*, 253:313, 1959. [27](#)
- [182] Lord Kelvin (Sir W. Thomson). On the division of space with minimum partitional area. *Phil. Mag.*, 24:503, 1887. [30](#)

- [183] S. Tomotika. On the instability of a cylindrical thread of a viscous liquid surrounded by another viscous fluid. *Proc. Roy. Soc.*, 150:322–337, 1935. [xix](#), [81](#), [85](#), [87](#), [215](#)
- [184] S. M. Troian, E. Herbolzheimer, S. A. Safran, and J. F. Joanny. Fingering instabilities of driven spreading films. *Europhys. Lett.*, 10:25–30, 1989. [190](#)
- [185] A. Tuteja, W. Choi, J. M. Mabry, G. H. McKinley, and R. E. Cohen. Robust omniphobic surfaces. *Proc. Natl. Acad. Sci. USA*, 19:18200–18205, 2008. [xxvii](#), [173](#), [226](#), [228](#)
- [186] G. Varas. *Air rise through an immersed granular bed - bulk and surface dynamics*. Ph.D. thesis, Ecole Normale Supérieure de Lyon - Université de Lyon, 2011. [xviii](#), [66](#), [67](#)
- [187] G. Varas, V. Vidal, and J-C Géminard. Morphology of air invasion in an immersed granular layer. *Phys. Rev. E*, 83:061302, 2011. [66](#)
- [188] G. Verbist and D. Weaire. A soluble model for foam drainage. *Europhys. Lett.*, 26:631, 1994. [132](#)
- [189] G. Verbist, D. Weaire, and A. M. Kraynik. The foam drainage equation. *J. Phys. Cond. Matter*, 8:3715, 1996. [130](#), [132](#)
- [190] A. Vrij and J. Th. G. Overbeek. Rupture of thin liquid films due to spontaneous fluctuations in thickness. *Rep. Prog. Phys.*, 90:3074–3078, 1968. [23](#)
- [191] P. B. Warren. Late stages for various wicking and spreading problems. *Phys. Rev. E*, 69:041601, 2004. [149](#)
- [192] E. W. Washburn. The dynamics of capillary flow. *Phys. Rev. Lett.*, 17:273, 1921. [123](#)
- [193] D. Weaire and S. Hutzler. *The Physics of Foams*. Oxford Univ. Press, 1999. [27](#), [150](#)
- [194] D. Weaire and R. Phelan. A counter-example to Kelvin’s conjecture on minimal surfaces. *Philo. Mag.*, 69:107–110, 1994. [30](#)
- [195] D. Weaire and N. Rivier. Soap, cells and statistics—random patterns in two dimensions. *Contemp. Phys.*, 25:59–99, 1984. [35](#)
- [196] D. Weaire, N. Pittet, S. Hutzler, and D. Pardal. Liquid oil that flows in spaces of aqueous foam without defoaming. *Phys. Rev. Lett.*, 71:2670–2673, 1993. [64](#), [65](#)
- [197] R. N. Wenzel. Resistance of solid surfaces to wetting by water. *Ind. Eng. Chem.*, 28:988–994, 1936. [167](#)

- [198] J. S. Wexler, I. Jacobi, and H. A. Stone. Shear-driven failure of liquid-infused surfaces. *Phys. Rev. Lett.*, 114:168301, 2015. [xxiv](#), [163](#), [174](#), [175](#), [178](#), [179](#), [182](#), [183](#), [185](#), [188](#), [189](#), [198](#), [204](#)
- [199] T. S. Wong, S. H. Kang, S. K. Y. Tang, E. J. Smythe, B. D. Hatton, A. Grinthal, and J. Aizenberg. Bioinspired self-repairing slippery surfaces with pressure-stable omniphobicity. *Nature*, 477:443–447, 2011. [xxvii](#), [228](#)
- [200] N. Wu, J. Dai, and F. J. Micale. Dynamic surface tension measurement with a dynamic Wilhelmy plate technique. *J. Col. Int. Sci.*, 215:258–269, 1999. [17](#)
- [201] J. Xiao, H. A. Stone, and D. Attinger. Source-like solution for radial imbibition into a homogeneous semi-infinite. *Langmuir*, 2012. [132](#), [142](#)
- [202] R. Xiao, N. Miljkovic, R. Enright, and E. N. Wang. Enhanced condensation on lubricant-impregnated nanotextured surfaces. *Sci. Reports*, 3:1988, 2013. [229](#)
- [203] P. Yazhgur. How antifoams act: a microgravity study. *NPJ Microgravity*, 1:2172–2177, 2015. [57](#)
- [204] C. S. Yih. Instability due to viscous stratification. *J. Fluid Mech.*, 27:337–352, 1967. [189](#)
- [205] T. Young. An essay on the cohesion of fluids. *Philo. Trans. Roy. Soc. Lond. A*, 95:65, 1805. [95](#)
- [206] W. Zisman. *Contact Angle, Wettability and Adhesion*. Chemistry Series, 1964. [96](#)

